UNIVERSITÀ
DEGLI STUDI
DI PADOVA

Università degli Studi di Padova

Dipartimento di Ingegneria Industriale

SCUOLA DI DOTTORATO DI RICERCA IN
SCIENZA ED INGEGNERIA DEI MATERIALI
CICLO XXVI

Tesi di Dottorato

NANOSTRUCTURED MATERIALS FOR PLASMONIC BASED GAS SENSORS

Direttore della Scuola: Ch.mo Prof. Gaetano Granozzi

_____

Supervisore: Ch.mo Prof. Alessandro Martucci

_____

Dottoranda: Michela Cittadini

_____

Abstract

My research work during the PhD was devoted to the development of optical gas sensors based on plasmonics. Sensors based both on Localized Surface Plasmon Resonance (LSPR) and Propagating Surface Plasmon Resonance (PSPR), also known as surface plasmon polaritons (SPP) have been studied. The thesis has been divided in two main chapters.

In the first one LSPR based gas sensor has been developed using gold nanoparticels (NPs) of different shapes like nanorods (NRs) with medium and high aspect ratio, 3 and 6 respectively, nanodumbbells (NDs) and nanostars (NSs). The LSPR is sensitive to changes in the local dielectric environment, and this allows the monitoring of the gases interacting with the matrices, and the output is a shift of the plasmon peak in terms of wavelength. The use of different shapes of NPs is oriented to the increase of sensitivity towards the changes in the local dielectric environment. This higher sensitivity is due to the local field enhancement effect linked to the elongated shapes or with the spikes, in the case of nanostars. The main difficulty about using these NPs is their tendency towards reshaping at the temperature's increase. This constraint enforces the gas sensing tests to be performed at low temperature, therefore, to catalyze the red-ox reaction between the target gases and the sensitive material, platinum NPs are needed.

The gold NRs were also investigated with Dark Field Microscopy (DFM), a technique which enables the monitoring of the single particles behavior in hydrogen flow. Their sensitivity has been tested in both a TiO_2 and ZnO matrix.

The ZnO sensitive material has been tested also directly as plasmonic material, because of its plasmon in the IR region triggered by the doping with Ga^{3+} or Al^{3+} ions, towards hydrogen and nitrogen oxide.

TiO_2 based materials have been also used, in comparison with phenyl-functionalized SiO2 based materials, coupled with Au NPs as Aromatic Volatile Organic Compound A-VOC (xylene, toluene and benzene) sensors.

All the studied materials showed good sensitivity towards the tested gases, and the most important thing is that almost all these really good performances are at low temperature, thanks to the heterogeneous catalysis promoted by the Pt NPs.

These sensitive oxide materials have been tested also, in the second chapter, using SPP, excited illuminating a gold sinusoidal nanometric layer constituting a plasmonic crystals with a sensitive film on the top, interacting with the analyte.

TiO_2 and phenyl-functionalized SiO_2 have been used as sensitive materials in plasmonic crystals to monitor A-VOC and VOC at room temperature and hydrogen at 300 °C, obtaining good performances, comparable to the one of the system based on LSPR.

Moreover the comparison of the same sensitive material in the two configurations, with localized and propagating plasmons, allowed a better understanding of the transducing mechanism.

Sommario

Il presente lavoro di tesi è focalizzato sullo sviluppo di sensori ottici di gas basati sulla plasmonica.
In particolare saranno studiati sensori basati sia su Risonanza Plasmonica Superficiale Localizzata (LSPR) che su Risonanza Plasmonica Superficiale Propagante (PSPR) noti anche come Plolaritoni Superficiali Propaganti (SPP).
Tale tesi è divisa in due capitol principali. Il primo capitolo è dedicato ai sensori basati sulla LSPR, questi sensori sono stati sviluppati usando nanoparticelle di oro (NPs) con forme diverse (quali nanorod (NRs) con aspect ratio media e alta, 3 e 6 rispettivamente, nanodumbell e nanostelle).
La LSPR è sensibile ai cambiamenti della costante dielettrica nell'intorno delle particelle, ciò permette di monitorare i gas che interagiscono con la matrice e ciò risulta in uno spostamento in lunghezza d'onda del picco plasmonico.
L'utilizzo di diverse forme di NPs è legato al all'obiettivo di migliorare la sensibilità del plasmone ai cambiamenti nell'ambiente circostante. Tale aumento della sensibilità è legato ad un fenomeno di local field enhancement relativo alle forme allungate o con punte, come nel caso delle nanostelle.
La maggiore difficoltà relativa all'uso di tali NPs sta nella loro tendenza al cambiare forma e sferoidizzare con la temperatura. Ciò permette di attuare i test di gas sensing solo a basse temperature, quindi per catalizzare le reazioni di ossido-riduzione dovute all'interazione tra i gas e il materiale sensibile vengono utilizzate NPs di platino.
I NRs di oro sono stati utilizzati nella microscopia Dark Field (DFM) con applicazioni sensoristiche; tale tecnica permette di monitorare il comportamento ottico dei singoli NRs durante l'interazione con l'idrogeno.
La sensibilità dei NRs è stata testata sia in matrice di ossido di titanio (TiO_2) che di ossido di zinco (ZnO).
Lo ZnO, in quanto material sensibile, è stato utilizzato anche direttamente come materiale plasmonico, grazie al plasmone nell'IR che viene innescato mediante drogaggio con ioni Ga^{3+} e Al^{3+}, per il sensing di idrogeno e ossido di azoto.
E' stato inoltre utilizzato il TiO_2 come materiale sensibile e le sue performances sono state confrontate con quelle dell'SiO_2 sol-gel funzionalizzato con gruppi fenile per il sensing dei VOC (Volatile Organic Compound) Aromatici, quali benzene, toluene e xylene.
Tutti i materiali studiati in tale capitolo mostrano una buona sensibilità ai gas testati, la cosa più importante è che gran parte delle misure sono state fatte a basse temperature, grazie alla catalisi eterogenea.

Tali materiali sono stati anche testati, nel secondo capitolo, utilizzando i SPP, accesi illuminando uno strato nanometrico sinusoidale di oro, facente parte di un cristallo plasmonico, insieme ad uno strato sensibile che quello che entrerà in contatto con l'analita.

TiO_2 e SiO_2 funzionalizzato con gruppi fenile sono stati usati come materiali sensibili nei cristalli plasmonici per monitorare VOC Aromatici e VOC a temperatura ambiente e idrogeno a 300 °C. Le prestazioni sono piuttosto buone, confrontabili con quelle dei sistemi basati su LSPR.

Inoltre, il confronto degli stessi materiali sensibili nelle due configurazioni, con plasmoni localizzati e propaganti, permette di capire più a fondo i meccanismi coinvolti.

This doctoral project has generated some results that have been published or presented at international conferences. Presentations and publications (also papers in preparation) are listed in the following. Moreover part of the work described in this thesis has been carried out at overseas facilities, and specialization classes or schools have been attended: they are listed in the following as well.

Refereed Journal Publications

M. Cittadini, M. Bersani, F. Perrozzi, L. Ottaviano, W. Wlodarski, A. Martucci, Graphene oxide coupled with gold nanoparticles for Localized Surface Plasmon Resonance based gas sensor, Carbon 69 (2014) 452-459

L. Brigo, M. Cittadini, L. Artiglia, G. A. Rizzi, G. Granozzi, M. Guglielmi, A. Martucci, G. Brusatin, Xylene sensing properties of aryl-bridged polysilsesquioxane thin films coupled to gold nanoparticles, J. Mater. Chem. C, 1 (2013) 4252-4260

L. Brigo, E. Gazzola, M. Cittadini, P. Zilio, G. Zacco, F. Romanato, A. Martucci, M. Guglielmi, G. Brusatin, Short and long range surface plasmon polariton waveguides for xylene sensing, Nanotechnology 24 (2013) 155502 (10pp)

Enrico Della Gaspera, Marco Bersani, Michela Cittadini, Massimo Guglielmi, Diego Pagani, Rodrigo Noriega, Saahil Mehra, Alberto Salleo, Alessandro Martucci, Low-Temperature Processed Ga-Doped ZnO Coatings from Colloidal Inks, J. Am. Chem. Soc. 135 (2013) 3439−3448

Luca Giancaterini, C. Cantalini, M. Cittadini, M. Sturaro, M. Guglielmi, A. Resmini, U. Anselmi-Tamburini, A. Martucci**,** "Au and Pt nanoparticles effects on the optical and electrical gas sensing properties of sol-gel based ZnO thin film sensors", submitted to Sensors & Actuators: B. Chemical

Muhammad U. Qadri, M. Cittadini, A. Martucci, Maria Cinta Pujol, Josep Ferré-Borrull, Eduard Llobet, Magdalena Aguiló and Francesc Díaz, "Optical absorption spectral response of WO_3 thin films with Pt catalyst towards H_2, CO and NO_x gases", submitted to Sensors & Actuators: B. Chemical.

M Cittadini, S. Collins, P. Mulvaney, A. Martucci, "Hydrogen Adsorption on Single Gold Nanocrystals - A Surface Plasmon Spectroscopy Study", in preparation.

M. Cittadini, E. Gazzola, L. Brigo, G. Brusatin, F. Romanato, M. Guglielmi, A. Martucci, "VOC sensing: comparison between localized surface plasmon resonance and propagating surface plasmon resonance", in preparation.

Presentations during National and International Conferences

MRS (Materials Research Society) fall meeting 2013 Boston, Massachusetts, USA, 1st – 6th December 2013, "Plasmonic gas sensors: comparison between localized surface plasmon resonance and surface plasmon polariton VOC sensor" (poster presentation).

Workshop on Nanophotonics 2012, International center of theoretical physics, Trieste, 3st-7th December 2012, "Au rods in TiO_2 films for SPR-based gas sensing" (poster presentation).

VIII Italian Workshop Sol-Gel, University of Trento, 21st-22nd June 2012, "UV Processable titanate nanosheets: a new inorganic resist" (oral presentation).

INSTM - 4° Forum Nazionale Giovani Ricercatori di Scienza e Tecnologia dei Materiali, Padova, 28th-30th May 2012, "Pt monolayers for plasmonic-based gas sensing" (poster presentation).

Visits overseas

Part of the work done during this doctoral project has been developed during visits at overseas facilities, listed below.

28th March 2012 – 28th May 2012: Visiting researcher at the Colloid Chemistry Group, at University of Vigo, Spain. Host: Prof. Luis M. Liz-Marzan. ESMI – European Project: "Thermal stability study of Au nanoparticles with different shapes by using a photosensitive layered titanates"

12th February 2013 – 20th May 2013 and 21st August 2013 – 30th September 2013: Visiting researcher at Bio21 Institute of the University of Melbourne, Melbourne (VIC) Australia. Host: Prof. Paul Mulvaney. "H_2 sensing on single gold nanorods with DFM technique"

Specialization schools

Summer school SAMPA (1_{st} Advanced School on Materials for Photonic Applications - Glasses, Optical Fibers and Sol-Gel Materials) São Paulo State University (UNESP), Brazil, October 2012

WINTER COLLEGE on OPTICS: ADVANCES in NANO OPTICS and PLASMONICS, Italian Society of Optics and Photonics (SIOF), Trieste, February 2012

Summer school on Plasmonics 2, University of Marseilles, Hyeres, France, October 2011

Collaborations and Acknowledgements

The first person I'd like to acknowledge and deeply thank is my supervisor, Prof. Alessandro Martucci, without whom my PhD wouldn't have been so satisfactory and rewarding.

The present work of thesis was realized thanks to a lot of fruitful collaborations:

Dr. Laura Brigo, Prof. Giovanna Brusatin, Mr. Enrico Gazzola, Prof. Filippo Romanato are acknowledged for all the experiments performed with PSPR technique.

In particular Mr. Enrico Gazzola for all the SEM presented in this work of thesis.

Prof. Luis M. Liz-Marzan and Prof. Jorge Pérez-Juste are deeply acknowledged for hosting me during my visit at the Colloid Chemistry Group, at University of Vigo, Spain, and for teaching me the synthesis of gold NPs of different shapes.

A grateful acknowledgement goes to Prof. Paul Mulvaney, for giving me the opportunity to spend two times a period at the Melbourne University, and for the opportunity to perform gas sensing measurement with the DFM technique.

Prof. Giovanni Mattei is deeply acknowledged for the TEM measurements and the precious discussion about the sensing results and mechanisms.

Prof. Gaetano Granozzi, Dr. Stefano Agnoli and Dr. Luca Artiglia are gratefully acknowledged for XPS analyses.

Prof. Carlo Cantalini (University of L'Aquila) is acknowledged for the ongoing collaborations in the electrical gas sensing field, and for the fruitful discussions.

Dr. Carlos Pecharromán García (University of Madrid) is acknowledged for the calculations about the LSPR.

Prof. Luca Ottaviano (University of L'Aquila) is acknowledged for the collaboration relative to graphene.

Prof. Umberto Anselmi-Tamburini (University of Pavia) is acknowledged for the collaboration relative to the ZnO.

Preface

In the present work of thesis are reported only the main results.

Moreover, regarding the experimental part all the synthesis are reported in Appendix A.2; the technique used to characterize the nanoparticles solutions and the thin films are described in Appendix A.1, to avoid repetitions every paragraph. The same applies to the apparati used for the gas sensing with the three different techniques, in transmission using LSPR, on single particles with the DFM and in reflection using PSPR.

The simulations and calculations regarding the behavior of the gold nanoparticles during the gas sensing tests, performed by Dr. Carlos Pecharromán García (University of Madrid) are reported in Appendix A.4.

In the end the references, to allow an easier consultation, are reported at the end of each paragraph.

List of Abbreviations

LSPR	Localized Surface Plasmon Resonance
PSPR	Propagating Surface Plasmon Resonance
SPP	Surface Plasmon Polaritons
TPB	Transverse Plasmon Band
LPB	Longitudinal Plasmon Band
Vis	Visible
NIR	Near Infrared
DFM	Dark Field Microscopy
SEM	Scanning Electron Microscope
TEM	Transmission Electron Microscopy
XPS	X-ray photoemission spectroscopy
XRD	X-Ray diffraction
AFM	Atomic Force Microscopy
UHV TPD	Ultra-high-vacuum temperature programmed desorption
NC	Nanocrystal
NPs	Nanoparticels
NRs	Nanorods
NDs	Nanodumbbells
NSs	Nanostars
VOC	Volatile Organic Compound
A-VOC	Aromatic Volatile Organic Compound
CTAB	Hexadecyltrimethylammonium bromide
PVP	Polyvinylpyrrolidone
AA	Ascorbic acid
DMF	Dimethylformamide
DMSO	Dimethyl sulfoxide
TMAH	Tetramethylammonium hydroxide
EtOH	Ethanol
MetOH	Methanol
IPA	Isopropanol
MEA	Monoethanolamine
MEK	Methyl ethyl ketone

TEOS	Tetraetossisilano
PTMS	Trimethoxyphenylsilane
dPDMS	Dimethoxydiphenylsilane
APTMS	(3-aminopropyl) trimethoxysilane
OAC	Optical Absorbance Change
OT	Operating Temperature
RT	Room Temperature
TAP	Thin film TiO_2-Au-Pt NPs
TA	Thin film TiO_2-Au NPs
TP	Thin film TiO_2- Pt NPs
ZAP	Thin film ZnO-Au-Pt NPs
ZA	Thin film ZnO-Au NPs
ZP	Thin film ZnO- Pt NPs
AZO	Al- doped ZnO
GZO	Ga- doped ZnO
TCOs	Transparent Conductive Oxides
GO	graphene oxide
r-GO	Partially reduced GO
AuL	Gold nanoparticles monolayer low concentration
AuH	Gold nanoparticles monolayer high concentration

Summary

Chapter 1

Overview on plasmonic optical gas sensors

Nanocomposite films are thin films formed by mixing two or more dissimilar materials having nano-dimensional phase(s) in order to control and develop new and improved structures and properties. The properties of nanocomposite films depend not only upon the individual components used but also on the morphology and the interfacial characteristics [1].

Nanocomposite films that combine materials with synergetic or complementary behaviors possess unique physical, chemical, optical and electrical properties and have attracted much attention for a wide range of device applications such as gas sensors. Various nanocomposite films consisting of either metal-metal oxide, metal-semimetal oxides, or graphene mixed with metals have been synthesized and investigated in the present work for their application as active materials for gas sensors. Design of the nanocomposite films for gas sensor applications needs the considerations of many factors, for example, the surface area, interfacial characteristics, electrical conductivity, nanocrystallite size, surface and interfacial energy, etc., all of which depend significantly on the material selection, deposition methods and deposition process parameters.

A gas sensor is an electronic device that consists of a transducer and a sensitive element (an active layer such as a nanocomposite film) that relies, for its operating mechanism, on one of its physical and chemical properties. Basically it operates as follows: a charge transfer occurs between gas molecules and the "sensitive" nanocomposite films, resulting in an electrical and/or optical signal that is related to the gas molecules type and number. Sensitive nanocomposite films with high sensitivities, improved selectivity and reduced operating temperatures have been here fabricated thanks to the nanoscale morphology, surface-to-volume ratio and quantum confinement.

Various types of transducers that utilize different operating mechanisms have been employed for nanocomposite film gas sensing applications, for example chemoresistive sensors [2], surface acoustic wave sensors [3] and optical sensors [4 5 6].

The present work is focused on optical sensors. Optical gas sensors are based on the modification of optical responses of a nanocomposite film induced by interaction with gas molecules. This approach presents a number of advantages over the chemoresistive sensor. Electromagnetic waves are described by a certain number of degrees of freedom such as intensity, wavelength, and polarization: optical sensing thus allows multi-parametric detection, which is not possible in

electrical sensing where only a single scalar quantity (electrical conductivity) is involved. Optical sensors do not need electrical contacts, do not suffer from electromagnetic noise and may allow optoelectronic integration and have the potential of multi-gas detection.

Gas sensing by optical methods is usually straightforward and could achieve higher sensitivity, selectivity and stability than non-optical methods with much longer lifetime. Their response time is relatively short, which enables a real time detection.

Optical methods for gas sensing are mostly based on spectroscopy and this analysis mainly involves techniques based on absorption and emission spectrometry. A separate group is represented by the so called Surface Plasmon Resonance (SPR) sensors, based on the gas induced variation of the oscillation frequency of the surface conduction electrons of thin metal layers.

The principle of absorption spectrometry is the concentration-dependent absorption (molar absorptivity ε) of the photons at specific gas wavelengths (i.e., Beer-Lambert law) [7].

The techniques based on absorption spectrometry can be divided into two main groups: transmission and reflection mode.

In the transmission mode the light emitted by a source (lamp or LED) passes through the active material and it is collected by a detector. When the material is exposed to the target gas, changes in the absorption properties are monitored by the detector as light intensity changes as a function of wavelength, allowing to establish a relationship between the sensitivity of the device and the analysis wavelength.

In the reflection mode, the active material is deposited on a reflective substrate: so the incoming electromagnetic wave passes through the sample, reflects on the substrate and the reflected light at a fixed angle is collected by the detector. Again, during target gas exposure, the reflection intensity as a function of wavelength is monitored.

Such simple experimental setups can be easily implemented on an optical fiber-based platform, where the fibers direct the emitted light from the source to the active material and collect the light after the interaction with it.

The law of emission spectrometry is that excited atoms will emit photons and then go back to the ground state [7].

There are two types of emission spectrometry sensors, that exploit the photoluminescence or chemoluminescence properties of the active material: in the case of photoluminescence a light source is used to excite electrons of the active compound that returning to the standard, low energy state, emit light at higher wavelengths, while in the case of chemoluminescence, the chemical reaction triggers the light emission. There are several ways in which the analyte can interact with

the active material: for example quenching the luminescence of quantum dots, or shifting the emission peak, or again promoting new emissions.

The Surface Plasmon Resonance (SPR) sensors are based on the optical excitation of surface plasmons by the method of attenuated total reection was demonstrated by Kretschmann[8] and Otto[9].

The present work focused on Surface Plasmon Resonance (SPR) sensors and it is devided into two main chapters, one dealing with optical plasmonic sensing based on localized surface plasmon resonance (LSPR) and the other dealing with optical plasmonic sensing based on propagating surface plasmon resonance (PSPR) for the detection of H_2, CO, NO_2, Volatile organic compound (VOC) and Aromatic VOC.

1.1 Optical gas sensors based on Localized Surface Plasmon Resonance (LSPR)

Materials that possess a negative real and small positive imaginary dielectric constant are capable of supporting a surface plasmon resonance (SPR). This resonance is a coherent oscillation of the surface conduction electrons excited by electromagnetic radiation [10]. Plasmonics is the study of these particular light-matter interactions, and in the present work is used for gas sensing application. This chapter is dedicated to the study of localized surface plasmon resonance (LSPR), light interacts with particles much smaller than the incident wavelength (Fig. 1.1.1). This leads to a plasmon that oscillates locally around the nanoparticle with a frequency known as the LSPR [11 12].

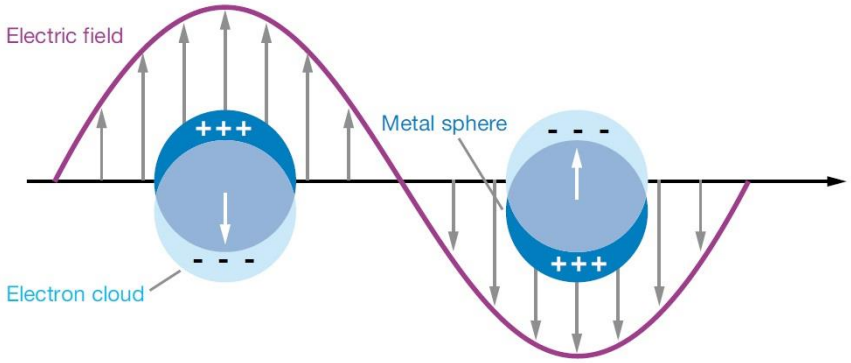

Fig. 1.1.1- Schematic diagrams illustrating a localized surface plasmon [1010].

Similar to the SPR, the LSPR is sensitive to changes in the local dielectric environment [13 14]. The most common method for LSPR sensing is the wavelength-shift measurement, in which the change in the maximum of the LSPR extinction curve is monitored as a function of changes in the local dielectric environment caused by analyte adsorption. This relationship is described in Equation 1 [10].

$$\Delta\lambda_{max} = m\,\Delta n\,[1 - \exp(^{-2d}/_{l_d})] \quad (1)$$

Where *m* is the bulk refractive-index response of the nanoparticle(s); Δn is the change in refractive index induced by the adsorbate; *d* is the effective adsorbate layer thickness; and l_d is the characteristic electromagnetic -field-decay length (approximated as an exponential decay). This relationship is the basis of LSPR wavelength-shift sensing experiments.

Moreover the absorbance at the SPR position is proportional to the electronic density, this is demonstrated with the Equation (2) proposed by Pecharromán.

$$A(\omega_{SPR}) = \frac{3zf\,\varepsilon_{SPR}}{2cL\gamma m_e \in_0} \frac{e^2 N_e}{[\varepsilon_\infty + (\frac{1}{L-1})\varepsilon_m]^2} \quad (2)$$

Where *f* is the fraction of NPs, L is the depolatization factor.

1.2 Optical gas sensors based on Propagating Surface Plasmon Resonance (PSPR)

This chapter deals about propagating plasmons, also known as surface plasmon polaritons.

In the case of surface plasmon polaritons, plasmons propagate in the *x*- and *y*-directions along the metal-dielectric interface, as shown in Figure 1.2.1, for distances on the order of tens to hundreds of microns, and decay evanescently in the *z*-direction with 1/e decay lengths on the order of 200 nm [15 16 17].

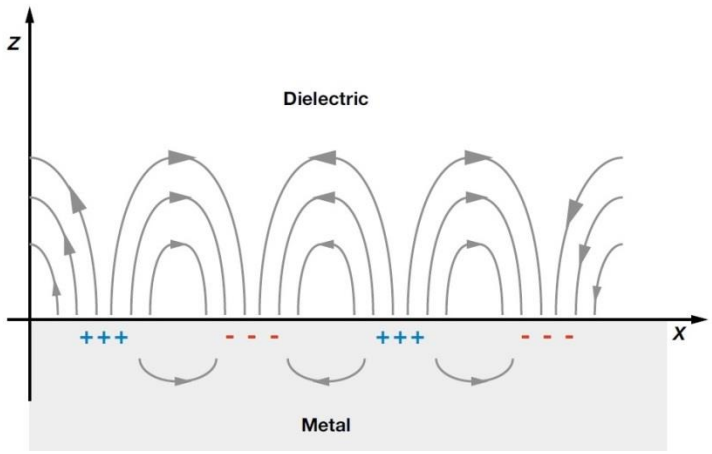

Fig. 1.2.1- Schematic diagrams illustrating a surface plasmon polariton (or propagating plasmon) [10].

Since SPPs are highly sensitive to changes of the refractive index in the vicinity of the surface, they are widely recognized as suitable probes for sensing devices [18 19 20 21 22]. The Surface Plasmon Resonance (SPR) sensors exploits the SPP properties to detect by optical means chemical or biological species, with aim of medical diagnostics, environmental monitoring and food safety. Among optical sensors, they are appreciated for the possibilities of extreme miniaturization and integration and for being a label-free technology.

The concept of SPR sensing is here illustrated, a SPP is excited on a metallic surface by an incident light beam; the excitation manifests itself as a fall of intensity of the reflected beam, as shown in Figure 1.2.2. The SPP evanescent field probes the surrounding environment; if the refracting index of the surrounding medium changes, the propagation constant of the SPP changes too, affecting the reflectance spectrum through the coupling conditions.

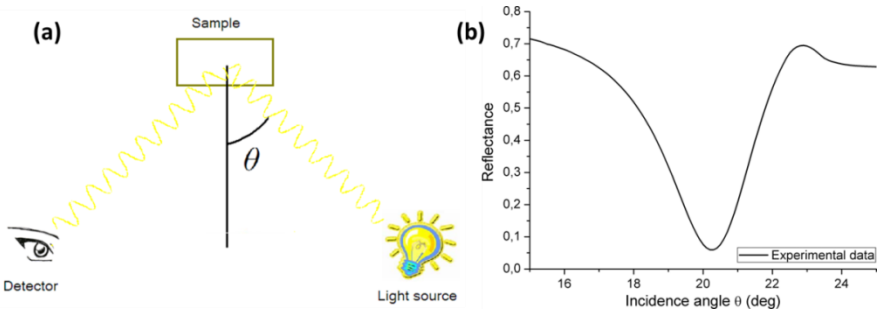

Fig. 1.2.2- Concept of the reflectance measurement. (b) Plasmonic resonance dip seen in an angular scan, corresponding to the excitation of gold/air single-interface SPP with light of wavelenght 650 nm impinging on a 470-nm grating.

The interaction between the sensitive layer and the gas molecules tested leads to a change in the surrounding environment, meaning the sensitive layer, and consequently to a shift in the plasmon resonance conditions; this can be observed in two modes: (*a*) angle resolved and (*b*) wavelength shift. In the first mode, it is measured the reflectivity of light from the metal surface as a function of the angle of incidence (at constant wavelength), in the second one as function of the wavelength (at constant angle of incidence).

References

[1] Dongfang Yang, Nanocomposite Films for Gas Sensing, Industrial Materials Institute, National Research Council Canada, Canada. www.intechopen.com

[2] Bijandra Kumar, Mickael Castro, Jean-François Feller, Tailoring the chemo-resistive response of self-assembled polysaccharide-CNT sensors by chain conformation at tunnel junctions, Carbon 2012, Volume 50, Issue 10, 3627–3634.

[3] Cristian Viespe, Constantin Grigoriu**,** Surface acoustic wave sensors with carbon nanotubes and SiO_2/Si nanoparticles based nanocomposites for VOC detection**,** Sens. Act. B- Chem 2010, Volume 147, Issue 1, 43–47.

[4] Alessandro Martucci, Nazanin Bassiri, Massimo Guglielmi, Lidia Armelao, Silvia Gross, Jean Claude Pivin, $NiOSiO_2$ sol-gel nanocomposite films for optical gas sensor, *J. Sol-Gel* Sci. Technol. 2003, Volume 26, Issue 1-3, 993-996.

[5] Alessandro Martucci, Mirko Pasquale, Massimo Guglielmi, Mike Post, Jean Claude Pivin, Nanostructured silicon oxide-nickel oxide sol-gel films with enhanced optical carbon monoxide gas sensitivity, J. Am. Ceram. Soc. 2003, Volume 86, Issue 9, 1638-1640.

[6] Alessandro Martucci, Dario Buso, Matthias De Monte, Massimo Guglielmi, Carlo Cantalini, Cinzia Sada, Nanostructured sol-gel silica thin films doped with NiO and SnO_2 for gas sensing applications, J. Mater. Chem. 2004, Volume 14, Issue 19, 2889-2895.

[7] Xiao Liu, Sitian Cheng, Hong Liu, Sha Hu, Daqiang Zhang, Huansheng Ning, A Survey on Gas Sensing Technology, Sensors 2012, Volume 12, 9635-9665.

[8] H. Raether and E. Kretschmann, Radiative Decay of Non-Radiative Surface Plasmons Excited by Light, Zeitschrift Für Naturforschung 1968, Volume 23, Issue 12, 2135-2136.

[9] A. Otto, Excitation of Surface Plasma Waves in Silver by the Method of Frustrated Total Reflection, Zeitschrift Für Physik a Hadrons and Nuclei 1968, Volume 216,Issue 4, 398-410.

[10] Katherine A. Willets, Richard P. Van Duyne, Localized Surface Plasmon Resonance Spectroscopy and Sensing, Annu. Rev. Phys. Chem. 2007, Volume 58, 267-297.

[11] A. J. Haes, C. L. Haynes, A. D. McFarland, S. Zou, G. C. Schatz, R. P. Van Duyne, Plasmonic materials for surface-enhanced sensing and spectroscopy, MRS Bull. 2005, Volume 30, 368–375.

[12] K. L. Kelly, E. Coronado, L. Zhao, G. C. Schatz, The optical properties of metal nanoparticles: the influence of size, shape, and dielectric environment, J. Phys. Chem. B 2003, Volume 107, 668–677.

[13] M. M. Miller, A. A. Lazarides, Sensitivity of metal nanoparticle surface plasmon resonance to the dielectric environment, J. Phys. Chem. B 2005, VOLUME 109, 21556–21565.

[14] T. R. Jensen, M. L. Duval, L. Kelly, A. Lazarides, G. C. Schatz, R. P. Van Duyne, Nanosphere lithography: effect of the external dielectric medium on the surface plasmon resonance spectrum of a periodic array of silver nanoparticles, J. Phys. Chem. B 1999, Volume 103, 9846–9853.

[15] J. M. Brockman, B. P. Nelson, R. M. Corn, Surface plasmon resonance imaging measurements of ultrathin organic films, Annu. Rev. Phys. Chem. 2000, Volume 51, 41–63.

[16] R. P. Van Duyne, Molecular plasmonics, Science 2004, Volume 306, 985–86.

[17] W. Knoll, Interfaces and thin films as seen by bound electromagnetic waves, Annu. Rev. Phys. Chem. 1998, Volume 49,569–638.

[18] J. Homola, S.S. Yee, G. Gauglitz, Surface Plasmon resonance sensors: review, Sens. Act. B 1999, Volume 54, 3-15.

[19] D.R. Shankaran, K.V. Gobi, N. Miura, Recent advancements in surface plasmon resonance immunosensors for detection of small molecules of biomedical, food and environmental interest, Sens. Act. B 2007, Volume 121, Issue 1, 158-177.

[20] D. Habauzit, J. Chopineau, B. Roig, SPR-based biosensors: A tool for biodetection of hormonal compounds, Anal. Bioanal. Chem. 2007, Volume 387, Issue 4, 1215-1223.

[21] F.S. Ligler, Perspective on optical biosensors and integrated sensor systems, Anal. Chem. 2009, Volume 81, 519-526.

[22] I. Abdulhalim, M. Zourob, A. Lakhtakia, Surface Plasmon Resonance for Biosensing: A Mini-Review, Electromagnetics 2008, Volume 28, 214–242.

Chapter 2

2.1 Comparison between the gas sensing performances of gold nanorods coupled with platinum embedded in a titanium or zinc oxide matrix

Nanoparticles have attracted much attention because of their size- and shape-dependent optical properties. Due to the coupling of conduction electrons to the electromagnetic field of the incident light, the optical response of noble metal nanoparticles is typically characterized by the presence of strong absorption and scattering peaks that are not present in the spectrum of the bulk metal, a phenomenon named localized surface resonance (LSPR) [1].

Considering the shape-dependent aspect it is necessary to point out that we will work with nanorods (NRs). In spherical gold particles a strong absorption band around 550nm arising from the excitation of plasmon by the incident light can be readily observed. Gold NRs, instead, are quite different from spherical particles as they have also a surface plasmon band at lower energy.

There are, in fact, two plasmon resonance absorption bands. One is around 520-550nm caused by transverse oscillation of electrons and is thus termed the "transverse plasmon band" (TPB). The other one lies in the visible or near infrared (NIR) region and is known as the "longitudinal plasmon band" (LPB). Gold nanoparticles (NPs), including spherical and rod-like NPs, are of great interest in particular in sensing because their extinction spectra are highly sensitive to the dielectric constant of the surrounding medium [2] [3].

El Sayed and co-workers [4] [2] have demonstrated both experimentally and theoretically that the LPBs are highly sensitive to changes in the dielectric properties of the surroundings and the sensitivity increases with the aspect ratio of the NRs.

In the present work, we will confirm that the TPB is less sensitive than the LPB, in gas sensing measurements, so that there is an advantage in using gold NRs instead of gold NPs [5] [6] [7]

Our strategy is to use colloidal synthesis of TiO_2 and ZnO NPs, Au NRs and Pt NPs to prepare crystalline films at low temperature. It has been demonstrated that TiO_2-Au and ZnO-Au films, can react with reducing and oxidant gases also at low temperature, but with long transient times. If Pt is added, it can act as a catalyst in the gas detection kinetics, making the absorption and the reaction of the gas faster, for example permitting to lower the operative temperature of the sensor, while Au NRs are not stable as they tend to spheroidize rising the temperature above 150°C [8].

The idea to use crystalline TiO_2 and ZnO as a matrix for Au NRs comes from their photocatalytic activity in the visible, enhanced by the surface plasmon resonance of the gold NPs in general, which make possible the optical detection of reducing (H_2) and oxidant (NO_2) gases [9] [10] [11].
Finally we want to compare the gas sensing performance of the two different matrix, TiO_2 and ZnO, to find the best one in terms of fast response to the gas and variation of absorbance.

2.1.1 Experimental

2.1.1.1 Nanoparticles synthesis

The Au NRs with aspect ratio (a.r.) of 3 and the Pt, TiO_2 and ZnO NPs synthesis procedure are reported in the appendixes A.2.2, A.2.6, A.2.7 and A.2.9, respectively.

2.1.1.2 Samples deposition

The starting solutions were prepared by mixing the methanol suspension of TiO_2 and ZnO NPs with PVP-capped Au NRs and Pt NPs in ethanol, with different molar percentage (Tab. 2.1.1).

Au:Pt molar ratio	**TiO_2 samples**	**ZnO samples**
10:2	TiO_2-AuNRs -Pt NPs (TAP10:2)	ZnO-AuNRs -Pt NPs (ZAP10:2)
10:1	TiO_2-AuNRs -Pt NPs (TAP10:1)	ZnO-AuNRs -Pt NPs (ZAP10:1)
10:0.5	TiO_2-AuNRs -Pt NPs (TAP10:0.5)	ZnO-AuNRs -Pt NPs (ZAP10:0.5)

Table 2.1.1- Nanocomposite thin films of TiO_2-AuNRs -Pt NPs with different molar ratios between Au and Pt.

All the films were deposited by spin coating at 3000rpm for 30 s on either SiO_2 or Si substrates and dried at 50°C for 5min and then other 4 layers were deposited, with the same parameter, then dried again at 60°C, for a total number of layers of 5.

2.1.1.3 Gas sensing measurements

Optical gas sensing tests were performed with operating temperature (OT) set at room temperature and 80 °C and the sensor was tested for both reducing and oxidant gases, H_2 and NO_2, respectively, all balanced with synthetic air. In particular, the concentrations of H_2 was set at 10000 ppm; the concentration of NO_2 was set at 1000 ppm, using NRs is possible to use that high concentration because the effects related to the NO_2 optical absorption in the visible range are out of the NRs

longitudinal plasmon band range. The detailed description of the gas sensing apparatus is reported in appendix A.3.1.

2.1.2 Results and discussion

2.1.2.1 Structural and optical properties

All the components were characterized, at first, in solution, to check their crystallinity and optical quality; in Figure 2.1.1 it is shown the absorption spectra of gold NRs with a. r. ~3, also confirmed by the TEM image, capped with PVP and redispersed in ethanol.

For TiO_2 NPs (Fig. 2.1.2) from the XRD pattern is possible to identify the typical peaks of crystalline anatase [JCPDS 84-1286], at 25.33° for the (101) plane, at 36.9° (103) plane, at 37.84° (004) plane, at 38.6° (112) plane, at 48.07° (200) plane, at 53.95° (105) plane, at 55.11° (211) plane. The obtained TiO_2 NPs are of good optical quality, as can be seen from the UV-Vis spectrum reported in Figure 2.1.2, as they are transparent in the visible and absorbs in the UV region, at ~330-340 nm, at the band gap wavelength.

For the ZnO NPs (Fig. 2.1.3) from the XRD pattern is possible to identify the typical peaks of crystalline wurtzite [JCPDS No. 36-1451] at 31.77° for the (100) plane, at 34.42° (002) plane, at 36.25° (101) plane, at 47.54° (102) plane and at 56.60 (103) plane.

And that the ZnO we obtained is of good optical quality, from the UV-Vis spectra, is transparent in the visible and absorbs in the UV region, at ~350nm, at the band gap wavelength.

Finally in Figure 2.1.4 are reported the UV-Vis spectra and the XRD pattern to check the crystallinity of the Pt NPs, the peaks for cubic Pt are clearly detected [JCPDS No. 04-0802]: in details, (100) and (200) reflections at about 39.8° and 46.2° are present, confirming the crystallinity of Pt NPs, and their dimension, also verified from the TEM image, around 10nm.

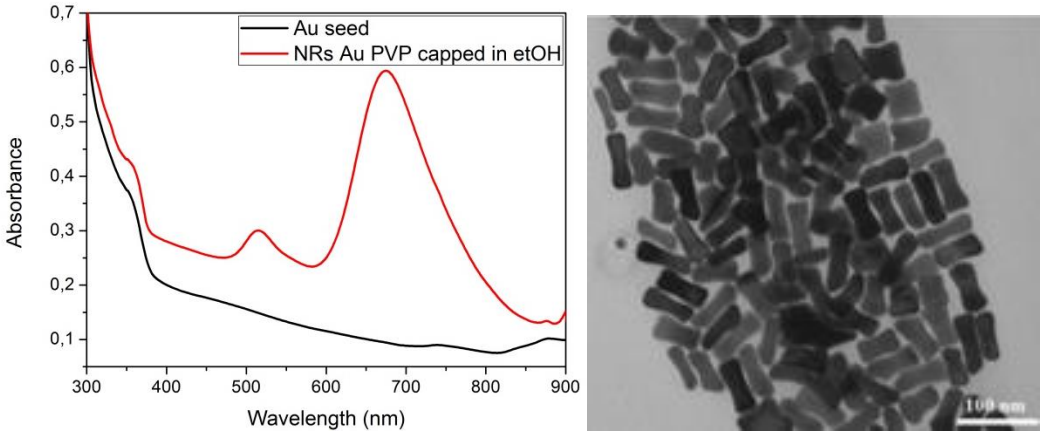

Fig. 2.1.1- UV-Vis spectra (left) of gold seed (black line) and of gold NRs (red line) with TEM image (right) of gold NRs.

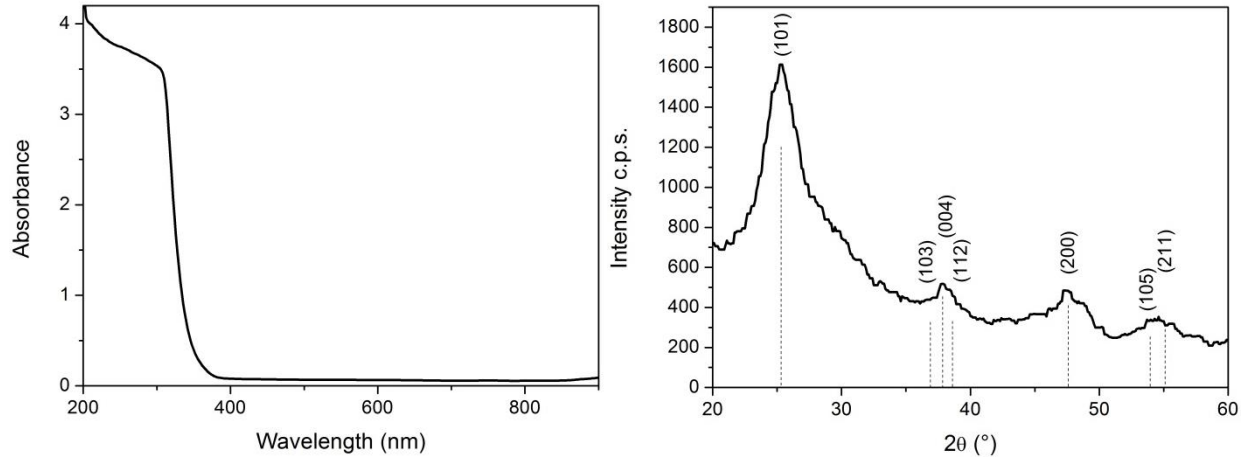

Fig. 2.1.2- UV-Vis spectrum of TiO_2 (left) and XRD pattern (right) showing the typical peaks of crystalline anatase.

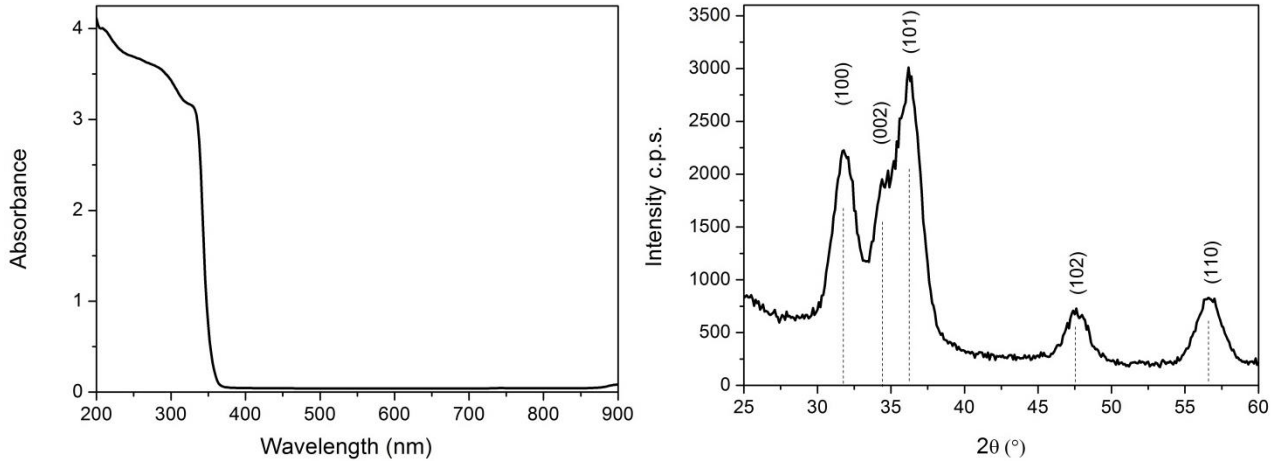

Fig. 2.1.3- UV-Vis spectrum of ZnO (left) and XRD pattern (right) showing the typical peaks of crystalline wurtzite.

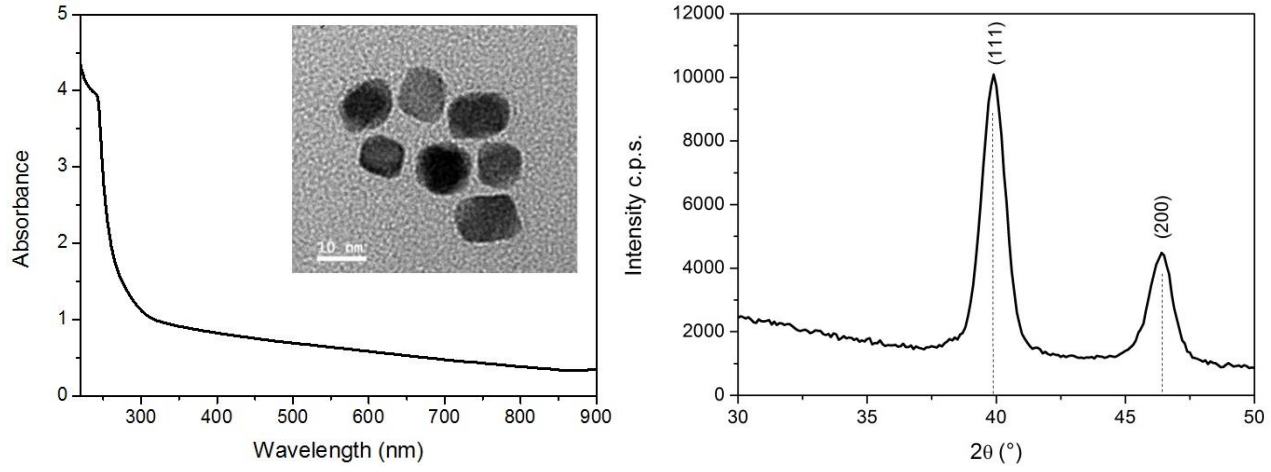

Fig. 2.1.4- UV-Vis spectrum and TEM image (left) and XRD pattern (right) of platinum NPs.

The thin film deposited from the synthesized NPs, reported in Table 2.1.1, have to be stabilized with a thermal treatment to perform gas sensing tests, so we studied the thermal stability of NRs inside the TiO_2 (TA) and ZnO (ZA) matrix, to find the maximum temperature for the thermal treatment avoiding the spheroidization of the Au NRs (Fig. 2.1.5).

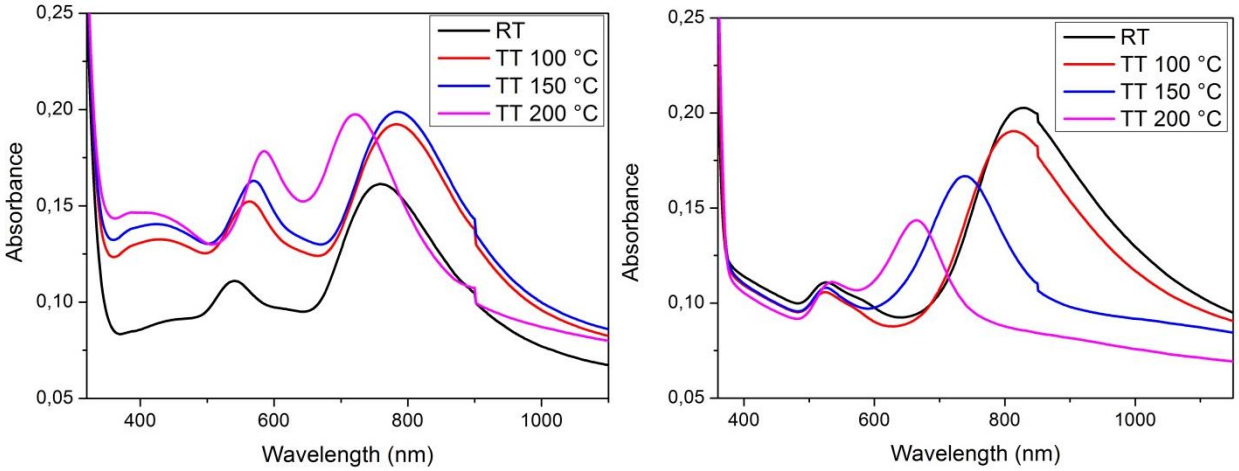

Fig. 2.1.5- Absorption spectra of the samples TA (left) / ZA (right) treated at different temperatures up to 200°C.

We found that until 150°C it is possible to avoid the spheroidization, but at 200°C the blue-shift due to the spheroidization predominates over the red shift due to the increment of the refractive index of the oxide matrix, due to the densification after the heat treatment. To confirm that at 100°C the NRs maintain their shape we perform also a SEM measurement on the treated thin film (Fig. 2.1.6) from which it is possible to see that the Au NRs still have an a.r. of 3. In the images are also visible spherical particles representing the Pt NPs.

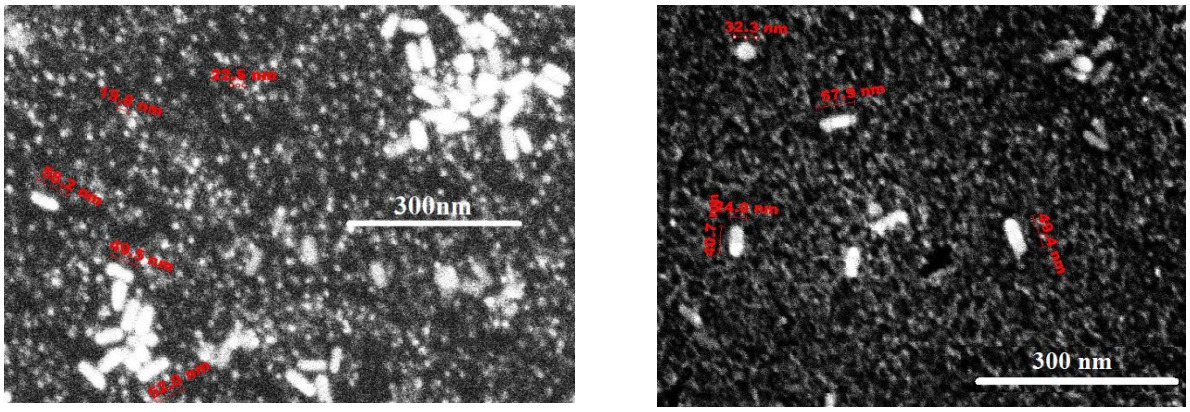

Fig. 2.1.6- SEM images of the samples TAP (left) / ZAP (right) treated at 100°C.

In Figure 2.1.7 is shown the absorption spectra of TiO_2 and ZnO nanocomposite films containing gold NRs and platinum NPs, it is possible to see the peaks of NRs clearly and also the typical broad absorption of the Pt NPs.

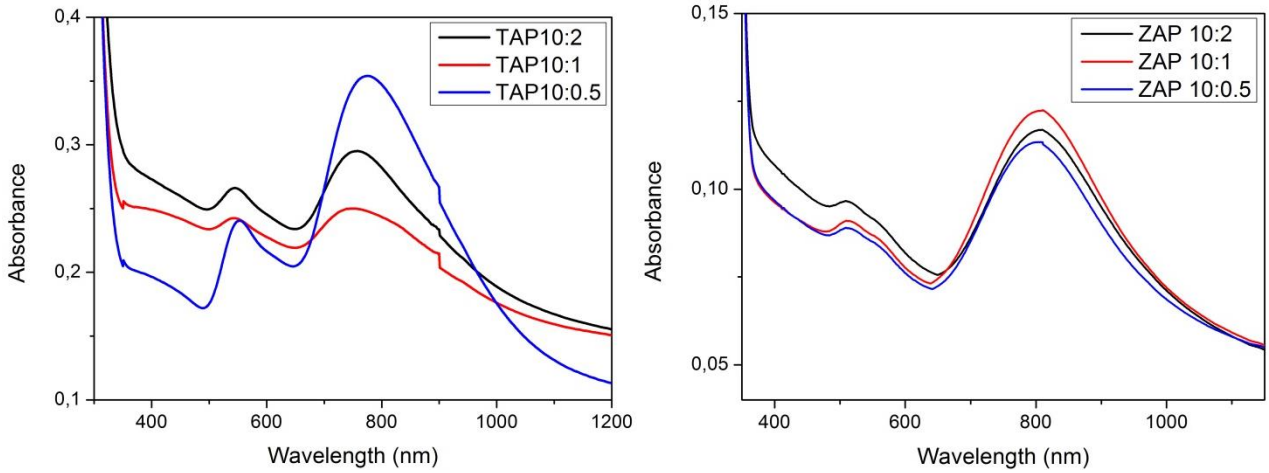

Fig. 2.1.7- Absorption spectra of the samples TAP (left) / ZAP (right) listed in Table 2.1.1.

2.1.2.2 Gas sensing tests

TAP/TAP nanocomposite films, annealed at 100°C, were tested as gas sensor. In Figure 2.1.8 are reported the best sensing results obtained with the samples with Au NRs and Pt into matrixes of TiO_2 and ZnO, towards H_2. In Figure 2.1.8 c. are reported the OAC curves, which represent the Optical Absorbance Change (OAC) parameter, defined as the difference between absorbance during gas exposure and absorbance in air ($OAC=Abs_{Gas}-Abs_{Air}$).

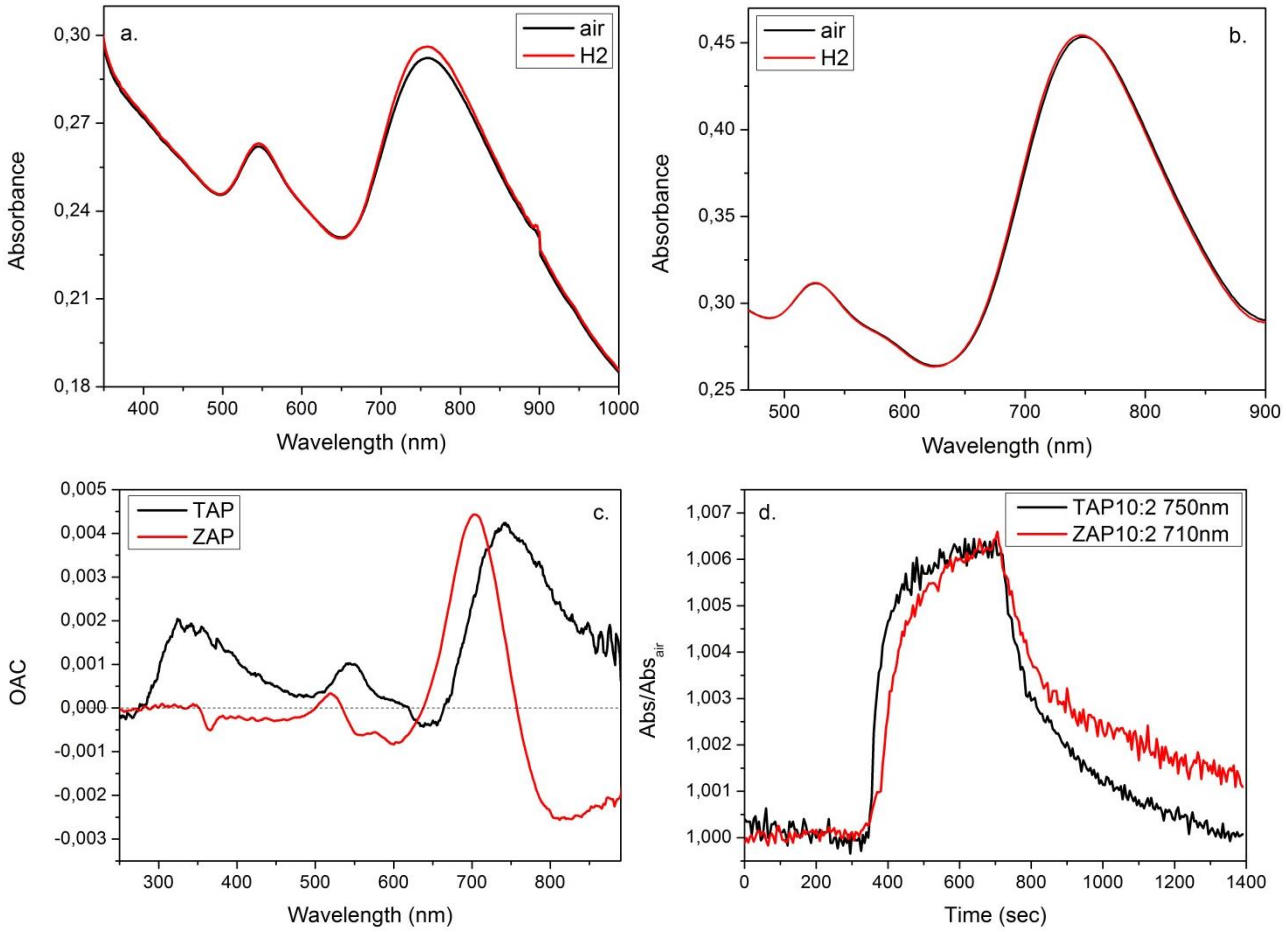

Fig. 2.1.8- Spectra of the samples in air and in H_2 10000 ppm (a. and b.) and comparison between the OAC curves (c.) and dynamic measurements of the H_2 sensing test at room temperature on the samples TAP and ZAP (d.).

In Figure 2.1.9 are presented the results obtained with both the matrices varying the molar ratio between Au and Pt; it is evident that the best performance is obtained with the highest amount of Pt, because of its catalytic behavior, in fact the response/recovery time are shorter and the variation in absorbance is higher. Moreover, with the ZnO matrix it is possible to note that there is a response only with 10:2 ratio between Au and Pt. It is also possible to note that the presence of H_2 induce a blue shift of the LSPR peak.

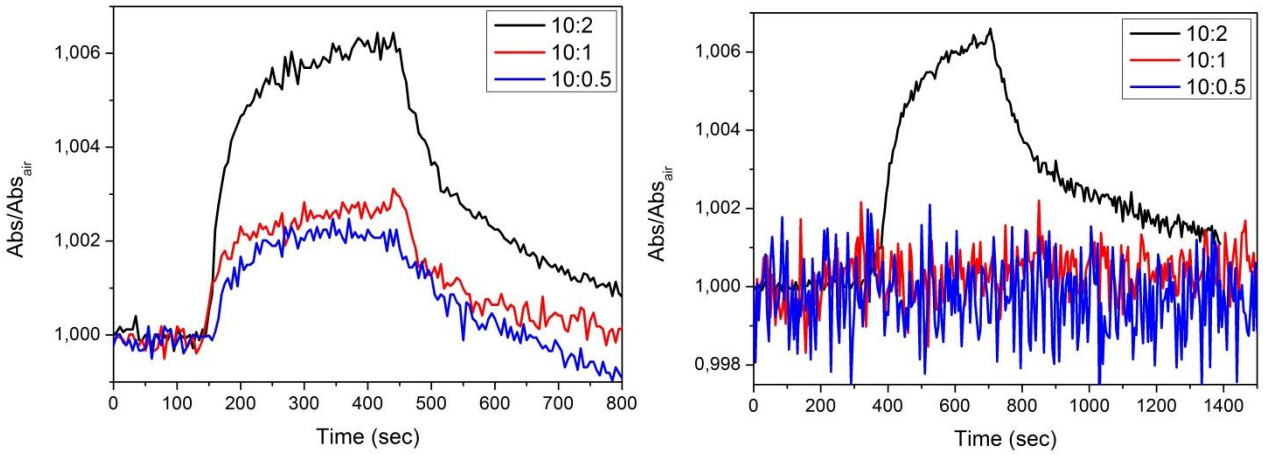

Fig. 2.1.9- Comparison between the dynamic gas sensing tests at room temperature with H_2 10000 ppm on the samples TAP (left) and ZAP (right) at the variation of the Au:Pt molar ratio.

For the NO_2 detection the samples are sensitive only at 80°C OT. Figure 2.1.10 a and b show the scan sensing measurement, and highlight the red shift of the plasmon bands in presence of NO_2.

In Figure 2.1.10 c and d it is possible to notice a wide peak of absorption around 400nm, which is due to the absorption of the gas (NO_2) 1000 ppm, so the sensing of this gas is possible only at wavelength greater than ~700nm, and the variation in absorbance, due to the interaction with NO_2, is shown in the insets of Figure 2.1.10 c and d. As already said the sensing with NO_2 is possible only with NRs, because the spherical NPs have a plasmon band in the region of absorption of the gas, around 500nm. For this reason it is selected only the region from 700nm to 900nm (Fig. 2.1.10 c and d in the inset).

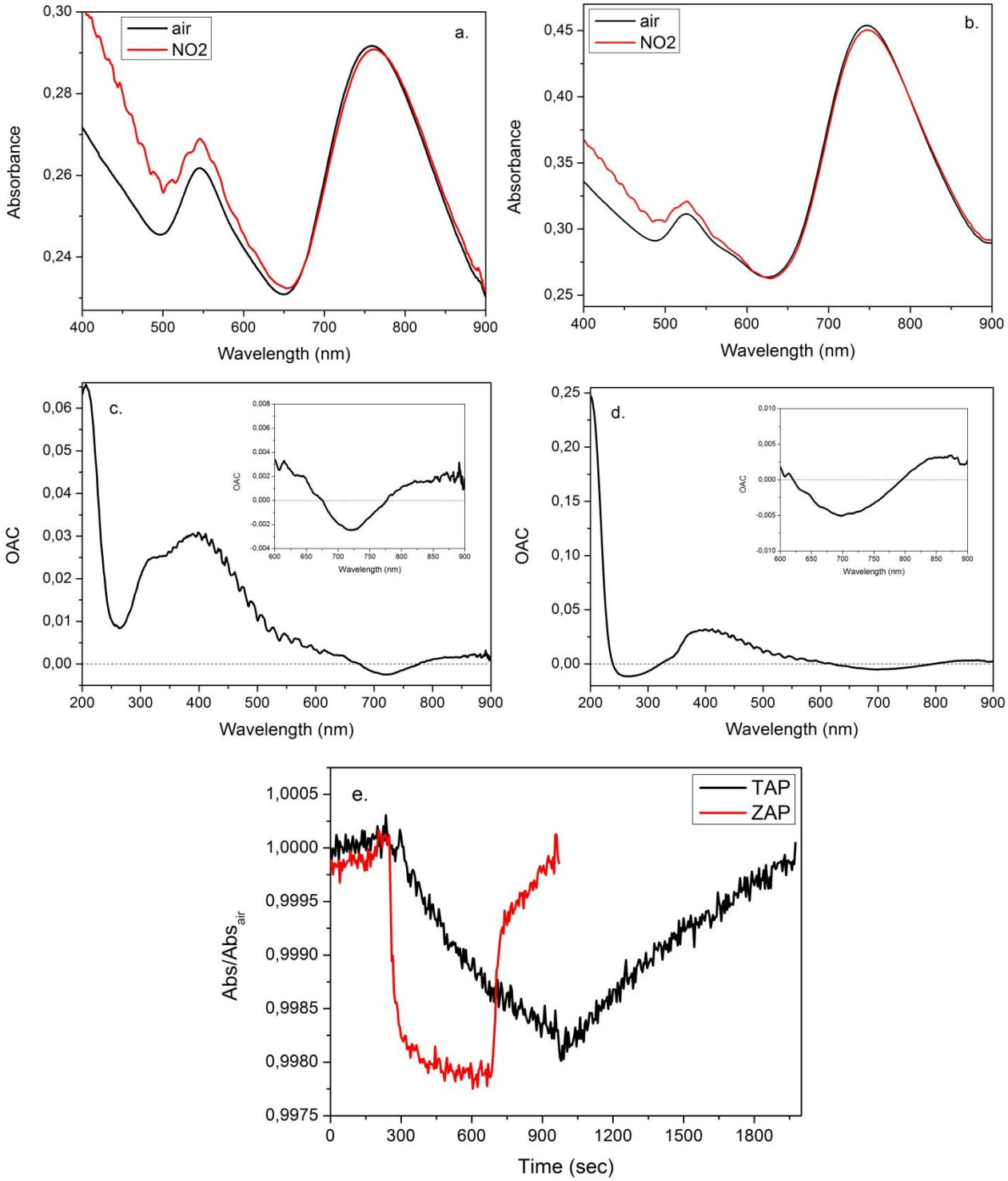

Fig. 2.1.10- Scan measurement on the samples TAP (a.) and ZAP 10:1 (b.), comparison between the OAC curves on the samples TAP (c.) and ZAP 10:1 (d.), with in the inset a magnification of the longitudinal plasmon band region, and dynamic measurements of the NO_2 1000 ppm sensing test at 80 °C, at 721 and 710 nm respectively (e.).

Figure 2.1.10 e compares the performances of TAP and ZAP samples, and it is evident that the sensitivity towards NO_2 is pretty similar towards the tested gases in terms of variation in absorbance, instead regarding the kinetics, are improved the one for the sample with the ZnO matrix.

The reducing gases (H_2) react with the oxygen absorbed on the surface of the semiconductor and donate electrons, while oxidant gases (NO_2) subtract electrons [12].

To better understand the mechanisms involved in this gas sensing measurements it is worth to discuss at first about the photocatalytic activity of TiO_2 and ZnO in the UV which is extended to the visible region if coupled with plasmons, in this case of gold NRs, through resonant energy transfer (RET) [910]. The gold particle converts the energy of incident photons into LSPR oscillations and transfers the plasmonic energy to the semiconductor matrix around the particle via RET. RET generates electron−hole pairs in the semiconductor by the dipole−dipole interaction between the plasmonic metal (donor) and semiconductor (acceptor), which greatly enhances the visible-light photocatalytic activity as compared to the semiconductor alone.

Consequently, since the incident photons are absorbed by the nanocomposite, an electron skips into the conduction band of the semiconductor and reacts with the adsorbed atmospheric oxygen on the semiconductor matrix, as described in reaction (1).

$$1/2O_2 + e_{(C.B.)}^- \rightarrow O^- (ads) \quad (1)$$

The reducing gases (H_2) react with the oxygen ions, absorbed on the surface of the porous semiconductor matrix, and donates electrons.

$$H_2 + O^{2-}(ads) \rightarrow H_2O + 2e^- \quad (2)$$

The reaction (2) [13] is catalyzed by Pt. The presence of the TiO_2 matrix led to higher electronic density on Pt, changing its chemisorption properties, weakening the Pt–H bonds, and increasing its H_2 oxidation activity [14], via hydrogen spillover as described by the reaction (3) [15]. Pt splits H_2 in protons, which reacts with the oxygen ions adsorbed, and inject electrons into the semiconductor's conducing band.

$$H_2 \rightarrow 2H^+ + 2e^- + O^{2-} (ads) \rightarrow H_2O + 2e^- \quad (3)$$

The high H_2 oxidation activity of the Pt NPs embedded in TiO_2 can be also attributed to the ability of TiO_2 to provide highly reactive oxygen atoms [1414]. The important catalytic role of Pt is highlighted in Figure 2.1.11 a and b, where the OAC curves of the TiO_2 and ZnO based samples are compared, respectively, with and without Pt NPs; it is evident that the Pt is fundamental for H_2 sensing, without Pt there is no sensitivity towards the gase. Instead with only Pt and no Au NRs, there is a small sensitivity and no wavelength dependent as in the case with Au NRs.

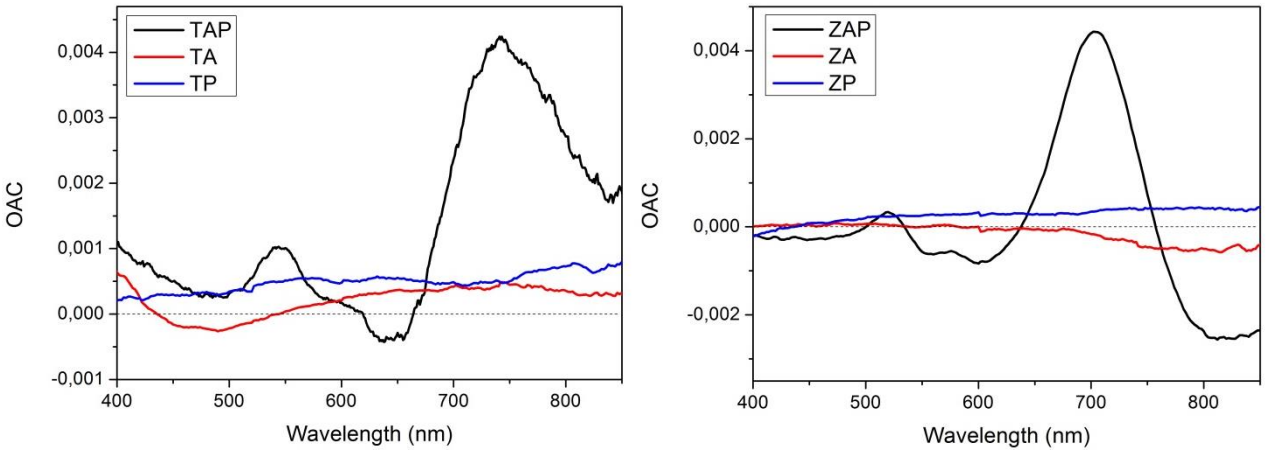

Fig. 2.1.11- Comparison between the OAC curves in H_2 10000 ppm for the TiO_2 based samples (left) and for the ZnO based samples (right) with Au NRs and Pt (TAP or ZAP), with only Au NRs (TA or ZA) and with only Pt (TP or ZP).

Oxidant gases (NO_2), instead, react with the oxygen ions absorbed on the surface of the porous semiconducting matrix, and subtract electrons.

$$NO_2 + e^- \rightarrow NO_2^-(ads) \quad (4)$$

$$NO_2^-(ads) + 2O^-(ads) \rightarrow NO_2 + 2O^{2-}(ads) \quad (5)$$

As shown in Figure 2.1.12 a and b, for TiO_2 and ZnO, respectively, the presence of Pt NPs is fundamental for the NO_2 detection as for H_2; without Pt there is no sensitivity, instead without Au NRs there is a low sensitivity but, as already said, there is no wavelength dependence of the gas response.

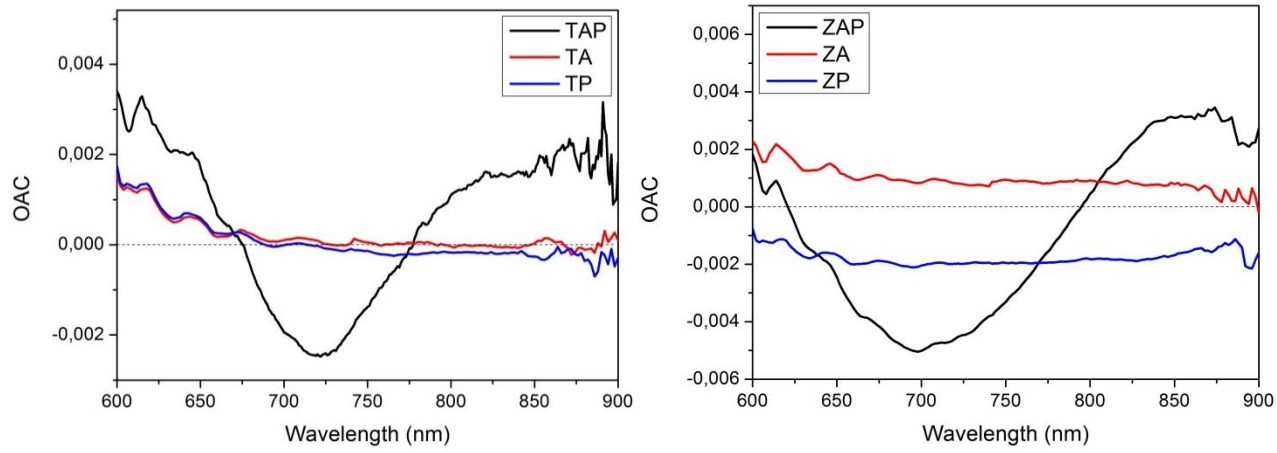

Fig. 2.1.12- Comparison between the OAC curves in NO_2 1000 ppm for the TiO_2 based samples (left) and for the ZnO based samples (right) with Au NRs and Pt (TAP or ZAP), with only Au NRs (TA or ZA) and with only Pt (TP or ZP).

This injection and subtraction of electrons in and from the conduction band imply that the plasmon band blue-shifts with reducing gasses and red-shifts with oxidant gases.

ZnO and TiO_2 have a similar band gap, similar photocatalytic properties [16] [17] so a similar behavior in the gas sensing, especially towards H_2.

On the other hand, ZnO has an higher electron mobility than TiO_2 [18] so higher conductivity [19] [20].

This is important for NO_2 because it is not reduced photocatalytically and it explains why ZnO has better performance in the sensing of NO_2. Result confirmed in literature [20].

Moreover, to investigate why there are advantages in gas sensing performance in using gold NRs than spherical NPs it is necessary to take into account a quality factor, which is, in the case of particle plasmons, the local-field enhancement. The spherical gold particles have relatively low-field enhancement factors, as a consequence of inter-band damping for small spheres and radiation damping for large spheres [21]. In contrast, gold NRs can have very high quality factors of up to 23 due to the very little radiation damping, and dephasing rate which drastically decreases increasing the aspect ratio of NRs [21]. These high quality factors should make gold NRs vastly superior to gold nanospheres in optical applications where large local-field enhancements are required [22] [23] [2] [4] [24] [25].

2.1.3 Conclusions

In this chapter the optical gas sensing performances of Au NRs coupled with catalytic Pt NPs embedded into a semiconducting matrix (TiO_2/ZnO) towards H_2 (10000 ppm) and NO_2 (1000 ppm) was investigated.

The sensors showed good and reversible responses with fast kinetics towards H_2 for both the semiconducting matrixes, while towards NO_2 the ZnO matrix showed the best performances.

The mechanisms involved in the sensing can be explained considering a combination between the photocatalytic behavior of TiO_2 and ZnO in the visible, if coupled with Au NRs, an exchange of electrons with the target gases through red-ox reactions mediated by the adsorbed oxygen and an improvement of the sensing performance due to the local-field enhancement in the longitudinal axis of the rods.

References

[1] Haowen Huang, Chunran Tang, Yunlong Zeng, Xianyong Yu, Bo Liao, Xiaodong Xia, Pinggui Yi, Paul K. Chu, Label-free optical biosensor based on localized surface plasmon resonance of immobilized gold nanorods, Colloids Surf. B: Biointerfaces 2009, Volume 71, 96–101.

[2] S. Link, M. B. Mohamed, and M. A. El-Sayed, Simulation of the Optical Absorption Spectra of Gold Nanorods as a Function of Their Aspect Ratio and the Effect of the Medium Dielectric Constant, J. Phys. Chem. B 1999, Volume 103, 3073-3077.

[3] M. G. Manera, J. Spadavecchia, D. Buso, C. de Julián Fernández, G. Mattei, A. Martucci, P. Mulvaney, J. Pérez-Juste, R. Rella, L. Vasanelli, P. Mazzoldi, Optical gas sensing of TiO_2 and TiO_2/Au nanocomposite thin films, *Sens. Act. B: Chem.* 2008, Volume 132, Issue 1, 107-115.

[4] P. K. Jain, S. Eustis, M. A. El-Sayed, Plasmon coupling in nanorod assemblies: optical absorption, discrete dipole approximation simulation, and exciton-coupling model, J. Phys. Chem. B 2006, Volume 110, 18243–18253.

[5] E. Della Gaspera, A. Antonello, M. Guglielmi, M. L. Post, V. Bello, G. Mattei, F. Romanato, A. Martucci, Colloidal approach to Au-loaded TiO_2 thin films with optimized optical sensing properties, *J. Mater. Chem.* 2011, Volume 21, Issue 12, 4293-4300.

[6] E. Della Gaspera, M. Guglielmi, G. Perotto, S. Agnoli, G. Granozzi, M.L. Post, A. Martucci, CO optical sensing properties of nanocrystalline ZnO–Au films: Effect of doping with transition metal ions, *Sens. Act. B: Chem.* 2012, Volume 161, 675-683.

[7] E. Della Gaspera, M. Bersani, G. Mattei, T.-L. Nguyen, P. Mulvaney, A. Martucci, Cooperative effect of Au and Pt inside TiO_2 matrix for optical hydrogen detection at room temperature using surface plasmon spectroscopy, Nanoscale 2012, Volume 4, 5972-5979.

[8] S. Link, Z.L. Wang, and M.A. El-Sayed, How does a gold nanorod melt?, J. Phys. Chem. B 2000, Volume 104, 7867-7870.

[9] M. Zhou, J. Zhang, B. Cheng, and H. Yu, Enhancement of visible-light photocatalytic activity of mesoporous Au-TiO_2 nanocomposites by surface plasmon resonance, Int. J. Photoenergy 2012, volume 2012, Article ID 532843, 10 pages.

[10] S. K. Cushing, J. Li, F. Meng, T. R. Senty, S. Suri, M. Zhi, M. Li, A. D. Bristow, N. Wu, Photocatalytic activity enhanced by plasmonic resonant energy transfer from metal to semiconductor, J. Am. Chem. Soc. 2012, Volume 134, 15033−15041.

[11] Hang Yu, Hai Ming, Jingjing Gong, Haitao Li, Hui Huang, Keming Pan, Yang Liu, Zhenhui Kang, Jie Wei and Dongtian Wang, Facile Synthesis of Au/ZnO Nanoparticles and Their Enhanced Photocatalytic Activity for Hydroxylation of Benzene, Bull. Mater. Sci. 2013, Volume 36, Issue 3, 367–372.

[12] N.A. Joy, M.I. Nandasiri, P.H. Rogers, W. Jiang, T. Varga, S.V.N.T. Kuchibhatla, S. Thevuthasan, et al., Selective plasmonic gas sensing: H_2, NO_2, and CO spectral discrimination by a single Au-CeO_2 nanocomposite film, Anal. Chem. 2012, Volume 84, 5025-5034.

[13] T. Y. Yang, H. M. Lin, B. Y. Wei, C. Y. Wu, C. K. Lin, UV Enhancement of the Gas Sensing Properties of Nano-TiO_2, Rev. Adv. Mater. Sci. 2003, Volume 4, 48-54.

[14] Sung Jong Yoo, Kug-Seung Lee, Yong-Hun Cho, Soo-Kil Kim, Tae-Hoon Lim & Yung-Eun Sung, Electrocatalytic Properties of TiO_2-Embedded Pt Nanoparticles in Oxidation of Methanol: Particle Size Effect and Proton Spillover Effect, Electrocatal 2011, Volume 2, 297–306.

[15] G. M. Psofogiannakis, G. E. Froudakis, DFT Study of the Hydrogen Spillover Mechanism on Platinum-Doped Graphite, J. Phys. Chem. C 2009, Volume 113, Issue 33, 14908–14915.

[16] Jing Liqiang, Xin Baifu, Yuan Fulong, Wang Baiqi, Shi Keying, Cai Weimin, Fu Honggang, Deactivation and regeneration of ZnO and TiO_2 nanoparticles in the gas phase photocatalytic oxidation of *n*-C_7H_{16} or SO_2, Appl. Catal. A: Gen. 2004, Volume 275, 49-54.

[17] Kaushik Mallick, Mike S Scurrell, CO oxidation over gold nanoparticles supported on TiO_2 and TiO_2-ZnO: catalytic activity effects due to surface modification of TiO_2 with ZnO, Appl. Catal. A: Gen. 2003, Volume 253, 527–536.

[18] Kwangsuk Park, Qifeng Zhang, Betzaida Battalla Garcia, Xiaoyuan Zhou, Yoon-Ha Jeong, and Guozhong Cao, Effect of an Ultrathin TiO_2 Layer Coated on Submicrometer-Sized ZnO Nanocrystallite Aggregates by Atomic Layer Deposition on the Performance of Dye-Sensitized Solar Cells, Adv. Mater. 2010, Volume 22, 2329–2332

[19] J. X. Wang, X. W. Sun, Y. Yang and C. M. L. Wu, N–P transition sensing behaviors of ZnO nanotubes exposed to NO_2 gas, Nanotechnology 2009, Volume 20, 465501

[20] Rishi Vyas, Sarla Sharma, Parul Gupta, Y.K. Vijay, Arun K. Prasad, A.K. Tyagi, K. Sachdev, S.K. Sharma, Enhanced NO_2 sensing using $ZnO–TiO_2$ nanocomposite thin films, J. Alloy Comp. 2013, Volume 554, 59–63

[21] C. Sönnichsen, T. Franzl, T. Wilk, G. von Plessen, J. Feldmann, O. Wilson, P. Mulvaney, Drastic Reduction of Plasmon Damping in Gold Nanorods, Phys. Rev. Let. 2002, Volume 88, Issue 7, 0774022- 0774024.

[22] K.-S. Lee, M. A. El-Sayed, Dependence of the Enhanced Optical Scattering Efficiency Relative to That of Absorption for Gold Metal Nanorods on Aspect Ratio, Size, End-Cap Shape, and Medium Refractive Index, J. Phys. Chem. B 2005, Volume 109, 20331–20338.

[23] Xianmao Lu, Matthew Rycenga, Sara E. Skrabalak, Benjamin Wiley, Younan Xia, Chemical Synthesis of Novel Plasmonic Nanoparticles, Annu. Rev. Phys. Chem. 2009, Volume 60, 167-192.

[24] J. Aizpurua, Garnett W. Bryant, Lee J. Richter, F. J. García de Abajo, Brian K. Kelley, T. Mallouk, Optical properties of coupled metallic nanorods for field-enhanced spectroscopy, Phys. Rev. B 2005, Volume 71, 235420.

[25] A. Mohammadi, V. Sandoghdar, M. Agio, Gold nanorods and nanospheroids for enhancing spontaneous emission, New J. Phys. 2008, Volume 10, 105015-105029.

2.2 Comparison between the gas sensing performances of different shapes of gold nanoparticles coupled with platinum embedded in a titanium oxide matrix

The interaction between the light and a nanostructured material gives arise to a strong electromagnetic field enhancement localized in the nanometer scale. This enhancement occurs due to the resonantly exited collective electron oscillations, known as LSPR [1].

LSPs, as widely known, are highly sensitive to the nanoparticles geometry and surrounding medium. Between the many different shapes of gold NPs, in the present paragraph, nanorods (NRs) with a.r. 3 and 6, nanodumbbells (NDs) and nanostars (NSs) are studied.

The objective of the present work is to take true advantage from the substitution of gold spherical NPs inside a matrix of metal oxide, TiO_2 anatase, with the different shaped nanoparticles, in order to involve a major sensitivity to the exchange of electrons in the gas sensing tests.

NRs, with different aspect ratio (3 and 6) should be more sensitive than the sphere because they have two directions of oscillation, transversal and longitudinal, and the second one is more sensitive to the variation of electron oscillating, this gives arise to bigger shift than the one expected for the spherical NPs.

NDs, instead, have a longitudinal plasmon peak more red-shifted than nanorods, but the highest sensitivity is expected at the two spheres at the ends of the rod.

The NSs, instead, have a plasmon band due to the tips and a shoulder due to the core, more blue-shifted. The band due to the tips depends on the length of the tips of the stars, on the width at half height and on the angle at the tips. This second band should be highly sensitive, even more than the one of nanorods because at the tips there is a localized electrical field.

The problem of that morphology of nanoparticles is the reshaping with the temperature, as they tend to spheroidize. The strategy adopted is to use colloidal synthesis of anatase NPs, Au NPs and Pt NPs to prepare crystalline films at low temperature [2]. It has been demonstrated that TiO_2-Au films can react with reducing gases also at low temperature, but with long transient times. If Pt is added, it can act as a catalyst in the gas detection kinetics, making the absorption and the reaction of the gas faster, for example permitting to lower the operative temperature, while Au NRs are responsible for the optical modification of the nanocomposites, making possible the optical detection.

These nanocomposites have been used as active materials for H_2, CO and NO_2 detection at low temperature (<100°C), for their instability at the increase of the temperature.

2.2.1 Experimental

2.2.1.1 Nanoparticles synthesis

The Au NRs with a.r. 6, the Au NDs and the Au NSs and the Pt and TiO_2 NPs synthesis procedure are reported in the appendixes A.2.3, A.2.4, A.2.5, A.2.6 and A.2.7, respectively.

2.2.1.2 Samples deposition

The starting solutions were prepared by mixing the methanol suspension of TiO_2 with the different PVP-capped Au NPs and Pt NPs in ethanol (Tab. 2.2.1).

Samples	Au:Pt molar ratio
TiO_2-AuNRsa.r. 3 -Pt NPs (TR6P)	10:2
TiO_2-AuNRsa.r. 6 -Pt NPs (TR6P)	10:2
TiO_2-AuNDumbbells -Pt NPs (TDP)	10:2
TiO_2-AuNStars -Pt NPs (TSP)	10:2

Tab. 2.2.1- Nanocomposite thin films of TiO_2-AuNPs (of different shapes) -Pt NPs with fixed molar ratios between Au and Pt.

All the film samples were deposited by spin coating at 3000rpm for 30 s on either SiO_2 or Si substrates and dried at 50°C for 5min and then other 4 layers were deposited, with the same parameter, then dried again at 60°C.

2.2.1.3 Gas sensing measurements

Optical gas sensing tests were performed with operating temperature (OT) set at room temperature and the sensor was tested for H_2 10000 ppm balanced with synthetic air.

2.2.2 Results and discussion

2.2.2.1 Structural and optical properties

All the components were characterized, at first, in solution, to check their crystallinity and optical quality; the absorption spectra and XRD pattern of TiO_2 NPs are already reported in Figure 2.1.2; for the Pt NPs the absorption spectrum and XRD pattern with the TEM image are already reported in Figure 2.1.4.

About the high a.r. NRs, thanks to the second addition of Ascorbic Acid (AA) (see Appendix 2.3) the amount of gold salt reduced is higher [3], and is possible to see in Figure 2.2.1 also a red-shift of the longitudinal plasmon peak with respect of the spectrum of the rods before the second AA addition. For this NRs the longitudinal plasmon peak reaches 1000nm; it is also possible to see in the TEM image (Fig. 2.2.1), that the NRs have an average length of 60nm and width of 10nm (a.r. 6).

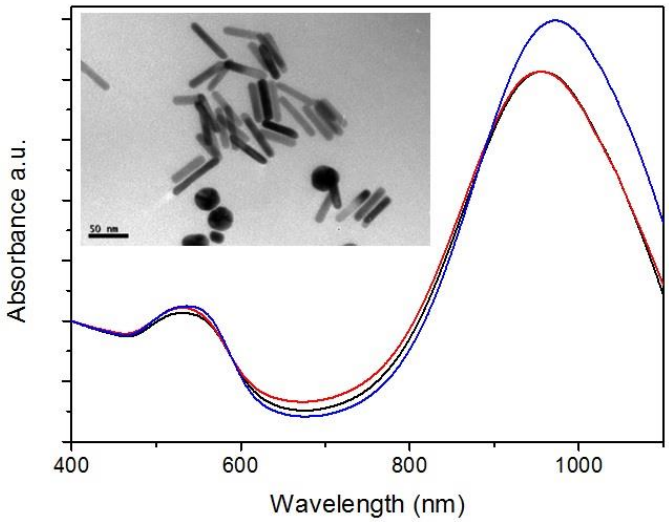

Fig. 2.2.1- UV-Vis spectra of Au NRs with a.r. 6: black line as synthesized NRs, red line NRs with the addition of AA after 24h, blue line NRs with the second addition of AA to reach the ratio AA/Au3+= 1,5; in the inset is presented the TEM image of the Au NRs with a.r. 6.

In Figure 2.2.2 are presented the absorption spectra of the gold NDs [4] and of the gold NRs used as seed, it is possible to see a shift of about 100nm of the longitudinal band from the seed longitudinal band, and the increase of the absorbance of the transvers peak is probably due to the fact that there are spherical byproducts increased in dimension because of the growth solution, containing Potassium Iodide (KI), and also to the spherical shape of the tips of NRs, typical of NDs, which can contribute to that phenomenon. Moreover, in the TEM image (Fig. 2.2.2) are presented the NDs and they have an average length about 60nm.

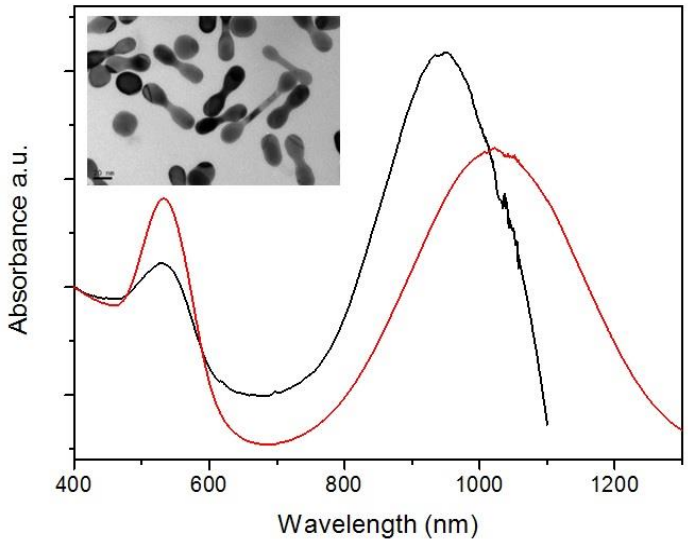

Fig. 2.2.2- UV-Vis spectra of Au NDs, with in black the spectrum of the Au NRs used as seed and in red the spectrum of the final NDs; in the inset is presented the TEM image of the Au NDs.

The gold NSs [5]absorption spectrum is reported in Figure 2.2.3 from which it is possible to identify the core's plasmon peak, which is a shoulder at 550nm, and the tips plasmon peak at 810nm, meaning that the average dimension of NSs synthesized (including the tips) is around 50nm as confirmed by the SEM image reported in Figure 2.2.3.

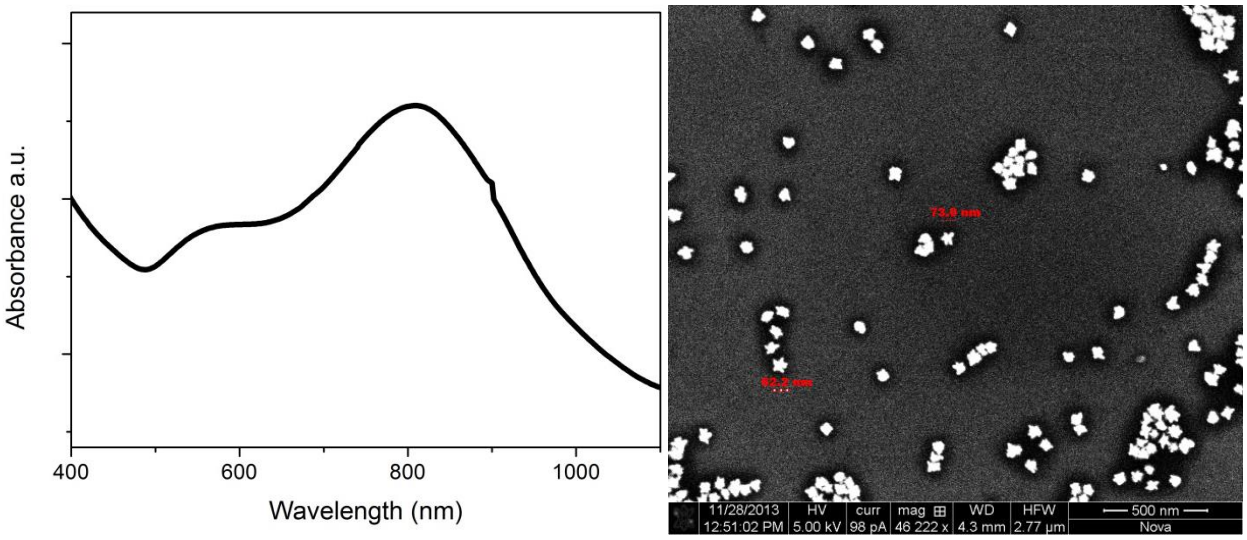

Fig. 2.2.3- UV-Vis spectrum (left) and the SEM image (right) of the NSs.

In Figure 2.2.4 are presented the absorption spectra of the samples reported in Table 2.2.1, and it is possible to identify the plasmonic peaks of the different NPs.

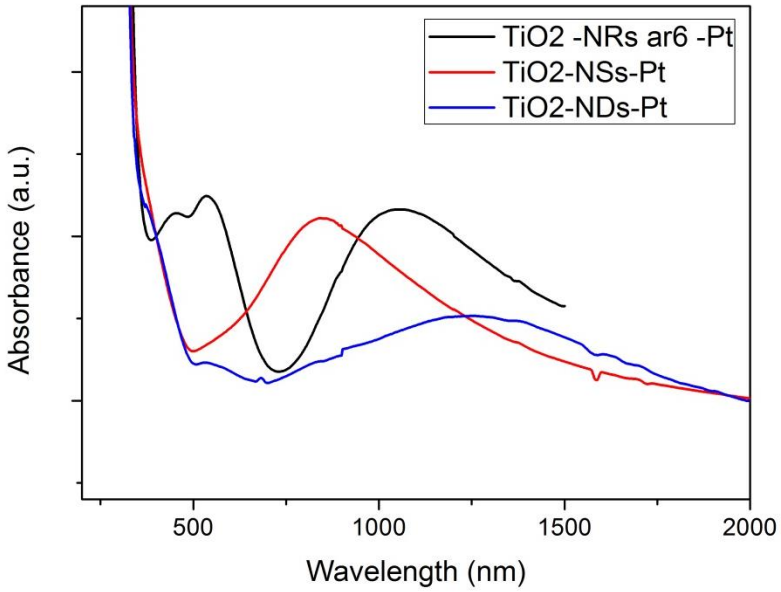

Fig. 2.2.4- Absorption spectra of the NRs with a.r. 6 (black line), the NSs (red line) and the NDs (blue line) embedded with Pt NPs inside a TiO_2 matrix.

The thin films have to be stabilized with a thermal treatment to perform gas sensing tests, so it has been studied the thermal stability of the different NPs inside the TiO_2 matrix, to find the maximum temperature for the thermal treatment avoiding the spheroidization (Fig. 2.2.5-7).

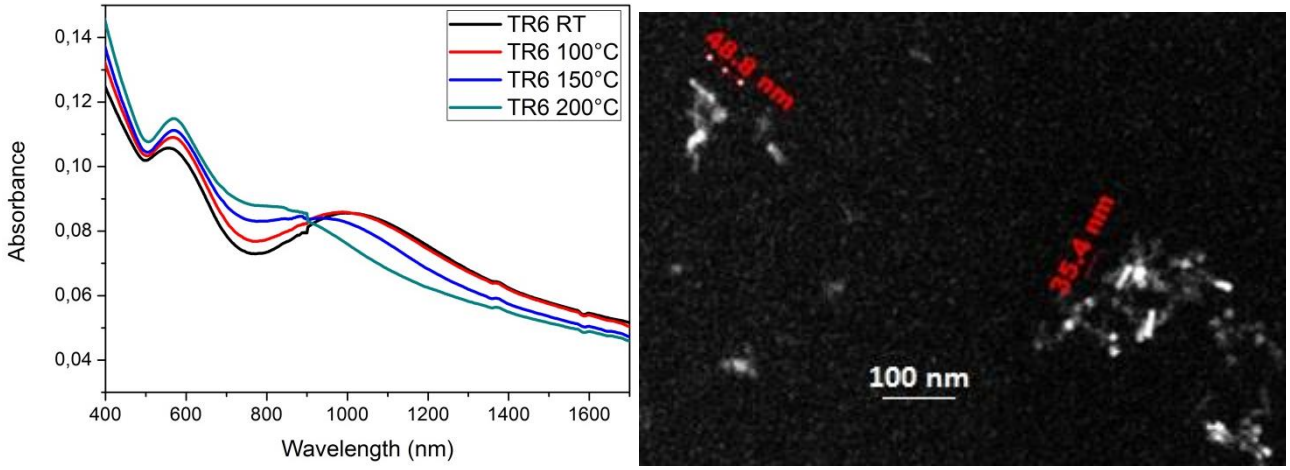

Fig. 2.2.5- Absorption spectra of the samples TiO_2-Au NRs a.r. 6 (TR6) treated at different temperatures up to 200°C (left) and SEM image (right) of the film annealed at 100°C.

In Figure 2.2.5 it is reported the evolution of the adsorption spectrum of the thin film with Au NRs with the temperature, and it is possible to monitor the tendency towards the spheroidization of the NRs. It is clear that the maximum temperature allowed to heat treat the thin film to stabilize them is 100°C. In Figure 2.2.5 it is also reported the SEM image of the thin film annealed at 100°C and it is evident that the shape of the NRs is kept; the brightest part of the particles are the most superficial, moreover not all the particles are horizontal in the film so some tips can be brighter than other.

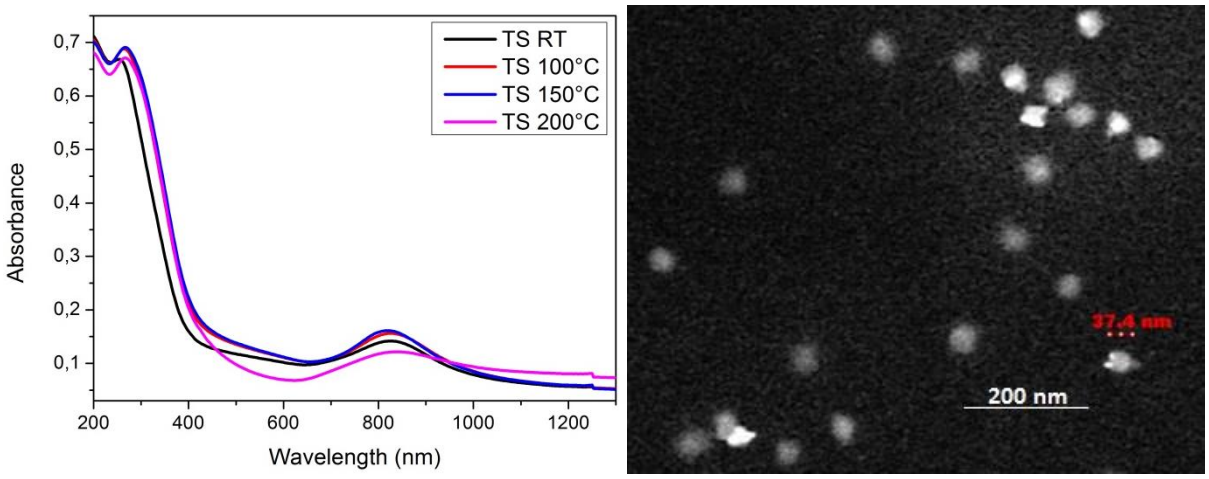

Fig. 2.2.6- Absorption spectra of the samples TiO_2-Au NSs (TS) treated at different temperatures up to 200°C (left) and SEM image (right) of the film heat treated at 70°C.

In Figure 2.2.6, as in Figure 2.2.5, it is reported the evolution of the absorption spectrum of a thin film containing Au NSs, at the increase of the temperature the peak corresponding to the tips disappears and the one corresponding to the core increases, the maximum temperature allowed to preserve the tips shape has to be lower than 100°C. In Figure 2.2.6 it is presented the SEM image of the thin film treated at 70°C and it is evident that the shape of the NSs is kept, in particular some particles showed clearly the bright tips.

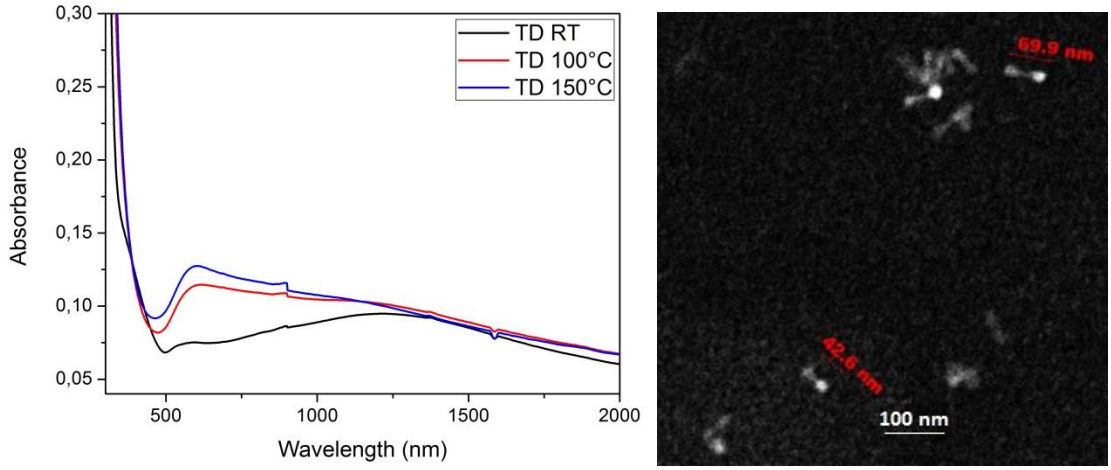

Fig. 2.2.7- Absorption spectra of the samples TiO_2-Au NDs (TD) treated at different temperatures up to 150°C (left) and SEM image (right) of the film heat treated at 70°C.

In Figure 2.2.7 it is clear that, as for NSs, the maximum temperature allowed is lower than 100°C and from the SEM image is evident the preservation of the dumbbell shape with the spherical tips; some of them are brighter because closer to the surface, in fact the particles can be vertical or tilted inside the TiO_2 matrix.

2.2.2.2 Gas sensing tests

The TR3P, TR6P, TDP and TSP nanocomposite films, annealed at the proper temperature as indicated in the previous paragraph, were tested towards H_2, in Figure 2.2.8 a-c the absorbance spectra of the samples TR3P, TR6P and TDP are reported, respectively, in air and in H_2. It is possible to note in all the samples a blue shift of the plasmon peaks of both the longitudinal and transverse LSPR band [6]. In Figure 2.2.8 d are reported the same spectra for the sample TSP and it is possible to note a blue shift of the LSPR corresponding to the tips of the Au NSs [7].

In Figure 2.2.9 are reported the OAC curves corresponding to the scan sensing measurements reported in Figure 2.2.8 for the different particles, it is reported also the OAC curve for the NRs with a.r. 3, already presented in chapter 2.1, this because we want to demonstrate that the increase in aspect ratio leads to an improvement in the sensing performances, because of the enhanced localized electrical field effect.

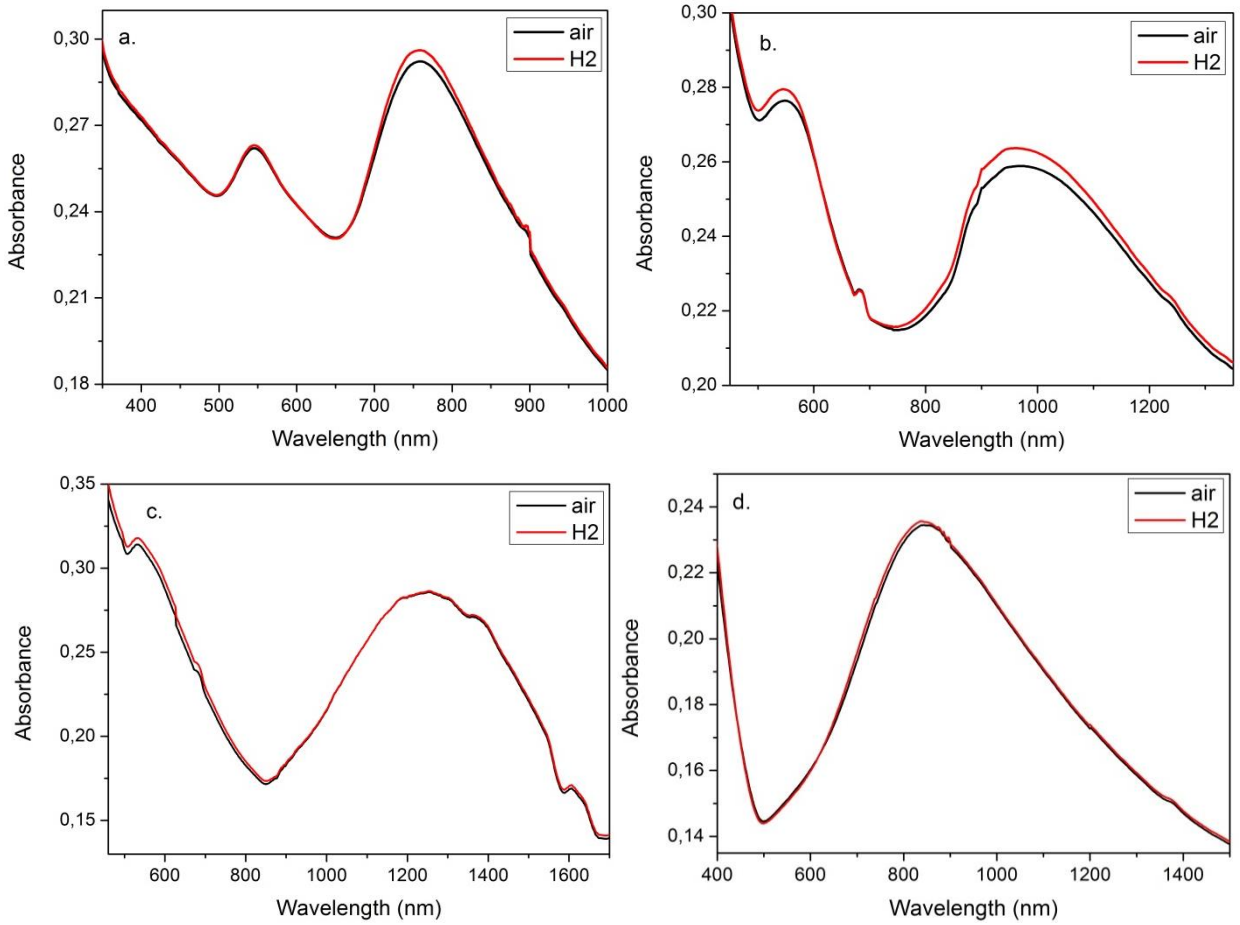

Fig. 2.2.8- Absorption spectra in air and in H_2 for TR3P film (a.), TR3P film (b.), TDP film (c.) and TSP film (d.).

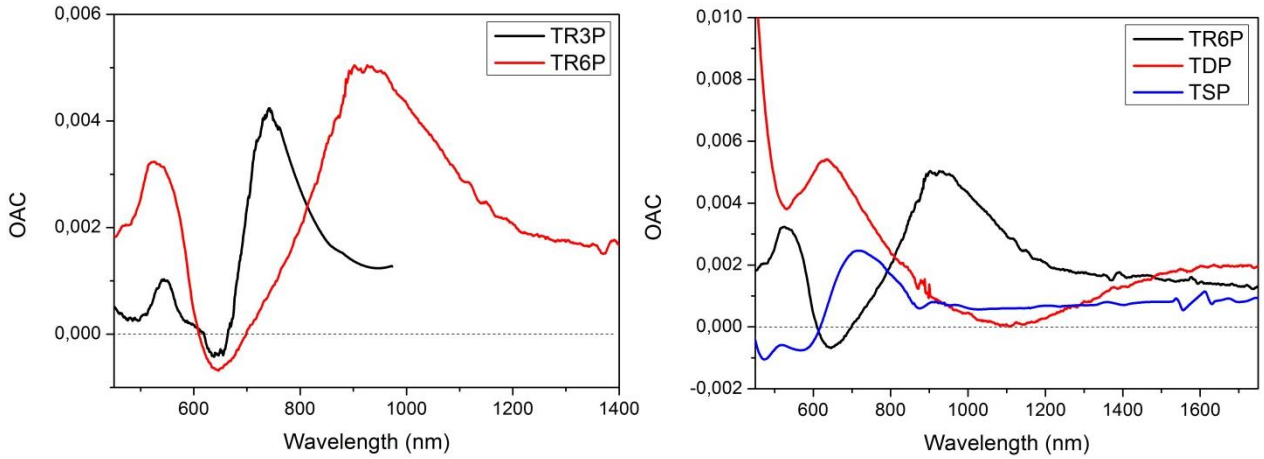

Fig. 2.2.9- Comparison between the OAC curves of TR3P and TR6P (left) and of TR6P, TDP and TSP (right).

The electric field surrounding the NRs is nonuniform, the longitudinal resonance is stronger and more sensitive than the transverse [8]. This is evident for the NRs with the two different a.r., in fact the shift of the longitudinal peak is higher (Fig. 2.2.8 a and b), this is highlighted in Figure 2.2.9, the variation of absorbance for the transverse peak at 520-540 nm for both the NRs is lower than the one for the longitudinal peak at 740 and 910, respectively for NRs with a.r. 3 and 6. For NDs the mechanism is more complicated, the surface curvature of the dumbbells greatly affects the surface charge distribution, local field enhancement and plasmon coupling. It is reported that the dumbbell-shaped particles structure results to have the "hot spots" of the local field in the spherical ends of the particle [9]. This means that the peak at 550 nm, relative to the spherical tips of the dumbbell, is expected to be more sensitive than the second one, the longitudinal.

Also the nanocomposite with NSs have been tested towards H_2; NSs can spatially focus the incoming light by means of electric field enhancement around their spikes [1]. This justifies why from the OAC curve (Fig. 2.2.9) in the region corresponding to the star's tips peak there is an high variation involving an higher sensitivity towards H_2. In Figure 2.2.8 d is reported the scan measurement in air and H_2, which shows, as expected, a blue shift of the plasmon bands, confirming the injection of electrons as in Figure 2.2.8 a, b and c, for the NRs and NDs based nanocomposite. The reaction involved was already reported in chapter 2.1, and involves the catalysis of Pt which splits the H_2 molecule, reaction 1.

$$H_2 \rightarrow 2H^+ + 2e^- + O^{2-}(ads) \rightarrow H_2O + 2e^- \qquad (1)$$

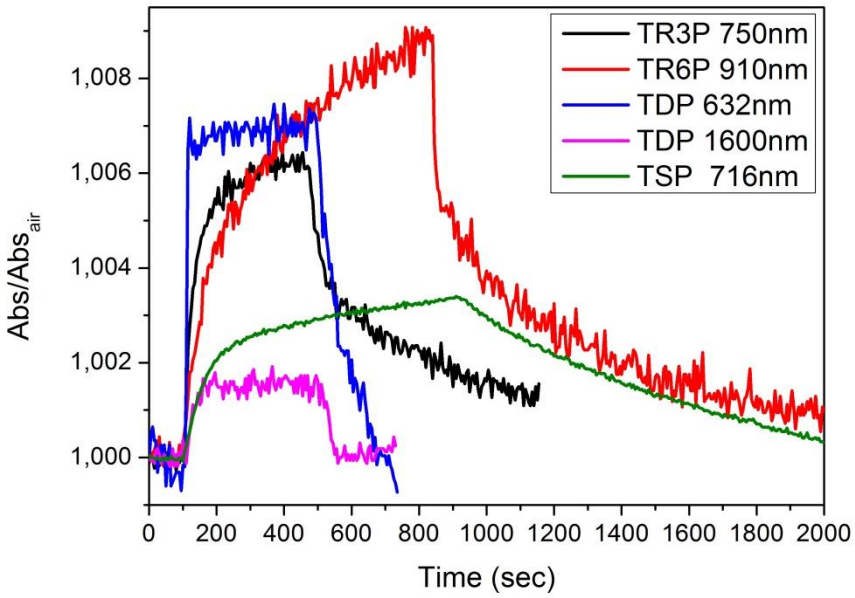

Fig. 2.2.10- Comparison between the dynamic gas sensing test at room temperature with H_2 on the TR3P film (black line), TR6P film (red line), TDP film (peak corresponding to the spherical tips blue line and to the rod part pink line) and TSP film (green line).

In Figure 2.2.10 are reported the dynamic gas sensing measurement at the fixed wavelength of maximum variation in absorption for the NRs with a.r. 3, 6 and the NDs embedded into the TiO_2 matrix and coupled with Pt NPs. For the NDs based nanocomposite is reported the dynamic measurement for both the plasmonic peaks, and what already explained about the higher sensitivity of the two spherical tips is confirmed. The stars based nanocomposite, as highlighted in Figure 2.2.10, are less performing than the elongated shapes like NRs or NDs. The particular morphology of the NSs can probably hinder an optimal contact at the interface with the TiO_2 matrix which can explain the poor results obtained with the NSs. High resolution TEM measurements should be performed on the nanocomposite film in order to better elucidate this point.

2.2.3 Conclusions

In this chapter the optical gas sensing performances of Au NRs, NDs and NSs coupled with catalytic Pt NPs embedded into a semiconducting matrix (TiO_2) towards H_2 10000 ppm have been investigated.

The sensors showed good and reversible responses with fast kinetics for all the gold NPs thanks to the catalytic role of the Pt. The NDs showed the best performances at the spherical tips respect to all the other samples, for an electrical field enhancement effect which makes the plasmon more sensitive to the changes in the dielectric surrounding and to the injection of electrons due to the interaction with the target gas.

References

[1] Sergey M. Novikov, Ana Sànchez-Iglesias, Mikotaj K. Schmidt, Andrey Chuvilin, Javier Aizpurua, Marek Grzelczak, Luis M. Liz-Marzán, Gold spiky nanodumbbells: anisotropy in gold nanostars, Part. Part. Syst. Charact. 2013, DOI: 10.1002/ppsc.201300257

[2] Enrico Della Gaspera, Alessandro Antonello, Massimo Guglielmi, Michael L. Post, Valentina Bello, Giovanni Mattei, Filippo Romanato, Alessandro Martucci, Colloidal approach to Au-loaded TiO_2 thin films with optimized optical sensing properties, J. Mater. Chem. 2011, Volume 21, 4293.

[3] Babak Nikoobakht, Mostafa A. El-Sayed, Preparation and Growth Mechanism of Gold Nanorods (NRs) Using Seed-Mediated Growth Method, Chem. Mater. 2003, Volume 15, Issue 10, 1957-1962.

[4] M. Grzelczak, A. Sánchez-Iglesias, B. Rodríguez-González, R. Alvarez-Puebla, J. Pérez-Juste, L.M. Liz-Marzán, Influence of Iodide Ions on the Growth of Gold Nanorods: Tuning Tip Curvature and Surface Plasmon Resonance, *Adv. Funct. Mater.* 2008, Volume *18*, 3870-3876.

[5] P.S. Kumar, I. Pastoriza-Santos, B. Rodríguez-González, F.J. García de Abajo, L.M. Liz-Marzán, High-Yield Synthesis and Optical Response of Gold Nanostars, *Nanotechnology* 2008, Volume 19, 015606(1-5).

[6] Stella M. Marinakos , Sihai Chen , Ashutosh Chilkoti, Plasmonic Detection of a Model Analyte in Serum by a Gold Nanorod Sensor, Anal. Chem. 2007, Volume 79, Issue 14, 5278–5283.

[7] Katherine A. Willets, Richard P. Van Duyne, Localized Surface Plasmon Resonance Spectroscopy and Sensing, Annu. Rev. Phys. Chem. 2007, Volume 58, 267–297.

[8] Abdennour Abbas, Limei Tian, Jeremiah J. Morrissey, Evan D. Kharasch, Srikanth Singamaneni, Hot Spot-Localized Artificial Antibodies for Label-Free Plasmonic Biosensing, Adv. Funct. Mater. 2013, Volume 23, Issue 14, 1789–1797.

[9] Jian Zhu, Ying-juan Ren, Tuning the plasmon shift and local electric field distribution of gold nanodumbbell: The effect of surface curvature transition from positive to negative, Appl. Surf. Sci. 2013**,** Volume 285, Part B, 649–656.

2.3 Dark field microscopy on single gold nanorods

Catalysts are substances that speed up reactions by providing an alternative pathway with lower activation energy than that required for the uncatalyzed reaction [1].A lot of research, fundamental and applied, has been done by university and industries as well to investigate how catalysts work and to increase their efficiency.

In the present chapter we use Dark Field Microscopy (DFM) coupled with surface plasmon spectroscopy, for the direct observation of the kinetics of H_2 gas interaction with single gold NR and, consequently, for monitoring of the electron exchange through the measurement of the single Au NR SPR band shift [2].

The DFM technique coupled with surface plasmon spectroscopy has already been widely used to monitor the electrons exchanges using different shapes of Au nanocrystals [2] or different metal nanocrystals [3] as well as in the case of heterogeneous catalysis [4]. Liu *et al.* used this technique on samples made by lithography consisting of a single Pd NP near the tip of a gold nanoantenna, for monitoring the optical properties changes during hydrogen exposure [5]; finally, Tittl *et al.* used silica shell-isolated gold NPs as a smart dust to investigate the hydrogen dissociation catalyzed by palladium [6].

This is the first direct measurement, with simply spin coated Au NRs and Pt catalyst NPs, of electron injection induced by H_2 to a single gold NRs, which work just as an optical probe, thanks to the catalytic activity of the Pt NPs, in the presence of a semiconducting metal oxide matrix.

The main goal was to study the conditions which lead to the improvement of the H_2 red-ox reaction efficiency and of the involved electrons injection. In a previous work [7] we alredy investigated the role of 10 nm Pt NPs as catalyst for the optical detection of H_2 trough TiO_2-Au nanocomposite films.

The first major barrier to progress is the need to understand the role of oxygen ions adsorbed on the metal oxide matrix in the electron injection. The second barrier is to understand if there is a double contribution to the SPR band shift and increased absorbance: from one side the electrons injection from the Pt NPs surface, where the H_2 molecules split, towards the gold NRs and on the other side, linked to the presence of a semiconducting matrix, the increase of the dielectric constant of the TiO_2 matrix as a consequence of the increase of the number of electrons due to the H_2 oxidation.

2.3.1 Experimental

2.3.1.1 Nanoparticles synthesis

The Au NRs with a.r. 3 and the Pt,TiO_2 and ZnO NPs synthesis procedure are reported in the appendixes A.2.2, A.2.6, A.2.7 and A.2.9, respectively.

2.3.1.2 Samples deposition

Samples for DFM measurements were deposited on fused silica quartz slides or silicon substrates by spin coating at 3000 rpm for 30 s and annealed for 10 min in air. The prepared samples are reported in Table 2.3.1. The sample Au NRs were spin coated starting from the aqueous solution at 3000 rpm for 30 s and dried at 70 °C for 10 min; the sample Au NRs + Pt NPs was prepared spin coating the ethanolic solution of Pt NPs at 3000 rpm for 30 s and dried at 150 °C, then the aqueous solution of Au NRs was spin coated on the Pt NPs monolayer, as already explained for the sample Au NRs, and annealed at 70 °C. The Pt NPs were deposited at the bottom because they need to be annealed to work properly as catalyst, instead Au NRs cannot be treated at temperatures higher than 70-80 °C instead they tend to spheroidize. The sample Au NRs + TiO_2 was prepared as the sample Au NRs and on the top was deposited a layer of TiO_2 NPs and finally the sample was annealed at 150 °C for 10 min. The sample Au NRs + (TiO_2-8%Pt NPs) was prepared as the sample Au NRs and on the top was deposited a solution of TiO_2 and Pt NPs mixed together and finally the sample was annealed at 150 °C for 10 min. Au NRs + TiO_2 + Pt NPs was prepared exactly as the sample Au NRs + TiO_2 and before the annealing at 150 °C for 10 min a monolayer of Pt NPs was spin coated on the top of the sample. Finally, the sample Au NRs + (SiO_2-8%Pt NPs) was prepared spin coating the Au NRs solution as for the sample Au NRs, then, the SiO_2 solution was mixed with the one of Pt NPs, and spin coated on the top of the Au NRs monolayer; the sample was annealed at 150 °C for 10 min.

Sample	Composition
Au NRs	Bare Au NRs on glass
Au NRs + Pt NPs	Au NRs and Pt NPs on glass
Au NRs + TiO_2	Au NRs on glass covered with TiO_2 film
Au NRs + (TiO_2-8%Pt NPs)	Au NRs on glass covered with TiO_2 film containing Pt NPs
Au NRs + TiO_2 + Pt NPs	Au NRs on glass covered with TiO_2 film on top of which Pt NPs have been deposited
Au NRs + (SiO_2-8%Pt NPs)	Au NRs on glass covered with SiO_2 film containing Pt NPs

Tab. 2.3.1- Sensitive layers composition for the different plasmonic crystals fabricated.

2.3.1.3 Gas sensing measurements

Optical gas sensing tests were performed at room temperature and the sensor was tested for H_2 at 50000 ppm balanced with synthetic air or N_2. The single-particle time-resolved gas sensing tests were performed using the apparatus reported in Appendix 3.2.

2.3.2 Results and discussion

2.3.2.1 Optical and structural characterization of the NPs

The absorption spectrum of the Au NRs with their TEM image are reported in Figure 2.3.1. It is possible to note, from the TEM measurement, that the NRs have a bone shape and their dimensions are 13±4nm of diameter and 40±9nm of length, so they have an aspect ratio around 3.

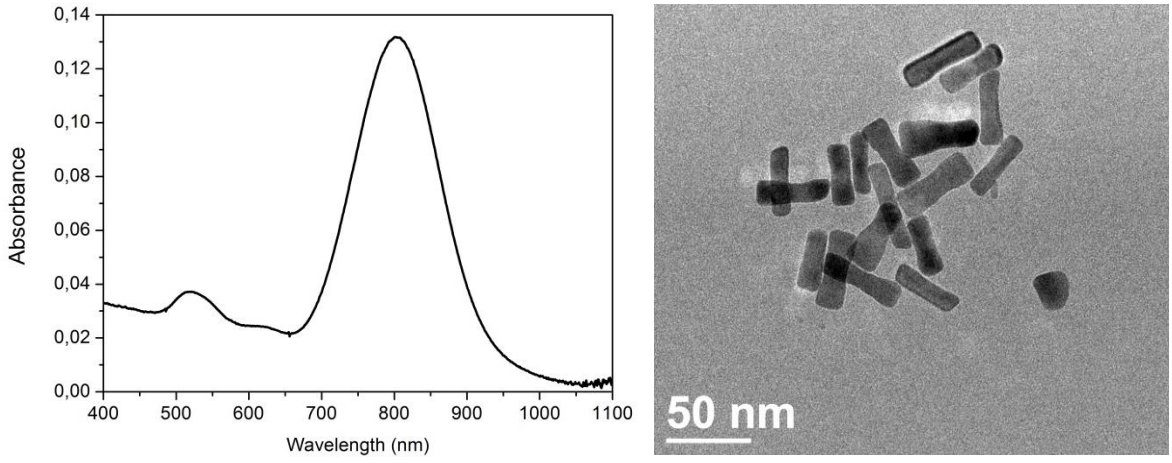

Fig. 2.3.1- UV-Vis spectra of Au NRs (left) and TEM image (right) of the same rods.

The UV-Vis spectrum and the XRD pattern of the Pt NPs are reported in the inset of Figure 2.3.2 a and b. It is possible to note the diffraction peaks typical of cubic Pt (JCPDS No. 04-0802), confirming the crystallinity of the Pt NPs. Moreover using the Scherrer's equation it was possible to evaluate the mean crystallite diameter of the Pt NPs which is 10±0.3 nm.

The TEM image of the Pt NPs (Fig. 2.3.2 c), shows that they have faceted (cubic) shaped and their dimension is 10nm, confirming the result obtained from the XRD analysis, suggesting that the Pt NPs are monocrystalline.

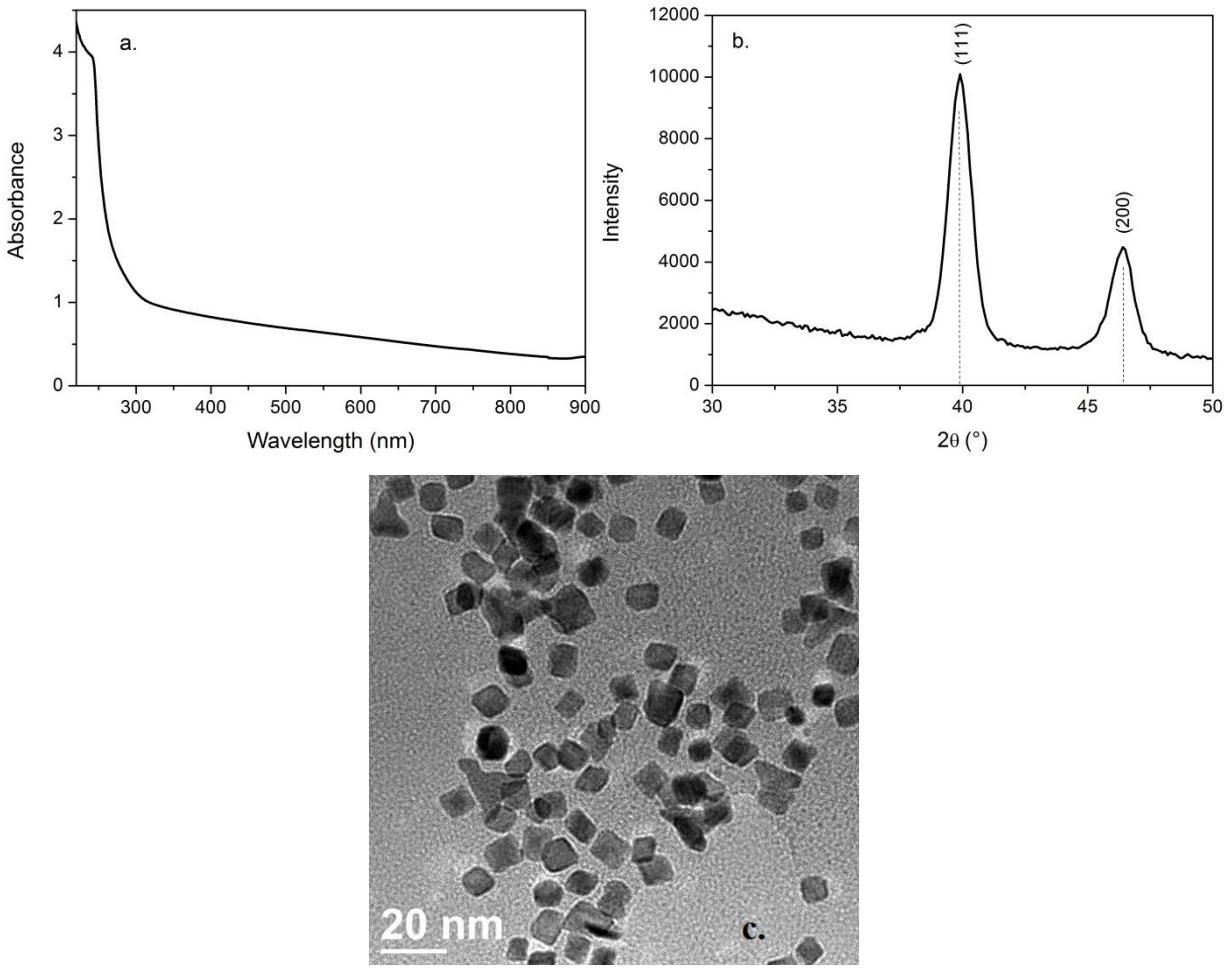

Fig. 2.3.2- UV-Vis spectra (a.), XRD pattern (b.) and TEM image (c.) of the Pt NPs.

In Figure 2.3.3a the UV-Vis spectrum of TiO_2 NPs in methanol solution is reported, showing a good transparency in the visible and the absorption edge in the near UV, this implies a good quality of NPs, without aggregation phenomena, which allows the use of this type of NPs with the DFM technique, requiring low scattering.

The diffraction pattern of TiO_2 NPs is reported in Figure 2.3.3b and shows the typical peaks of tetragonal anatase structure (JCPDS No. 86-1157) [8]. The TEM image of the TiO_2 NPs is also reported in Figure 2.3.3c, from which it is possible to note that the mean diameter is around 5nm moreover the red spot a TiO_2 NPs in which it is possible to note the lattice plane.

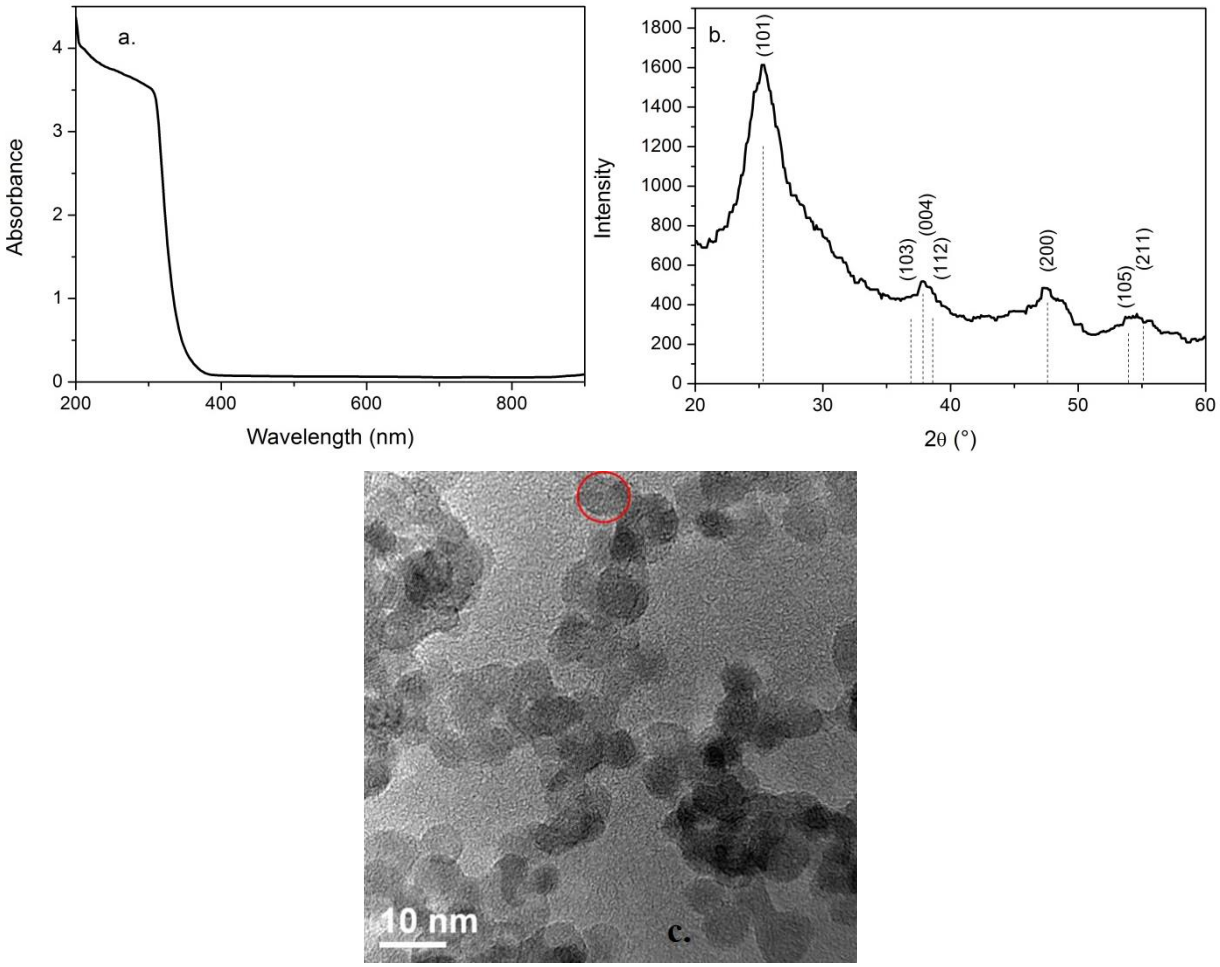

Fig. 2.3.3- UV-Vis spectra (a.), XRD pattern (b.) and TEM image (c.) of the TiO_2 NPs.

2.3.2.2 Optical and structural characterization of the sensitive layers

From the SEM images reported in Figure 2.3.4 it is possible to note that both the SiO_2 and TiO_2 layer used for covering the bare Au NRs are very homogenous and smooth. The refractive index and thickness of the same layers measured by ellipsometry are reported in Table 2.3.2.

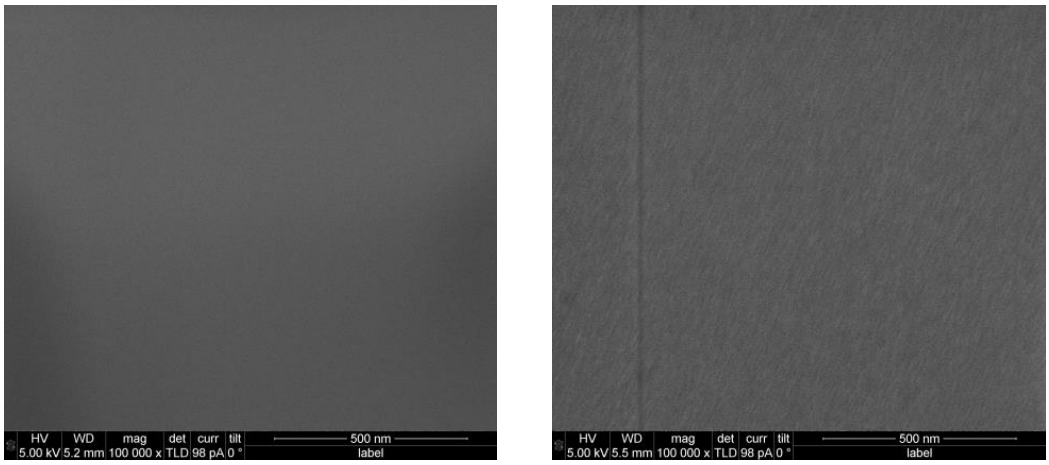

Fig. 2.3.4- SEM image of the SiO_2 (left) and TiO_2 (right) layer used for covering the bare Au NRs.

Sample	Thickness (nm)	Refractive index *n* (at 630nm)
TiO_2	42	1.89
SiO_2	100	1.43

Tab. 2.3.2- Thickness and refractive index values for the different sample measured by ellipsometry.

2.3.2.3 Gas sensing test with DFM technique

Using the DFM in real time mode, images of gold NR (Fig. 2.3.6 on the left) were captured every 60 sec during 3 cycles of exposure to hydrogen 5% v, with N_2 or air, as carrier. Thanks to the coupling with a spectrograph it was possible to obtain the scattering spectra of each monitored NR as a function of the time.

To resolve the spectral shifts associated with hydrogen exposition, it has been employed a Lorentzian fitting method which allows the extrapolation of the curve maximum position.

Each NR works as optical probe and convert the injection of electrons due to the hydrogen reaction into optical signal changes, which are manifested in resonance intensity and resonance position with a response time on the order of few seconds to few minutes depending on the presence of a matrix and of the catalyst.

From the presented tests it is possible to compare the performances of Au NRs in contact with different metal oxides (SiO_2 and TiO_2) and with or without the presence of Pt NPs. The different tested samples are reported in Table 2.3.1.

2.3.2.3.1 Gas sensing test on Au NRs

The sample with only Au NRs, showed no sensitivity to H_2 either in N_2 or in air as carrier, in particular, with air as carrier it is possible to see in Figure 2.3.5 a continuous drift. This implies that the oxygen ions do not have any influence on the sensing behavior of bare gold, and there are no hydrogen ions adsorbed on Au surface. Moreover it is possible to say that in this case, at RT, Au does not have any active role in the sensing mechanism.

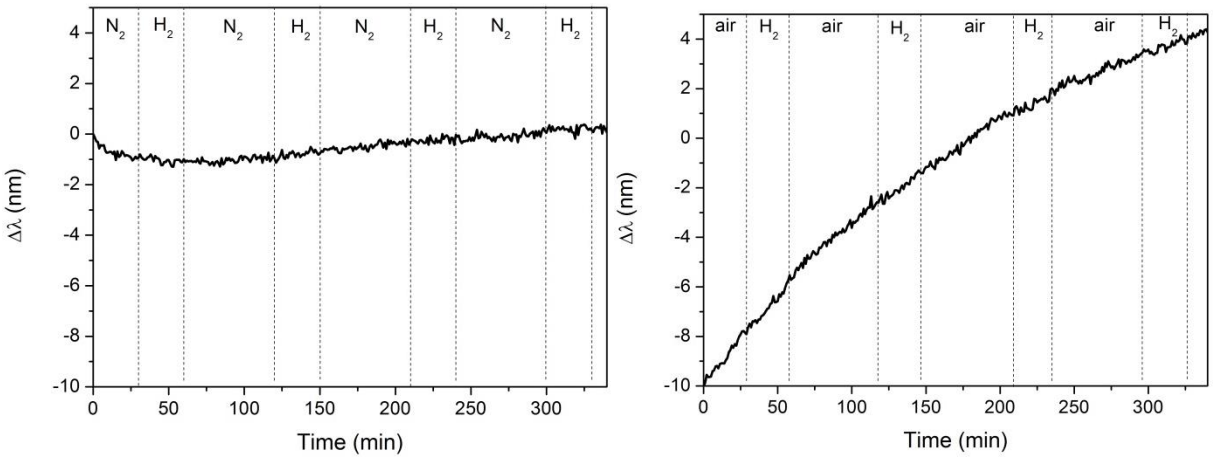

Fig. 2.3.5- Time resolved test with the shifts for a single Au NR performed exposing the sample to multiple N_2-H_2 (left) and air-H_2 (right) cycles.

2.3.2.3.2 Gas sensing test on Au NRs + Pt NPs

Considering the sample with Au NRs coupled with Pt NPs, only some NRs showed sensitivity to H_2 in N_2 flow, as shown in Figure 2.3.6 a (yellow marked). Probably the working NRs are only the one close or in contact with Pt NPs, which, as a consequence, can easily crosstalk with Pt and this allows the injection of electrons from the Pt surface into the NRs and the blue shift in the LSPR showed in Figure 2.3.6 b..

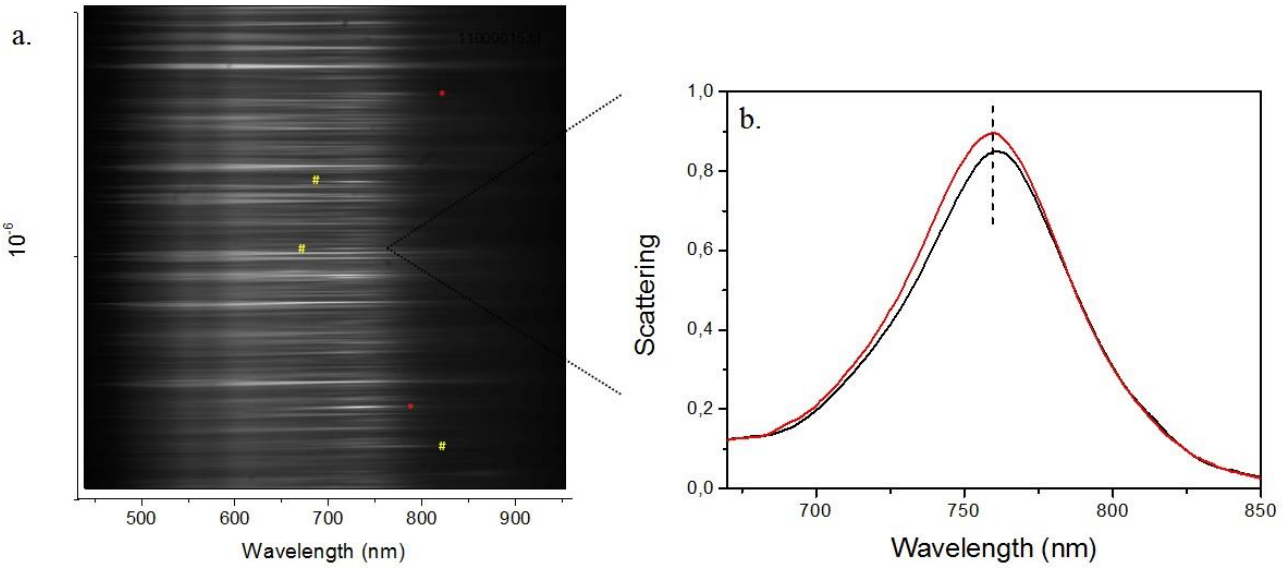

Fig. 2.3.6- a. DFM image of a dynamic gas sensing measurement for single Au NRs coupled with Pt NPs, the sensitive Au NRs are marked in yellow while in red are marked those not sensitive; b. single Au NR scattering spectrum in N_2 (black line) and in H_2 (red line) flux, it is evident the longitudinal SPR peak shift.

The mechanism proposed is the H_2 molecules spillover (1) on Pt NPs surface, thanks to the catalytic activity of Pt, which produce electrons that are consequently injected into the Au NRs closer to the Pt NPs, responsible for the spillover, and cause the blue-shift and the increase in intensity of its plasmon peak.

$$H_2 \overset{Pt}{\rightarrow} 2H^+ + 2e^- \quad (1)$$

In Figure 2.3.7 and 8 a. are reported the optical trajectories corresponding to the hydrogen cycles; the spectral scattering intensity is color-coded over time. The black lines denote the wavelengths of the maximum of the plasmonic peak and to better visualize the shift the time resolved shift Δλ is also reported. These images are presented for the NRs coupled with Pt samples in H_2 with carrier N_2 (Fig. 2.3.7 b.) and air (Fig. 2.3.8 b.).

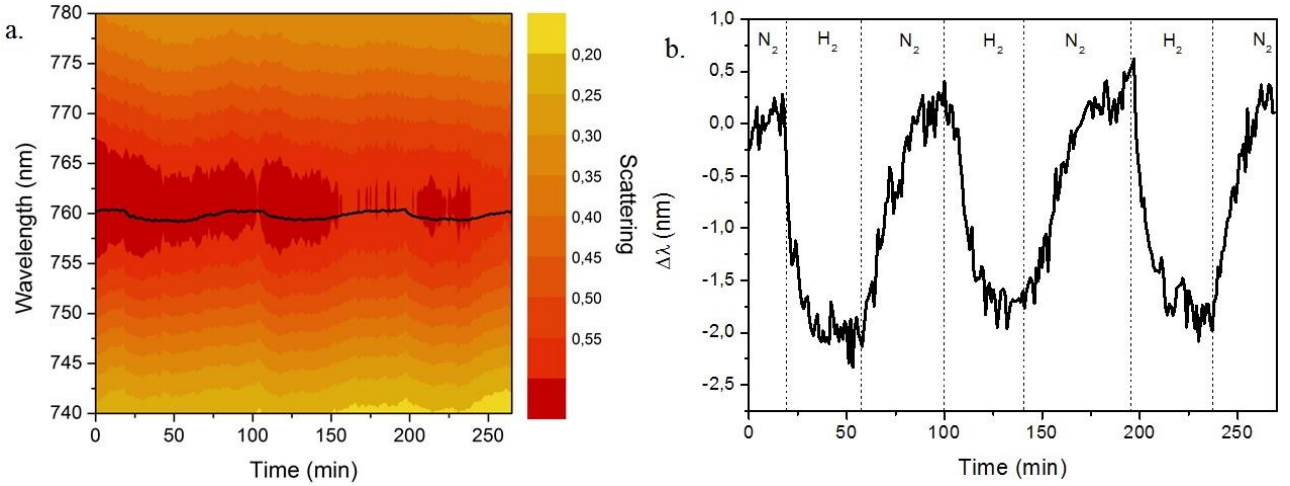

Fig. 2.3.7- Time resolved test with color-coded spectral scattering intensity (a.) and shift (b.) for Au NRs + Pt NPs sample performed exposing the sample to multiple N_2-H_2 cycles.

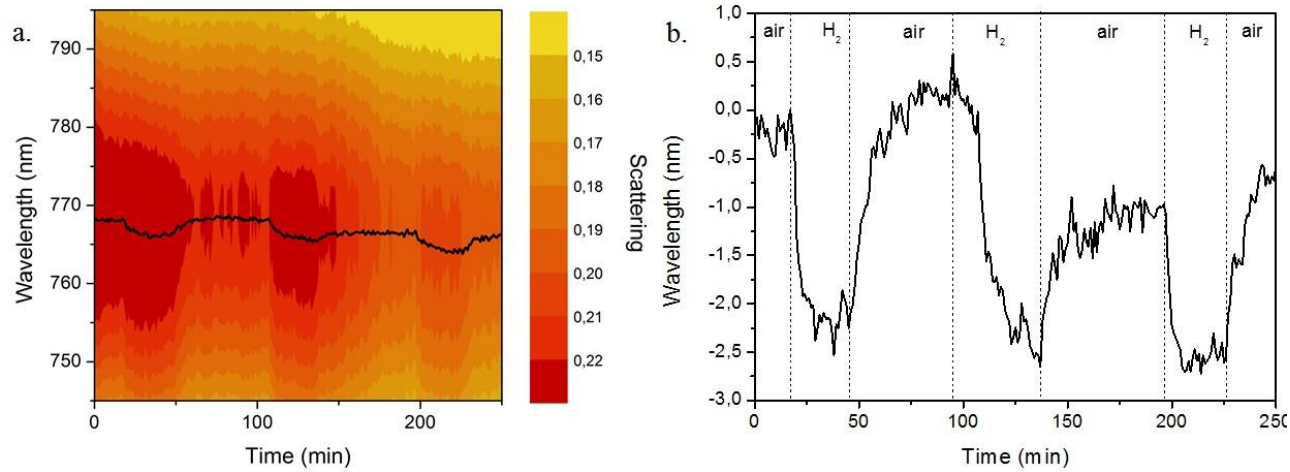

Fig. 2.3.8- Time resolved test with color-coded spectral scattering intensity (a.) and shift (b.) for Au NRs + Pt NPs sample performed exposing the sample to multiple air-H_2 (b) cycles.

From Figure 2.3.6 b it is possible to note that the H_2 affects both the position (there is a blue-shift) and the intensity (there is an increase of the intensity) of the LSPR peak of the Au NRs. The blue-shift is better visualized in Figure 2.3.9, from which it is possible to note a 2 nm shift both for N_2 and air gas carrier for a chosen NR sensitive to H_2. Using as carrier air, like in N_2 flow, not all the NRs are sensitive. Regarding the sensitivity, the presence of oxygen ions does not affect the shift neither the kinetics (Fig. 2.3.9).

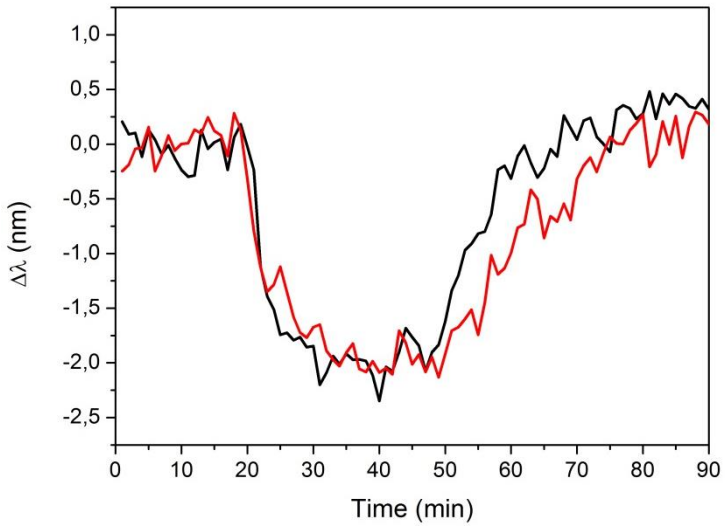

Fig. 2.3.9- Comparison between the time resolved test for Au NRs + Pt NPs sample performed exposing the sample to a H_2 5% cycle using as carrier N_2 (red line) or air (black line).

2.3.2.3.3 Gas sensing test on Au NRs + TiO_2

To understand the role in the sensing of a semiconducting material surrounding the Au NRs, without the presence of Pt to catalyze the H_2 oxidation, a time resolved test for single Au NRs covered with TiO_2 matrix was performed in both N_2 and air, as carrier. The NRs in TiO_2 are not sensitive to H_2 in N_2 flux (Fig. 2.3.10), implying the absence of oxygen ions adsorbed on the sample. This proves that the H_2 does not interact directly with the oxygen of the matrix reducing Ti^{4+} to Ti^{3+}.

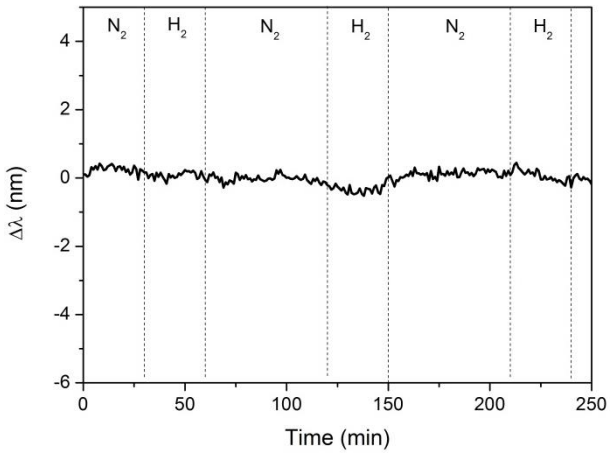

Fig. 2.3.10- Time resolved test with the shifts for a single Au NR covered with TiO_2 performed exposing the sample to multiple N_2-H_2 cycles.

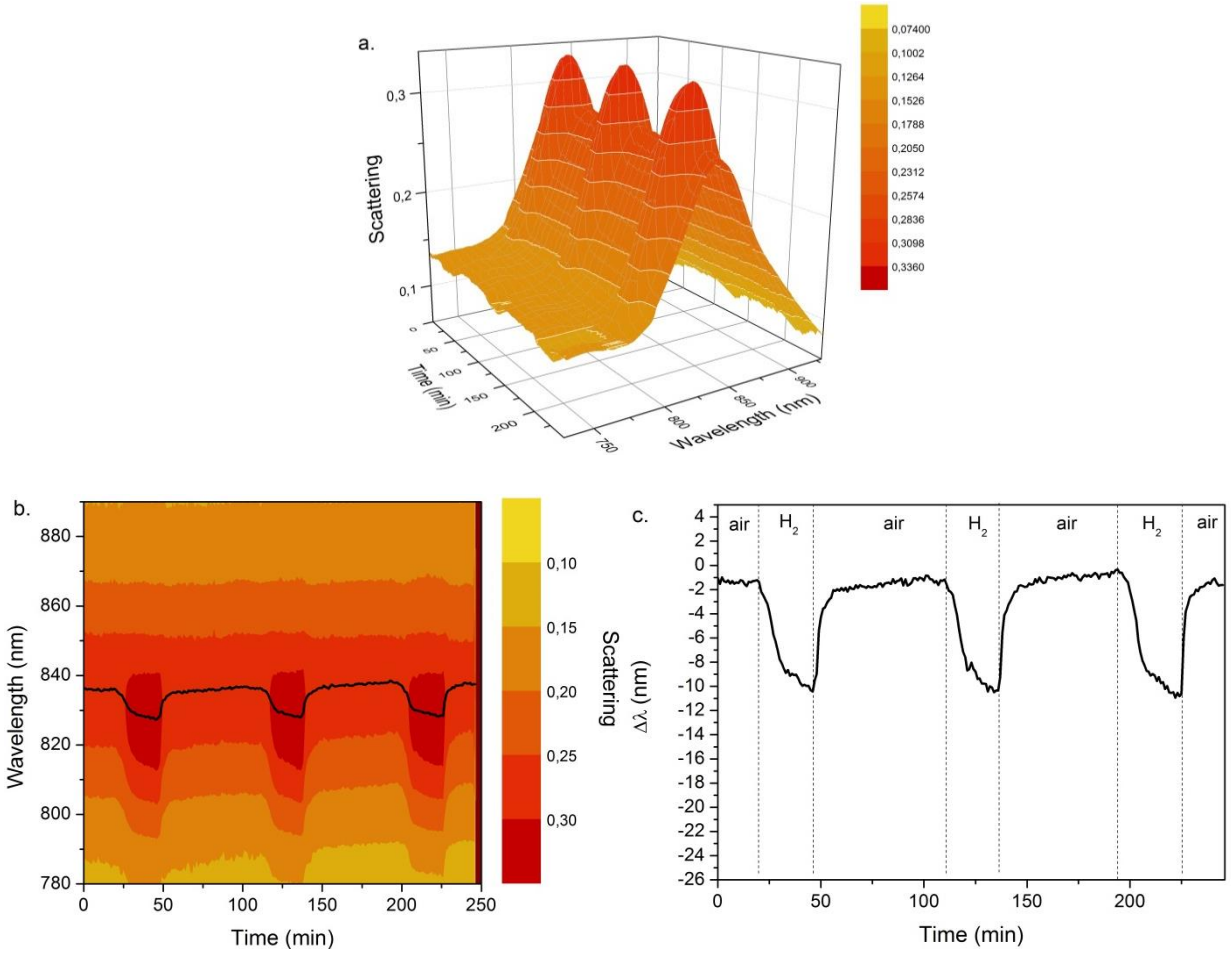

Fig. 2.3.11- Time resolved test with color-coded spectral scattering intensity 3-dimensional a. and bi-dimensional b. and with the shift c. for single Au NRs covered with TiO_2 performed exposing the sample to multiple air-H_2 cycles.

In air flow (Fig. 2.3.11), instead, with oxygen ions adsorbed on TiO_2, even in the absence of Pt NPs, there is sensitivity towards H_2, because the oxygen presence is needed and is enough on its own to allow the H_2 oxidation and the matrix reduction, without any catalyst, as shown in reaction 2.

$$H_2 + O^{2-} \rightarrow H_2O + 2e^- \quad (2)$$

2.3.2.3.4 Gas sensing test on the Au NRs + (TiO_2-8%Pt NPs) sample

Performing the single-particle time-resolved gas sensing test on Au NRs coupled with Pt NPs embedded in a TiO_2 matrix, it is visible a clear blue-shift of the longitudinal SPR peak, together with a strong increase of the LSPR peak absorbance (Fig. 2.3.12a) during H_2 exposure balanced with N_2. From Fig. 2.3.12 b and c it is possible to note that the shift is of 6 nm and the trend of the response and recovery are always the same for all the cycles and the tested Au NRs.

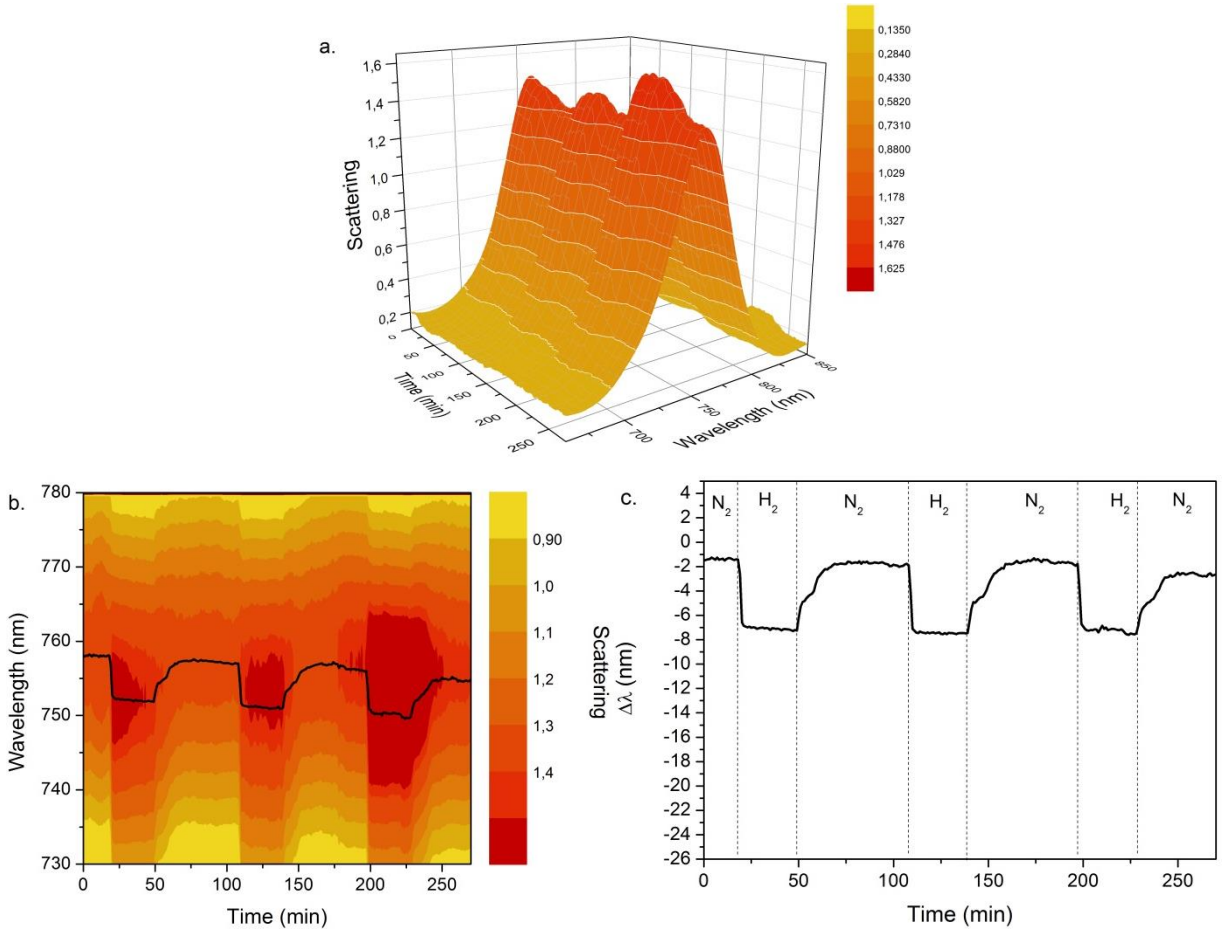

Fig. 2.3.12- Time resolved test with color-coded spectral scattering intensity 3-dimensional a. and bi-dimensional b. and with the shift c. for single Au NRs covered with TiO_2 matrix with embedded Pt NPs performed exposing the sample to multiple N_2-H_2 5% cycles.

It has been demonstrated with this experiment (Fig. 2.3.12) that the shift monitored for the different samples is not just the absorption and desorption of oxygen ions but a real electrons injection; because in N_2 flux the shift is 6 nm and there is no O_2 from the atmosphere influencing the sensing mechanism. The shift, therefore, is not due to desorption of oxygen ions in H_2 flux, neither to the reduction of the Ti^{4+} to Ti^{3+}, as previously said, but a real electrons injection.

In Figure 2.3.13, instead, it is shown the same test performed using as carrier air and the shift in this case is around 20 nm. This suggests that oxygen ions have an important role in H_2 oxidation in presence of the TiO_2 matrix.

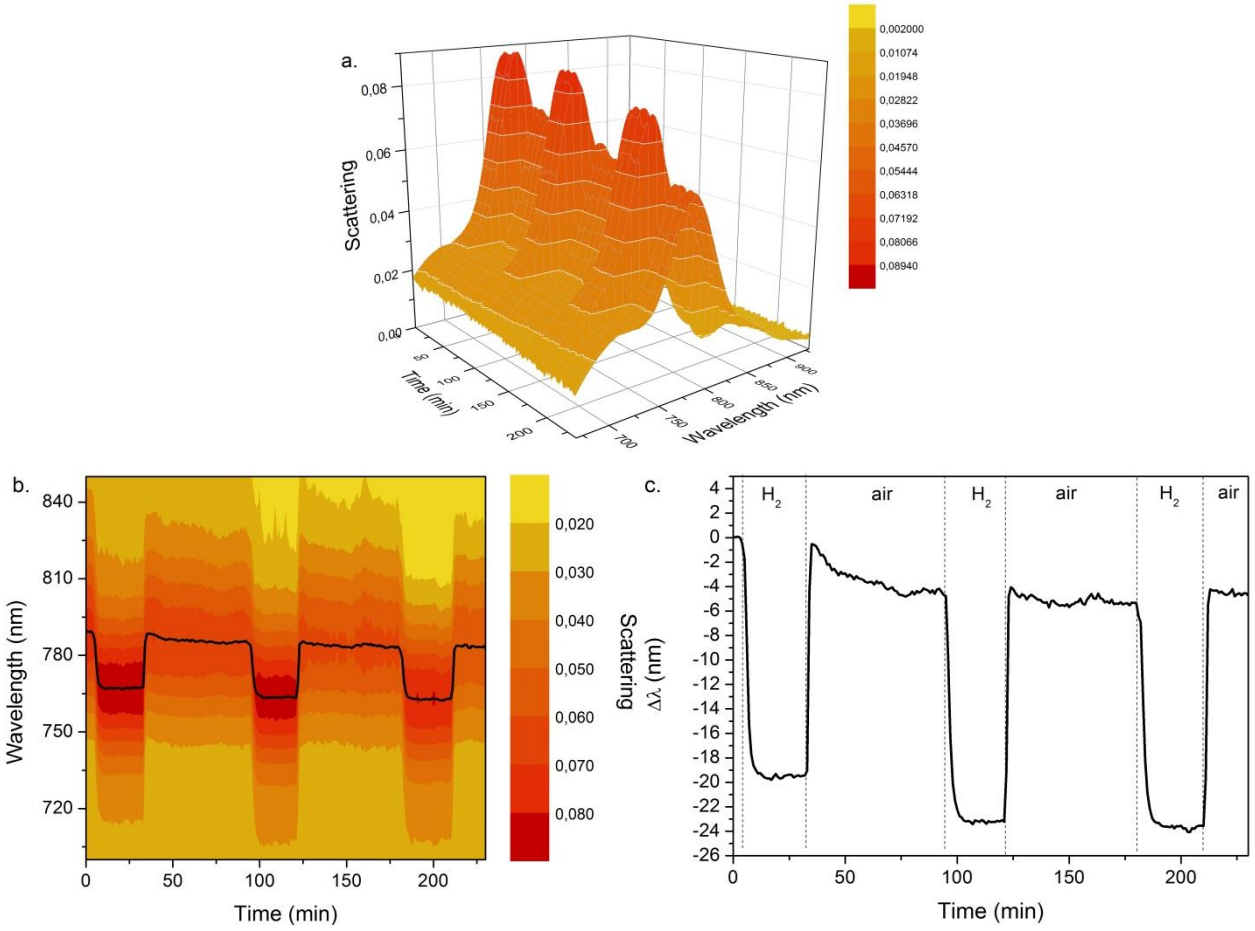

Fig. 2.3.13- Time resolved test with color-coded spectral scattering intensity 3-dimensional a. and bi-dimensional b. and with the shift c. for single Au NRs covered with TiO_2 matrix with embedded Pt NPs performed exposing the sample to multiple air-H_2 5% cycles.

When the test is performed in presence of oxygen ions (carrier air) the H_2 spillover (1) and the consequent electrons injection is more efficient, probably because there are more reactive sites for H_2 oxidation thanks to reactions (3), in fact the shift is 20 nm, ~3 times more than in N_2 (Fig. 2.3.14).

$$H_2 + O^{2-} \xrightarrow{Pt} 2H^+ + 2e^- + O^{2-} \rightarrow H_2O + 2e^- \quad (3)$$

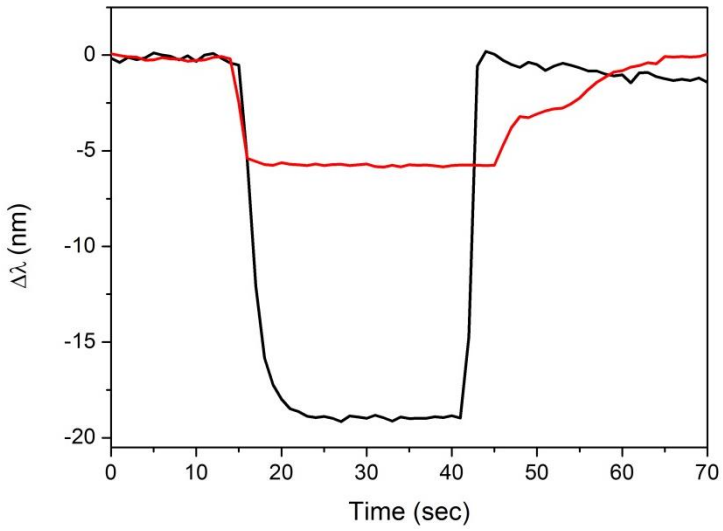

Fig.2.3.14–Comparison between the time resolved test for the Au NRs + (TiO_2-8%Pt NPs) sample performed exposing the sample to a N_2-H_2 cycle (red line) or air-H_2 cycle (black line).

2.3.2.3.5 Gas sensing test on the Au NRs + TiO_2 + Pt NPs sample

To prove that there is not a direct contact but a tunneling phenomenon from Pt NPs to Au NRs through a double injection mechanism, into the conduction band of TiO_2 and then from it into the NRs, a sample has been made with Au NRs, a layer of TiO_2 matrix and a Pt NPs layer on the top of the TiO_2 matrix, in which a charge transfer, through contact, from Pt towards Au NRs is not possible because there are 40 nm of TiO_2 in between. From Figure 2.3.15-17 it is possible to note that in air flux the shift is of ~14 nm, instead in N_2 it is only of 3 nm. This means that the improvement, in oxygen presence, in the sample Au NRs + (TiO_2-8%Pt NPs) in air flux, is due mostly to an increase in the contribution of the TiO_2 matrix, where probably the oxygen present in air can be absorbed.

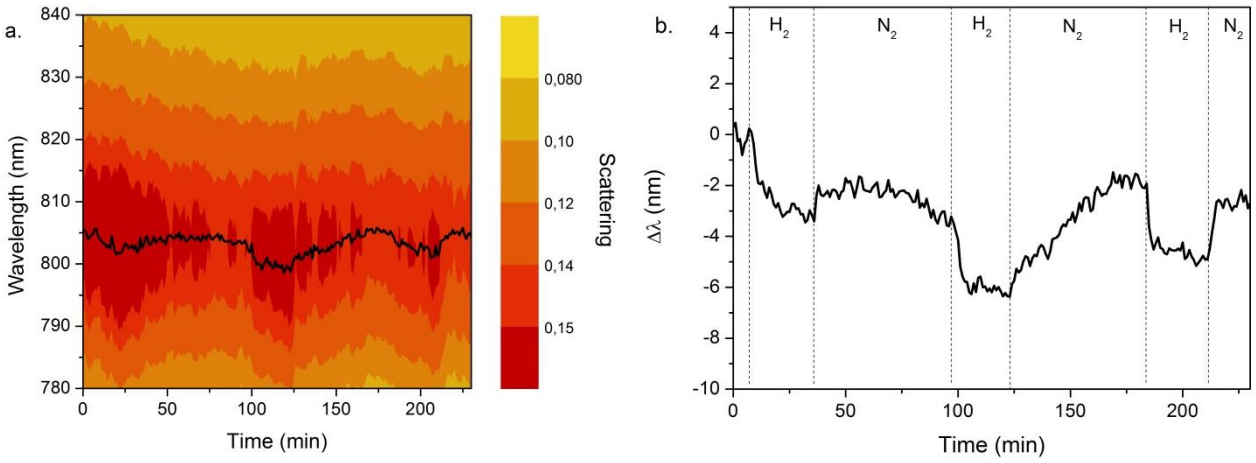

Fig. 2.3.15- Time resolved test with color-coded spectral scattering intensity (a.) and shift (b.) for Au NRs covered with TiO_2 matrix with a Pt NPs monolayer on the top of TiO_2 performed exposing the sample to multiple N_2-H_2 cycles.

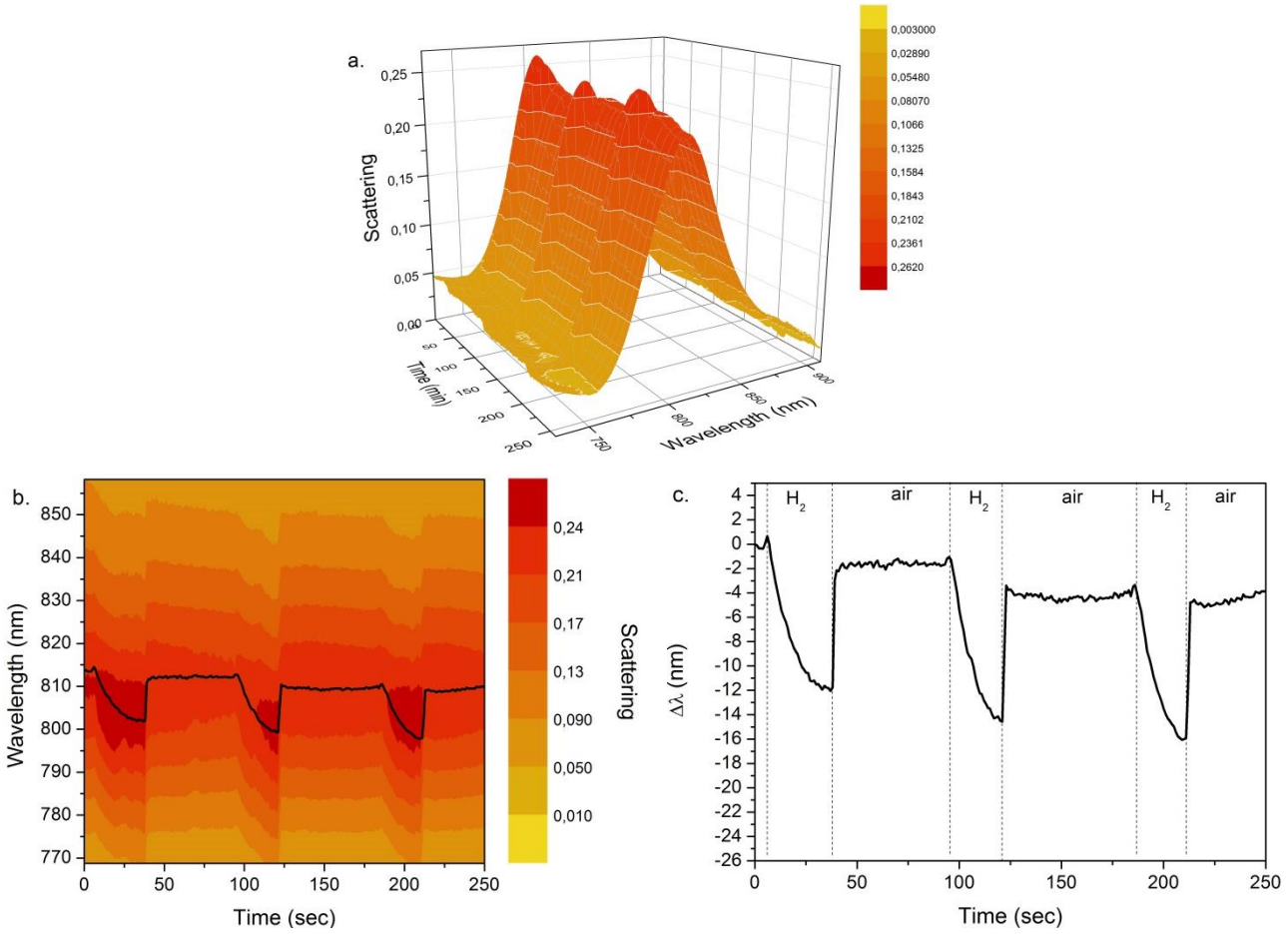

Fig. 2.3.16- Time resolved test with color-coded spectral scattering intensity 3-dimensional a. and bi-dimensional b. and with the shift c. for single Au NRs covered with TiO_2 matrix with a Pt NPs monolayer on the top of TiO_2 performed exposing the sample to multiple air-H_2 cycles.

In Figure 2.3.17 a. comparison between the time resolved tests for Au NRs + TiO_2 (blue line), Au NRs + (TiO_2-8%Pt NPs) (black line) and Au NRs + TiO_2 + Pt NPs (red line) samples is reported. Comparing the response of the samples Au NRs + TiO_2 (blue line) and Au NRs + (TiO_2-8%Pt NPs) (black line) it is possible to say that in presence of Pt NPs the shift is 2 times higher thanks to its catalytic behavior.

It is possible to note that the dynamics are faster and the shift is higher in presence of Pt embedded in the matrix (black line), moreover, with Pt NPs on the top (red line), the shift is higher than the sample without Pt (blue line) and the recovery is faster than the response. In the case of N_2 as carrier, as already reported, the shift as smaller and without Pt NPs there is no sensitivity.

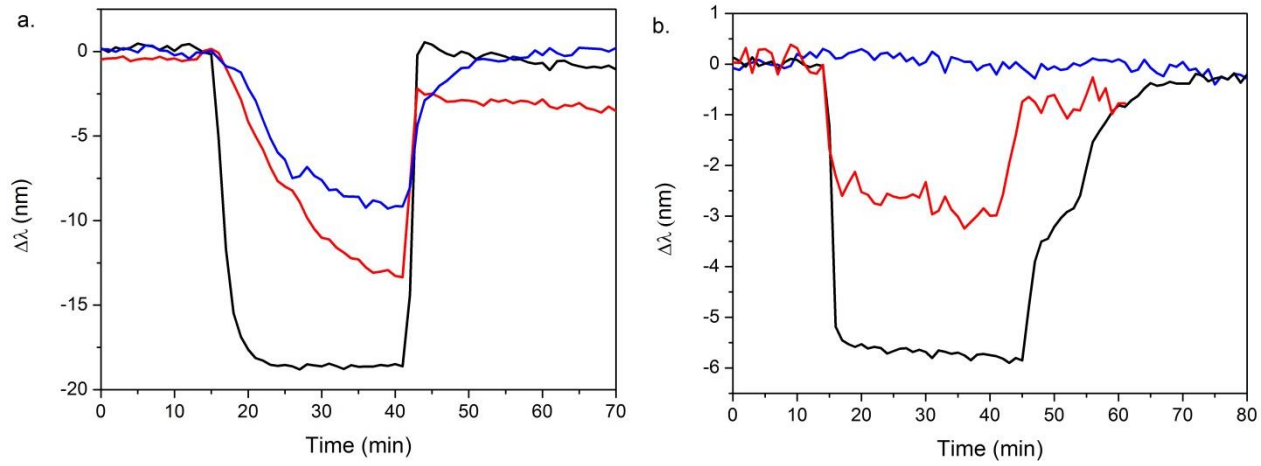

Fig. 2.3.17- Comparison between the time resolved test for Au NRs + TiO_2 (blue line), Au NRs + (TiO_2-8%Pt NPs) (black line) and Au NRs + TiO_2 + Pt NPs (red line) samples performed exposing them to an air-H_2 (a.) and N_2-H_2 (b.) cycle.

2.3.2.3.6 Gas sensing test on the Au NRs + (SiO_2 8% Pt NPs) sample

In order to confirm the effectiveness of the TiO_2 matrix for the electron injection through the semiconducting matrix, a control test has been performed with an insulating matrix of SiO_2 in presence of Pt NPs, to show that such matrix does not allow the electrons coming from the H_2 spillover to tunnel from Pt NPs to the Au NRs. For such sample no Au SPR peak shift has been detected during H_2 exposure (Fig. 2.3.18).

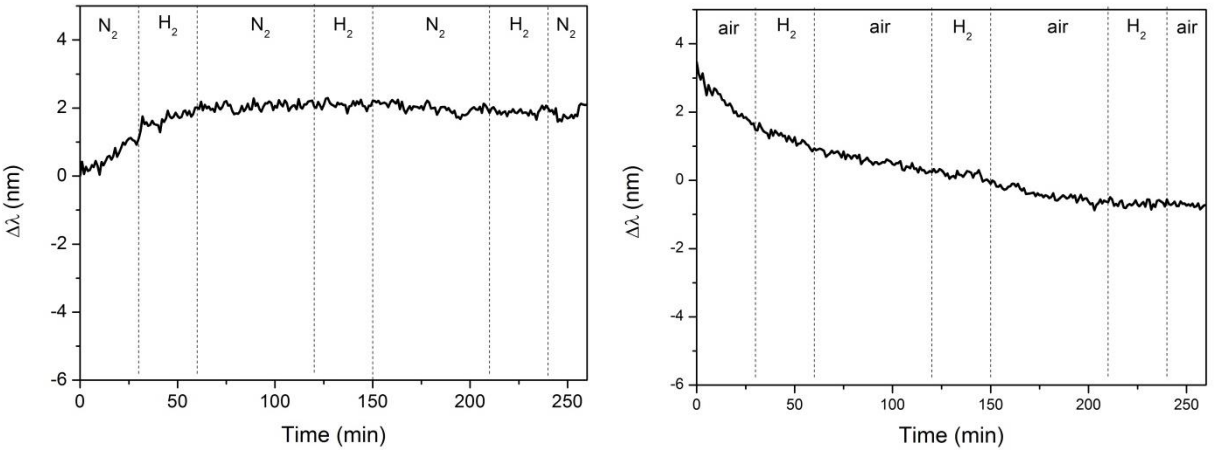

Fig. 2.3.18- Time resolved test with the shifts for a single Au NR covered with SiO_2 matrix with embedded Pt NPs performed exposing the sample to multiple N_2-H_2 (left) and air-H_2 (right) cycles.

From the data reported till now it possible to say that there is a charge-transfer from the Pt NPs surface into Au NRs, when the NRs are covered by a TiO_2 matrix, which is an high-k dielectric, and this give arise to a particular mechanism in the H_2 gas sensing. In a nanocomposite Au/TiO_2+Pt film, charge carriers (electrons) generated by the H_2 spillover are captured mainly in the Au nanoparticles covered by the dielectric matrix. Some of them can be captured by traps in the dielectric and at Au NRs/TiO_2 interfaces, but the concentrations of localized energy states (traps) and delocalized energy states (states in the NPs) do not restrict the charge carrier capture [9].

Moreover, it is known [10] that there is always a charge-carrier injection/extraction at the metal-dielectric contact, this can give a further explanation to the overall effect here presented, as already said, in fact, into the semiconducting matrix, all the NRs give the same trend in the response; moreover this is not true in absence of a matrix.

So, in H_2 flux, in presence of a matrix, there is an electron injection, from the Pt surface where takes place the spillover reaction or, in absence of Pt, from the O^{2-} sites on TiO_2 surface into the Au NRs, through tunneling in the matrix which redistributes the electrons from its conduction band [11] between all the NRs [12]. This is estimated to be the main current transport mechanism.

This electrons injection, as already said and widely reported, cause a plasmon blue-shift [13], on the other hand, from Figure 2.3.6b, 2.3.11a, 2.3.12a 2.3.13a and 2.3.16a it is clear that there is also a strong plasmon absorbance increase, stronger than the shift and even stronger in presence of a semiconducting matrix.

In order to understand this increase we tried to derive the relationship between the absorbance of a nanocomposite made of Au NPs dispersed in a matrix (in the case of high dilution) and the electron density of the Au NPs.

Than from equation 4 it is possible to conclude that the absorbance at the LSPR position (ω_{LSPR}) is proportional to the electronic density:

$$A(\omega_{SPR}) = \frac{3zf\varepsilon_{SPR}}{2cL\gamma m_e \epsilon_0} \frac{e^2 N_e}{[\varepsilon_\infty + (\frac{1}{L-1})\varepsilon_m]^2} \quad (4)$$

where f is the volume fraction of NPs, L is the depolatization factor, ε_m is the dielectric constant of the matrix, ε_{SPR} is dielectric constant of medium at the SPR, N_e is the number of electrons oscillating (the other terms of the equation 4 were obtained from the calculations reported in Appendix A.4 and performed by Pecharromán). This explains why there is a strong absorbance increase of the plasmon band in H_2 flux.

Another effect that can influence the position and height of the LSPR peak of Au NPs embedded in a matrix is the variation of the dielectric function of the matrix. So, there could be also an effect related to a change in the polarizability of the TiO_2 matrix due to the H_2 reactions, which involves an increase in its dielectric constant.

The increase in the dielectric constant depends on the number of electrons in the conduction band of TiO_2 and implies an increase in the absorbance all over the spectrum, this has been verified exposing a TiO_2-Pt sample, without Au, to a flux of N_2 to obtain the desorption of the O^{2-} ions absorbed on the TiO_2 matrix. Then on the sample without O^{2-} ions absorbed, a gas sensing test has been made, with H_2 5%. From Figure 2.3.19 it is possible to note that there is a blue shift, which involves an electron injection at the band gap, for the Burstein-Moss effect [14]; instead at the tail

there is a strong increase in absorbance, linked to the increase of *k* because of the electrons injection. The same test has been performed in flux of air, as in the single particles measurement, the increase in absorbance is more evident in presence of O^{2-} ions adsorbed on the matrix surface (Fig. 2.3.19 inset b). Regarding the increase of the real part of the refractive index, *n*, in presence of N_2 and H_2 cycles, no significant changes have been found in the visible range.

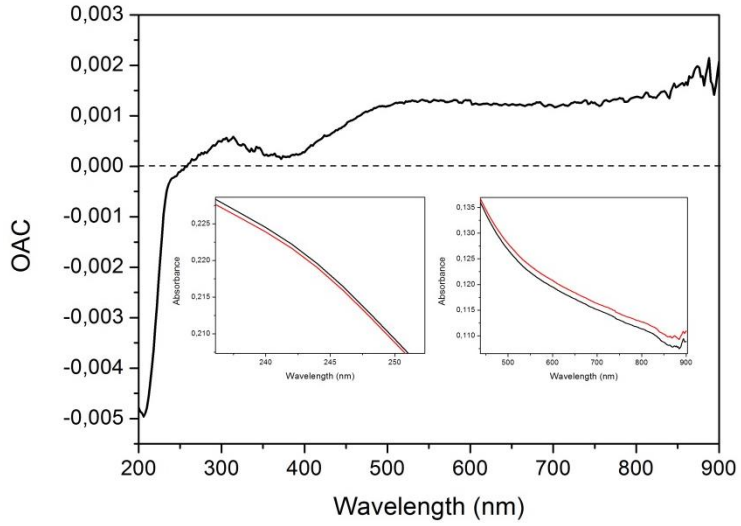

Fig. 2.3.19- Optical absorption change (OAC) curve for a TiO_2-Pt sample exposed N_2 and 50000ppm H_2. In the insets are presented a magnification of the absorption spectra at the band gap in N_2 (inset a) and at the tail in air (inset b) and 50000ppm H_2 flux.

To better visualize and compare the increase in absorbance, due to the increase of *k* of the TiO_2 matrix, a time resolved test has been performed (Fig. 2.3.20), at a fixed wavelength, and the results reported for the single particle gas sensing measurement are confirmed, without the catalysis of the Pt and without oxygen adsorbed there is no electron injection and consequently no increase in the matrix *k* value.

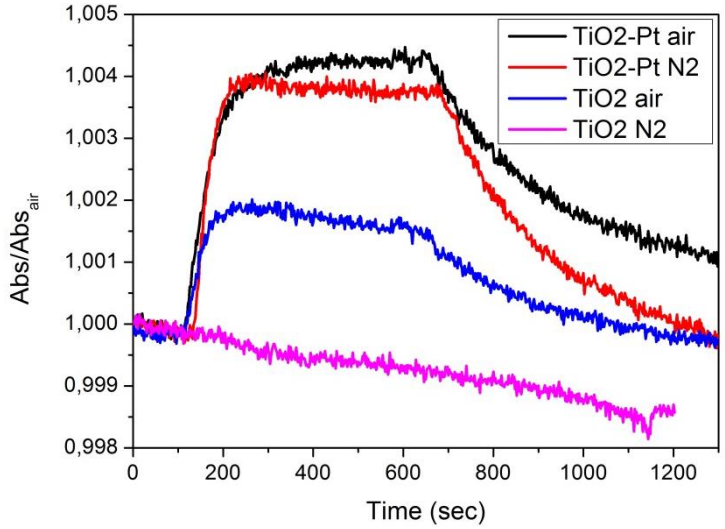

Fig. 2.3.20- Comparison between the time resolved test with the optical absorption technique for TiO_2 in N_2 (pink line) and in air (blue line) and for TiO_2 + Pt NPs in N_2 (red line) am d in air (black line) samples performed exposing them to H_2 50000ppm.

2.3.3 Conclusions

In this chapter we have studied the influence that a semiconductive matrix and the oxygen ions adsorbed on it have on the electrons exchanges involved in a red-ox reaction. Moreover, as highlighted from the results, it is possible to affirm that Au NRs do not have any active role in the H_2 gas reaction mechanism, they are just an optical probe, in fact the test on bare Au NRs did not give any response, instead the test with bare Au NRs coupled with Pt NPs gave a shift of the Au LSPR band of 2 nm, due to the catalytic role of Pt NPs.

Moreover, it is possible to say that the semiconducting matrix, together with the Pt NPs presence, has a really important role in increasing the efficiency of the electrons injection, also with an overall effect on all the Au NRs observed, due to the redistribution of the electrons injected between all the NRs. Another important factor is the oxygen ions presence absorbed on the metal oxide matrix, which has a fundamental role in the sensing mechanism, even in Pt absence, but together with Pt there is a huge improvement, a shift of 20 nm, 3 times higher than without oxygen.

The mechanism proposed in the present work is the electron tunneling through the matrix from Pt surface, where the H_2 molecules are splitted, into the Au NRs.

References

[1] http://www.essentialchemicalindustry.org/processes/catalysis-in-industry.html

[2] C. Novo, A. M. Fuston, P. Mulvaney, Direct observation of chemical reactions on single gold nanocrystals using surface plasmon spectroscopy, Nat. nanotechnol. 2008, Volume 3, 598-602.

[3] C Sönnichsen, T Franzl, T Wilk, G von Plessen, J Feldmann, Plasmon resonances in large noble-metal Clusters, New J. Phys. 2002, Volume 4, 93.1–93.8.

[4] Moonjung Eo, Jayeon Baek, Hyeon Don Song, Suseung Lee, Jongheop Yi, Quantification of electron transfer rates of different facets on single gold nanoparticles during catalytic reactions, Chem. Commun. 2013, Volume 49, 5204-5206.

[5] Na Liu, Ming L. Tang, Mario Hentschel, Harald Giessen, A. Paul Alivisatos, Nanoantenna-enhanced gas sensing in a single tailored nano focus, Nat. Mater. 2011, Volume 10, 631-636.

[6] Tittl A, Yin X, Giessen H, Tian XD, Tian ZQ, Kremers C, Chigrin DN, Liu N., Plasmonic smart dust for probing local chemical reactions, Nano Lett. 2013, Volume 13, Issue 4, 1816-1821.

[7] E. Della Gaspera, M. Bersani, G. Mattei, T. L. Nguyen, P. Mulvaney, A. Martucci, Cooperative effect of Au and Pt inside TiO_2 matrix for optical hydrogen detection at room temperature using surface plasmon spectroscopy, Nanoscale 2012, Volume 4, 5972-5979

[8] A. Antonello, G. Brusatin, M. Guglielmi, V. Bello, G. Mattei, G. Zacco, A. Martucci, Nanocomposites of titania and hybrid matrix with high refractive index, J. Nanopart. Res. 2010, Volume 13, 1697-1708.

[9] O. Bratus', A. Evtukh, E. Kaganovich, A. Kizjak, I. Kizjak, E. Manoilov, Charge storage characteristics of gold nanoparticlesembedded in alumina matrix, Semiconductor Physics, Quantum Electronics & Optoelectronics, 2009. V. 12, N 1. P. 53-56.

[10] Eugen R Neagu, Change-carrier injection and extraction at metal-dielectric contact under an applied electric field, Indian Journal of Pure&Applied Physics, Vol. 46 November 2008, 809-814

[11] Prof. Saraswat, School of Engineering, Stanford University, http://www.stanford.edu/class/ee311/NOTES/GateDielectric.pdf

[12] Vaidyanathan Subramanian, Eduardo E. Wolf, and Prashant V. Kamat, Catalysis with TiO_2/Gold Nanocomposites. Effect of Metal Particle Size on the Fermi Level Equilibration, J. Am. Chem. Soc. 2004, 126, 4943-4950

[13] Paul Mulvaney, Jorge Pérez-Juste, Michael Giersig, Luis M. Liz-Marzàn, Carlos Pecharromàn, Drastic Surface Plasmon Mode Shifts in Gold Nanorods due to electron charging, Plasmonics 2006, Volume 1, 61–66

[14] V. K. Miloslavskii, P. S. Pogrebniak, The Burstein-Moss Effect in Polycrystalline ZnO Films, physica status solid (b) 1972, Volume 51, Issue 2, K99–K102

2.4 Gallium doped Zinc Oxide infrared plasmon based-sensing at low temperature

Zinc oxide (ZnO) is a promising material for gas sensing applications because of its chemical sensitivity to gases, its high chemical stability, suitability to doping, non-toxicity, abundance in nature and low cost. Many researchers have already studied ZnO thin films for the optical detection of toxic gases [1], organic vapours [2] [3], which is a subject of growing importance in both domestic and industrial environments. Doping ZnO with trivalent cations like Al^{3+} or Ga^{3+} greatly enhance the conductivity without altering the transparency in the visible of ZnO. Al- or Ga- doped ZnO (GZO and AZO) are among the most used transparent conductive oxides (TCOs), together with tin-doped indium oxide (ITO). ITO has already been tested for H_2 [4], and also for the volatile organic compound (VOC) electrical sensing by N.G. Patel et al. [5].Even GZO and AZO have been used for electrical sensing of VOC by P.P. Sahay et al. [6], of liquid petroleum gas by P.P. Sahay [7], of NO_2 and H_2S by N. Vorobyeva [8].

Here we use GZO and AZO as optical gas sensor at low temperatures (80°C) exploiting their plasmoinc behavior [9][10]. Gold and silver present the SPR peak in the visible region, instead the TOCs have a SPR peak in the NIR region, due to the fact that the electron density that can be introduced in semiconductors by doping is lower than typical metals [11].The advantage of TCO towards metals, is that their plasmon resonance frequencies can be adjusted on the basis of the chemical doping level [12].

In this chapter we monitor the GZO/AZO plasmon band shift in reducing and oxidizing gas, related to exchange of electrons between the gas and the TCO thin film.

2.4.1 Experimental

2.4.1.1 Nanoparticles synthesis

The GZO/AZO NPs and the Pt NPs synthesis procedure are reported in the appendixes A.2.6, A.2.10, respectively.

2.4.1.2 Samples deposition

The GZO/AZO colloids, dispersed in toluene, were deposited on glass and silicon substrates by spin coating at 3000rpm for 30sec. Then the thin films have been thermally treated to stabilize them, but it is known that thermal treatment of TCOs in air causes a decrease in the IR absorption, because of a recombination of the oxygen vacancies [13] [14], moreover it makes the sample reducing its

transparency because of the carbon residues, so the samples have been UV treated for 45min to decompose the organic compounds and then treated at 450°C in reducing atmosphere (95%Ar-5%H_2) [15]. This treatments have the effect of increasing the free charge density from 28,7 cm^2/Vs to 24,0 cm^2/Vs, because of the increase defect density, as already reported in our previous work [15]. In order to promote the gas (H_2 and NO_2) reaction at low temperature, Pt NPs have been spin coated (0,1 M Pt solution at 3000rpm for 30sec) on top of the GZO and AZO films. . Finally the samples have been treated on hot plate at 100°C for 15min to stabilize them for the gas sensing tests. The samples prepared are summarized in Table 2.4.1.

Samples without Pt	**Samples with Pt**
GZO 5%	GZO 5%/Pt
GZO 3%	GZO 3%/Pt
GZO 1%	GZO 1%/Pt
AZO 5%	AZO 5%/Pt
AZO 3%	AZO 3%/Pt
AZO 1%	AZO 1%/Pt

Tab. 2.4.1- GZO and AZO samples with different level of Al or Ga doping deposited on fused silica and coupled with Pt NPs.

2.4.1.3 Gas sensing measurements

Optical gas sensing tests were at room temperature and at 80 °C and the sensor was tested for both reducing and oxidant gases, H_2 and NO_2, respectively, all balanced with synthetic air. In particular, the concentrations of H_2 was set at 10000 ppm; the concentration of NO_2 was set at 1000 ppm, using the GZO/AZO plasmonic peak in the NIR region it is possible to use that high concentration because the effects related to the NO_2 optical absorption in the visible range are out of the plasmon band range.

2.4.2 Results and discussion

2.4.2.1 Structural and optical properties

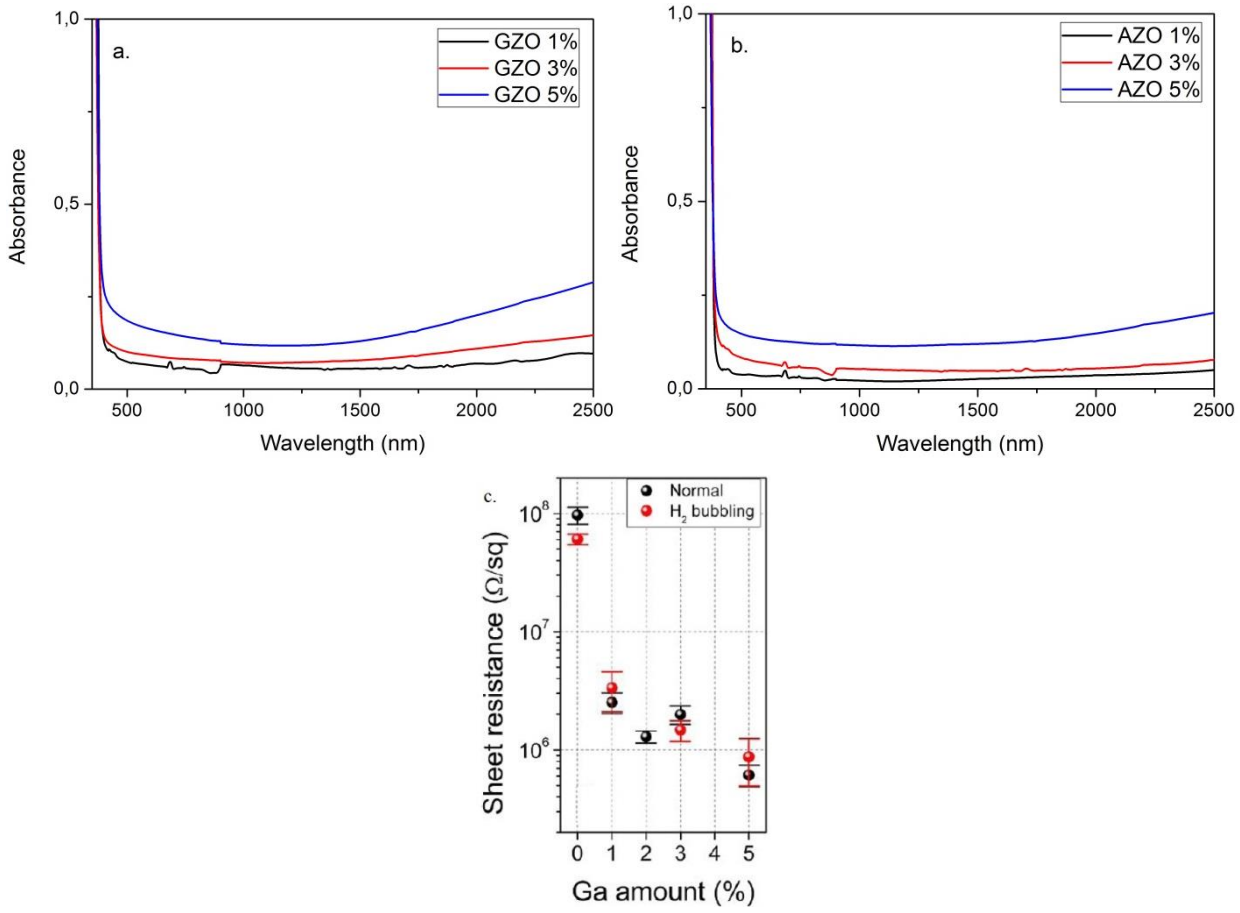

Fig. 2.4.1- UV-Vis absorption spectra of GZO 1-5% (a.) and AZO 1-5% (b.) deposited on fused silica; sheet resistance of ZnO films according to Ga amount (c.).

From the absorption spectra reported in Figure 2.4.1 it is possible to note an increase in the NIR region of the thin film absorbance, this is due to the SPR triggered by the substitution of Zn^{2+} ions in the ZnO lattice with elements of the XIII group, as Al^{3+} or Ga^{3+}, which increase the number of free electrons in the structure. A clear decrease in sheet resistance of ~2 orders of magnitude has been observed in the doped films with respect to the undoped case (Fig. 2.4.1 c), as a consequence of the increased density of free carriers generated by Ga^{3+} doping. The decrease is very pronounced for low Ga concentrations, while for higher doping levels, the incremental resistance change is not as large.

SPR behavior is explained by the Drude free electron model, which describes the transport properties of electrons in any conducting material by portraying the conduction electrons as a non-interacting classical gas surrounding immobile positive ions. In response to electromagnetic waves, the conduction electrons oscillate and create an electric field on the surface that has a limited

penetration depth (skin depth). The collective response of the conduction electrons to the alternating electric field can be compared to a forced harmonic oscillator. The restoring force is the Coulombic attraction of the electrons with the nuclei in the lattice. The resonant frequency of the forced harmonic oscillator is also known as the plasma frequency [16]. Comparing the absorption spectra of GZO and AZO both doped 5% it is possible to note (Fig. 2.4.2) that GZO has a higher SPR onset in the NIR. As anticipated before, the absorption in the NIR is the onset of the plasmon resonance arising from the free carriers provided by Ga doping: Fourier transform IR (FTIR) spectra of a GZO3 sample deposited on silicon substrate (Figure 2.4.2 on the right) show the broad surface plasmon resonance peak centered around 6 μm, and interestingly, the peak is shifted at shorter wavelengths after the annealing in reducing atmosphere, suggesting an increase in the amount of free carriers. In fact, as described by Mie theory [17], the surface plasmon resonance frequency is proportional to the square root of the free electron concentration, and an increase in the electron amount causes an increase in the surface plasmon resonance frequency, consistent with the observed blue shift.

In Figure 2.4.3 the SEM images are reported and uniform coatings can be observed.

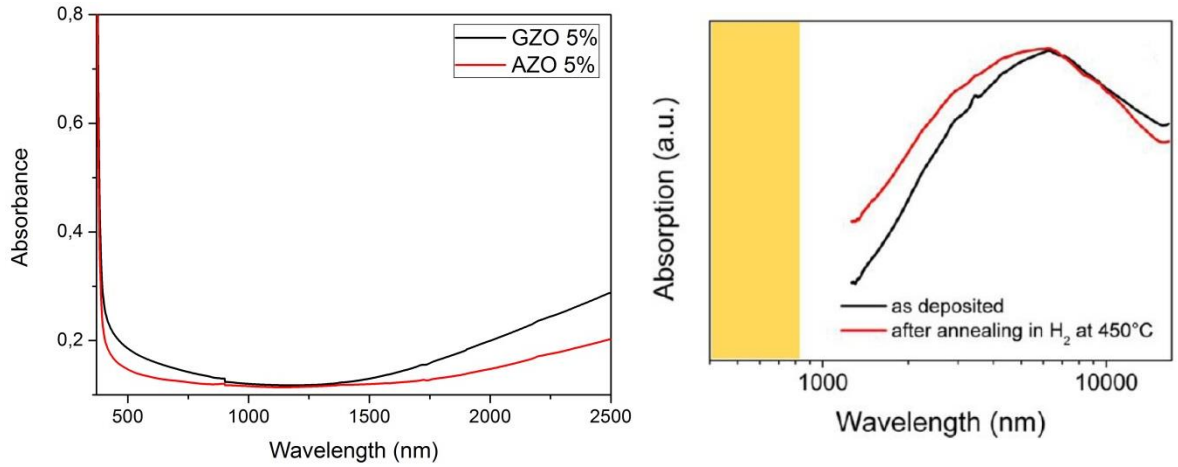

Fig. 2.4.2- Comparison between the UV-Vis absorption spectra of GZO 5% and AZO 5% (left) and FTIR spectra (right) of a GZO3 film as deposited (black line) and after the annealing in 95% Ar/ 5% H_2 atmosphere at 450°C (red line); the orange box highlights the visible range.

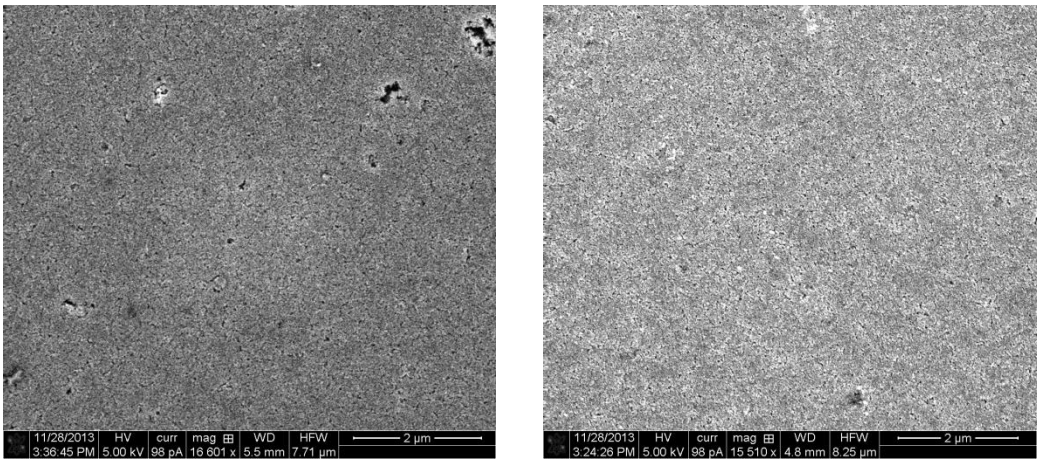

Fig. 2.4.3- SEM images of GZO 5% and AZO 5%.

Moreover, to optimize the gas sensing performances of the samples, a monolayer of 0,1M Pt NPs has been deposited via spin coating on the top of the TCO thin films, in Figure 2.4.4 is reported the change in the absorption spectra for GZO 5%. The deposition of the Pt NPs slightly affect the absorption spectra and the GZO films retain their absorption band in the NIR.

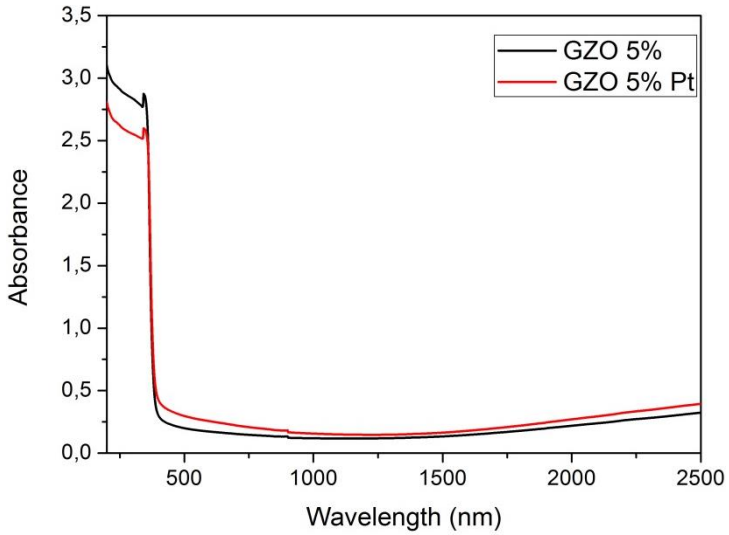

Fig. 2.4.4- Comparison between the UV-Vis absorption spectra of GZO 5% pre and post Pt NPs deposition.

Finally we performed XRD measurements on the samples with and without the Pt NPs monolayer, to verify the crystallinity of the components.

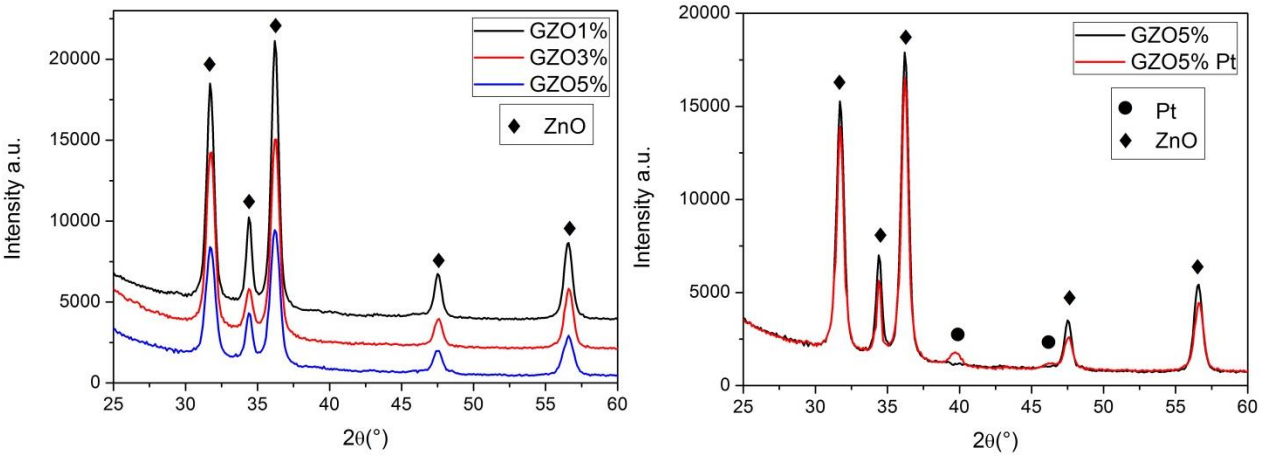

Fig. 2.4.5- Comparison between the XRD patterns of GZO 1-5% and of GZO 5% pre and post Pt NPs deposition.

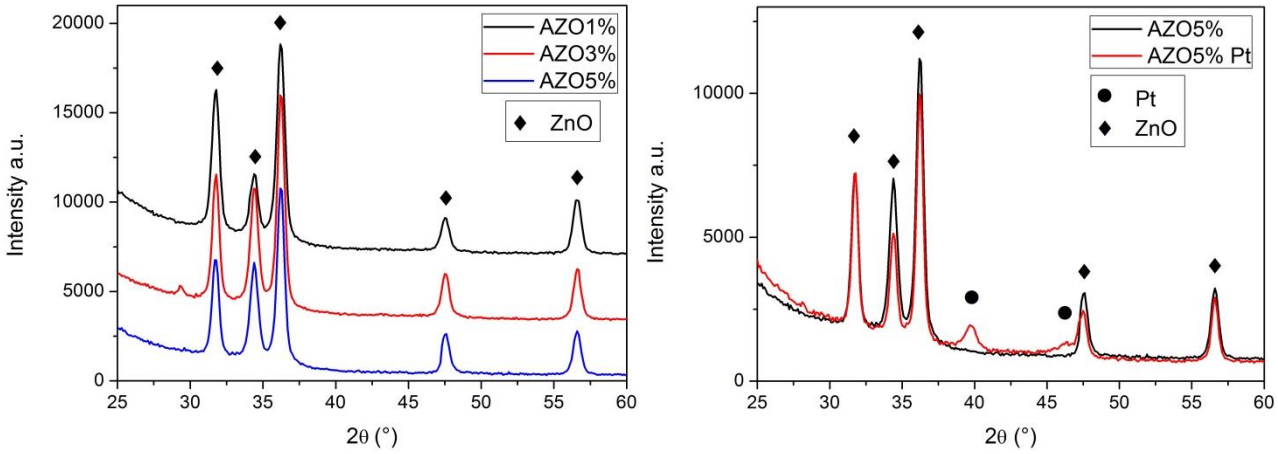

Fig. 2.4.6- Comparison between the XRD patterns of AZO 1-5% and of AZO 5% pre and post Pt NPs deposition.

XRD data show (Fig. 2.4.5-6) only ZnO-related peaks assigned to the hexagonal wurtzite structure (JCPDS no. 36-1451); at 31.77° for the (100) plane, at 34.42° (002) plane, at 36.25° (101) plane, at 47.54° (102) plane and at 56.60 (103) plane.

No significant variation in XRD peaks has been detected between the different samples, only a variation in their relative intensity and broadening. These effects are assigned to variations in the shape and size of the nanocrystals due to the presence of dopant ions in the growth solution and not to changes in the crystal structure.

Transmission electron microscopy (TEM) analyses showed the presence of rather spherical nanoparticles for pure ZnO as well as for low Ga concentration, but slightly elongated for higher Ga concentration, confirming the influence of the dopant salt in the NC shape (Fig. 2.4.7).

Moreover, about the Pt NPs, it is possible to note the peaks typical of cubic Pt (JCPDS No. 04-0802): (100) and (200) reflections at about 39.8° and 46.2°, confirming the crystallinity of Pt NPs.

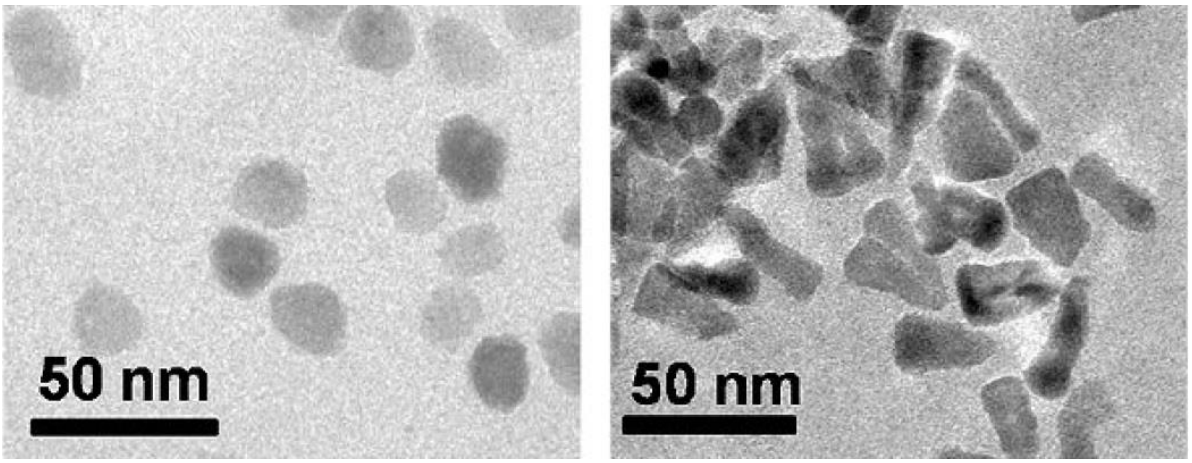

Fig. 2.4.7- TEM images of (left) pure ZnO and (right) GZO3 NCs.

About the refractive index of the films, measured with ellipsometric technique, for GZO is ~1.7 at 550 nm and ~1.6 at 550 nm for AZO, the variation of *n* related to the amount of doping of Ga^{3+} or Al^{3+} is neglectable.

Moreover, the experimental Ψ and Δ values in the visible and NIR range have been fitted assuming a simple Cauchy dispersion for the refractive index of pure ZnO, but the model diverged for GZO films. In order to improve the fitting results, a Drude oscillator was added in the NIR region in order to better fit the IR absorption, as shown in the inset of Figure 2.4.8, confirming again the metal-like behavior in the IR region due to the large number of free carriers. All the samples have a thickness around 100nm.

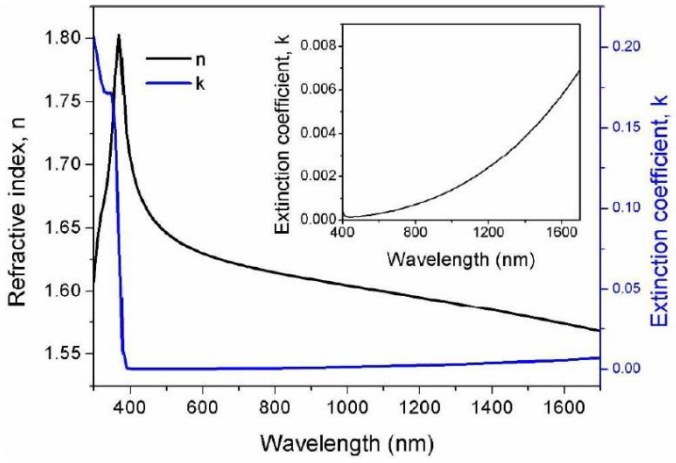

Fig. 2.4.8- Refractive index and extinction coefficient dispersion curves of a GZO3 film. The inset shows a smaller region of the extinction coefficient curve.

2.4.2.2 Gas sensing tests

The gas sensing tests have to be performed at an operating temperature of maximum 80°C, because it is like an annealing in air which would cause the LSPR feature to disappear, consistent with the trapping of free carriers by filling structural oxygen vacancies [[18]].

On the doped ZnO surface, oxygen ions are adsorbed, as described in reaction (1), the most stable oxygen ion at RT are O^- [19].

$$1/2O_2 + e_{(C.B.)}^- \rightarrow O^-(ads) \quad (1)$$

Regarding the reaction with the target gases , for H_2, the oxidizing reaction, already widely reported is:

$$H_2 + O^-(ads) \rightarrow H_2O + e^- \quad (2)$$

for NO_2 instead it is:

$$NO_2 + e^- \rightarrow NO_2^-(ads) \quad (3)$$

$$NO_2^-(ads) + 2O^-(ads) \rightarrow NO_2 + 2O^{2-}(ads) \quad (4)$$

These reactions can be catalyzed by Pt, which in the case of H_2, splits the molecule in H+ and e-, making easier the injection of electrons in the GZO/AZO structure, in this way the number of electrons oscillating in the semiconductor structure increases, causing a blue-shift of the SPR onset, as visible in figure 6, on the countrary, with NO_2, a subtraction of electrons is involved, so there is a red-shift of the SPR of GZO/AZO, also in this case visible in Figure 2.4.9.

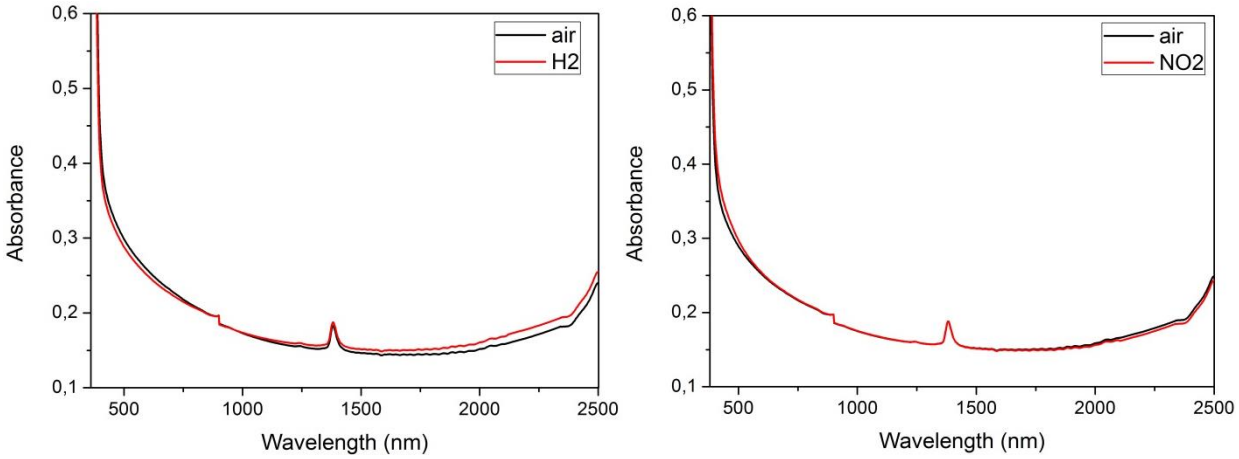

Fig. 2.4.9- Absorption spectra of the sample GZO 5% in air and target gas (H_2 and NO_2).

To better visualize the gas effect, the Optical Absorbance Change (OAC) parameter, defined as the difference between absorbance during gas exposure and absorbance in air ($OAC=Abs_{Gas}-Abs_{Air}$) is also reported in Figure 2.4.10. For all the prepared samples, CO did not induce any variation of the absorption. It is possible to note that, apart the variation in the NIR region due to the modification of the SPR peak, there is also a strong change in the visible at the band gap. Intersentigly the effect of the two gases is opposite, as H_2 is a reducing gas while NO_2 is oxidizing.

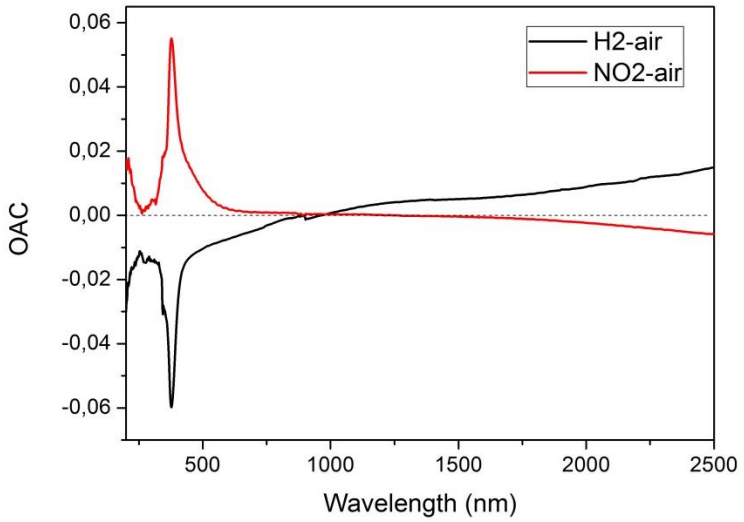

Fig. 2.4.10- OAC curves for the sample GZO 5% in H_2 and in NO_2.

In Figure 2.4.11 are reported the gas sensing tests for both the samples GZO and AZO doped at 5%, at RT and at 80°C, which are the only samples to be sensitive to the tested gases without the presence of Pt. It is possible to note that at 80°C the delta in absorbance is higher and the dynamics are faster.

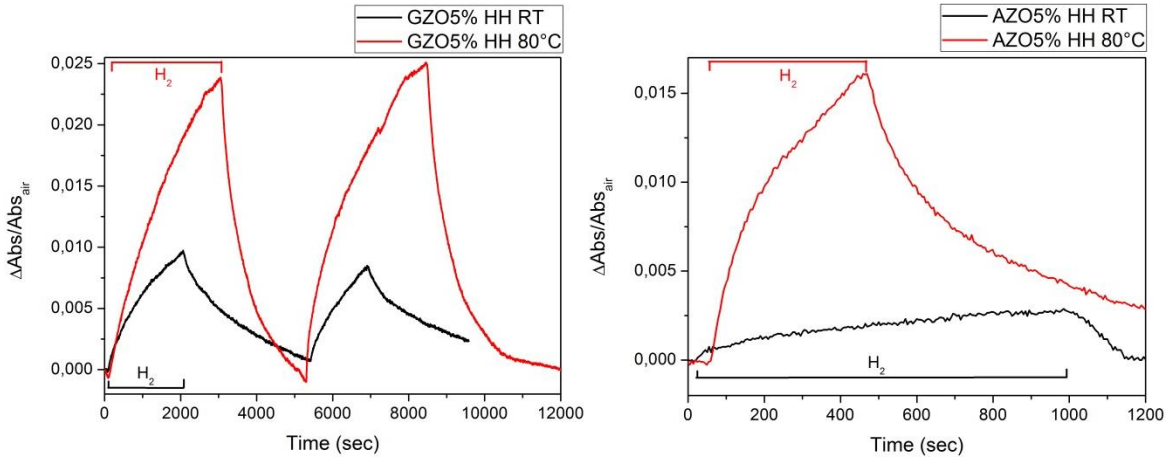

Fig. 2.4.11- Time resolved tests for GZO and AZO samples performed at 2400 nm after exposure to multiple air-H_2 cycles at RT and at 80°C.

Comparing the performances of AZO and GZO 5%, the best sensitivity is for GZO, probably because it has a higher number of oxygen vacancies and consequently higher number of free charges, which participate to the sensing, as reported in the conductivity measurement (Fig. 2.4.1 c). Thanks to the coupling with Pt NPs, with their catalytic behaviour towards the redox reactions of H_2 and NO_2 in particular, the GZO and AZO film increase their sensitivity and lower the response and recovery times (Fig. 2.4.12).

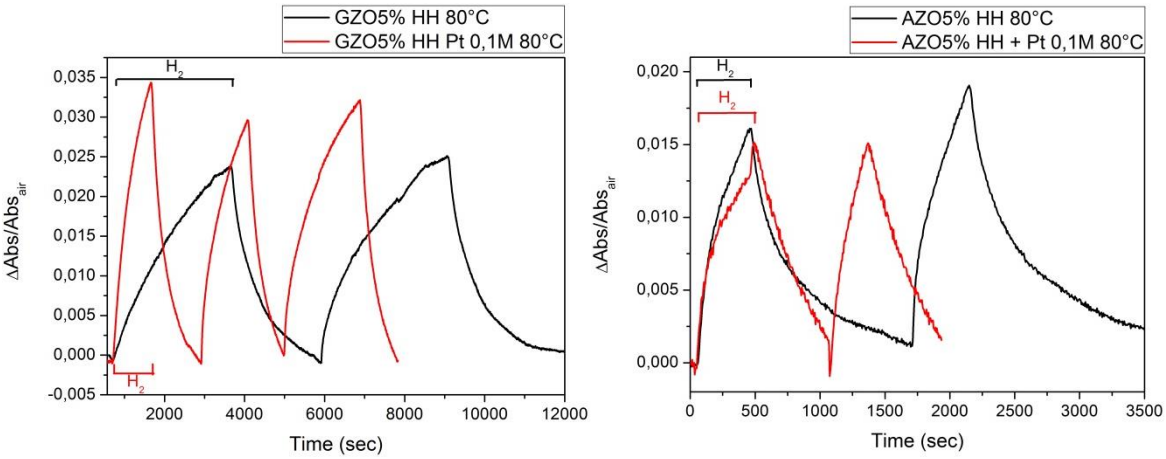

Fig. 2.4.12- Time resolved tests for GZO and AZO 5% at 80°C with and without Pt at 2400 nm.

Moreover, looking at the influence of the amount of doping (Fig. 2.4.13) on the sensing performances, it is possible to notice that gas sensing response increases as the Ga^{3+} or Al^{3+} content increases while the dynamics are always quite fast because of the presence of Pt NPs. The increase of gas sensing response can be related to the higher centration of free electrons with the increase of the Ga or Al doping.

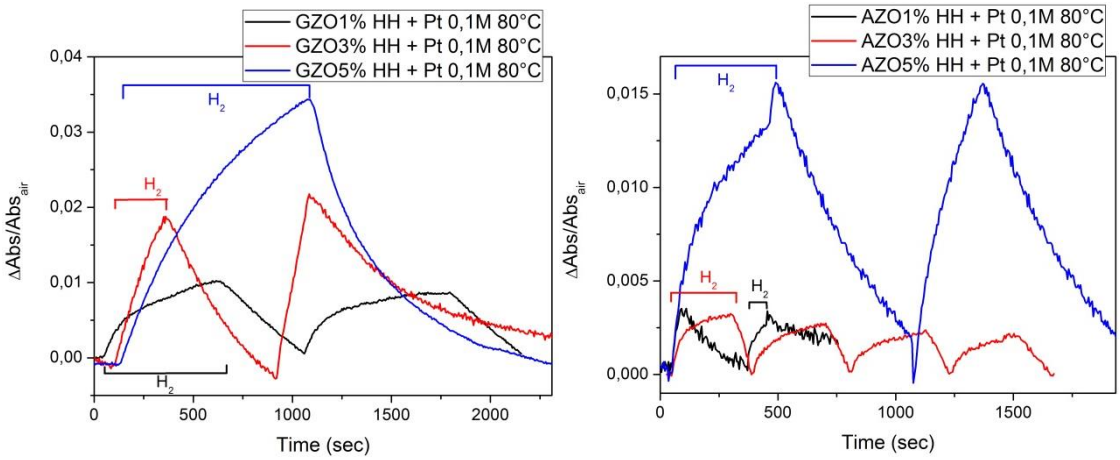

Fig. 2.4.13- Time resolved tests for GZO and AZO 1-5% at 80°C with Pt NPs at 2400 nm.

In Figure 2.4.14 are reported the sensing measurement of the GZO e AZO coupled with Pt NPs, performed at 80°C, towards H_2, CO 10000 ppm and NO_2 1000 ppm; the sensitivity towards H_2 is good, as already showed, for both the samples, instead towards CO only the GZO based film are sensitive. Regarding the sensitivity towards NO_2, the GZO based film is more performing, especially in terms of recovery time.

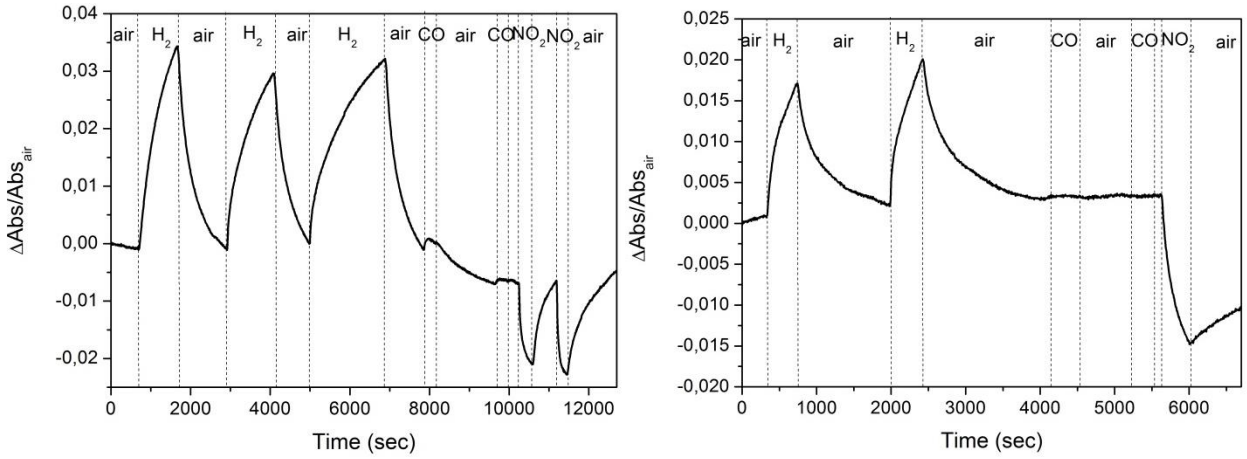

Fig. 2.4.14- Time resolved tests for GZO/AZO 5% Pt at 80°C at 2400 nm with H_2 and NO_2.

Going in deep in this gas sensing mechanism it is possible to say that, like already widely done by our group with Au NPs [1] [20] [21] [22] [23] [24] [25], we are exploiting in the same way the SPR peak of GZO and AZO.

The only difference between the sensing with Au and with plasmonic semiconductors is that we cannot monitor the maximum of the plasmon band but only its onset, because the maximum is out of the spectrophotometer working region, in the IR.

Some gas sensing tests have been performed at the GZO/AZO band-gap, at the corresponding wavelength there is, in the OAC curve (Fig. 2.4.10), a marked variation in absorbance, but, from the dynamic tests at 374 nm (Fig. 2.4.14) it is possible to notice that the performances are not as good as at the SPR onset wavelength, 2400nm.

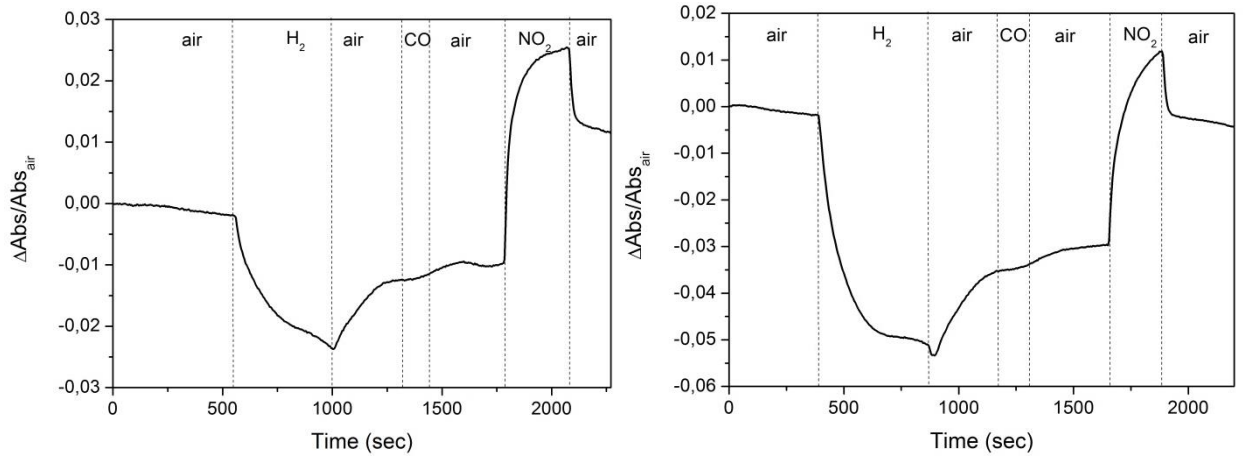

Fig. 2.4.15- Time resolved tests for GZO (left), AZO (right) 5% Pt at 80°C at 375 nm with H_2 and NO_2.

2.4.3 Conclusions

In this chapter we have investigated the optical gas sensing performances of plasmonic semiconductors: GZO/AZO coupled with Pt NPs towards H_2 at 10000 ppm and NO_2 at 1000 ppm.
The sensors show good responses towards H_2 and NO_2 with reversible response, while no detectable response is observed toward CO. In particular the GZO and AZO 5% doped are the only samples, if compared to the 3 and 1% doped, to be sensitive at RT even without Pt to H_2 in particular; moreover the GZO5%-Pt sample shows the best sensing performances thanks to the higher doping and the catalytic behaviour of Pt NPs.
The mechanism involved in the sensing with reducing (H_2) and oxidant (NO_2) gases using GZO/AZO is just a combination between the plasmonic behavior in the NIR of doped ZnO, and an exchange of electrons with the target gases through red-ox reactions mediated by the adsorbed oxygen and the Pt catalysis.

References

[1] E. Della Gaspera, M. Guglielmi, G. Perotto, S. Agnoli, G. Granozzi, M. Post, A. Martucci, CO optical sensing properties of nanocrystalline ZnO–Au films: Effect of doping with transition metal ions, Sens. Act. B 2012, Volume 161, 675-683.

[2] P.P. Sahay, S. Tewari, S. Jha, M. Shamsuddin, Sprayed ZnO thin films for ethanol sensors, J. Mater. Sci. 2005, Volume 40, 4791–4793.

[3] P.P. Sahay, Zinc oxide thin film gas sensor for detection of acetone, J. Mater. Sci. 2005, Volume 40, 4383–4385.

[4] Kwang Soo Yoo, Sang Hyoun Park, Ju Hyun Kang, Nano-grained thin-film indium tin oxide gas sensors for H_2 detection, Sens. Act. B 2005, Volume 108, 159–164.

[5] N.G. Patel, P.D. Patel, V.S. Vaishnav, Indium tin oxide (ITO) thin film gas sensor for detection of methanol at room temperature, Sens. Act. B 2003, Volume 96, 180–189.

[6] P.P. Sahay, R.K. Nath, Al-doped ZnO thin films as methanol sensors, Sens. Act B 2008, Volume 134, 654–659.

[7] P.P. Sahay, R.K. Nath, Al-doped zinc oxide thin films for liquid petroleum gas (LPG) sensors, Sens. Act B 2008, Volume 133, 222–227.

[8] Nataliya Vorobyeva, Marina Rumyantseva, Darya Filatova, Elizaveta Konstantinova, Diana Grishina, Artem Abakumov, Stuart Turner, Alexander Gaskov, Nanocrystalline ZnO(Ga): Paramagnetic centers, surface acidity and gas sensor properties, Sens. Act B 2013, Volume 182, 555– 564.

[9] M. A. Noginov, Lei Gu, J. Livenere, G. Zhu, A. K. Pradhan, R. Mundle, M. Bahoura, Yu. A. Barnakov, V. A. Podolskiy, Transparent conductive oxides: Plasmonic materials for telecom wavelengths, Appl. Phys. Lett. 2011, Volume 99, 021101.

[10] Masayuki Kanehara, Hayato Koike, Taizo Yoshinaga, Toshiharu Teranishi, Indium Tion Oxide Nanoparticles with Compositionally Tunable Surface Plasmon Resonance Frequencies in the Near-IR region, J. Am. Chem. Soc. 2009, Volume 131, 17736-17737.

[11] Debin Li, C.Z. Ning, All-semiconductor active plasmonic system in mid-infrared wavelengths, Opt. Express 2011, Volume 19, Issue 15, 14594.

[12] Guillermo Garcia, Raffaella Buonsanti, Evan L. Runnerstrom, Rueben J. Mendelsberg, Anna Llordes, Andre Anders, Thomas J. Richardson, Delia J. Milliron, Dynamically Modulating the Surface Plasmon Resonance of Doped Semiconductor Nanocrystals, Nano Lett. 2011, 11, 4415–4420.

[13] N. Yamada, I. Yasui, Y. Shigesato, H. Li, Y. Ujihira, K. Nomura, Doping mechanisms of Sn in In_2O_3 powder studied using 119Sn Mössbauer spectroscopy and X-ray diffraction, Jpn. J. Appl. Phys. 1999, Volume 38, 2856–2862.

[14] Q. B. Ma, Z. Z. Ye, H. P. He, L. P. Zhu, J. Y. Huang, Y. Z. Zhang, B. H. Zhao, Influence of annealing temperature on the properties of transparent conductive and near-infrared reflective ZnO:Ga films, Scr. Mater. 2008, Volume 58, 21-24.

[15] Enrico Della Gaspera, Marco Bersani, Michela Cittadini, Massimo Guglielmi, Diego Pagani, Rodrigo Noriega, Saahil Mehra, Alberto Salleo, Alessandro Martucci, Low-Temperature Processed Ga-Doped ZnO Coatings from Colloidal Inks, J. Am. Chem. Soc. 2013, Volume 135, 3439−3448.

[16] Crissy Rhodes, Stefan Franzen, Surface plasmon resonance in conducting metal oxides, J. Appl. Phys. 2006, Volume 100, 054905.

[17] P. Mulvaney, L. M. Liz-Marzan, M. Giersig, T. Ung, Silica encapsulation of quantum dots and metal clusters, J. Mater. Chem. 2000, Volume 10, 1259−1270.

[18] N. Yamada, I. Yasui, Y. Shigesato, H.L. Ujihira, K. Nomura, Donor compensation and carrier-transport mechanisms in tin-doped In_2O_3 films studied by means of conversion electron 119Sn Mössbauer spectroscopy and Hall effect measurements, Jpn. J. Appl. Phys. 2000, Volume 39, 4158–4163.

[19] E. Della Gaspera, M. Guglielmi, A. Martucci, L. Giancaterini, C. Cantalini, Enhanced optical and electrical gas sensing response of sol-gel based NiO-Au and ZnO-Au nanostructured thin films, Sens. Actuators B 2012, Volume 164, 54–63.

[20] E. Della Gaspera, M. Bersani, G. Mattei, T.L. Nguyen, P. Mulvaney, A. Martucci, Cooperative effect of Au and Pt inside TiO_2 matrix for hydrogen detection at room temperature using surface plasmon spectroscopy, Nanoscale 2012, Volume 4, 5972-5979.

[21] C. de Julin Fernndez, M.G. Manera, J. Spadavecchia, D. Buso, G. Pellegrini, G. Mattei, A. Martucci, R. Rella, L. Vasanelli, M. Guglielmi, P. Mazzoldi, Gold/Titania nanocomposites thin films for optical gas-sensing devices, Proceedings of the 2005 SPIE Conference, 5836, 703-710.

[22] D. Buso, M. Guglielmi, A. Martucci, G. Mattei, P. Mazzoldi, C. Sada, M. L. Post, Au and NiO nanocrystals doped into porous sol-gel SiO2 films and the effect on optical CO detection, Nanotechnology 2006, Volume 17, 2429-2433.

[23] D. Buso, J. Pacifico, A. Martucci, P. Mulvaney, Gold Nanocrystals Doped TiO_2 Semiconductor Thin Films. Optical Characterization, Adv. Funct. Mater. 2007, Volume 17, 347-354.

[24]G. Mattei, P. Mazzoldi, M. L. Post,D. Buso, M. Guglielmi, A. Martucci, Cookie like Au/NiO nanoparticles with optical gas sensing properties, Adv. Mater. 2007, Voume 19, 561-564.

[25] D. Buso, G. Busato, M. Guglielmi, A. Martucci, V. Bello, P. Mazzoldi, G. Mattei, M.L. Post, Selective optical detection of H_2 and CO with SiO_2 sol gel films containing NiO and Au nanoparticles, Nanotechnology 2007, Volume 18, Issue 47, 1-7.

2.5 Graphene oxide coupled with gold nanoparticles for gas sensing

In recent years, graphene has been attracting considerable attention due to its unique morphological and electronic properties [1 2]. Despite its interesting features some of the interest has diverted towards its partially oxidized form, graphene oxide (GO), that has emerged as an alternative to graphene for selected applications, thanks to its low cost, production scalability, ease of processing and good compatibility both with aqueous and organic solvents [1 3].

GO consists in atomically-thin graphene sheets that are covalently decorated with oxygen-containing functional groups, either on the basal plane or at the edges, so that it contains a mixture of sp^2- and sp^3-hybridized carbon atoms. In particular, tailoring of the size, shape and relative fraction of the sp^2-hybridized domains of GO by chemical or thermal reduction provides opportunities for tailoring its optoelectronic properties. For example, as-synthesized GO is insulating but just by varying the oxidation level, with a controlled de-oxidation, a partially reduced GO can act as a semiconductor [4].

It has been shown that GO can act as a photocatalyst for the production of H_2 from a 20 vol % solution of methanol in water [5]; other studies [6] have explained this behavior by ab-initio modeling, suggesting that GO is particularly effective thanks to its clean band gap and providing criteria for the determination of the ideal oxidation state for a given application. Furthermore, its highly 2-dimensional nature, which determines huge surface-to-volume ratio, and efficient UV absorption make it a very promising material for photocatalysis [7] and suggest potential applications wherever its peculiar optoelectronic properties can be exploited.

Here we used partially reduced GO coupled with Au NPs for optical gas sensing with the aim of combining the semiconducting and photocatalytic activity behavior of the partially reduced GO and the LSPR of gold NPs. The synergistic interplay between these materials resulted in an enhancement of the photocatalytic properties of GO [8], extending them to the visible range where the LSPR of Au NPs can be used as an optical probe. The LSPR is known to be extremely sensitive to the changes in the dielectric properties of the surrounding medium, a characteristic that has been widely exploited for the preparation of sensing devices [9 10]. Here we expect an even larger enhancement of this effect induced by the electronic coupling of Au NPs and GO and the interactions of GO with reducing and oxidizing gases. While the use of GO for gas sensing has been covered in multiple reports [11 12 13], with the GO-Au NPs system already employed as a resistive gas sensor [14], only very recently GO has been used in an optical fiber array for the detection of vapors [15] and here GO is used as sensing material in an optical sensor for the detection of reducing and oxidizing gases. Moreover Au NPs exhibit a well-established, wavelength-dependent optical

response, which can be exploited as a mean to improve the selectivity of the sensor using wavelength modulation.

2.5.1 Experimental

2.5.1.1 Nanoparticles synthesis

The Au NPs monolayers were synthesized and deposited as described in appendix A.2.12.

2.5.1.2 Preparation of Au monolayer

Au monolayers have been prepared on fused silica slides or silicon. The substrate was first functionalized with (3-aminopropyl) trimethoxysilane (APTMS) as described in [16]. To deposit the monolayer, we used Au NPs PVP capped using the procedure reported in [16]. The monolayers were formed by spin-coating at 3000 rpm for 30 sec the liquid suspensions of gold NPs directly onto the APTMS. In this study, we prepared Au monolayers with 2 different extents of surface coverage, hereafter indicated as low (L), and high (H). L and H samples have been obtained by spinning 15 and 30 mM Au NPs solution, respectively. The as-deposited monolayer samples were thermally treated at 150 °C for 30 min in air. Following this stabilizing treatment, the samples were used as substrates for the GO deposition.

2.5.1.2 Sample preparation and GO deposition

Commercial (Graphene Supermarket) GO solution with a concentration of 0.5 mg/mL has been spin coated on the Au monolayers in two successive depositions, the first at 3000 rpm and the second at 2000 rpm in order to increase the flakes density, and the resulting samples were annealed at 150°C for one hour in air. As the annealed GO samples resulted partially reduced (see results and discussion section) such samples have been labeled as rGO.

2.5.2 Results and discussion

2.5.2.1 Structural and optical properties

The UV-Vis spectra of the gold monolayer are reported in Figure 2.5.1. In accordance with previous publications, an increase of the surface coverage results in both an increase of intensity and a red shift of the Au NPs LSPR peak [17 18]. The increase in absorbance with higher surface coverage is simply related to the larger cross-section of the NPs interacting with the incoming beam, while the red shift of the plasmon absorption can be ascribed to the decrease in the interparticle distance: the

stronger coupling of the localized plasmon on neighboring Au NPs results in the red-shift of the plasmon resonance [[19]].

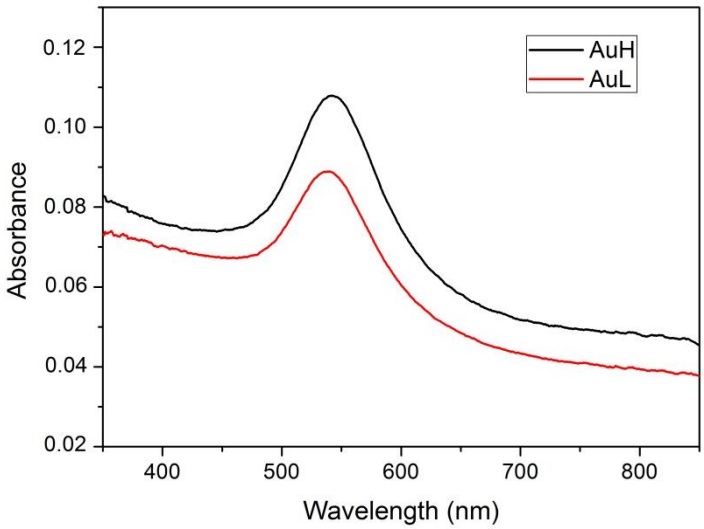

Fig. 2.5.1- UV-Vis absorption spectra of the AuH and AuL NPs monolayers deposited on fused silica.

SEM images of the metal NP monolayers are reported in Figure 2.5.2, from which it is possible to note that the Au NPs are homogeneously dispersed on a micron scale and lie almost entirely on a single monolayer. A mean particle diameter D = 14±1 nm has been estimated.

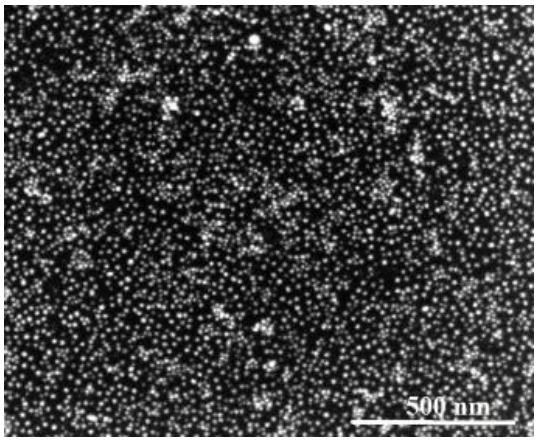

Fig. 2.5.2- SEM image of the AuH monolayer deposited on silicon.

SEM pictures of the rGO deposited by spin coating on a silicon substrate are reported in Figure 2.5.3. The typical flakes dimensions range from hundreds of nm to few μm. The substrate coverage is not complete, and some overlapping of the flakes is noticeable as well.

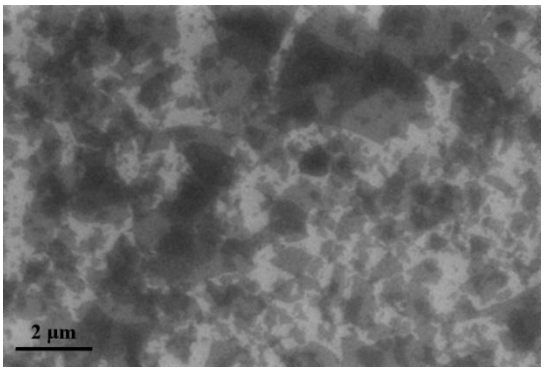

Fig. 2.5.3- SEM image of rGO deposited on silicon.

These observations are confirmed by the AFM images of the metal NP monolayers coated with rGO (Fig. 2.5.4); showing that there are regions in which the NPs are not coated with rGO flakes (marked with a circle in the figure). Yet most of the NPs are covered by rGO (square marked region in the picture) and in particular the area covered by rGO flakes can be recognized by the enhanced smoothness both in the height image (on the left) and in the phase image (on the right). The measured surface roughness is 3.2 nm on the rGO flakes and 4.5 nm on the bare Au NPs.

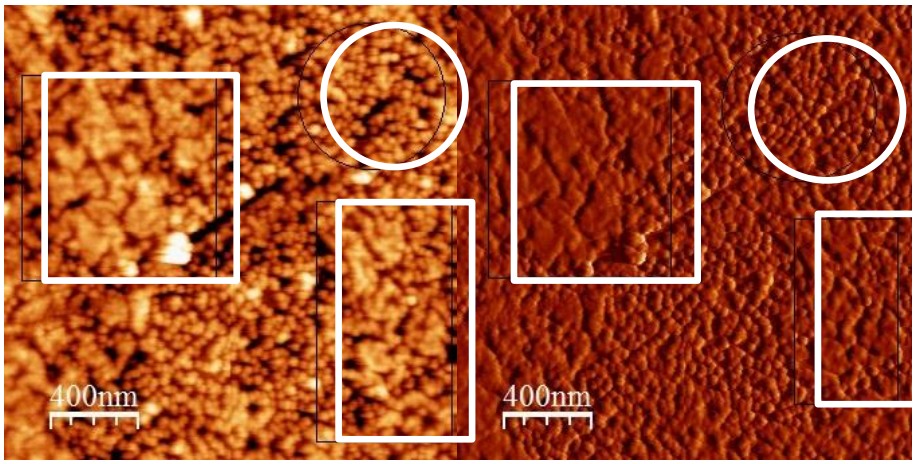

Fig. 2.5.4- AFM height (left) and phase (right) images of rGO deposited on AuH monolayer on silica glass substrate. Square marked area represents regions where the Au NPs are covered by rGO flakes. Circle marked area represents regions where the Au NPs are not covered by rGO flakes.

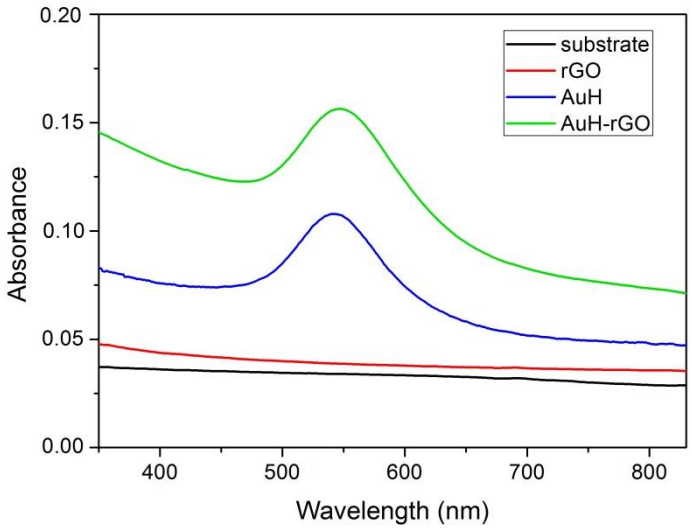

Fig. 2.5.5- UV-Vis absorption spectra of rGO, AuH and AuH-rGO samples. The absorption spectrum of the bare glass substrate is also reported for comparison.

The optical absorption spectra of the different samples are reported in Figure 2.5.5. It is possible to notice that the deposition of the rGO flakes on top of the Au NPs induces a small red shift of the LSPR peak, which can be attributed to the variation of the dielectric constant of the NPs environment and/or to the coupling of the localized surface plasmon of the gold NPs with the surface plasmon polariton of the GO [[20]].

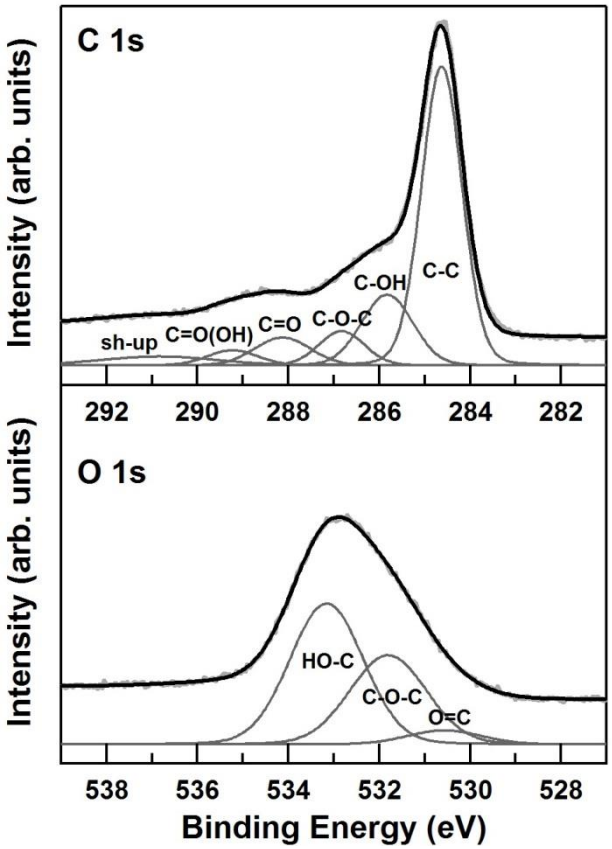

Fig. 2.5.6- C1s XPS spectra (top) and O1s XPS spectra (bottom) collected on single-layered GO thin film deposited on silicon and annealed in air at 150°C. The deconvolution of the experimental peaks showing the contribution of the different components is also shown.

XPS measurements are reported in Figure 2.5.6. The carbon/oxygen ratio was found to be 3.1, while the nominal ratio was 1.9. This means, according to literature, that the annealing in air at 150 °C leads to the partial reduction of GO [21 22].

The C 1s signal of our rGO consists of five different chemically shifted components which can be deconvoluted into: C=C/C-C in aromatic rings (284.6 eV); C-OH (285.8 eV); C-O-C (286.8 eV); C=O (288.1 eV); C=O(OH) (289.2 eV); and π-π* satellite peak (shake-up) (290.8 eV) (figure 6). These assignments are in agreement with previous works [23 24]. The C-O bonds come from epoxy and hydroxyl groups in the basal plane. Our observations indicate that the majority of oxygen species consist of C-O (in the form of C-OH and C-O-C, respectively 16.3 and 8.5 at %) while more oxidized species such as C=O and C=O(OH) are present in lesser amounts.

In Figure 2.5.6 it is also presented the O1s signal that appears at a binding energy in the range 529-535eV, and can be deconvoluted, like in C1s signal, into C=O (530.6 eV), C-O-C (531.8 eV) and C-OH (533.2 eV). As we already said, the majority of oxygen species consist of C-O (40.7 and 46.6 at %) while more oxidized species such as C=O are present in lesser amounts (7.8 at %).

2.5.2.2 Gas sensing tests

Figure 2.5.7 shows the absorption spectra of AuH-rGO when exposed to air and 100 ppm H_2 or 1 ppm NO_2 in air: to better visualize the gas effect, the Optical Absorbance Change (OAC) parameter, defined as the difference between absorbance during gas exposure and absorbance in air ($OAC=Abs_{Gas}-Abs_{Air}$) is also reported in the insets, together with the OAC for bare rGO. For all the prepared samples, CO gas did not induce any variation of the absorption.

It is possible to notice that H_2 (which is a reducing gas, Fig. 2.5.7a) induces a blue-shift of the Au LSPR peak, while the interaction with NO_2 (which is an oxidizing gas, Fig. 2.5.7b) induces a red-shift of the Au LSPR peak. The OAC spectra reported in the insets of Figure 2.5.7a and b show that the bare rGO samples are not sensitive to any gas, thus demonstrating that the presence of the Au NPs is necessary in order to have a detectable variation of the absorbance. On the other hand, bare Au monolayers showed very small variations (see the insets of Fig. 2.5.7), indicating that rGO enhances and amplifies the interaction of the gas with the Au NPs.

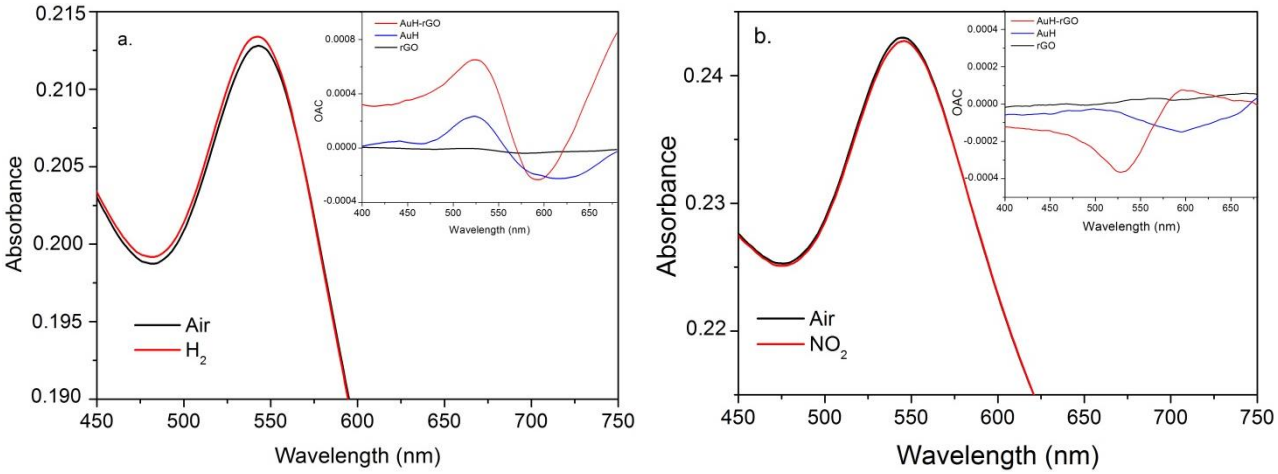

Fig. 2.5.7- Optical absorption spectra of AuH-rGO when exposed to air and 100 ppm H_2 in air (a) and when exposed to air and 1 ppm NO_2 in air (b). The insets show the OAC of GO, AuH and AuH-rGO.

Dynamic tests have been conducted in the 500-600 nm wavelength range, corresponding to the LSPR peak region. The dynamic gas sensing tests are reported in Figure 2.5.8 and 2.5.9, showing a variation of the absorbance ranging from 0.1% (for 100 ppm) up to 0.5% (for 10000 ppm) for H_2 and a variation of 0.1% for 1 ppm NO_2, while CO could not be detected.

As this is the first time the GO is used as sensitive material for optical gas sensor based on the variation of optical absorbance, it is not possible to make a comparison whit other published data on GO. On the other hand, optical gas sensor based on the variation of the Au LSPR has been extensively studied [[9] [25] [26] [27]]. The variation of the absorbance induced by the different gas reported in the present study is of the same order of magnitude of those reported for Au NPs dispersed in TiO_2 film [[25]] which thickness is 3 times higher than our Au-rGO samples.

The prepared samples have been tested several times for about one year, obtaining very reproducible results in terms of Au LSPR peak shift and variation in absorbance.

The different wavelength dependence of the target gas showed in the insets of Figure 2.5.7, can be used for developing a selective gas sensor. As demonstrated in Figure 2.5.9, at 528 nm the sensor gives a positive absorbance change for H_2, a negative variation for NO_2, and no variation for CO.

The behaviors of the different samples in the gas sensing tests are reported in Table 2.5.1. The AuH-rGO samples showed the best performances; none of the tested samples was responsive to CO.

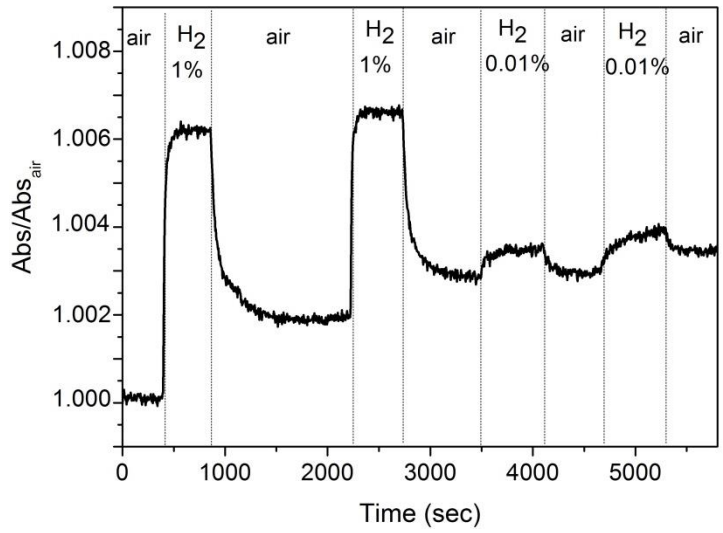

Fig. 2.5.8- Time-resolved tests for AuH-rGO samples performed at 526 nm after exposure to multiple air-H_2 cycles.

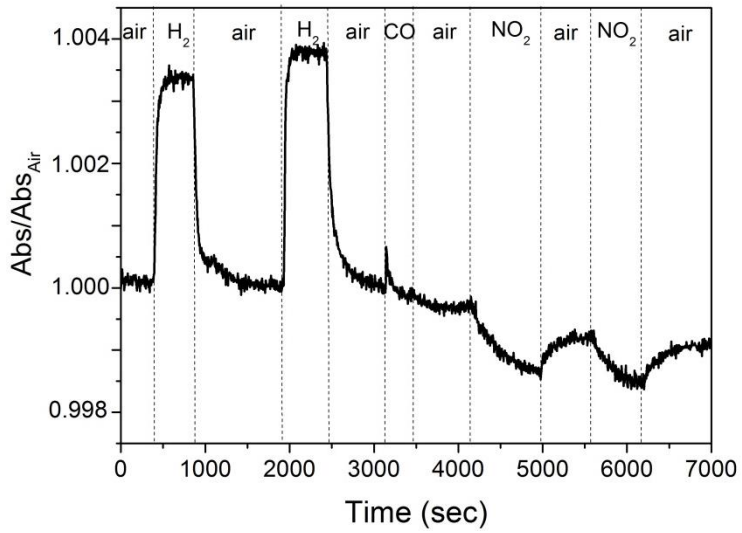

Fig. 2.5.9- Time-resolved tests for AuH-rGO samples performed at 528 nm after exposure to multiple air-gas (10000 ppm H_2, 10000 ppm CO, 1ppm NO_2) cycles.

Sample	**Gas**	**ΔAbs**	**Response time (min)**	**Recovery time (min)**
AuH-rGO	H_2 10000 ppm	0,005	1	2
	H_2 100 ppm	0,00075	2	4
	CO 10000 ppm	/	/	/
	NO_2 1 ppm	0,001	12	15
AuL-rGO	H_2 10000 ppm	0,0015	1	3
	CO 10000 ppm	/	/	/
	NO_2 1 ppm	0,0003	15	17

Tab. 2.5.1- Sensing performances for the different samples.

The reported response and recovery times are in agreement with already published data for conductometric gas sensors [28].

Bare Au NPs monolayer gave much slower dynamic repose to H_2 and NO_2 with respect to the Au monolayer coated with rGO, confirming the importance of the presence of rGO.

In order to understand the gas sensing interaction mechanism it is worth to analyze the interaction of reducing and oxidant gas with metal oxides.

In the case of metal oxides based gas sensors, atmospheric oxygen adsorbs preferentially on the surface defects of the oxides, resulting in changes of the conductivity and the optical properties according to the n- or p-type nature of the oxide vacancies [29 30]. The interaction of the target gases with the absorbed oxygen induce a variation of the charge densities which can be monitored by measuring the variation in conductivity [31] or the variation of the optical absorption [32].

Regarding graphene, it has been reported that oxygen can be adsorbed on it [33 34 35], changing its electronic [36] and optical properties [35]. It has also been demonstrated that these effects are enhanced in the case of coupling with noble metal NPs [37].

For metal oxides it has been demonstrated that UV light exposure can remove the adsorbed oxygen species leading to a variation of the charge densities [38 39]. This effect is reversible as soon as the UV source is removed and oxygen is restored in the environment. To analyze this effect we exposed rGO and Au-rGO samples to UV light keeping the samples in nitrogen stream. UV−visible spectroscopy was performed: after turning off the UV lamp while maintaining the sample under a nitrogen stream, we observed an absorption increase (Figure 10) due to removal of adsorbed oxygen. When air is re-introduced inside the cell, the effect is lost in a time scale of a few tens of minutes.

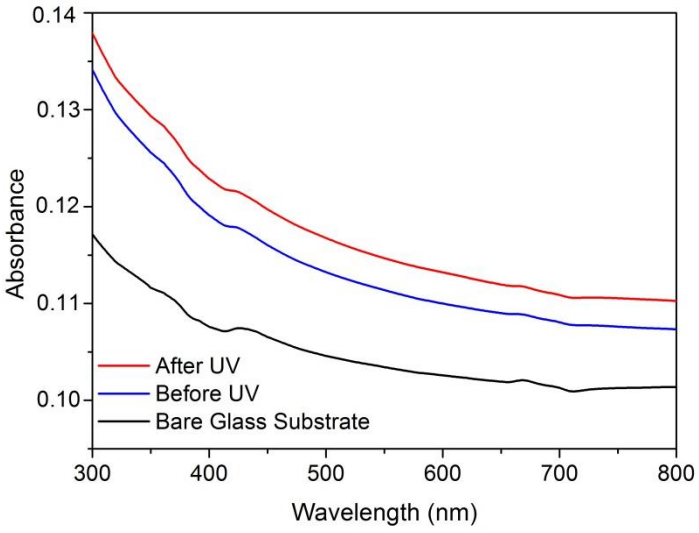

Fig. 2.5.10- Optical absorption spectra of rGO under N_2 atmosphere before and after exposure to UV light. The absorption spectrum of the bare glass substrate is also reported for comparison.

The reducing gases (H_2 and CO) react with the oxygen absorbed on the surface of the rGO and donate electrons, while oxidant gases (NO_2) subtract electrons. In both cases there is a change in the charge density of the rGO that can be monitored by measuring the variation in conductivity [28 29] or in the optical absorption, as reported for the first time in the present paper. The presence of the Au NPs greatly enhances such effect. Changes in the Au NPs electron density can alter the plasmon frequency causing a shift in the LSPR band position [40]. Moreover the presence of Au NPs can improve the visible-light photocatalytic activity through resonant energy transfer (RET) [41]. The Au NPs convert the energy of incident photons into LSPR oscillations, transferring the energy to the rGO. In this way it is possible to excite electron-hole pairs with visible light, through the Au NPs-rGO coupling [42 43].

The sensing reactions for reducing (H_2, CO) and oxidant (NO_2) gases can be explained as follow. The reducing gases react with the oxygen absorbed on the surface of the GO and donate electrons. Oxidant gases instead, react with the oxygen ions absorbed on the surface of the GO matrix and subtract electrons. These reactions are catalyzed by the presence of Au NP_S which enhance the visible-light photocatalytic activity of GO through RET. This injection or subtraction of electrons in and from the GO implies a shift in the LSPR due to the strong electromagnetic coupling between the metal NP and the GO sheets. The plasmon band blue-shifts with reducing gases and red-shifts with oxidant gases as already observed for Au NPs dispersed in metal oxide matrices [25 26 27].

The peculiarity of partially oxidized GO, completely different from the other nanostructured materials already tested in optical gas sensing like metal oxide, is the mechanism of carrier transport, linked to the particular structure of this material.

GO, in fact, is a graphene sheet functionalized with oxygen groups in form of epoxy and hydroxyl groups on the basal plane and various other types at the edges. The C-O bonds are covalent and thus disrupt the sp^2 conjugation of the hexagonal graphene lattice, making GO an insulator. The electronic structure of GO is heterogeneous due to presence of mixed sp^2 and sp^3 hybridizations and therefore cannot be readily explained by traditional valence and conduction band states. Lateral transport occurs by hopping between localized states (sp^2) (Fig. 2.5.11) at the Fermi level. The density of such localized states can be increased by removing oxygen using a variety of chemical and thermal treatments, which facilitate the transport of carriers, making reduced GO a semimetal.

The vertical resistivity of non-reduced GO is an order of magnitude lower than the lateral resistivity. This is attributed to the fact that the sp^2 clusters are isolated laterally but are in contact with the metal NPs underneath. Thus, carriers (both holes and electrons) can be injected and transported *via* the isolated sp^2 clusters.

In our case, with partially oxidized GO, the transport is intriguing due to the presence of substantial electronic disorder arising from variable sp^2 and sp^3 carbon ratios. The sp^2 clusters densities is sufficient to permit the conduction, because the sp^2 domains are percolating.

Kaiser et al. analysis indicated that transport in their reduced GO (r-GO) occurs via variable range hopping between localized sp^2 states (sp^3 bonding represent transport barriers), so we have tunneling between sp^2 sites [44].

Conduction in r-GO is limited by defects and occurs from a combination of hopping and thermal activation at midgap states, as is commonly observed in noncrystalline materials [45].

Kaiser et al. reported that electrical conduction in r-GO can be explained by variable-range hopping (VRH) through the localized states. In the VRH model, the temperature dependence of the conductivity σ can be described by:

$$\sigma = A \exp(-B/T^{1/3}) \quad (1)$$

The parameters *A* and *B* are expressed as:

$$A = eR_0\nu_{ph}/K_B \quad (2)$$

$$B = (3\alpha^2/N(E_F)k_B)^{1/3} \quad (3)$$

where *e* is the electronic charge, R_0 is the optimum hopping distance, ν_{ph} is the frequency of the phonons associated with the hopping process, k_B is the Boltzmann constant, R is the wave function decay constant, and $N(E_F)$ is the density of states near the Fermi level.

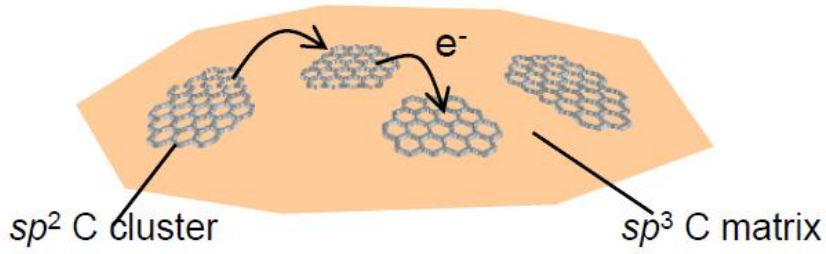

Fig. 2.5.11- Carrier transport via hopping in partially oxidized GO [46].

This hopping and thermal activation mechanisms inject (H_2) or subtract (NO_x) electrons into the gold NPs, varying their number of electrons oscillating and thus changing the SPR peak.

2.5.3 Conclusions

In this paragraph we have investigated the optical gas sensing performances of rGO coupled with Au NPs thin films towards H_2 (10000 ppm and 100 ppm), CO (10000 ppm) and NO_2 (1 ppm).
The sensors showed good and reversible responses with fast kinetics towards H_2 and NO_2, while no detectable response was observed towards CO. In particular the AuH-rGO sample showed the best sensing performances thanks to the higher NPs concentration. It was also demonstrated that the coupling of Au NPs with rGO provided a wavelength-dependent sensing response for different gas, allowing the realization of a selective sensor.
The mechanisms involved in the sensing of reducing (H_2 and CO) and oxidant (NO_2) gases using GO is just a combination between the photocatalytic behavior of GO in the visible, if coupled with Au NPs, and an exchange of electrons with the target gases through red-ox reactions mediated by the adsorbed oxygen.

References

[1] Y. Zhu, S. Murali, W. Cai, X. Li, J. Suk Won, J.R. Potts, et al. Graphene and Graphene Oxide: Synthesis, Properties, and Applications, Adv. Mater. 2010, Volume 22, Issue 35, 3906-3924.

[2] Z.J. Li, B.C. Yang, S.R. Zhang, C.M. Zhao, Graphene oxide with improved electrical conductivity for supercapacitor electrodes, Appl. Surf. Sci. 2012, Volume 258, 3726-3731.

[3] K.A. Mkhoyan, A.W. Contryman, J. Silcox, D.A. Stewart, G. Eda, C. Mattevi, et al. Atomic and Electronic Structure of Graphene-Oxide, Nano Lett. 2009, Volume 9, Issue 3, 1058-1063.

[4] K.P. Loh, Q. Bao, G. Eda, M. Chhowalla, Graphene oxide as a chemically tunable platform for optical applications, Nat. Chem. 2010, Volume 2, Issue 12, 1015-1024.

[5] T-F. Yeh, J-M. Syu, C. Cheng, T-H. Chang, H. Teng, Graphite Oxide as a Photocatalyst for Hydrogen Production from Water, Adv. Funct. Mater. 2010, Volume 20, Issue 14, 2255-2262.

[6] X. Jiang, J. Nisar, B. Pathak, J. Zhao, R. Ahuja, Graphene oxide as a chemically tunable 2-D material for visible-light photocatalyst applications, J. Catal. 2013, Volume 299, 204-209.

[7] K. Krishnamoorthy, R. Mohan, S.J. Kim, Graphene oxide as a photocatalytic material, Appl. Phys. Lett. 2011, Volume 98, Issue 24, 4101-4103.

[8] J. Huang, L. Zhang, B. Chen, N. Ji, F. Chen, Y. Zhang, et al. Nanocomposites of size-controlled gold nanoparticles and graphene oxide: Formation and applications in SERS and catalysis, Nanoscale 2010, Volume 2, 2733-2738.

[9] J.M. Bingham, J.N. Anker, L.E. Kreno, R.P. Van Duyne, Gas Sensing with High-Resolution Localized Surface Plasmon Resonance Spectroscopy, J. Am. Chem. Soc. 2010, Volume 132, Issue 49, 17358-17359.

[10] S. Zeng, K-T. Yong, I. Roy, X-Q. Dinh, X. Yu, F. Luan, A Review on Functionalized Gold Nanoparticles for Biosensing Applications, Plasmonics 2011, Volume 3, 491-506.

[11] Y. Liu, X. Dong, P. Chen, Biological and chemical sensors based on graphene materials, Chem. Soc. Rev. 2012, Volume 41, 2283–2307.

[12] G. Lu, L.E. Ocola, J. Chen, Reduced graphene oxide for room-temperature gas sensors, Nanotechnology 2009, Volume 20, Issue 44, 445502-445510.

[13] F. Schedin, A.K. Geim, S.V. Morozov, E.W. Hill, P. Blake, M.I. Katsnelson, et al. Detection of individual gas molecules adsorbed on grapheme, Nat. Mater. 2007, Volume 6, 652–655.

[14] V. Tjoa, W. Jun, V. Dravid, S. Mhaisalkar, N. Mathews, Hybrid graphene–metal nanoparticle systems: electronic properties and gas interaction, J. Mater. Chem. 2011, Volume 21, 15593-15599.

[15] S. Some, Y. Xu, Y. Kim, Y. Yoon, H. Qin, A. Kulkarni, et al. Highly Sensitive and Selective Gas Sensor Using Hydrophilic and Hydrophobic Graphenes, Scientific Reports 2013, 3:1868 DOI: 10.1038/srep01868

[16] E. Della Gaspera, M. Karg, J. Baldauf, J. Jasieniak, G. Maggioni, A. Martucci, Au Nanoparticle Monolayers Covered with Sol–Gel Oxide Thin Films: Optical and Morphological Study, Langmuir 27 (2011), pp. 13739-13747.

[17] S. Gao, N. Koshizaki, H. Tokuhisa, E. Koyama, T. Sasaki, J.K. Kim, et al. Highly Stable Au Nanoparticles with Tunable Spacing and Their Potential Application in Surface Plasmon Resonance Biosensors, Adv. Funct. Mater. 2010, Volume 20, 78-86.

[18] D. Buso, L. Palmer, V. Bello, G. Mattei, M. Post, P. Mulvaney, et al. Self-assembled gold nanoparticle monolayers in sol-gel matrices: synthesis and gas sensing applications, J. Mater. Chem. 2009, Volume 19, 2051-2057.

[19] R.G. Freeman, K.C. Grabar, K.J. Allison, R.M. Bright, J.A. Davis, A.P. Guthrie, et al. Self-Assembled Metal Colloid Monolayers: An Approach to SERS Substrates, Science 1995, Volume 267, 1629-1632.

[20] J.R. Rani, J. Lim, J. Oh, D. Kim, D. Lee, J-W. Kim, et al. Substrate and buffer layer effect on the structural and optical properties of graphene oxide thin films, RSC Adv. 2013, Volume 3, 5926-5936.

[21] I. Jung, D.A. Dikin, R.D. Piner, R.S. Ruoff, Tunable Electrical Conductivity of Individual Graphene Oxide Sheets Reduced at "Low" Temperatures, Nano. Lett. 2008, Volume 8, Issue 12, 4283-4287.

[22] C. Mattevi, G. Eda, S. Agnoli, S. Miller, K.A. Mkhoyan, O. Celik, et al. Evolution of Electrical, Chemical, and Structural Properties of Transparent and Conducting Chemically Derived Graphene Thin Films, Adv. Funct. Mater. 2009, Volume 19, 2577-2583.

[23] C. Hontoria-Lucas, A.J.L. Peinando, J.D.D. Lopez-Gonzalez, M.L. Rojas-Cervantes, R.M. Martin-Aranda, Study of oxygen-containing groups in a series of graphite oxides: Physical and chemical characterization, Carbon 1995, Volume 33, 1585-1592.

[24] D-Q. Yang, E. Sacher, Carbon 1s X-ray Photoemission Line Shape Analysis of Highly Oriented Pyrolytic Graphite: The Influence of Structural Damage on Peak Asymmetry, Langmuir 2006, Volume 22, 860-862.

[25] E. Della Gaspera, M. Bersani, G. Mattei, T.L. Nguyen, P. Mulvaney, A. Martucci, Cooperative effect of Au and Pt inside TiO_2 matrix for optical hydrogen detection at room temperature using surface plasmon spectroscopy, Nanoscle 2012, Volume 4, Issue 19, 5972-5979.

[26] D. Buso, M. Post, C. Cantalini, P. Mulvaney, A. Martucci, Gold nanoparticle-doped TiO_2 semiconductor thin films: Gas sensing properties, Adv. Funct. Mater. 2008, Volume 18, Issue 23, 3843-3849.

[27] N.A. Joy, M.I. Nandasiri, P.H. Rogers, W. Jiang, T. Varga, S.V.N.T. Kuchibhatla, S. Thevuthasan, et al. Selective plasmonic gas sensing: H_2, NO_2, and CO spectral discrimination by a single Au-CeO_2 nanocomposite film, Anal. Chem. 2012, Volume 84, 5025-5034.

[28] S. Prezioso, F. Perrozzi, L. Giancaterini, C. Cantalini, E. Treossi, V. Palermo, et al. Graphene Oxide as a Practical Solution to High Sensitivity Gas Sensing, J. Phys. Chem. C 2013, Volume 117, Issue 20, 10683-10690.

[29] M-W. Ahn, K-S. Park, J-H. Heo, J-G. Park, D-W. Kim, K.J. Choi, et al. Gas sensing properties of defect-controlled ZnO-nanowire gas sensor, Appl. Phys. Lett. 2008, Volume 93, 263103-263105.

[30] J.A. Dirksen, K. Duval, T.A. Ring, NiO thin-film formaldehyde gas sensor, Sens. Actuators B 2001, Volume 80, 106-115.

[31] A. Martucci, D. Buso, M. De Monte, M. Guglielmi, C. Cantalini, C. Sada, Nanostructured sol-gel silica thin films doped with NiO and SnO_2 for gas sensing applications, J. Mat. Chem. 2004, Volume 14, 2889-2895.

[32] A. Martucci, M. Pasquale, M. Guglielmi, M. Post, J.C. Pivin, Nanostructured silicon oxide nickel oxide sol–gel films with enhanced optical carbon monoxide gas sensitivity, J. Am. Ceram. Soc. 2003, Volume 86, Issue 9, 1638-1640.

[33] S. Ryu, L. Liu, S. Berciaud, Y-J. Yu, H. Liu, P. Kim, et al. Atmospheric oxygen binding and hole doping in deformed graphene on a SiO_2 substrate, Nano Lett. 2010, Volume 10, 4944-4951.

[34] H.J. Yan, B. Xu, S.Q. Shi, C.Y. Ouyang, First-principles study of the oxygen adsorption and dissociation on graphene and nitrogen doped graphene for Li-air batteries, J. Appl. Phys. 2012, Volume 112, 104316-104320.

[35] J. Docherty, C-T. Lin, H.J. Joyce, R.J. Nicholas, L.M. Herz, L-J. Li, et al. Extreme sensitivity of graphene photoconductivity to environmental gases, Nature Comm. 2012, Volume 3, 1228.

[36] J.Y. Dai, J.M. Yuan, Adsorption of molecular oxygen on doped graphene: atomic, electronic, and magnetic properties, Phys. Rev. B 2010, Volume 81, 165414-165420.

[37] T. Zhang, Q. Xue, M. Shan, Z. Jiao, X. Zhou, C. Ling, et al. Adsorption and Catalytic Activation of O_2 Molecule on the Surface of Au-Doped Graphene under an External Electric Field, J. Phys. Chem. C 2012, Volume 116, 19918-19924.

[38] D.A. Melnick, Zinc Oxide Photoconduction, an Oxygen Adsorption Process, J. Chem. Phys. 1957, Volume 26, 1136-1146.

[39] K. Tanaka, G. Blyholder, Adsorbed oxygen species on zinc oxide in the dark and under illumination, J. Phys. Chem. 1972, Volume 76, 3184-3187.

[40] G. Sirinakis, R. Siddique, I. Manning, P.H. Rogers, M.A. Carpenter, Development and characterization of Au-YSZ surface plasmon resonance based sensing materials: High temperature detection of CO, J. Phys. Chem. B 2006, Volume 110, 13508-13511.

[41] S.K. Cushing, J. Li, F. Meng, T.R. Senty, S. Suri, M. Zhi, M. Li, et al. Photocatalytic Activity Enhanced by Plasmonic Resonant Energy Transfer from Metal to Semiconductor, J. Am. Chem. Soc. 2012, Volume 134, Issue 36, 15033−15041.

[42] J. Niu, Y.J. Shin, J. Lee, Y. Son, J.H. Ahn, H. Yang, Shifting of surface plasmon resonance due to electromagnetic coupling between graphene and Au nanoparticles, Opt. Express 2012, Volume 20, Issue 18, 19690-19696.

[43] J. Niu, Y.J. Shin, J. Lee, J.H. Ahn, H. Yang, Graphene induced tunability of the surface plasmon resonance, Appl. Phys. Lett. 2012, Volume 100, Issue 6, 1116-1120.

[44] S. S. Li, K. H. Tu, C. C. Lin, C. W. Chen, and M. Chhowalla, Solution-processable graphene oxide as an efficient hole transport layer in polymer solar cells, ACS Nano 2010, Volume 4, Issue 6, 3169–3174.

[45] G.Eda, C.Mattevi, H.Yamaguchi, H.Kim & M.Chhowalla, Insulator to Semimetal Transition in Graphene Oxide, J. Phys. Chem. C 2009, Volume 113, 15768-15771.

[46] Manish Chhowalla, Opto-electronic Properties of Graphene Oxide and Partially Oxidized Graphene, Materials Science and Engineering, Rutgers University, New Jersey, USA.

2.6 Aromatic VOC sensing with porous SiO_2 matrices functionalized with phenyl groups coupled with in situ grown gold nanoparticles

Aromatic Volatile Organic Compounds (A-VOCs) like xylene, toluene and benzene, have received a great attention in the field of the evaluation of indoor air quality. Indoor pollutants, such as formaldehyde, benzene, toluene and xylene, may cause the environmental illnesses known as building-related sickness [1 2].

Two different silica based materials functionalized with one or two phenyl groups, fabricated from two precursors, PTMS (trimethoxy phenylsilane) and dPDMS (diethoxy (diphenyl)silane), have been used as gas sensors towards these A-VOC, thanks to the π-π interaction between the benzene ring of the target gas and the phenyl ring of the silica matrix stacked together. This interaction has been monitored using the LSPR peak of gold NPs grown in situ starting from an Au salt ($HAuCl_4$) reduced via thermal treatment.

2.6.1 Experimental

2.6.1.1 Materials' synthesis

The silica phenyl functionalized sol-gel materials with Au NPs grown in situ were prepared as described in the appendixes A.2.14 and A.2.15.

2.6.1.2 Nanocomposite thin film deposition

Thin films were deposited by dip coating technique [3] with a withdraw speed of 60cm/min on quartz and treated in a muffle furnace at 400 °C for 30 min in air. The average thickness is around 500nm. The samples synthetized are presented in Table 2.6.1.

Samples	Thermal treatment
TEOS/PTMS + Au^{3+}	400°C
TEOS/dPDMS + Au^{3+}	400°C

Tab. 2.6.1- List of the SiO_2 based film with phenyl groups fabricated by sol-gel.

The two different types of matrix has been deposited, one with TEOS (Fig. 2.6.1a) and PTMS, a precursor with one phenyl ring (Fig. 2.6.1b), the other with TEOS and dPDMS, a precursor with two phenyl rings (Fig. 2.6.1c).

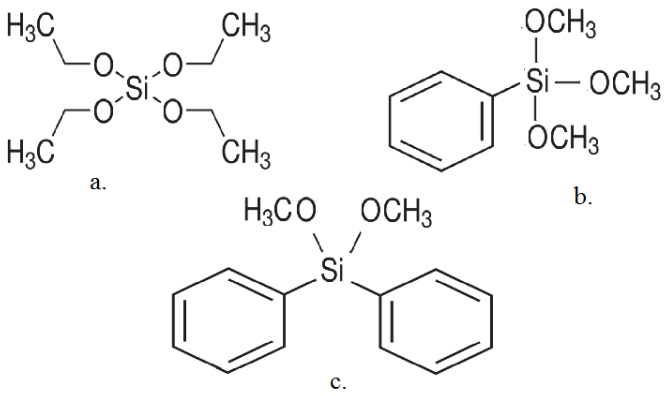

Fig. 2.6.1- SiO_2 precursors' structure, a. TEOS, b. PTMS, c. dPDMS [4].

2.6.1.3 Gas sensing measurements

Optical gas sensing tests were performed at room temperature and the sensor was tested for A-VOC, benzene 30 ppm, toluene 30 ppm and xylene (orto-, meta-, para- each 10 ppm) all balanced in air.

2.6.2 Results and discussion

2.6.2.1 Optical and structural characterization of the thin films

From the absorption spectra reported in Figure 2.6.2 it is possible to verify the formation of gold NPs, as a result of the heat treatment, which are responsible for the LSP peak at 540 nm as well as the presence of the phenyl groups with the characteristic peak at 270 nm. This presence means that the heat treatment was not enough to pyrolyze them, and this is a key point for the development of this work being the phenyl groups responsible for the A-VOC sensing mechanism.

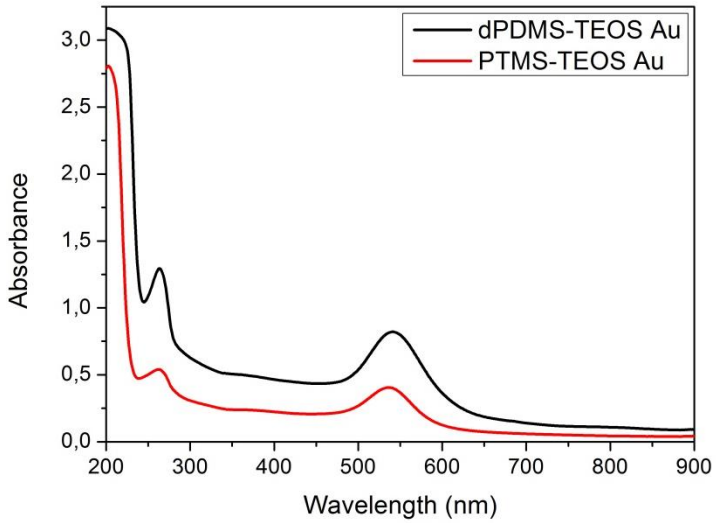

Fig. 2.6.2 - Absorption spectra of the samples with TEOS- dPDMS or PTMS.

In Figure 2.6.2 it is also evident that the Au peak in the dPDMS matrix is more red-shifted than the one in the PTMS matrix; moreover the phenyl correspondent peak, at 270 nm, in the dPDMS sample is higher, because the amount of phenyl rings is doubled.

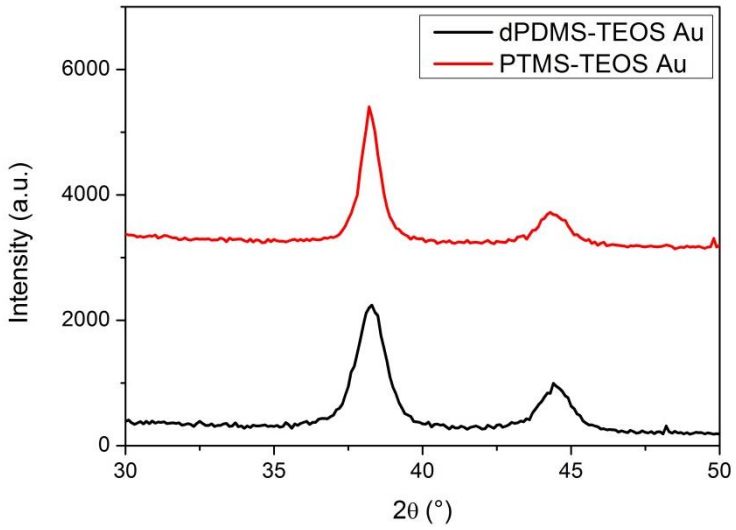

Fig. 2.6.3 – XRD patterns of the samples with TEOS- dPDMS or PTMS.

Figure 2.6.3 shows the XRD patterns of the samples containing 5% molar Au within the two different SiO_2 matrices after the final annealing at 400 °C: the theoretical diffraction peaks for Au are (JCPDS No. 040714) at 38° and 44,5°. All the samples show crystalline phases, indicating that, as already found in the absorption spectra, the thermal treatment has promoted the reduction of Au ions dispersed inside the oxide films.

From the XRD patterns, using the Scherrer equation, it was possible to confirm the formed gold crystals with dimensions around 20 nm, this systems and data have been already widely discussed in previous work with also the SEM image support [5] [6].

From the ellipsometric measurements the thickness of the films was evaluated to be 560-600nm and the refractive index at 630 nm was 1,526.

2.6.2.2 Gas sensing tests

PTMS and dPDMS Au nanocomposite films annealed at 400°C were tested as optical gas sensors for A-VOC (Fig. 2.6.4) detection. For these samples the mechanism involved in the process of sensing takes place at room temperature (RT), for this reason the tests are carried on at RT.

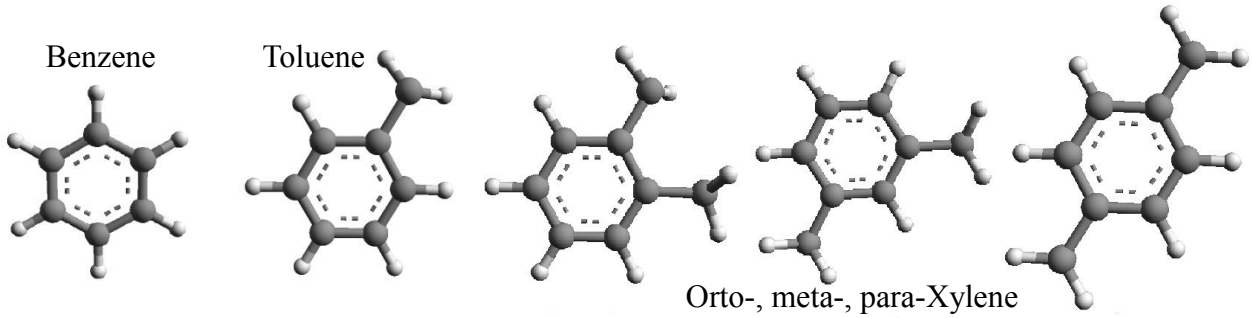

Fig. 2.6.4- Benzene, Toluene, orto- meta- para- Xylene molecules simulate using the software ArgusLAb, with in grey the carbon atoms and in white the hydrogen atoms.

Both the samples are sensitive to the A-VOCs. The Au SPR peak during gas exposure undergoes an increase in the SPR absorbance and a small red-shift (Fig. 2.6.5). This effect is related to the interaction π-π, between the phenyl group of the silica matrix and the benzene ring of the gas target.

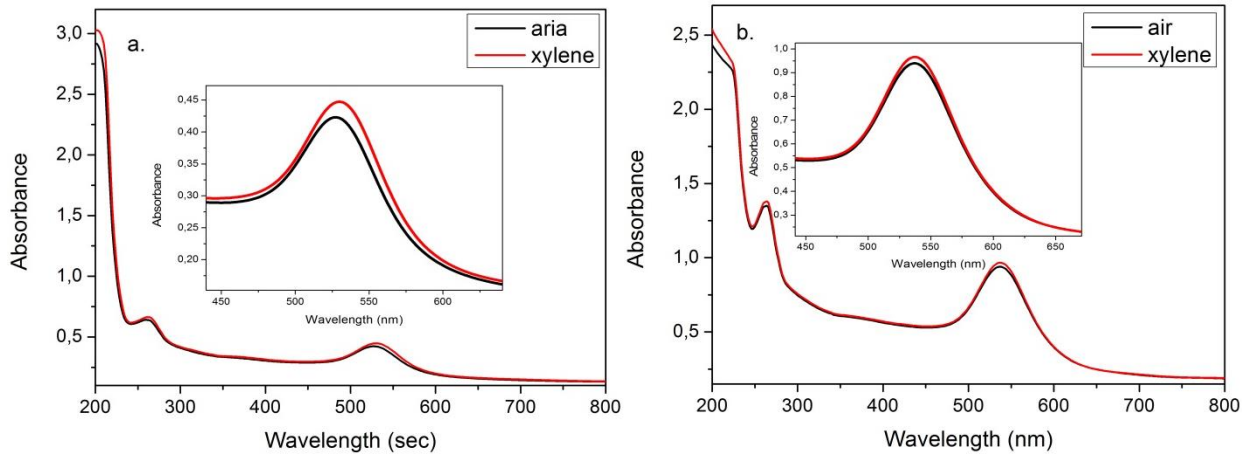

Fig. 2.6.5- Absorption spectra of PTMS (a.) and dPDMS (b.) film in air (black line)and in xylene(red line) , with a magnification of the LSPR peak in the insets.

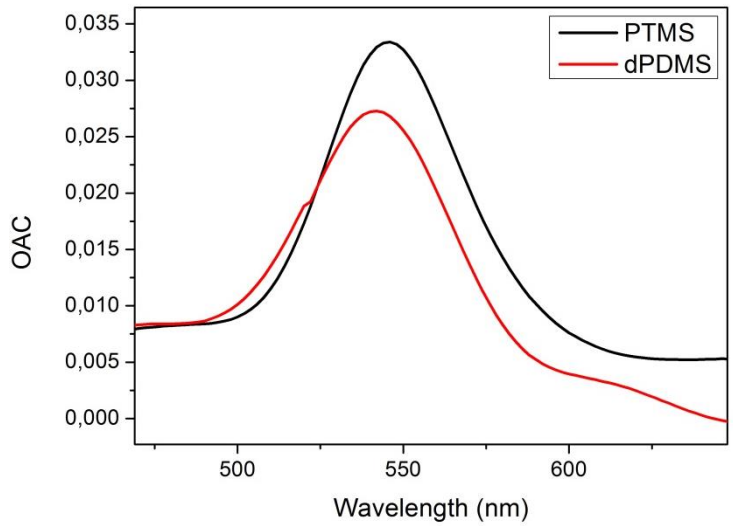

Fig. 2.6.6 – Comparison of the OAC curve for xylene between PTMS and dPDMS samples.

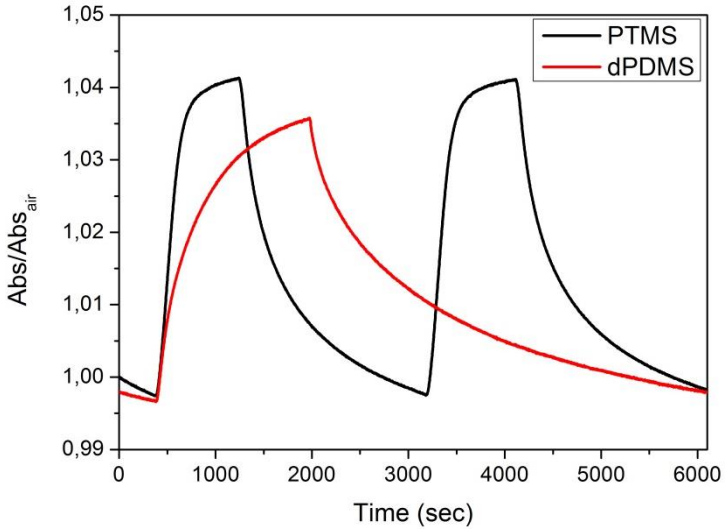

Fig. 2.6.7 – Dynamic measurements of the gas sensing test with xylene on the samples PTMS (a.) and dPDMS (b.) Au.

From Figure 2.6.6 and 2.6.7 it is possible to note that the sample with two phenyl group is less performing than the one with just one phenyl group, in particular in terms of time of response and of recovery.

To better investigate the π-π stacking interaction between the phenyl rings of the samples and different phenyl groups, with different substituents, the best sample, TEOS-PTMS, has been tested also towards toluene and benzene with one CH_3 substituent and with no substituents, respectively. In Figure 2.6.8 are presented the OAC curve comparing the variation in absorbance induced by the three gases, it is evident that xylene induces a higher variation than toluene and benzene. In the phenyl absorption region it is evident an increase in absorbance (Fig. 2.6.8 a) in AVOC flux, due mainly to the π-π stacking interaction and also to the increase in the number of phenyl groups. The maximum of variation in absorbance, in AVOC flux, is in the SPR region (Fig. 2.6.8 b) at 550 nm.

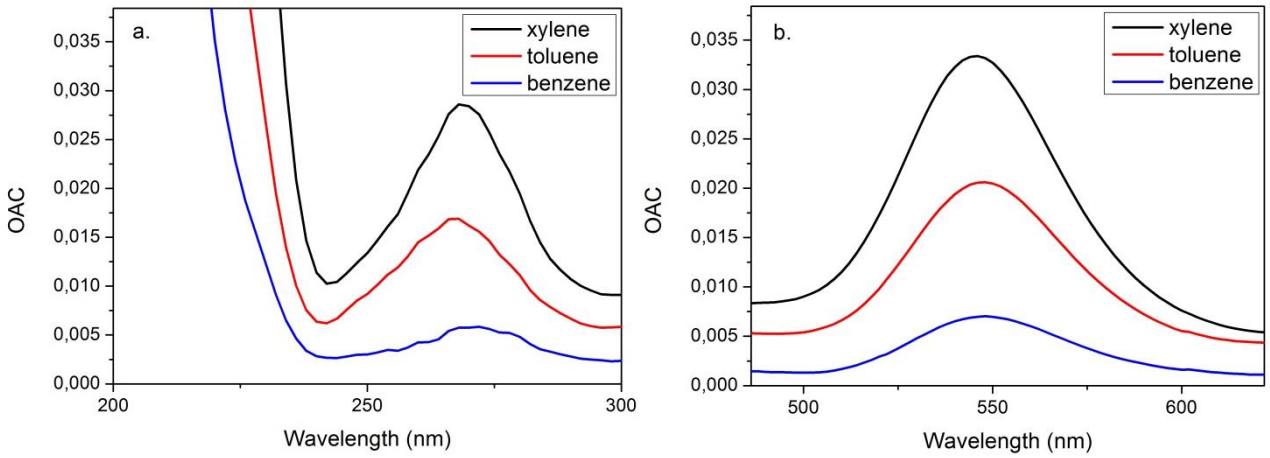

Fig. 2.6.8 – Comparison between the OAC (Optical absorption change) curves of benzene (blue), toluene (red) and xylene (black) for the sample TEOS/PTMS Au in the phenyl absorption (270 nm) region (a.) and in the SPR absorption (550 nm) region (b.).

In Figure 2.6.9 are presented the results of the dynamic sensing measurement towards xylene, toluene and benzene on the PTMS/ TEOS Au which showed the best performances.

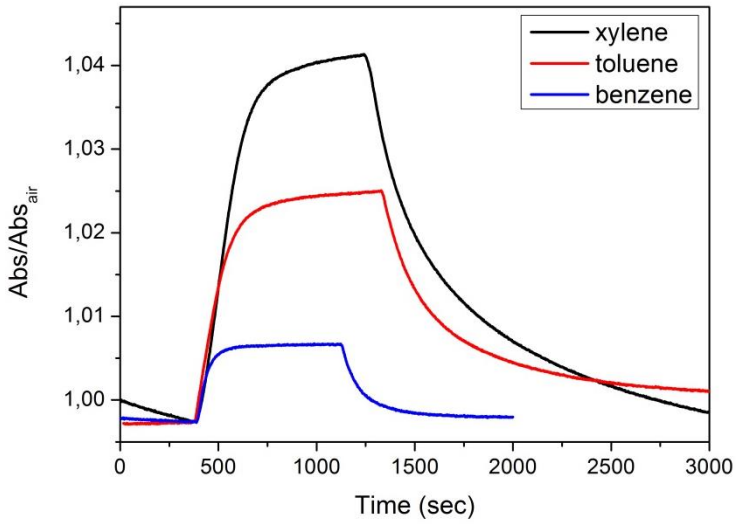

Fig. 2.6.9– Dynamic gas sensing test with xylene, toluene and benzene on the sample PTMS-TEOS Au at 550nm.

From the dynamic measurement is possible to notice that the sensitivity towards all the three gases is good, and also that the performances are higher at the increase of the number of substituents (-CH_3 groups) (Fig. 2.6.10).

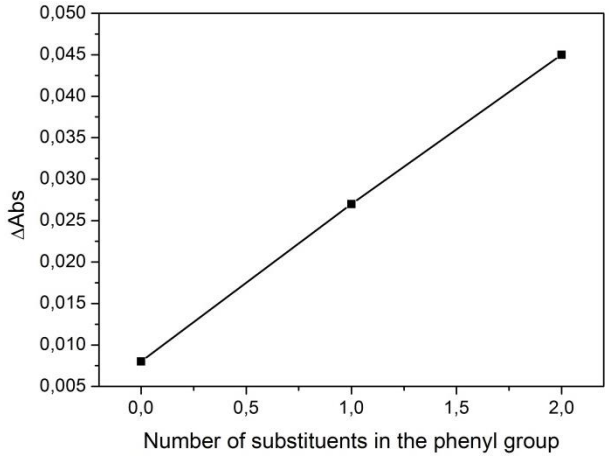

Target gas	*ΔAbsorbance*
Benzene	0,008
Toluene	0,027
o-, m-, p-Xylene	0,045

Fig. 2.6.10 – Delta of Absorbance as a function of the increasing of the number of substituents (-CH_3 groups) in the phenyl group. The values of the Delta of Absorbance are reported in the Table.

To prove that there is this interaction, which is function of the number of substituents in the benzene ring of the AVOC, and not just an increase in *n*, due to the fact that the AVOC have a higher *n* than the air filling the pores, TPD measurement (Appendix A.1.7) have been performed on a similar matrix of porous silica functionalized with phenyl groups, ph-PSQ (Phenyl-bridged polysilsesquioxanes) [7].

TPD curves from a ph-PSQ film were initially acquired for different xylene loadings (1.0, 3.0, 5.0 and 10.0 L) at low temperature (about 150 K), in order to observe the shape of the desorption profiles (not shown). Two clear desorption components were seen: a low intensity feature, centred at about 300 K, due to the monolayer desorption, and an intense peak at about 230 K. Since no saturation was observed on increasing the analyte loading, this peak was assigned to the multilayer desorption. In order to avoid multilayer condensation and to resolve the monolayer desorption peak, the sample was thermalized at 258 K and a 20.0 L dosing of the xylene was performed.

Figure 2.6.13 a. shows the xylene monolayer desorption peaks acquired at different β values in the 60-120 K/min range. These data show a single broad peak centred at about 300 K that slightly shifts to higher temperatures as β increases. By plotting $\ln(T_m^2/\beta)$ as a function of $1/T_m$ (Fig. 2.6.13 b) it was possible to calculate, through linear regression, a desorption energy of xylene from the ph-PSQ film ΔE_d = 38±14 kJ/mol. This means that there is an interaction, the π-π stacking, and is this interaction that we monitor in the gas sensing test.

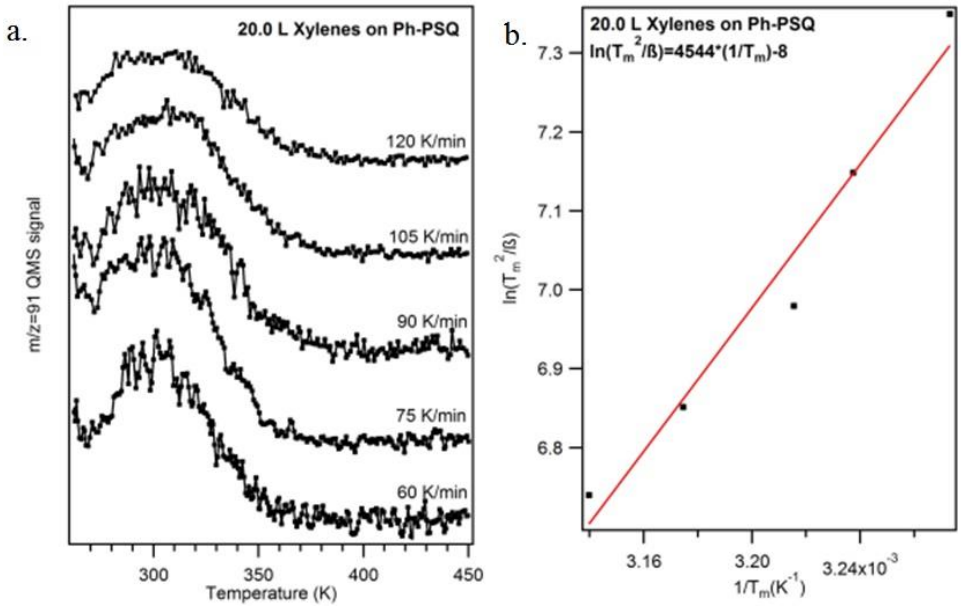

Fig. 2.6.13 - Xylene monolayer desorption spectra at different β values ,in the 60-120 K/min range, for a ph-PSQ film (a.); linear regression of the experimental points ($1/T_m$, $\ln(T_m^2/\beta)$) to obtain an estimate of ΔE_d (b.).

To better understand the mechanisms involved in this kind of gas sensing based on the π-π stacking between the phenyl group of the sensible sol-gel thin film and the target gas, A-VOCs, we have to take into account the effect of single and multiple substituents on sandwich and T-shaped π-π interactions.

In the early 2000s Lee [8], Sherrill and Sinnokrot [9] [10] [11] [12] [13], Wheeler [14] performed a series of computational studies in gas-phase which raised doubts about the simple electrostatic model championed by Hunter and Sanders [15] [16] [17] [18].

This new theories by Sherrill and co-workers use symmetry-adapted perturbation theory (SAPT), which takes into account the electrostatic, dispersion, induction and exchange-repulsion components of the interaction energy. This analysis showed that dispersion is more important than electrostatic in the overall binding so the π-π stacking interactions are not governed primarily by electrostatic effects, this contradict the Hunter and Sanders model [1111].

Hunter and Sanders used a simple mathematical model in which they predict that electron-withdrawing substituents strengthen the interaction because they decrease the electrostatic repulsion between the negatively charged π clouds. The reverse effect is predicted for electron-donating substituents.

Moreover Hunter and Sanders' theory predicts that electron-withdrawing groups, reducing the negative quadropole of the aromatic ring, favor parallel displaced and sandwich conformations. Contrastingly, electron-donating groups, increasing the negative quadropole, increase the interaction strength in a T-shaped configuration with the proper geometry.

Sherrill et al. showed that both electron-donating substituents and electron-withdrawing substituents stabilize the substituted benzene molecule of the target gas stacked with the phenyl group of the matrix in the sandwich configuration [13]; while the Hunter-Sanders model said that electron donors should weaken stacking interactions.

This unconventional prediction by Sherril, Sinnokrot and Ringer [9-13] that all substituted sandwich benzene dimers have a stronger attraction than the unsubstituted benzene dimer, regardless of the electron-donating or electron-withdrawing nature of the substituent, this involves that electron-donating substituents increase binding in face to face π–π interactions, in other words favors the sandwich stacking (Fig. 2.6.14).

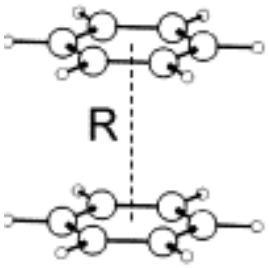

Fig. 2.6.14 - Sandwich conformation for the π-π staking interaction between phenyl groups [19].

Wheeler in 2011 [14] extended the theory of the direct interaction of substituents in π-stacking interactions recognizing that the direct interactions between the substituents and the unsubstituted ring were due to local interactions. In other words, substituents effects do not arise from the interaction of the substituents with the other ring in its entirely, but only the nearest vertex.

Other computational work from the Sherill group revealed that the effect of each substituent in the sandwich configuration is additive [11].

In our case considering benzene, and substituted benzene: toluene (one CH_3) and xylene (two CH_3) Ringer said that all substituted sandwich dimers have a smaller interaction energy than sandwich benzene dimer (Fig. 2.6.15), regardless of the electron-donating or electron-withdrawing nature of the substituents [11].

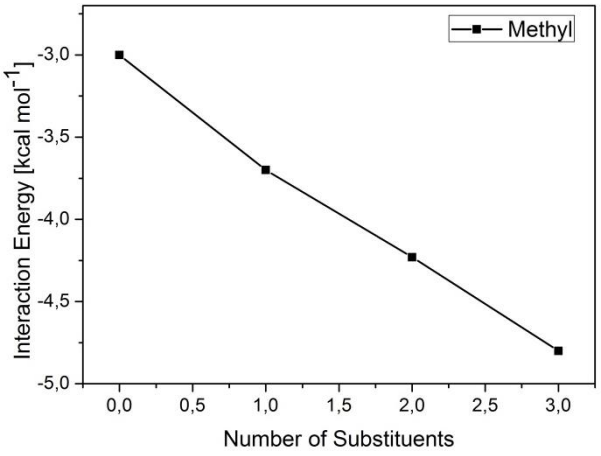

Fig. 2.6.15- Total internal energy versus number of CH_3 substituents for sandwich configuration [11].

This is why the xylene binds more strongly than toluene and toluene than benzene to the phenyl group and we monitor it in the gas sensing measurement (Fig. 2.6.8).

In other words the interaction energy of xylene, with the phenyl group of the matrix, is lower than the one of toluene and the biggest is the one of benzene because of the substituent effect [11], which involves electrostatic, dispersion, induction and exchange-repulsion factors. The exchange-repulsion and dispersion are more important than the electrostatics [12].

The dispersion factor is a weak intermolecular interaction arising from quantum induced instantaneous polarization multipoles in molecules and is an attractive kind of interaction, this agree with the theory that phenyl group in phenyl-trimethoxysilane because of the high polarisability of the π-bonding electrons, changes its electron distribution in response to an interaction (π- π stacking) with other, in our case, aromatic molecules, benzene, toluene and xylene [20].

The exchange-repulsion factor is linked to a force that arises between neighboring molecules when they are close enough that their electron clouds overlap and, as a consequence of the Pauli exclusion principle, electrons are squeezed out from the region between the nuclei, which repel each other [21].

Thanks to the exchange-repulsion and dispersion factors is possible to deduce that in the π-π stacking there is a charge penetration effect, due to the fact that the two negatively charged π clouds on the top of benzene ring and phenyl group of the matrix, in the sandwich, interpenetrate each other.

Moreover regarding the gold NPs role they do not have an active role in the gas sensing, contarily they behave as optical probe. The surface plasmon in metallic nanoparticles, generated by the

interaction of electromagnetic radiation with the metal sphere, is affected by the change in the dielectric medium in which nanoparticles are immersed.

Thus, the resonance properties depend on the properties of the particles and on those of the medium because they polarize each other and the charge density has to adjust not only to the incident fields but also to the fields caused by polarization [[22]].

2.6.3 Conclusions

In this work we have investigated the best performances in the gas sensing behaviour of gold/silica nanocomposites thin films comparing the configurations with one or with two benzene rings towards benzene, toluene and orto-, meta-, para- xylene.

The different nanostructured Au doped SiO_2 thin films have been simply synthesized by sol-gel technique. Au doped SiO_2 films are made of Au NPs grown in situ in the SiO_2 based matrix via thermal treatment.

All type of film showed optical response to the investigated A-VOC with reversible dynamic.

Au-SiO_2 film with only one benzene ring and treated at 400°C show the best response to the A-VOC.

The mechanism involved in the A-VOC sensing using SiO_2 functionalized with phenyl groups matrix, is found to be the π-π stacking interaction.

The effect of the different A-VOC results in the variation in Absorbance depending on their different binding energies, which allows a stronger or milder affinity with the sensitive material.

References

[1] S. Zampolli, I. Elmi, F. Ahmed, M. Passini, G.C. Cardinali, S. Nicoletti, L. Dori, An electronic nose based on solid state sensor arrays for low-cost indoor air quality monitoring applications, Sens. Actuators B 2004, Volume 101, 39-46.

[2] Zeng Wen, Liu Tian-mo, Gas-sensing properties of SnO_2–TiO_2-based sensor for volatile organic compound gas and its sensing mechanism, Physica B 2010, Volume 405, 1345–1348.

[3] C. J. Brinker, G. C. Frye, A. J. Hurd, C. S. Ashley, Fundamentals of sol-gel dip coating, Thin Solid Films 1991, Volume 201, 97-108.

[4] www.sigmaaldrich.com

[5] D. Buso, G. Busato, M. Guglielmi, A. Martucci, V. Bello, G. Mattei, P. Mazzoldi, M. Post, Selective optical detection of H_2 and CO with SiO_2 sol gel films containing NiO and Au nanoparticles, Nanotechnology 2007, Volume 18, 475505 (1-7).

[6] D. Buso, M. Guglielmi, A. Martucci, G. Mattei, P. Mazzoldi, C. Sada, M. Post, Growth of cookie-like Au/NiO nanoparticles in SiO_2 sol-gel films and their optical gas sensing properties, Crystal Growth and Design 2008, Volume 8, Issue 2, 744-749.

[7] L. Brigo, M. Cittadini, L. Artiglia, G. A. Rizzi, G. Granozzi, M. Guglielmi, A. Martucci, G. Brusatin, Xylene sensing properties of aryl-bridged polysilsesquioxane thin films coupled to gold nanoparticles, J. Mater. Chem. C 2013,1**,** 4252-4260.

[8] Eun Cheol Lee, Dongwook Kim, Petr Jurečka, P. Tarakeshwar, Pavel Hobza, Kwang S. Kim, Understanding of Assembly Phenomena by Aromatic-Aromatic Interactions: Benzene Dimer and the Substituted Systems, J. Phys. Chem. A 2007; Volume 111, Issue 18, 3446 – 3457.

[9] M. O. Sinnokrot, C. D. Sherrill, High-accuracy quantum mechanical studies of π–π interactions in benzene dimers, J Phys Chem A 2006, Volume 110, Issue 37, 10656–10668.

[10] S. A. Arnstein, C. D. Sherrill, Substituent Effects in Parallel-Displaced π-π Interactions, Phys. Chem. Chem. Phys. 2008, Volume 10, 2646-2655.

[11] A. L. Ringer, M. O. Sinnokrot, R. P. Lively, C. D. Sherrill, The Effect of Multiple Substituents On Sandwich and T-Shaped π-π Interactions, Chem. Eur. J. 2006, Volume 12, 3821-3828.

[12] M. O. Sinnokrot, C. D. Sherrill, Substituent Effects in π-π Interactions: Sandwich and T-Shaped Configurations, J. Am. Chem. Soc. 2004, Volume 126, 7690-7697.

[13] M. O. Sinnokrot, C. D. Sherrill, Unexpected Substituent Effects in Face-to-Face π-Stacking Interactions, J. Phys. Chem. A 2003, Volume 107, 8377-8379.

[14] Steven E. Wheeler, K. N. Houk, Substituent Effects in the Benzene Dimer are Due to Direct Interactions of the Substituents with the Unsubstituted Benzene, J. Am. Chem. Soc. 2008, Volume 130, Issue 33, 10854–10855.

[15] C. A. Hunter, K. R. Lawson, J. Perkins, C. J. Urch, Aromatic interactions, J Chem Soc 2001, Volume 2, 651-669.

[16] C. A. Hunter, J. K. M. Sanders, The nature of π-π Interactions, J. Am. Chem. Soc.1990, Volume 112, Issue 14, 5525–5534.

[17] S. L. Cockroft, J. Perkins, C. Zonta, H. Adams, S. E. Spey, C. M. R. Low, J. G. Vinter, K. R. Lawson, C. J. Urch, C. A. Hunter, Substituent effects on aromatic stacking interactions, Org. Biomol. Chem. 2007, Volume 5, 1062–1080.

[18] F. Cozzi, M. Cinquini, R. Annunziata, J. S. Siegel, Dominance of polar/π over charge-transfer effects in stacked phenyl interaction, J. Am. Chem. Soc. 1993, Volume 115, 5330–5331.

[19] M. S. Gordon, L. V. Slipchenko, H. Li, J. H. Jensen, The effective fragment potential: a general method for predicting intermolecular interactions, Annual report in computational chemistry 2007, Volume 3, 177-193.

[20] G. R. Atkins, R. M. Krolikowska, A. Samoc, Optical properties of an ormosil system comprising methyl- and phenyl-substituted silica, J. Non-Crystalline Solids 2000, Volume 265, 210-220.

[21] McGraw-Hill Science & Technology Dictionary.

[22] S. K. Ghosh, T. Pal, Interparticle coupling effect on the surface plasmon resonance of gold nanoparticles: from theory to applications, Chem. Rev. 2007, Volume 107, Issue 11, 4797–4862.

Chapter 3

3.1 Xylene, Toluene and Benzene gas sensing with SPP

Aromatic Volatile Organic Compounds (A-VOC) sensing has been widely performed, with carbon nanotubes [1], aryl-bridged polysilsesquioxane [2 3] because of their dangerousness [4].

In chapter 2.7 we developed a sensor based on LSPR peak of Au NPs embedded in a SiO_2 porous sol-gel film containing phenyl groups, here we present an A-VOC sensor based on plasmonic crystals, in which the sensitive layer is either a porous silica film functionalized with phenyl groups [5], or a semiconducting layer of nanocrystalline TiO_2.

These two materials can be promising candidate to monitor A-VOCs because of the strong interaction between the benzene rings of the target gas with the phenyl group of the SiO_2 matrix, involving π-π stacking (as already demonstrated in chapter 2.7), and with the TiO_2 matrix, involving a Ti^{4+}•••π-electrons or OH•••π-electrons interaction.

Surface Plasmon Polaritons (SPPs) are electromagnetic waves coupled to collective electron oscillations, propagating along a conductor-insulator interface and exponentially decaying away from it. The field confinement at the interfaces makes SPPs particularly sensitive to changes in the dielectric properties of the media in which they propagate. SPPs are largely employed in sensing devices, because changes in the propagation characteristics and in the spatial profile of the SPP modes can be related to variations in the refractive index of the dielectric region, and thus to the presence of the analyte. SPPs can be coupled to photons in the presence of a prism, a grating or a spatially localized scattering centre.

SPPs are not only confined in the transverse direction with respect to the interface, but also attenuated in the direction parallel to it. Confinement and propagation distance are tightly related variables, since as propagation distance increases, confinement becomes weaker. These two parameters are crucial issues for the design and fabrication of sensing nanodevices. A greater penetration of the SPP in the insulator can provide a better probing of its dielectric properties and detect smaller changes in its refractive index. Otherwise, to detect the presence of small molecules at the conductor-insulator interface, a greater confinement can be required for probing only the region occupied by the molecule.

We have fabricated a plasmonic sensor in symmetric dielectric-metal-dielectric configuration, with sinusoidal grating coupling. The structure consists of a thin metallic film bounded by two dielectric

layers. Grating couplers are an attractive approach for fabrication of low-cost SPR sensing structures, because they do not require expensive optics, and are compatible with mass production.

Figure 3.1.1 shows a scheme of the multilayer structure that characterizes the sensor, in which a is the grating pitch, θ is the incidence angle of the incoming photons, and α is the azimuth. If $\mathbf{k}_{\|PH}$ is the on-plane component of the incoming photon momentum ($\mathbf{k}_{\|PH} = \mathbf{k}_0\, n_d\, \text{sen}\theta$, with n_d being the refractive index of the medium from which light impinges), $\mathbf{k}_G$ is the grating wave vector of modulus $k_G = 2\pi/a$ and direction perpendicular to the grooves, and $\mathbf{k}_{SP}$ is the SPP momentum, the coupling condition for the excitation of SPPs is given by: $\mathbf{k}_{SP} = -\mathbf{k}_{\|PH} + n\,\mathbf{k}_G$, for n integer number.

The developed metal slab waveguide exhibits two SPP modes with different profiles and dispersion characteristics, resulting from the superposition of the SPPs at its two metal-dielectric interfaces. These modes are classified with respect to their magnetic field profile inside the structure as symmetric and antisymmetric modes. The symmetric mode is also called Long Range SPP (LRSPP), since it exhibits lower confinement and greater propagation distance, while the antisymmetric mode is called Short Range SPP (SRSPP), and it presents greater confinement and attenuation [6].

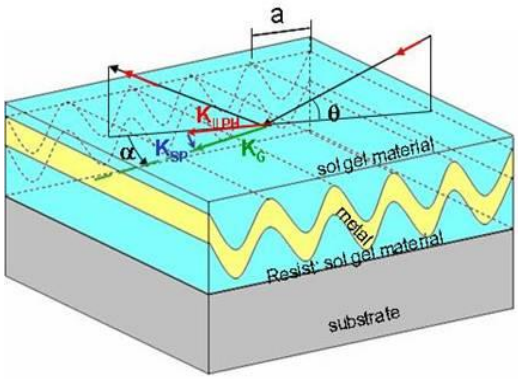

Fig. 3.1.1- Sketch of the multilayer structure of a surface plasmon metallic gratings with a functional and porous sol-gel material, for the excitation of LRSPPs and SRSPP. a is the grating pitch, θ is the incidence angle of the incoming photon, and α is the azimuth. If $\mathbf{k}_{\|PH}$ is the on-plane component of the incoming photon momentum, $\mathbf{k}_G$ is the grating wave vector, and $\mathbf{k}_{SP}$ is the SPP momentum, the coupling condition for the excitation of SPPs is given by: $\mathbf{k}_{SP} = -\mathbf{k}_{\|PH} + n\,\mathbf{k}_G$, for an integer n.

In order to test the gas sensing performance, samples were mounted in gas chambers optically coupled to the ellipsometer. Reflectance spectra were recorded during successive cycles of exposures to air and to the target A-VOC. Plasmonic dips were monitored, and their angular shift for a fixed wavelength of the incident light beam, or their red-shift for a fixed angle of incidence, were correlated to the interaction with the analyte.

In order to deeply understand the interaction of these materials with the A-VOC and to make a comparison between the two kind of gas sensors treated in this thesis, the LSPR and the PSPR

based, the same sensitive materials have been used as matrices to embed gold NPs and make the same tests performed in chapter 2.

3.1.1 Experimental

3.1.1.1 Sensitive material synthesis

A silica phenyl functionalized sol-gel solution, the TiO_2 and Au NPs were prepared as described in the appendixes A.2.11, A.2.7 and A.2.1, respectively.

3.1.1.2 Plasmonic grating structure

In this section is described the plasmonic crystal already presented by Brigo *et al.* [3[3]] (Fig. 3.1.2 a). A gold layer of 7 nm has been evaporated on a 37 nm of silver, also evaporated on a patterned organic-inorganic hybrid sol-gel SiO_2-based film, treated at 500°C (dielectric 1) and with period 500nm, as shown in the AFM image (Fig. 3.1.2 b).

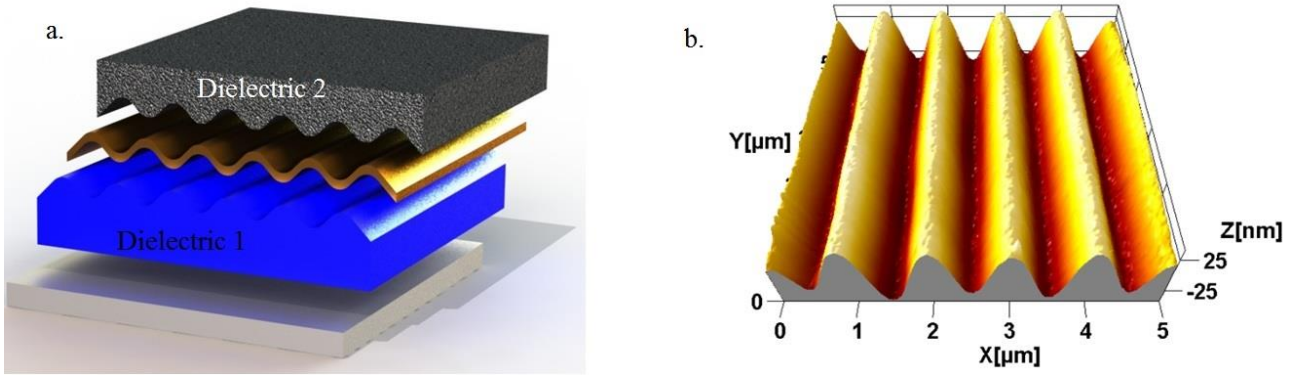

Fig. 3.1.2 - Structure of the plasmonic crystal (a.) and AFM image (b.).

3.1.1.3 Nanocomposite thin films synthesis

The starting solutions were prepared by mixing the methanol suspension of TiO_2 NPs or the SiO_2 phenyl functionalized solution with PVP-capped Au NPs in ethanol.

Samples	**Kind of support**
TiO_2-4%Au NPs	Flat
SiO_2-4%Au NPs	Flat
TiO_2	Metallic grating
SiO_2	Metallic grating

Tab. 3.1.1- Sensitive layers composition for the different plasmonic crystals fabricated.

All the thin films were deposited by spin coating at 3000rpm for 30 s on either SiO_2 and plasmonic gratings, as reported in Table 3.1.1, dried at 100°C for 5min and finally annealed in a muffle furnace at 300°C for 1 h in air.

3.1.1.4 Gas sensing measurements

Optical gas sensing tests were performed in reflection and with operating temperature (OT) set at room temperature and the sensor was tested for A-VOC, benzene 30ppm, toluene 30ppm and xylene (orto-, meta-, para- each 10ppm) balanced in air, with a flow rate of 0.4 L/min.

The sensor was probed in a direct illumination condition, when using a customized commercial cell (J. A. Woollam Co. Heat Cell) equipped with fixed input and output windows perpendicular to the incoming and reflected beams. In this case, measurements could be carried out at a single, fixed angle of incidence of 70°.

Reflectance spectra were recorded in dry air, after exposure to a controlled concentration of the analyte (30 ppm), and again in air atmosphere to regenerate the sensor. Such measurements were repeated for a number detection/regeneration cycles, each exposure step lasting few tens of minutes. The sensor was mounted in the null azimuth and in the azimuthally rotated configuration, choosing the wavelengths and incidence angles giving the best SPR response for each configuration.

At high azimuth an increase in sensitivity is theoretically expected [7]: in fact, it can be shown that if the SPP momentum k_{SP} changes of a small quantity δ, then the resonant transferred momentum $\frac{2\pi\, sin(\theta)}{\lambda}$ will change of a quantity $\frac{-k_{SP}\delta}{\sqrt{k_{SP}^2 - k_G^2(\sin\alpha)^2}}$ that increase in modulus with the azimuth α.

3.1.2 Results and discussion

3.1.2.1 Structural and optical properties of the sensitive film

From the absorption spectra (Fig. 3.1.3 a) is possible to verify the presence of gold NPs, for the TiO_2 based sample the Au plasmonic peak has higher absorbance and is more red-shifted than in the TEOS/PTMS based sample.

Moreover, for the TEOS/PTMS sample it is possible to note the presence of the phenyl groups from the relative peak at 270nm. This presence means that the heat treatment was not enough to cause their pyrolysis, and this is a key point for the development of this work being the phenyl groups responsible for the A-VOCs sensing mechanism.

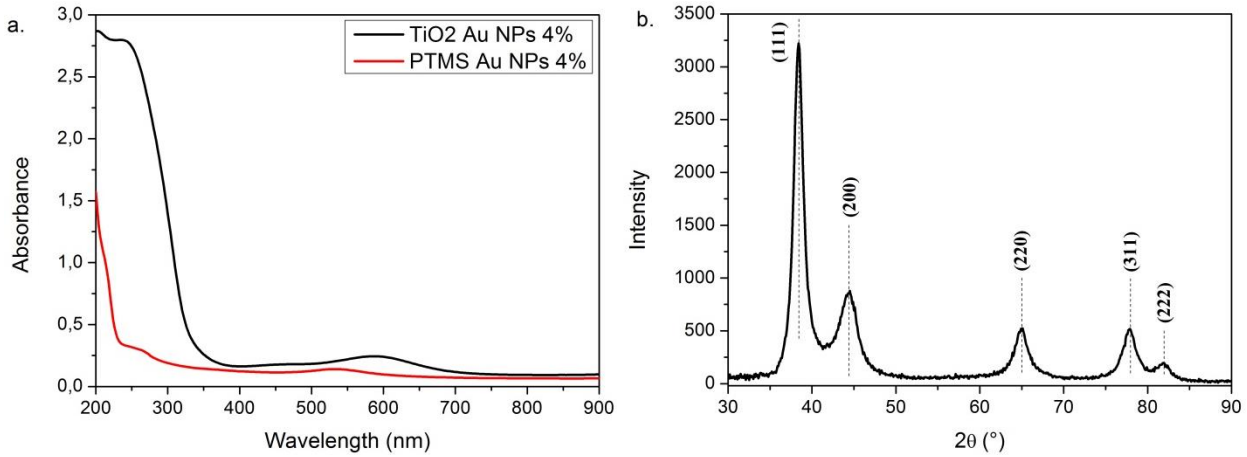

Fig. 3.1.3- Absorption spectra of the samples with TEOS- PTMS and TiO_2 with Au NPs (a.) XRD patterns of the Au NPs (b.).

The Figure 3.1.3 b. shows the XRD patterns of the Au NPs, used in the SiO_2 phenyl-functionalized and TiO_2 thin films, the theoretical diffraction peaks for crystalline Au are (JCPDS No. 040714) highlighted [8 9].

3.1.2.2 Structural and optical properties of the plasmonic grating

Refractive index and thickness of the dielectric 1 and 2 are reported in Table 3.1.2.

Name		***n* (λ=630nm)**	**Thickness**
Dielectric2	SiO_2	1.49	176 nm
	TiO_2	1.92	129 nm
Dielectric1		1.51	200 nm

Tab. 3.1.2- Thickness and refractive index (*n*) of the two dielectrics of the plasmonic crystal.

In Figure 3.1.4 are shown the experimental spectra compared with the simulated one, at an incident angle of 70° for both the plasmonic crystals fabricated. A set of dips can be seen, associated to the resonant coupling of the incident radiation with SPP modes supported by the thin film structure. The simulations produce very similar spectra for the two structures.

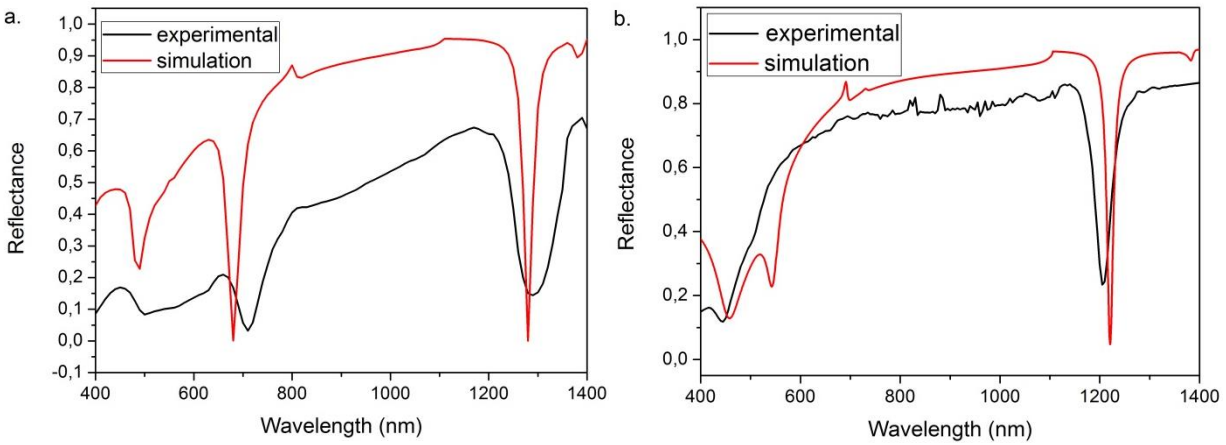

Fig. 3.1.4- Experimental reflection spectra, with overlaid the theoretical simulations, of the plasmonic crystals with sensitive layer TiO_2 (a) and SiO_2 (b), with front side illumination at 70°.

The plasmonic crystal with SiO_2 as sensitive layer should be more sensitive because of its symmetric configuration, as dielectric 1 and dielectric 2 have similar refractive index and thickness (see Table 3.1.2).

In this symmetric configuration the SPP waves propagating along the metal surface, are extremely sensitive to alterations of the surface optical properties. This makes them ideal probes to investigate variations induced by chemical reactions between the target gas and the surface itself.

3.1.2.3 PSPR based gas sensing test

Figure 3.1.5, 3.1.6 and 3.1.7 show the reflection spectra of the samples TiO_2 and SiO_2 phenyl functionalized when exposed to multiple air-A-VOC cycles, and it is possible to visualize the red-shift of the dips caused by the interaction of the plasmonic crystal with the gases.

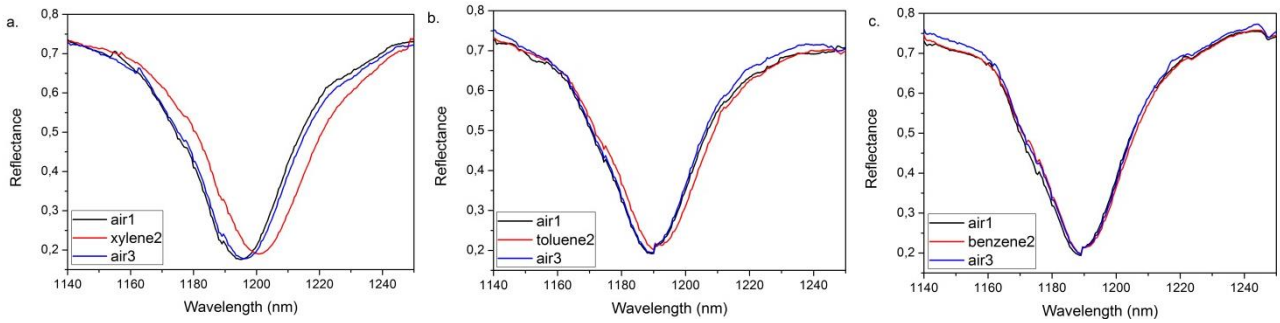

Fig. 3.1.5- Sensing test with xylene (a.), toluene (b.) and benzene (c.) on the plasmonic crystal with sensitive layer of SiO_2 phenyl functionalized (dip at 1190nm, long range).

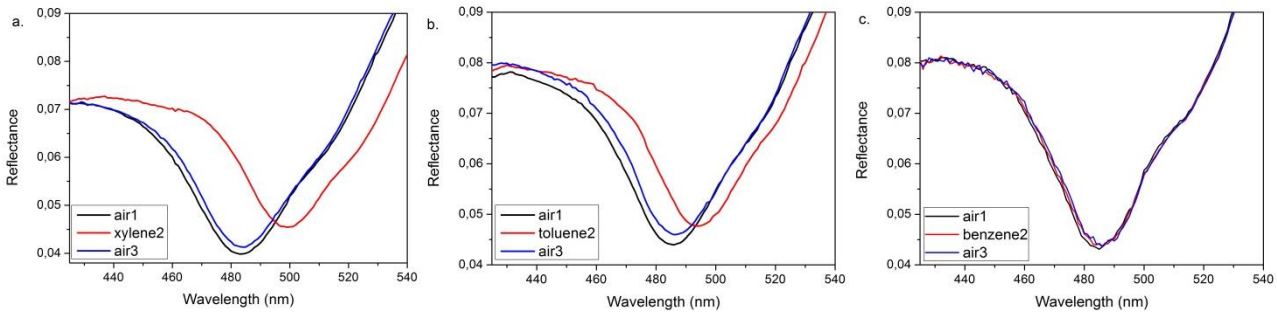

Fig. 3.1.6- Sensing test with xylene (a.), toluene (b.) and benzene (c.) on the plasmonic crystal with sensitive layer of TiO_2 (dip at 490nm, long range).

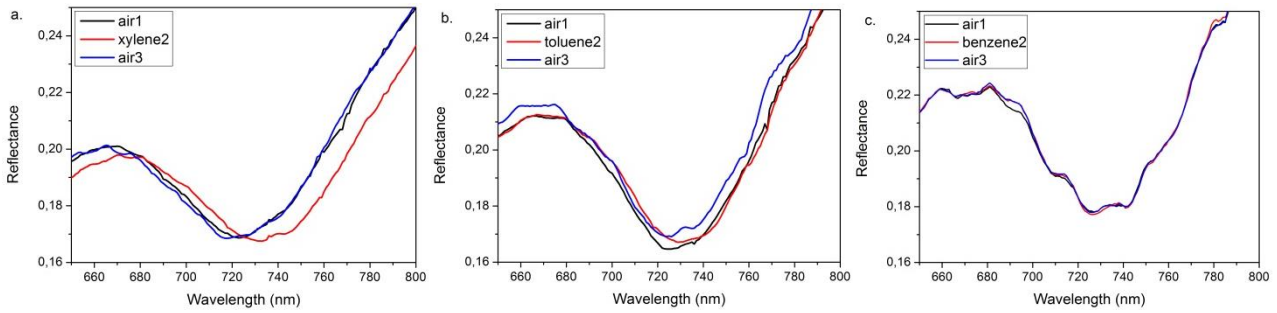

Fig. 3.1.7- Sensing test with xylene (a.), toluene (b.) and benzene (c.) on the plasmonic crystal with sensitive layer of TiO_2 phenyl functionalized (dip at 730nm, short range).

The shifts showed in Figure 3.1.5, 3.1.6 and 3.1.7 are summarized in Table 3.1.3, comparing the performances of the TiO_2 matrix with the one of the SiO_2 phenyl functionalized matrix.

	Refractive index	Shift of the dip 1250nm (long range) TiO_2	Shift of the dip 730nm (short range) TiO_2	Shift of the dip 490nm (long range) TiO_2	Shift of the dip (long range) 1190nm SiO_2
Xylene	1.4995	2nm	11nm	15nm	6 nm
Toluene	1.497	1nm	5nm	7nm	2.5 nm
Benzene	1.5011	/	/	/	0.5 nm

Table 3.1.3- Refractive index of the A-VOC and shift of the dip for the plasmonic crystals with dielectrics TiO_2 and SiO_2, in air and A-VOC flux.

3.1.2.4 LSPR based gas sensing test

Also with the LSPR based technique both the films, TiO_2-Au NPs and SiO_2-Au NPs, are sensitive to the A-VOC. The Au SPR peak during gas exposure undergoes a red shift and a strong increase in absorbance (Fig. 3.1.8). This effect can be related to the interaction π-π coupling, between the ring of the TEOS-PTMS matrix and the one of the gas target and in the case of the TiO_2 matrix the Ti^{4+}•••π-electrons of the A-VOC ring interaction.

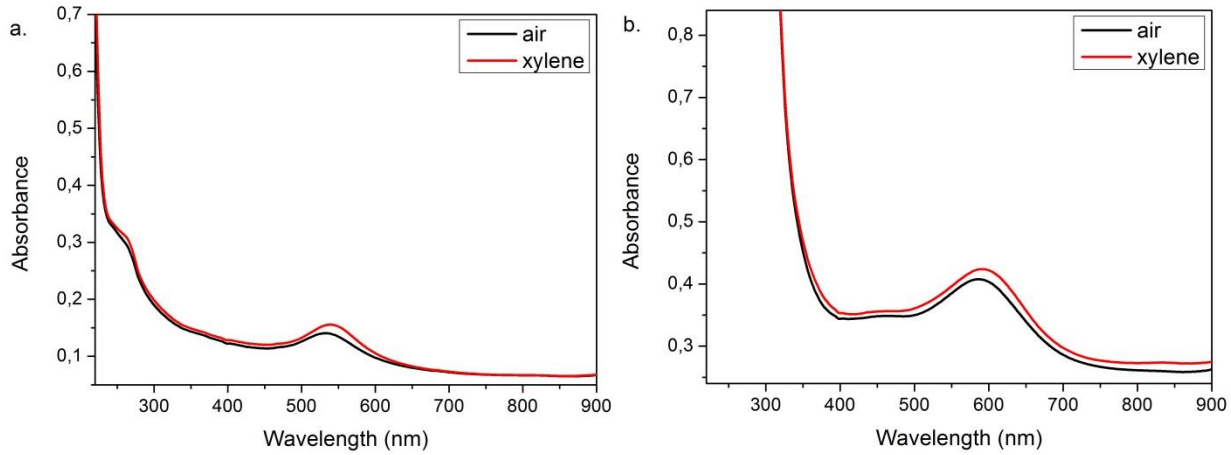

Fig. 3.1.8- Scan measurement of the gas sensing test in air flux and in xylene on the samples TEOS/PTMS (a.) TiO_2 (b.) with Au NPs.

From the OAC curves (Fig. 3.1.9) and dynamic measurements (Fig. 3.1.10-3.1.12) it is possible to note that the sensitivity towards all the three gases is good, and also that the variation in Absorbance is higher increasing the number of substituents (-CH_3 groups).

Moreover the sensitivity of the TiO_2 matrix is higher than the one of the SiO_2 matrix functionalized with phenyl groups, probably because the semiconductivity enhances the interaction mechanism that will be now exposed. However both the sensitivity of the matrixes towards the A-VOC are relevant.

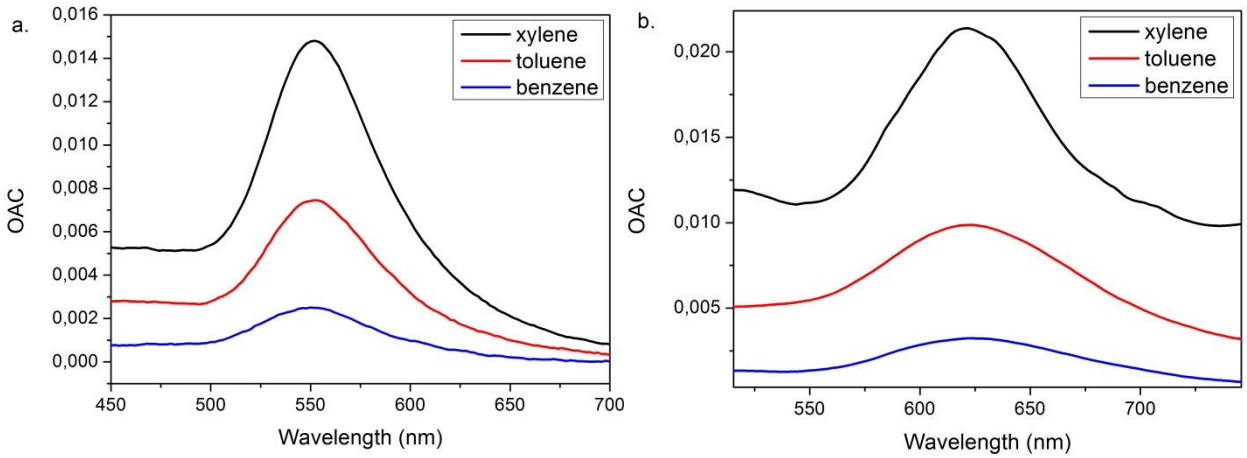

Fig. 3.1.9- OAC (Optical absorption change) curve in xylene, toluene and benzene flux for the sample TEOS-PTMS (a.) and TiO_2 (b.) -Au NPs.

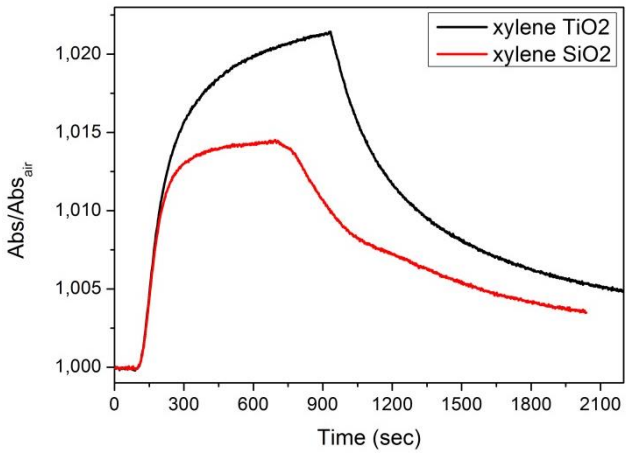

Fig. 3.1.10- Gas sensing test towards xylene at room temperature, comparing the performances of the TiO_2 matrix with the one of the TEOS-PTMS matrix with Au NPs at, respectively, λ 620 nm and 552 nm.

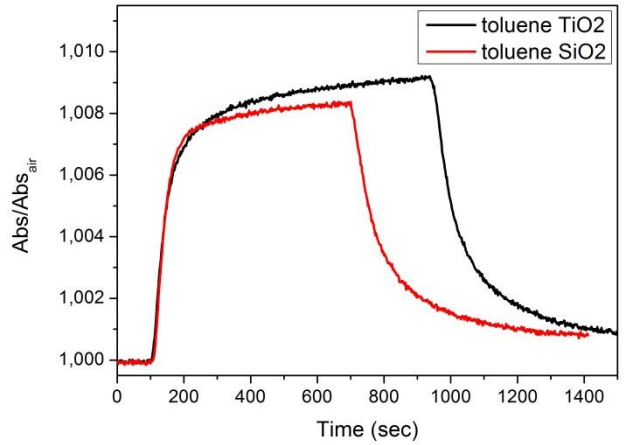

Fig. 3.1.11- Gas sensing test towards toluene at room temperature, comparing the performances of the TiO_2 matrix with the one of the TEOS-PTMS matrix with Au NPs at, respectively, λ 620 nm and 552 nm.

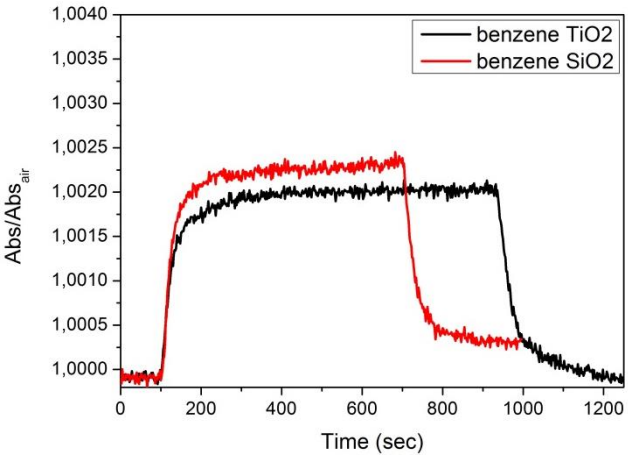

Fig. 3.1.12- Gas sensing test towards benzene at room temperature, comparing the performances of the TiO_2 matrix with the one of the TEOS-PTMS matrix with Au NPs at, respectively, λ 620 nm and 552 nm.

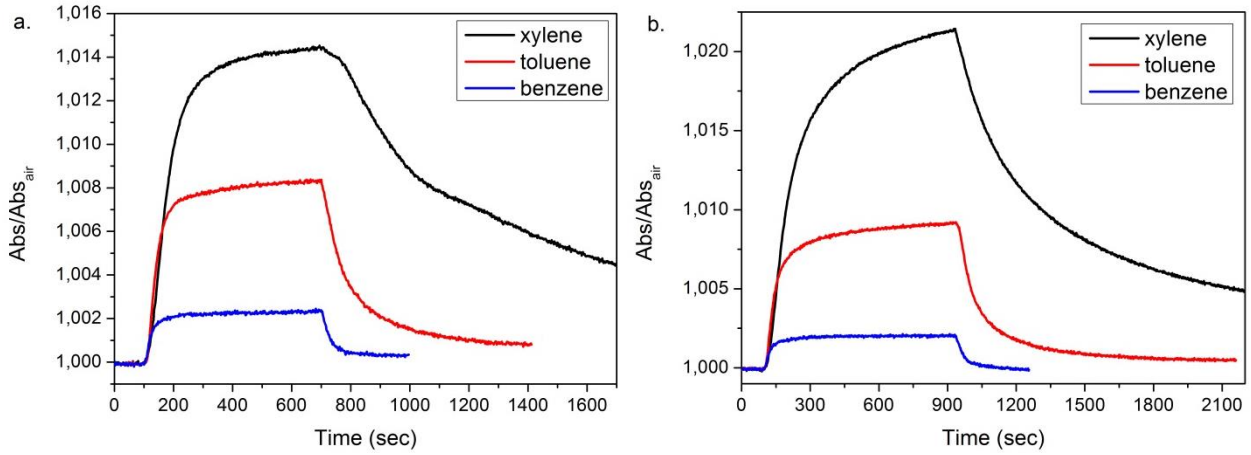

Fig. 3.1.13- Gas sensing test on the TEOS-PTMS Au NPs (a.) and on the TiO_2 Au NPs (b.) samples at room temperature, comparing the performances towards the three different Aromatic VOC at λ 552 and 620nm, respectively.

From XPS measurements (Fig. 3.1.14) it is possible to interpret the scan measurement (Fig. 3.1.8) and the OAC curves (Fig. 3.1.9). The XPS measurement shows that the interaction between the A-VOC, reducing gases, and the TiO_2 leads to an injection of electrons, so the Ti^{4+} is transformed in Ti^{3+}, and in Figure 3.1.14 is highlighted the increase in the number of Ti^{3+} after the interaction with xylene.

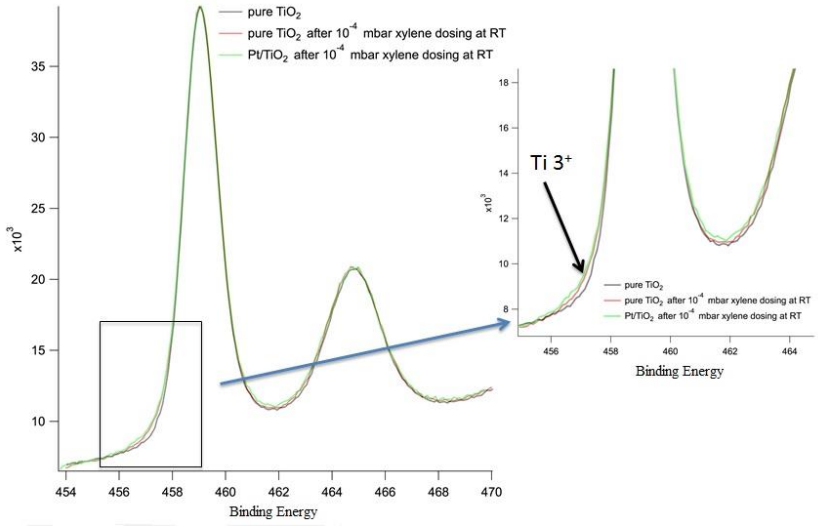

Fig. 3.1.14- High resolution XPS scanning spectra in function of the binding energies, at room temperature in vacuum and after xylene exposure.

The interaction between the oxide matrixes and the A-VOC involves the reaction between the A-VOC molecule and the adsorbed oxygen [10], as reported in reaction (1), (2) and (3), for benzene, toluene and xylene respectively [11].

$$C_6H_6 + 7.5\ O_2 \rightarrow 6CO_2 + 3H_2O \qquad (1)$$

with the injection of electrons (30 e^- from the benzene molecule) into the matrix:

$$7.5\ O_2 + \ 30\ H^+ + \ 30\ e^- \rightarrow \ 15\ H_2O$$

$$C_7H_8 + 9O_2 \rightarrow 7CO_2 + 4\ H_2O \qquad (2)$$

with the injection of electrons (36 e^- from the toluene molecule) into the matrix:

$$9\ O_2 + \ 36\ H^+ + \ 36\ e^- \rightarrow \ 18\ H_2O$$

$$C_8H_{10} + 10.5O_2 \rightarrow 8CO_2 + 5\ H_2O \qquad (3)$$

with the injection of electrons (42 e^- from the xylene molecule) into the matrix:

$$10.5\ O_2 + \ 42\ H^+ + \ 42\ e^- \rightarrow \ 21\ H_2O$$

Pecharromán, as already explained in Appendix A.4, reports that the absorbance at the SPR position is proportional to the electron density, this is in agreement with the strong absorbance increase of the plasmon band in A-VOC flux.

From the XPS results, the OAC curves and the scan measurement it is possible to say that the blue shift, which is a smaller effect of the electrons injection than the increase in absorbance, already mentioned, is completely overcome by the red shift.

The red shift may be due to an increase of refractive index of the overall thin film caused by the substitution of the air, whose refractive index is ~1 [12], with A-VOC molecules filling the pores of the oxide matrix, which have a higher refractive index (n=1,497 toluene, 1,4995 xylene and 1,5011 benzene).

From the PSPR measurements, it is possible to see that there is a strong red shift of the plasmonic dip and it should not depend on the *n* of the A-VOC because it does not follow the *n* increase (see Tab. 3.3.1).

Moreover, the mechanism involved works for both an insulating matrix functionalized with phenyl ring and for a semiconducting matrix. This implies that the shift monitored is not because of an electrons injection/subtraction, because with an insulating material there is no transport of electrons, but probably to an interaction between the π electrons of the target gases and the surface exposed by the material. In the first case it involves another ring and in the second case the Ti-O-Ti structure, with in addiction the effect of having a semiconducting matrix.

A π-conjugated system occurs when π systems are "linked together", meaning that there is a continuous array of "p" orbitals that can align to produce a π bonding overlap along the whole system [13]. This case can fit a π-π stacking configuration [14 15], because it involves an overlapping of "p" orbitals, moreover, this expansion of the π conjugation from the gas ring towards the phenyl group of the matrix can cause a red-shift in the absorption spectrum [16].

The TiO_2 based plasmonic crystal is more sensitive to the aromatic molecules because of its semiconducting property which makes the propagating polariton more involved in the interaction mechanism. The XPS measurements reported in Figure 3.1.14, relative to the interaction xylene TiO_2, show a reduction of the semiconducting matrix, Ti^{4+} to Ti^{3+}. This implies a blue-shift but is overcome by the red shift due to the Ti^{4+}•••π-electron interaction.

Moreover, it is possible to note, as already reported in chapter 2.7, that the shift increases at the increasing of the number of substituent in the A-VOC molecules: benzene, and substituted benzene, toluene (one CH_3) and xylene (two CH_3).

Ringer [17] said that all substituted sandwich dimers have a smaller interaction energy than sandwich benzene dimer, this is why the xylene binds more strongly than toluene and toluene than benzene to the phenyl group and this is evident from the gas sensing measurement (Fig. 3.1.5-7 and 3.1.13).

3.1.3 Conclusions

In the present paper are investigated the performances of two plasmonic crystal, one insulating and functionalized with phenyl groups and the other semiconducting, towards 30 ppm of benzene, toluene and orto-, meta-, para- xylene.

Both the types of nanocomposite, with both the sensing technique, LSPR and PSPR based, showed good optical response to the investigated A-VOC with reversible dynamics, but the more efficient material resulted to be the semiconducting one.

The mechanism involved in the sensing with A-VOC is linked to the π-electrons interaction with the two types of matrix.

References

[1] Lan Jia ; Yu Wu ; Baicheng Yao ; Feiya Yang ; Yunjiang Rao, A sensitivity enhanced gas sensor based on carbon nanotubes around microfiber, Proc. SPIE 8351, Third Asia Pacific Optical Sensors Conference, 835120 (January 31, 2012); doi:10.1117/12.916028.

[2] L. Brigo, M. Cittadini, L. Artiglia, G. A. Rizzi, G. Granozzi, M. Guglielmi, A. Martucci, G. Brusatin, Xylene sensing properties of aryl-bridged polysilsesquioxane thin films coupled to gold nanoparticles, J. Mater. Chem. C 2013, Volume 1**,** 4252-4260.

[3] L. Brigo, E. Gazzola, M. Cittadini, P. Zilio, G. Zacco, F. Romanato, A. Martucci, M. Guglielmi, G. Brusatin, Short and long range surface plasmon polariton waveguides for xylene sensing, Nanotechnology 2013, Volume 24, 155502 (10pp).

[4] S. Zampolli, I. Elmi, F. Ahmed, M. Passini, G.C. Cardinali, S. Nicoletti, L. Dori, An electronic nose based on solid state sensor arrays for low-cost indoor air quality monitoring applications, Sens. Actuators B 2004, Volume 101, 39-46.

[5] Zeng Wen, Liu Tian-mo, Gas-sensing properties of SnO_2–TiO_2-based sensor for volatile organic compound gas and its sensing mechanism, Physica B 2010, Volume 405, 1345–1348.

[6] Dror Sarid, Long-Range Surface-Plasma Waves on Very Thin Metal Films, Phys. Rev. Lett. 47, 1927 (1981).

[7] F. Romanato, K. H. Lee, H. K. Kang, G. Ruffato, and C. C. Wong, Sensitivity enhancement in grating coupled surface plasmon resonance by azimuthal control, Optics Express 2009, Volume 17, Issue 14, 12145-12154

[8] D. Buso, G. Busato, M. Guglielmi, A. Martucci, V. Bello, G. Mattei, P. Mazzoldi, M. Post, Selective optical detection of H_2 and CO with SiO_2 sol gel films containing NiO and Au nanoparticles, Nanotechnology 2007, Volume 18, 475505 (1-7).

[9] D. Buso, M. Guglielmi, A. Martucci, G. Mattei, P. Mazzoldi, C. Sada, M. Post, Growth of cookie-like Au/NiO nanoparticles in SiO_2 sol-gel films and their optical gas sensing properties, Crystal Growth and Design 2008, Volume 8, Issue 2, 744-749.

[10] Yi Zeng, Tong Zhang, LijieWang, Minghui Kang, Huitao Fan, RuiWang, Yuan He, Enhanced toluene sensing characteristics of TiO2-doped flowerlike ZnO nanostructures, Sens. Act. B 2009, Volume 14, 73-78.

[11] Department of Civil and Environmental Engineering, Helsinki University of Technology, http://civil.tkk.fi

[12] Bengt Edlén, The Refractive Index of Air, *Metrologia* 1966, Volume 2, Issue 2, 71

[13] http://www.chem.ucalgary.ca/courses/350/Carey5th/Ch10/ch10-1-1.html

[14] Chunxue Yuan, Shohei Saito, Cristopher Camacho, Stephan Irle, Ichiro Hisaki, Shigehiro Yamaguchi, A π-Conjugated System with Flexibility and Rigidity That Shows Environment-Dependent RGB Luminescence, J. Am. Chem. Soc. 2013, Volume 135, Issue 24, 8842–8845.

[15] Jean-Luc Brédas, David Beljonne, Veaceslav Coropceanu, Jerome Cornil, Charge-Transfer and Energy-Transfer Processes in π-Conjugated Oligomers and Polymers: A Molecular Picture, Chem. Rev. 2004, Volume 104, 4971-5003.

[16] Kohjiro Hara, Tadatake Sato, Ryuzi Katoh, Akihiro Furube, Yasuyo Ohga, Akira Shinpo, Sadaharu Suga, Kazuhiro Sayama, Hideki Sugihara, Hironori Arakawa, Molecular Design of Coumarin Dyes for Efficient Dye-Sensitized Solar Cells, J. Phys. Chem. B 2003, Volume 107, 597-606.

[17] A. L. Ringer, M. O. Sinnokrot, R. P. Lively, C. D. Sherrill, The Effect of Multiple Substituents On Sandwich and T-Shaped π-π Interactions, Chem. Eur. J. 2006, Volume 12, 3821-3828.

3.2 Ethanol, Methanol and Isopropanol gas sensing with SPP

In the previous chapter we used a plasmonic grating as platform for sensing A-VOC deposting on it two different kind of sensitive material (porous SiO_2 functionalized with phenyl groups, or nanocrystalline TiO_2 porous film). In this chapter we use the same plasmonic grating coated with nanocrystalline TiO_2 porous film for other ethanol, methanol or isopropanol vapors which will be indicated as Volatile Organic Compounds (VOCs). In order to catalyze the reaction of the VOCs, Pt NPs have been dispersed inside the TiO_2 films. At the end we will also compare the same sensitive material both using propagating surface plasmon and localized surface plasmon as optical transducing platform.

Titanium oxide is known for its many properties such as the photo-catalysis and it used in the sensing of automotive exhaust gases [1 2], in the electric and optical sensing of hydrogen [3], carbon monoxide [4] and VOC [5 6 1].

TiO_2 layer has already been used as sensitive material for VOC in SPR sensor [1], but in such study it was used a prism coupling configuration, here we will use a grating coupling [7 8 9 10].

3.2.1 Experimental

3.2.1.1 Nanoparticles synthesis

The TiO_2 and Pt NPs were prepared as described in the appendixes A.2.11, A.2.7 and A.2.6, respectively.

3.2.1.2 Nanocomposite thin films synthesis

The starting solutions were prepared by mixing the methanol suspension of TiO_2 NPs with PVP-capped Au and/or Pt NPs in ethanol, with different molar percentage (Tab. 3.2.1).

Samples	Kind of support	Transducing platform
TiO_2	Plasmonic grating	SPP
TiO_2-4%Pt NPs	Plasmonic Grating	SPP
TiO_2-4%Au NPs	Flat glass	LSPR
TiO_2-2%Au-2%Pt NPs	Flat glass	LSPR

Tab. 3.2.1- Sensitive layers composition for the different sensing platforms.

All the thin films were deposited by spin coating at 3000 rpm for 30 s on either SiO_2 and plasmonic gratings (already described in the section 3.1.1.2) as dielectric 2 (Fig. 1 chapter 3.1), dried at 100°C for 5 min and finally annealed in a muffle furnace at 300°C for 1 h in air. The final thickness, measured by spectroscopic ellipsometry, was about 100 nm and the refractive index was around 1.9 at 630 nm.

3.2.1.3 Gas sensing measurements

The tests have been performed at RT, bubbling ethanol, methanol and isopropanol (Fig. 3.2.1), in a nitrogen flux (N_2) with a flow rate of 0.4 L/min, therefore the concentration can be estimated to be about 3000ppm [11].

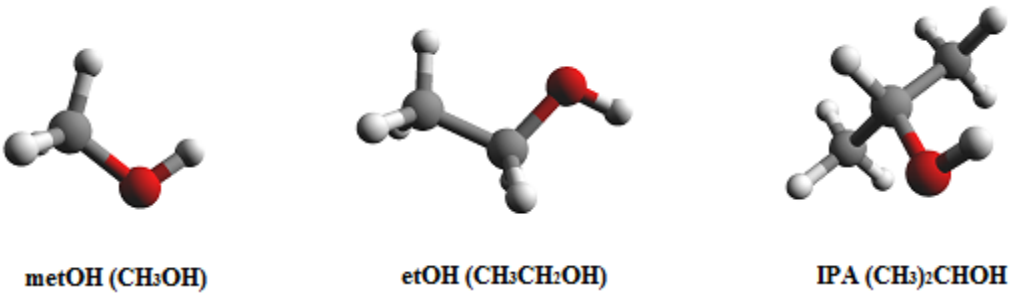

Fig. 3.2.1- 3D representation of the VOC molecules tested (simulated with the Argus Lab software). In grey the carbon atoms, in white the hydrogen atoms and in red the oxygen atoms.

3.2.2 Results and discussion

3.2.2.1 Structural and optical properties of the sensitive film

In Figure 3.2.2 the absorption spectra of TiO_2 nanocomposite films containing gold and/or platinum NPs are shown. From the absorption spectra it is possible to notice the plasmon peak of gold NPs with diameter of 15 nm at 560 nm, while the typical absorption spectrum of platinum NPs with diameter of 10 nm is reported in Figure 3.2.3.

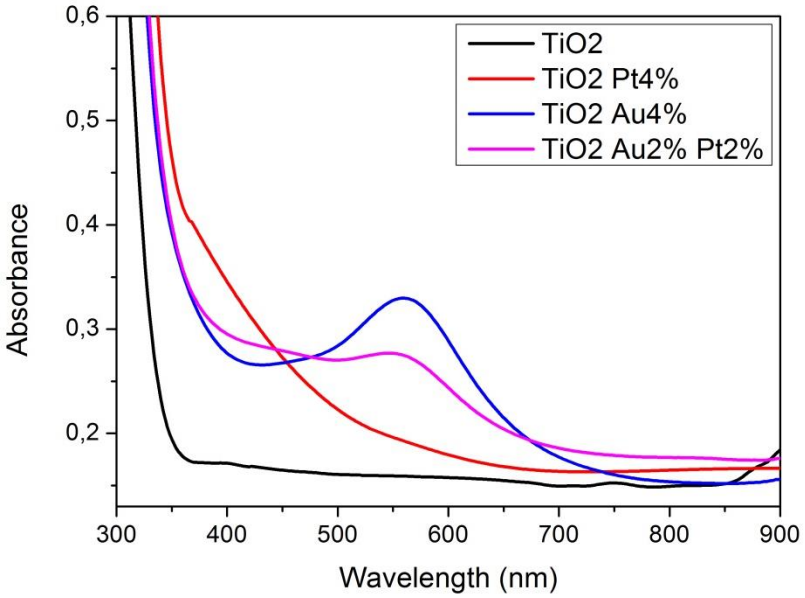

Fig. 3.2.2- Absorption spectra of the films with TiO_2, Au and/or Pt NPs deposited on silica glass.

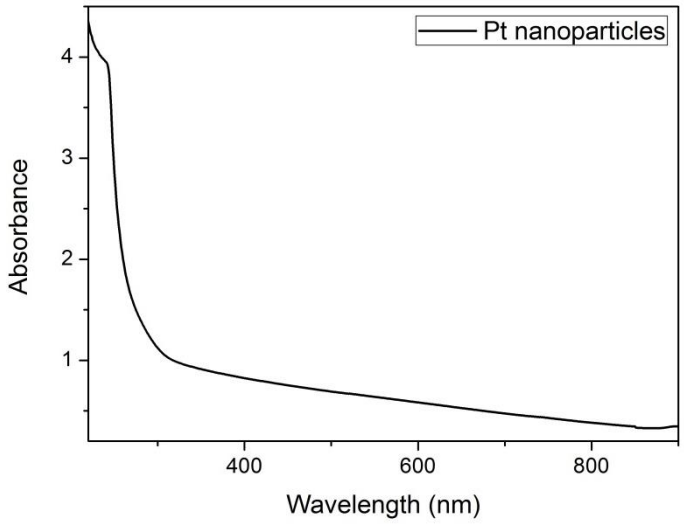

Fig. 3.2.3- Absorption spectrum of Platinum NPs dispersed in methanol.

In Figure 3.2.4 are presented the XRD patterns of the TiO_2 based nanocomposite containing gold and/or platinum NPs. All the samples have been characterized to check their crystallinity and crystal dimension. It is possible to identify the typical peaks of cubic Pt (JCPDS No. 04-0802): (100) and (200) reflections at about 39.8° and 46.2°, confirming the crystallinity of Pt NPs.

Finally the diffraction peaks of cubic Au NPs at about 38.2° and 44.4° corresponding to (111) and (200) planes reflections (JCPDS No.04-0784) are clearly identified.

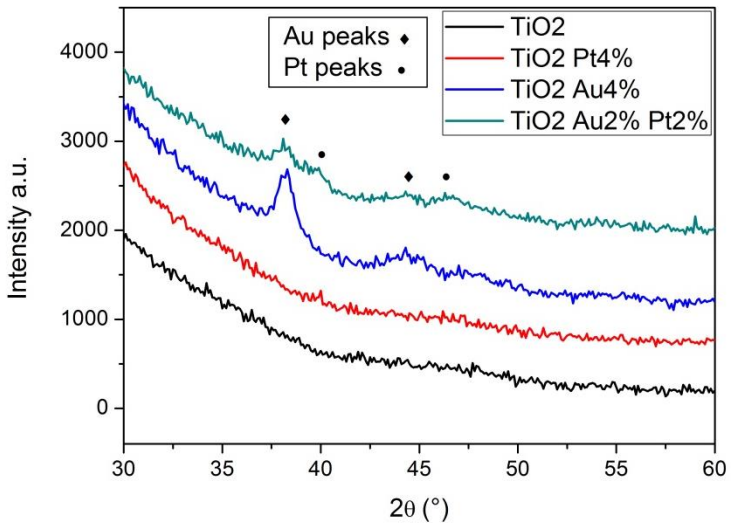

Fig. 3.2.4- XRD patterns of the films with TiO_2, Au and/or Pt NPs.

This type of films has already been deeply characterized by Della Gaspera *et al.* [12], therefore this work will be focused on the plasmonic crystal structure and on the VOC sensing behaviour.

3.2.2.2 Structural and optical properties of the plasmonic grating

On the plasmonic gratings it was deposited a nanocomposite film (dielectric 2) with the composition and structure already reported in the section *3.3.1.2*. Refractive index and thickness of the dielectric 1 and 2 are reported in Table 3.2.2.

Name		*n* (λ=630nm)	Thickness
Dielectric 2	TiO_2-Pt	1.93	81 nm
	TiO_2	1.92	129 nm
Dielectric 1		1.51	200 nm

Tab. 3.2.2- Thickness and refractive index (*n*) of the two dielectrics of the plasmonic crystal.

The experimental spectra compared with the simulated one, at an incident angle of 70° are reported in Figure 3.2.5. A set of dips can be seen, associated to the resonant coupling of the incident radiation with SPP modes supported by the thin-film structure. The simulations produce very similar spectra for the two structures, because the effective refractive indexes of TiO_2 and TiO_2-Pt are only slightly different, and they reproduce quite well the spectral position of the dips.

However, the dips look much more flattened when the Pt NPs are embedded in the sensitive layer, meaning that the energy is re-irradiated. In the performed simulations the TiO_2 is represented by a uniform effective material, thus not keeping into account effects produced by the NPs.

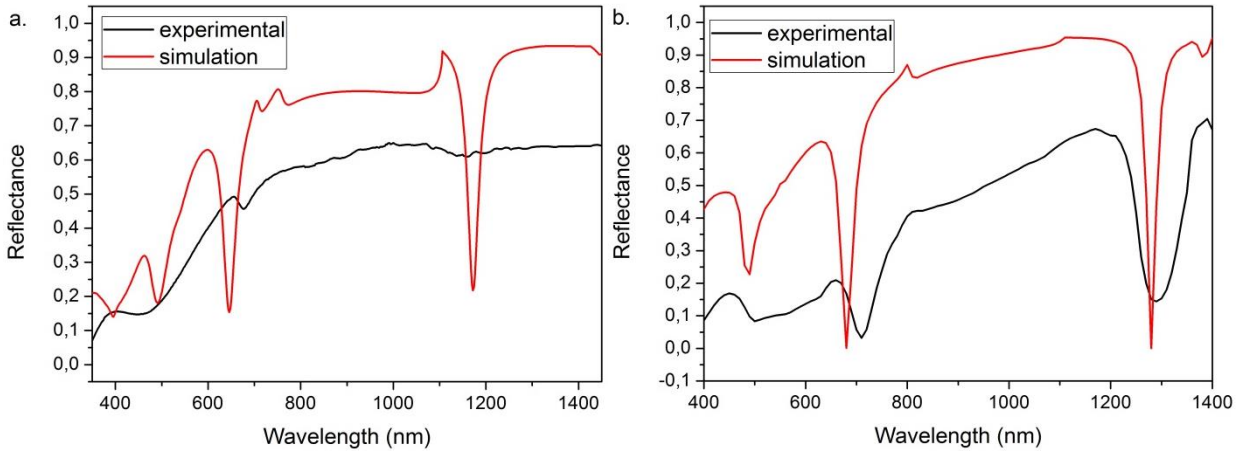

Fig. 3.2.5- Experimental reflection spectra, with overlaid the theoretical simulations, of the plasmonic crystals with sensitive layer TiO_2-4%Pt (a.) and TiO_2 (b.) with front side illumination at 70°, respectively.

3.2.2.3 PSPR based gas sensing test

Figure 3.2.6 to 3.2.8 show the reflection spectra of the samples TiO_2 and TiO_2 - 4% Pt when exposed to multiple N_2-VOC cycles, and it is possible to notice the red-shift of the dips caused by the interaction of the plasmonic crystal with the gases.

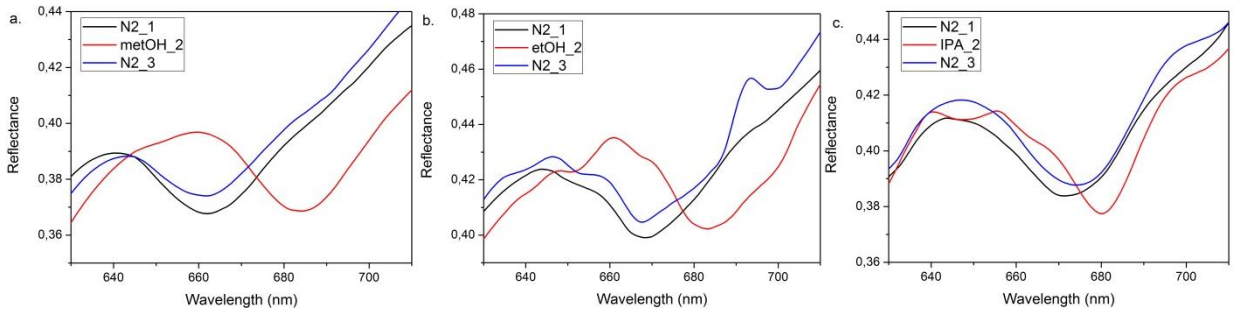

Fig. 3.2.6- Sensing test with methanol (a.), ethanol (b.) and isopropanol (c.) on the plasmonic crystal with sensitive layer of TiO_2-Pt (dip at 660 nm).

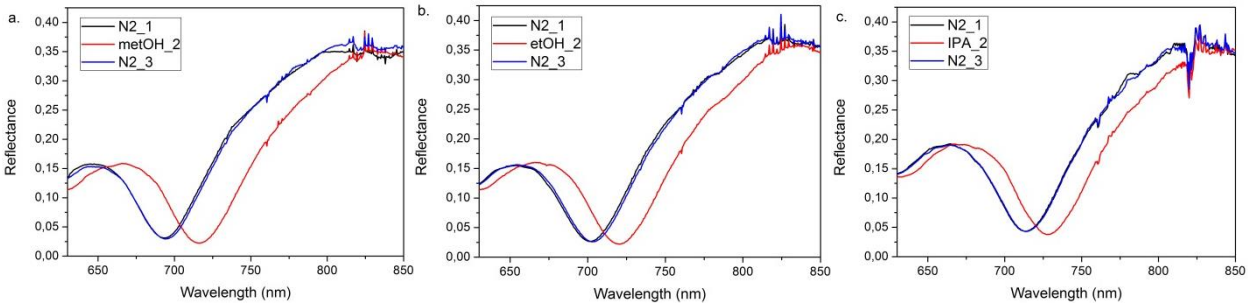

Fig. 3.2.7- Sensing test with methanol (a.), ethanol (b.) and isopropanol (c.) on the plasmonic crystal with sensitive layer of TiO_2 (dip at 700 nm).

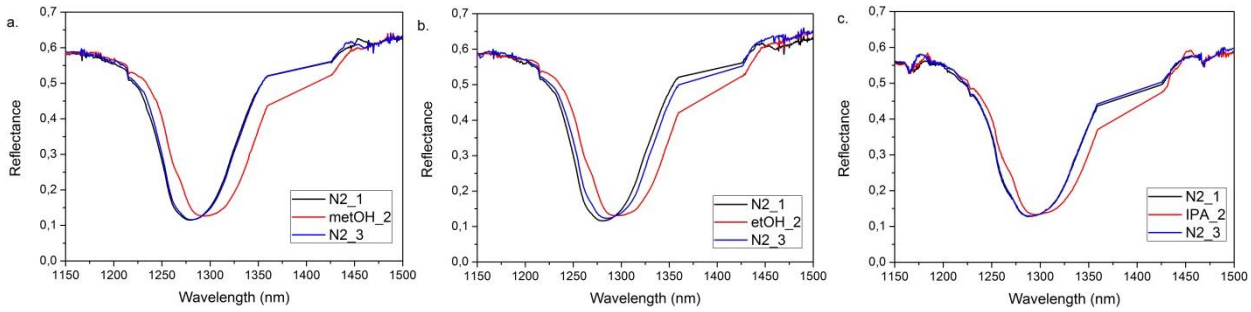

Fig. 3.2.8- Sensing test with methanol (a.), ethanol (b.) and isopropanol (c.) on the plasmonic crystal with sensitive layer of TiO_2 (dip at 1300 nm).

The shifts showed in Figure 3.2.6 to 3.2.8 are summarized in Table 3.2.3, and compared. It is possible to notice that the biggest shift is obtained with methanol and the smallest with isopropanol, for both the crystals.

	n	***n* film TiO_2 at 630nm (N_2)**	**TiO_2 shift dip1**	**TiO_2 shift dip2**	**TiO_2-Pt shift dip**
MetOH	1.33	1,9764	23 nm	15 nm	25 nm
EtOH	1.36	1,9906	18.5 nm	12.5 nm	14 nm
IPA	1.37	2,008	14.5 nm	6.5 nm	7 nm

Tab. 3.2.3- Shift of the dip for the plasmonic crystals with dielectrics TiO_2-4%Pt and TiO_2 respectively, in nitrogen and methanol, ethanol and isopropanol flux with their refractive index measured at 630nm.

3.2.2.4 LSPR based gas sensing test

Figure 3.2.9 shows the absorption spectra of the sample TiO_2-2%Au-2%Pt when exposed to IPA 3000 ppm in N_2: it is possible to notice the gas effect.

The parameter use to define the sample sensitivity is the Optical Absorbance Change (OAC), defined as the difference between absorbance during gas exposure and absorbance in air ($OAC=Abs_{Gas}-Abs_{Air}$) and it is reported in the insets in Figure 3.2.9.

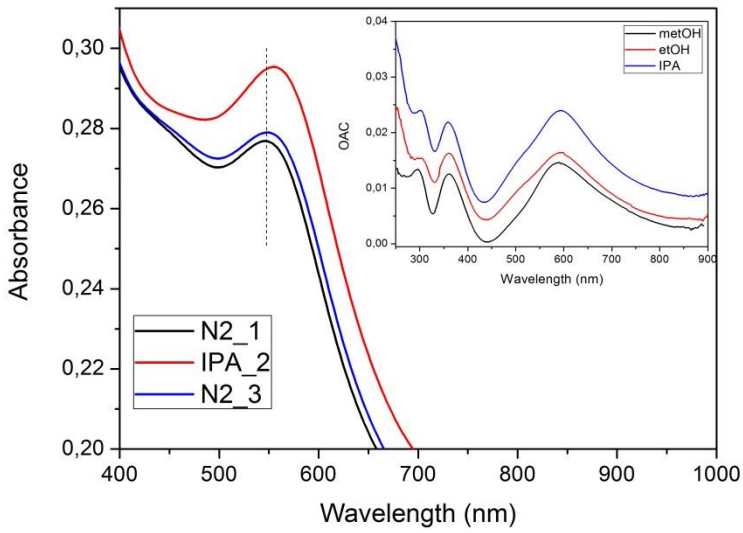

Fig. 3.2.9- Gas sensing test (scan mode) in N_2 flux and in bubbled isopropanol on the sample TiO_2 - 2% Au -2%Pt NPs; in the inset is reported the comparison of the OAC curves for the three different VOC.

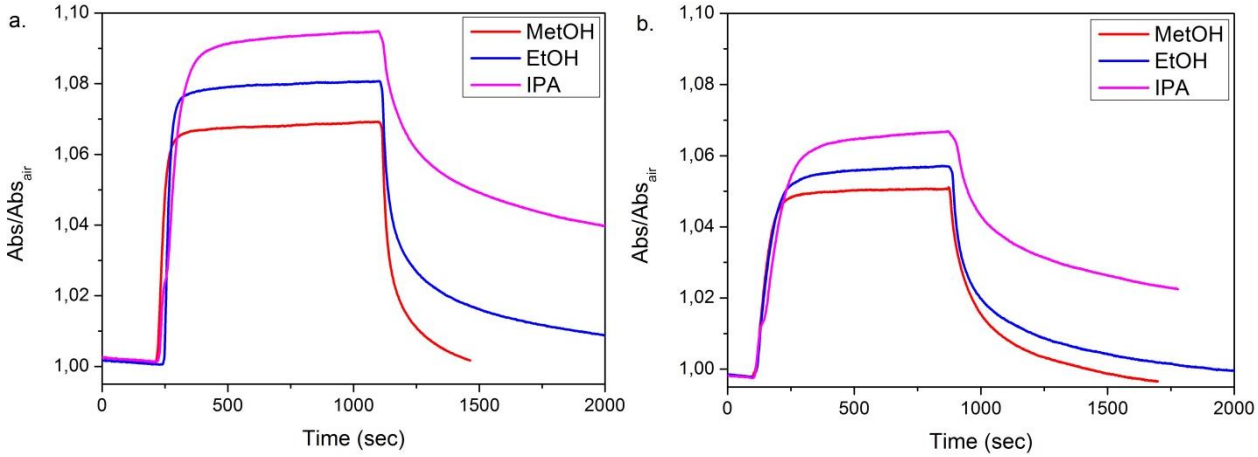

Fig. 3.2.10- Gas sensing test (dynamic mode) with bubbled ethanol, methanol and isopropanol on the sample TiO_2 - 2% Au - 2% Pt NPs at 590nm (a.) and TiO_2 - 4% Au NPs at 596nm (b.).

From Figure 3.2.10 it is possible to notice that isopropanol, like ethanol and methanol, induces a red shift of the Au LSPR peak, probably due to an increase of the refractive index, *n*, of the film.

The increase of refractive index of the overall thin film is due to the substitution of the air, whose refractive index is ~1 [13], with VOC molecules filling the pores of the oxide matrix, which have a higher refractive index (Tab. 3.2.3). Together with the red shit there is also a strong increase in the SPR absorption, which can be explained by the XPS results (Fig. 3.2.11).

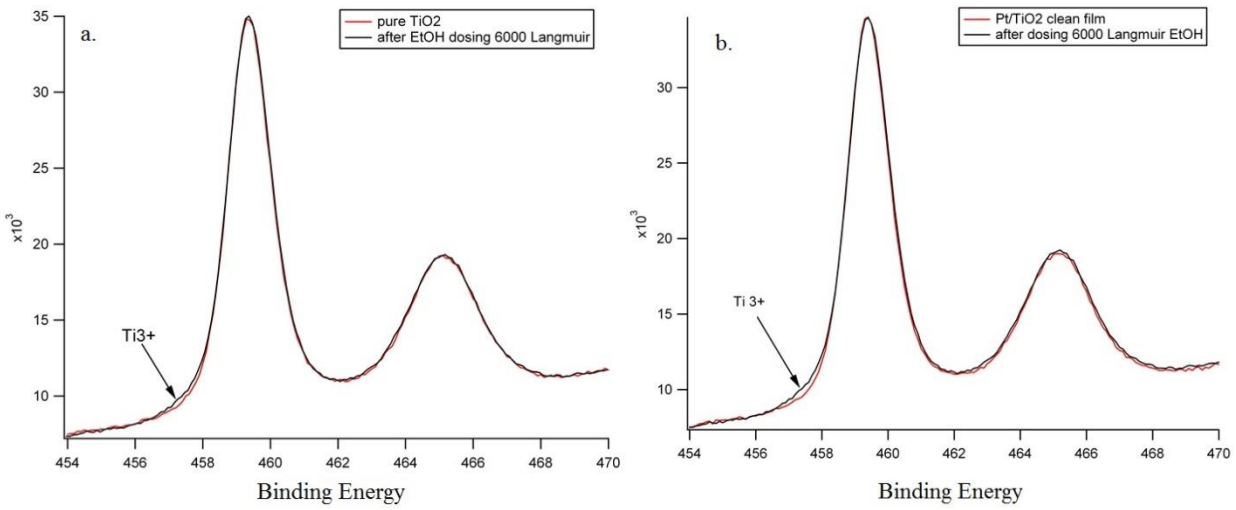

Fig. 3.2.11- High resolution XPS scanning spectra in function of the binding energies, at room temperature in vacuum and after ethanol exposure for TiO_2 (a.) and TiO_2 Pt (b.).

From the XPS results (Fig. 3.2.11) it is possible to note that there is an interaction between the TiO_2 and the ethanol molecules, which involves a reduction of Ti^{4+} to Ti^{3+}. This involves an injection of electrons which causes the strong increase of the SPR, presented in Figure 3.2.9, and a blue shift. However, again from Figure 3.2.9, it is possible to say that this blue shift is completely overcome by the red shift due to the increase of refractive index of the thin film.

This electrons injection justifies the increase of the absorption shown in the inset of Figure 3.2.9 from methanol to isopropanol, and this behavior is the same for all the tested samples; reaction (1) reports generally the VOC oxidation and the involved electrons injection [14].

$$VOC + O^{2-} \rightarrow VOC\text{-}O + 2e^{-} \quad (1)$$

Moreover, the VOC oxidation, as shown in Figure 3.2.10 b and 3.2.11 b, is catalyzed by Pt.

Yoo *et al.* [15] found out that Pt has a catalytic activity towards the VOC oxidation. This gives explanation to the results obtained with the XPS measurement (Fig. 3.2.11) and to the results obtained with the dynamic test, which showed improved performances in presence of Pt and an higher increase in absorbance (Fig. 3.2.10 a and b).

The oxidation of VOC such as methanol apparently creates clean active sites on the Pt, and thus, the efficient dehydrogenation of the catalyst is continued, which is the so-called proton spillover effect.

A reaction scheme for the methanol oxidation on Pt/TiO_2 is presented in reaction 2-9. The VOC molecules tend to bind to the Pt surface and here we have the deprotonation of the VOC and the proton produced will bind to another site on the Pt surface. This creates clean active sites on the Pt, and there is an efficient and continued dehydrogenation of the catalyst. The continuous increment in the number of clean active reaction sites of Pt promotes the transport of protons, produced on the Pt during the methanol oxidation, into the TiO_2 matrix.

$$Pt\text{-}\ CH_3OH \rightarrow Pt\text{-}CH_2OH + Pt\text{-}H \quad (2)$$

$$Pt\text{-}H \rightarrow Pt + nH_xTiO_2 \quad (3)$$

$$nH_xTiO_2 \rightarrow nTiO_2 + H^+ + e^- \quad (4)$$

$$Pt\text{-}\ CH_2OH + OH_{ads} \rightarrow CHOH + H_2O + Pt \quad (5)$$

$$Pt\text{-}\ CHOH \rightarrow Pt\text{-}COH + Pt\text{-}H \quad (6)$$

$$Pt\text{-}H \rightarrow Pt + nH_xTiO_2 \quad (7)$$

$$nH_xTiO_2 \rightarrow nTiO_2 + H^+ + e^- \quad (8)$$

$$Pt\text{-}\ COH + OH_{ads} \rightarrow CO_2 + H_2O + Pt \quad (9)$$

This reaction scheme shows how TiO_2 injects an electron into the gold NPs, increasing its SPR absorbance.

All these consideration are referred also to the PSPR case. The strong red shifts, reported in Table 3.2.3, do not follow the increase of *n* of the VOC filling the thin film's pores. This, together with the XPS results (Fig. 3.2.11) lead to the conclusion that the red shifted obtained is the combination between the blue shift due to the electrons injection (reaction 1) and the red shift due to the value of *n* of the VOC and the shift is that strong because of the high concentration of the gas, 3000 ppm.

3.2.3 Conclusions

In this chapter it has been investigated the optical gas sensing performances of a sensitive layer of TiO_2 doped with Pt NPs towards VOCs at a concentration of 3000 ppm. The mechanism involved is a combination between the VOC oxidation, with the involved electrons injection which cause an increase in absorbance at the SPR, and a blue shift, which is overlapped by the red shift due to the high refractive index of the VOC filling the pores. With the LSPR based sensing technique it is possible to monitor the electrons injection thanks absorbance. On the other hand, with the PSPR technique, it is only possible to monitor the combination between the two effects, electrons injection and red shift due to the increase of *n* of the film. This difference is due to the high refractive index of the VOC vapors filling the TiO_2 pores.

References

[1] C. De Juliàn Fernàndez, M.G. Manera, J. Spadavecchia, D. Buso, G. Pellegrini, G. Mattei, A. Martucci, R. Rella, L. Vanelli, M. Guglielmi, P. Mazzoldi, Gold/Titania nanocomposites thin films for optical gas sensing devices. In: Proceedings of SPIE- Microtechnologies for the New Millennium. Sevilla, Spain, 9 May 2005, vol. 5836-84, p. 703-710, doi: 10.1117/12.608964.

[2] P. K. Dutta, A. Ginwalla, B. BHogg, B. R. Patton, B. Chwierth, Z. Liang, P. Gouma, M. Mills, S. Akbar, Interaction of Carbon Monoxide with Anatase Surfaces at High Temperatures: Optimization of a Carbon Monoxide Sensor, J. Phys. Chem. 1999, Volume 103, 4412-4422.

[3] Enrico Della Gaspera, Adriana Mura, Enrico Menin, Massimo Guglielmi, Alessandro Martucci, Reducing gases and VOCs optical sensing using surface plasmon spectroscopy of porous TiO_2–Au colloidal films, Sens. Act. B 2013, Volume 187, 363- 370.

[4] E. Della Gaspera, A. Antonello, M. Guglielmi, M.L. Post, V. Bello, G. Mattei, F. Romanato, A. Martucci, Colloidal approach to Au-loaded TiO_2 thin films with optimized optical sensing properties, J. Mat. Chem. 2011, Volume 21, 4293-4300.

[5] M. G. Manera, G. Leo, M. L. Curri, P. D. Cozzoli, R. Rella, P. Siciliano, A. Agostano, L. Vasanelli, Investigation on alcohol vapours/TiO_2 nanocrystal thin films interaction by SPR technique for sensing application, Sens. Actuators B 2004, Volume 100, 75-80.

[6] G. Sberveglieri, G. Faglia, E. Comini, M.Z. Atashbar, W. Wlodarski, Titanium dioxide thin films prepared for alcohol microsensor applications, Sens. Actuators B 2000, Volume 66, 139-141.

[7] X. F. Li, S. F. Yu, Extremely High Sensitive Plasmonic Refractive Index Sensors Based on Metallic Grating, Plasmonics 2010, Volume 5, Issue 4, 389-394.

[8] M. J. Jory, P. S. Vukusic, J. R. Sambles, Development of a prototype gas sensor using surface plasmon resonance on gratings, Sens. Actuators B 1994, Volume 17, 203-209.

[9] Homola J, Koudela I, Yee SS, Surface plasmon resonance sensor based on diffraction gratings and prism couplers: sensitivity comparison, Sens Actuators B 1999, Volume 54, 16-24.

[10] K. H. Yoon, M. L. Shuler, S. J. Kim, Design optimization of nano-grating surface plasmon resonance sensors, Opt. Express 2006, Volume 14, Issue 11, 4842-4849.

[11] Enrico Della Gaspera, Adriana Mura, Enrico Menin, Massimo Guglielmi, Alessandro Martucci, Reducing gases and VOCs optical sensing using surface plasmon spectroscopy of porous TiO2–Au colloidal films, Sensors and Actuators B 2013, Volume 187, 363– 370

[12] E. Della Gaspera, M. Bersani, G. Mattei, T.-L. Nguyen, P. Mulvaney, A. Martucci, Cooperative effect of Au and Pt inside TiO_2 matrix for optical hydrogen detection at room temperature using surface plasmon spectroscopy, Nanoscale 2012, Volume 4, 5972-5979.

[13] Bengt Edlén, The Refractive Index of Air, Metrologia 1966, Volume 2, Issue 2, 71

[14] B.L. Zhu, C.S. Xie, W.Y. Wang, K.J. Huang, J.H. Hu, Improvement in gas sensitivity of ZnO thick film to volatile organic compounds (VOCs) by adding TiO_2, Materials Letters 2004, Volume 58, 624– 629.

[15] Sung Jong Yoo, Kug-Seung Lee, Yong-Hun Cho, Soo-Kil Kim, Tae-Hoon Lim & Yung-Eun Sung. Electrocatalytic Properties of TiO_2-Embedded Pt Nanoparticles in Oxidation of Methanol: Particle Size Effect and Proton Spillover Effect, Electrocatal 2011, Volume 2, 297-306.

3.3 Hydrogen sensing with SPP

In the previous two paragraphs, SPP based sensor have been developed for VOCs in order to exploit the variation of the refractive index of the sensitive layer induced by the different vapors. In fat it is well know that the refractive index of the different used VOCs is higher than air (*n*=1.497 toluene, 1.4995 xylene, 1.5011 benzene, 1,33 methanol, 1.36 ethanol, 1.37 isopropanol).

Here we want to exploit the possibility to detect H_2, which contribution to the variation of the refractive index is negligible, using a sensitive layer that can chemically react with H_2 trough red-ox reactions that can induce changes in the charge densities of the oscillating plasmons.

The hydrogen detection is becoming an essential condition because of safety issues, in fact in the recent years, the use of hydrogen as energy source is attracting much attention thanks to its calorific power.

Hydrogen is a clean, sustainable and abundant source; at standard temperature and pressure, is also colorless, odorless, tasteless, non-toxic, but on the other hand is volatile, extremely flammable and this makes complex to handle and store it. A leakage of hydrogen more than 4% (the lower explosive limit, LEL) in air would lead to an easily ignited explosive atmosphere [1].

For that reasons, many kind of hydrogen sensors has been developed [2] [3] [4] [5]; in particular SPR phenomenon was first used for sensing technology in 1982 [6].

The application of metallic diffraction grating for SPR sensing is advocated by Cullen et al. [7]. Since then, SPR sensors based on grating are studied as an alternative to Attenuated total reflectance systems [1] [8] [9] [10] [11].

Many works present hydrogen sensors device using metallic grating covered with palladium [1] [12] because palladium acts like a catalyst to split the H_2 molecules into atomic hydrogen.

This paper describes the use of a low cost symmetric plasmonic crystal, to detect hydrogen, fabricate just using sol-gel materials. In this plasmonic grating is avoided the use of palladium either expensive matrixes of semiconducting oxides like tungsten [1212].

Moreover, to produce the grating we used a soft imprinting based technique [13], which involves the use of a soft elastomeric mold to form high resolution plasmonic crystal sensor.

This plasmonic crystals enable the monitoring of little quantity of H_2, about 1%v., instantaneously and avoiding the use of expensive catalyst like Pt or Pd.

3.3.1 Experimental

3.3.1.1 Sensitive material synthesis

Silica phenyl functionalized sol-gel solution, TiO_2 and Au NPs were prepared as described in the appendixes A.2.11, A.2.7 and A.2.1, respectively

3.3.1.2 Samples preparation

All the thin films were deposited via spin coating at 3000 rpm for 30 s on either SiO_2 flat glass substrate or on plasmonic gratings (already described in the section 3.1.1.2) as dielectric 2 (Fig. 3.1.1); the nanocomposite were prepared by mixing the TiO_2 or SiO_2 solution with the Au NPs solution, 4% molar, and spin coated at 3000rpm for 30 s. Both type of the samples (Tab. 3.3.1) were dried at 100°C for 5min and finally annealed in a muffle furnace at 300°C for 1 h in air.

Samples	**Support/Substrate**	**Transducing platform**
SiO_2 (from TEOS/PTMS)	Plasmonic grating	SPP
SiO_2- 4% Au NPs (from TEOS/PTMS)	Flat fused silica	LSPR
TiO_2	Plasmonic grating	SPP
TiO_2- 4% Au NPs	Flat fused silica	LSPR

Tab. 3.3.1- Sensitive layers composition for the different sensing platforms.

3.3.1.3 Gas sensing measurements

Optical gas sensing tests with PSPR and LSPR based technique were performed in reflection and in transmission, respectively, with operating temperature (OT) set at 300 °C and the sensor was tested for H_2 10000 and 50000 ppm balanced with N_2.

3.3.2 Results and discussion

3.3.2.1 Structural and optical properties of the TiO_2 and SiO_2 Au nanocomposite

In Figure 3.3.1 are reported the absorption spectra of the TiO_2 and SiO_2 based nanocomposite with embedded Au NPs, it is evident the red-shift of the plasmon peak for the TiO_2 based sample due to the higher refractive index of the matrix.

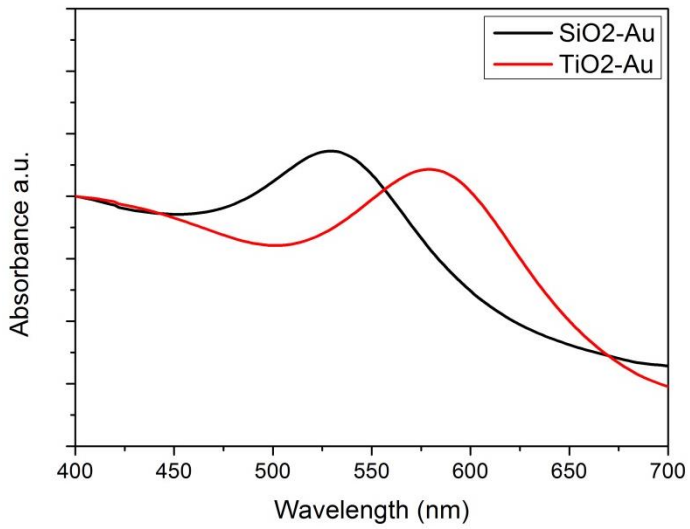

Fig. 3.3.1- Absorption spectra of the SiO_2-Au and TiO_2-Au nanocomposites film deposited on silica glass.

3.3.2.2 Structural and optical properties of the plasmonic crystal

On the plasmonic gratings it was deposited a nanocomposite film (dielectric 2) with the composition and structure already reported in the section *3.3.2.2*. Refractive index and thickness of the dielectric 1 and 2 are reported in Table 3.3.2.

Name		*n* (λ=630nm)	Thickness
Dielectric 2	SiO_2	1.49	176 nm
	TiO_2	1.92	129 nm
Dielectric1		1.51	200 nm

Tab. 3.3.2- Thickness and refractive index (*n*) of the two dielectrics of the plasmonic crystal.

In Figure 3.3.2 are shown the experimental spectra compared with the simulated one, at an incident angle of 70°. A set of dips can be seen, associated to the resonant coupling of the incident radiation with SPP modes supported by the thin-film structure. The simulations produce very similar spectra for the two structures.

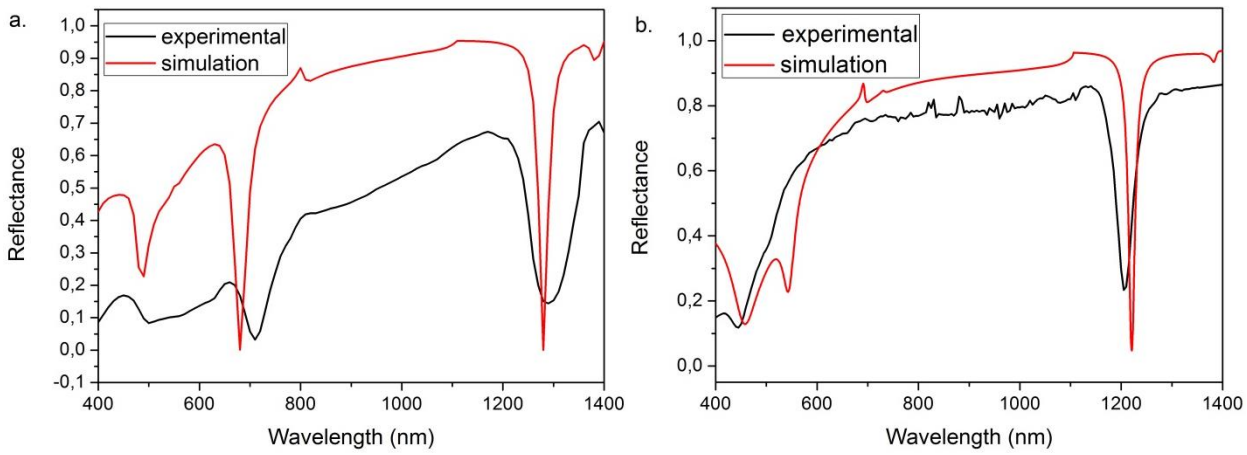

Fig. 3.3.2- Experimental reflection spectra, with overlaid the theoretical simulations, of the plasmonic crystals with sensitive layer TiO_2 (a) and SiO_2 (b), with front side illumination at 70°.

The first plasmonic crystal structure has been chosen in order to obtain a more sensible device, with a symmetric configuration made of a SiO_2 layer, of the same thickness, underneath (dielectric1) and on the top (dielectric 2) of the metallic layer.

In this symmetric configuration the SPP, waves propagating along the metal surface, are extremely sensitive to alterations of the surface optical properties and propagates deeper. This makes them ideal probes to investigate variations induced by chemical reactions between the target gas and the surface itself.

The second one was fabricated in order to have the performances of a semiconducting material as sensitive layer in conjunction with a "quasi-symmetric" configuration which, as already said, increase the plasmonic crystal sensitivity.

The problem with the semiconducting TiO_2 matrix is that it has a high refractive index, higher than the one of dielectric1, as reported in Table 3.3.2, this gives a non-symmetric plasmonic crystal and a lower sensitivity .

To obtain a "quasi-symmetric" configuration with the TiO_2 sensitive layer the refractive index of the dielectic1 with a certain thickness has to be the same of the dielectric 2 with the same thickness this is obtained considering the dielectric 2 as TiO_2 plus air to reach the thickness of the dielectric 1, so it was tuned the TiO_2 layer thickness in order to have the average refractive index, mediated with the one of the air, of the dielectric 2 equal to the one of the dielectric 1.

3.3.2.3 PSPR based gas sensing

Figure 3.3.3 shows the reflection spectra of the samples SiO_2 phenyl functionalized and TiO_2 when exposed to multiple N_2-H_2 cycles, and it is possible to visualize the blue-shift of the dips caused by the interaction of the plasmonic crystal with the gas.

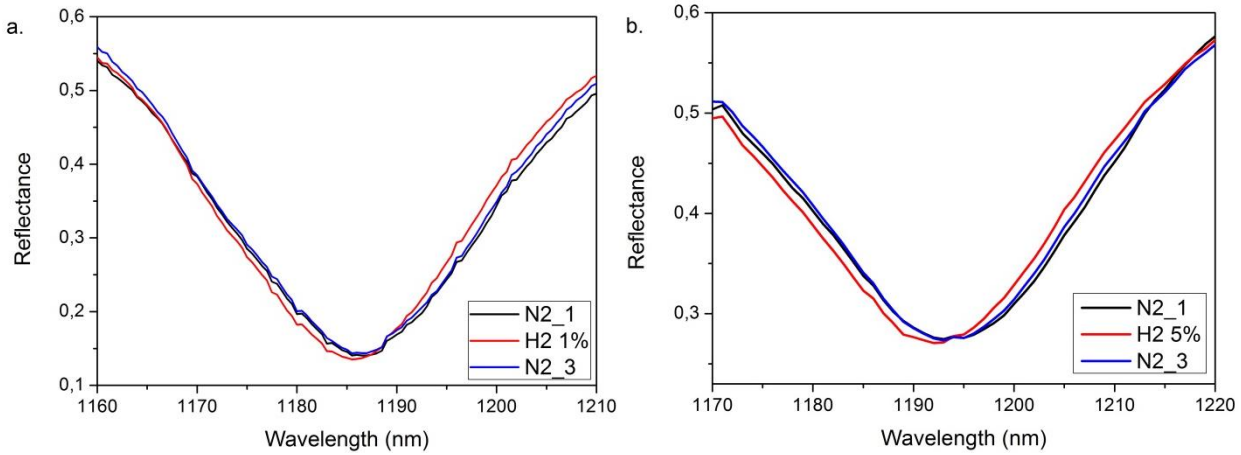

Fig. 3.3.3- Sensing test with hydrogen 1% (a.) and 5% (b.) on the plasmonic crystal with sensitive layer of SiO_2.

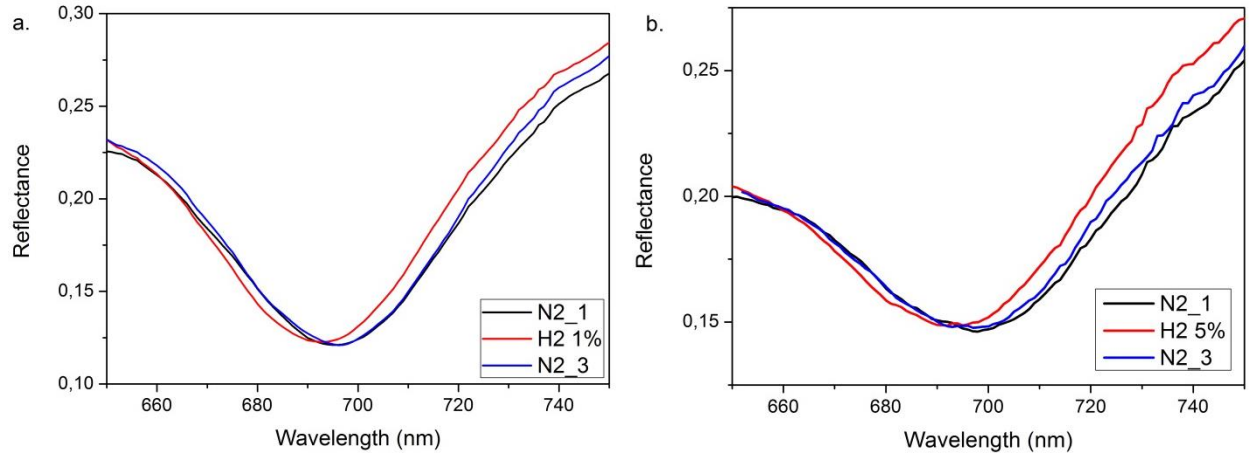

Fig. 3.3.4- Sensing test with hydrogen 1% (a.) and 5% (b.) on the plasmonic crystal with sensitive layer of TiO_2.

The shifts showed in Figure 3.3.3 and 3.3.4 are summarized in Table 3.3.3; it is possible to notice that the sensitivity of the plasmonic crystal coated with the semiconductive layer is higher than the one coated with the insulating one and increases at the increase of the gas concentration (from 10000 ppm to 50000 ppm).

		Shift in H_2 1% flux [nm]	Shift in H_2 1% flux [nm]
TiO_2	Dip at 700 nm	3	7
	Dip at 1200 nm	1	5
SiO_2	Dip at 1185 nm	1	2

Table 3.3.3- Shift of the dip for the plasmonic crystals with dielectrics TiO_2 and SiO_2, in N_2 and H_2 flux.

3.3.2.4 LSPR based gas sensing

The same test has been performed, to verify the shifts, using the flat samples with the optical absorption based technique monitoring the shift of the LSPR triggered by the Au NPs embedded in the sensitive material, the results are shown in fig. 3.3.5 and 3.3.6. The shift is a blue-shift with an

increase in absorbance, which implies an electron injection as already explained in chapter 2.2, and this is in accordance with the result obtained with the plasmonic crystals.

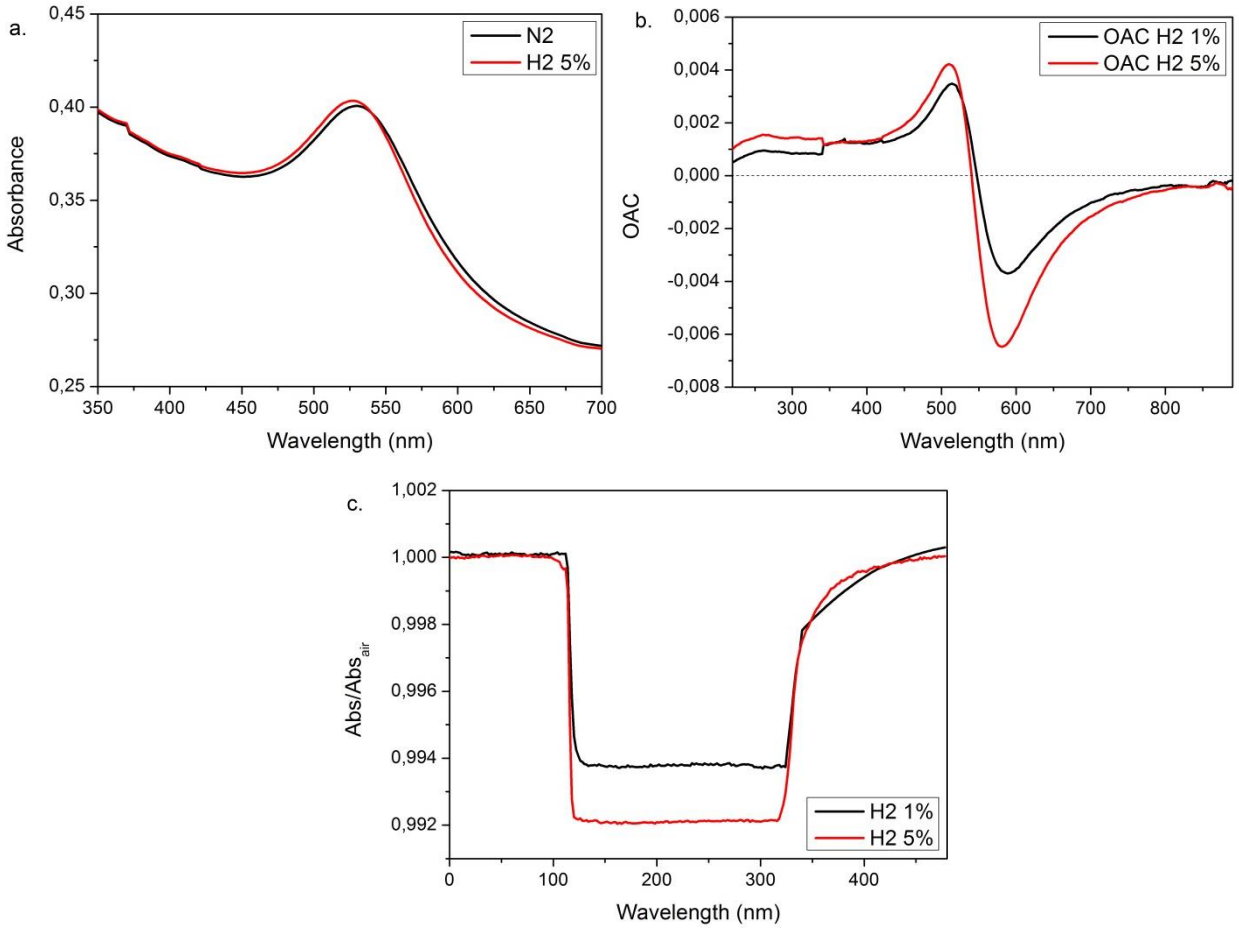

Fig. 3.3.5- Gas sensing test on the SiO_2 sample (a.) scan measurement in N_2 and H_2 5% flux (b.) OAC curve in H_2 1 and 5% flux and (c.) dynamic measurement, comparing the performances towards H_2 1 and 5% at 580 nm.

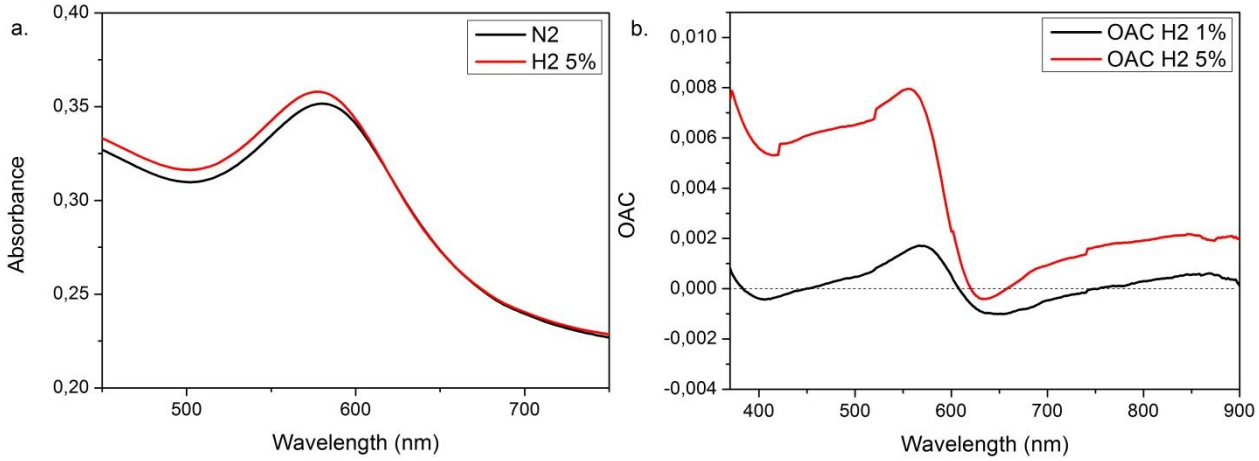

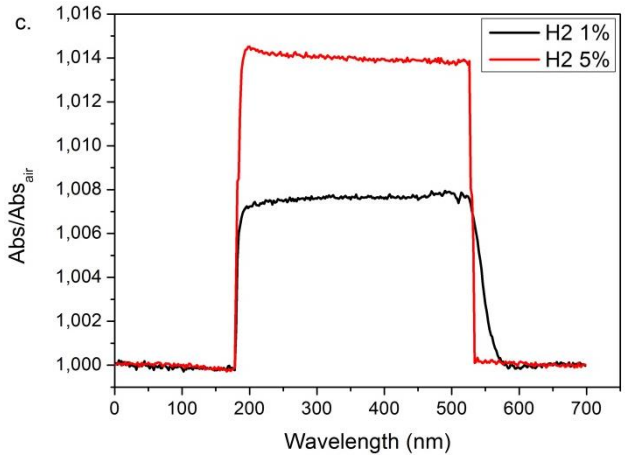

Fig. 3.3.6- Gas sensing test on the TiO_2 sample (a.) scan measurement in N_2 and H_2 5% flux (b.) OAC (Optical absorption change) curve in H_2 1 and 5% flux and (c.) dynamic measurement, comparing the performances towards H_2 1 and 5% at 562 nm.

With both the techniques it is possible to monitor the presence of hydrogen. It is therefore extremely important to give a complete description of the mechanisms involved in the detection, recognition and response to specific target gases.

The overall gas detection in fact can be described as a three steps process: adsorption of the target gas molecules, reaction on the active material surface and final desorption of the reaction products. These three phenomena must be temporally placed in the two main events in gas detection: the response (or the N_2-to-gas transient) and the recovery (or the gas-to-N_2 transient) of the sensor signal.

This good sensitivity of SiO_2 layer towards H_2 is not expected, because SiO_2, unlike TiO_2 and ZnO, is not a semiconductor, but it is an insulator, so there should not be electron conduction for the sensing mechanisms.

At room temperature, in fact, gas sensing with SiO_2 matrix is not possible, there is no response to the gas target (see chapter 2.3); performing, instead, the gas sensing tests at 300°C, it works; this because there are probably another phenomena involved.

In fact, if an insulating material is heated, the vibrational energy of the atoms located at the nodes of the lattice increases. This energy is transferred to the electrons which cannot "move" within the band in which they are located, so they try to find other states. The pulses that the electrons receive from the atoms of the lattice are sufficient to permit that a part of them jump in the empty band (may be the defect state) where they can enter into conduction [[14]].

Regarding the TiO_2 sensitive layer it is important to say that, with the grating-based gas sensing, the measurement performed at RT did not give any result, there was no sensitivity even if TiO_2 is a semiconductor.

Instead at 300°C the plasmonic crystal is working, this because the reaction of the kinetics of H_2 reaction with TiO_2 is thermal activated [15].

The H_2 sensing in the plasmonic crystal configuration is working only at 300°C for both the materials (TiO_2 and SiO_2) probably because the conductivity at 300°C can be originated from the following reasons: the oxygen vacancies in the oxide matrix result in the formation of intragap states lying just below the conduction edge. Many of these intragap are shallow donors. At room temperature this states are absent, that's why SiO_2 is an insulator and TiO_2 is working better at 300°C. The intragap states ionize at higher temperatures and the free-carrier electron density increases [15] [16].

These considerations explain the sensing mechanism. It is dominated, in the case of plasmonic crystal, by the coupling of the visible light into surface plasmon polaritons, SPPs, propagating along the metal-dielectric interface, which makes the polaritons sensitive to the changes in the sensitive layer in which are injected electrons due to the reducing reaction (1) of H_2. In the case of the optical absorption based technique, the embedded Au NPs' LSPR is excited by the incident light and is sensitive to the changes in the sensitive layer due to the electrons injection as already explained (reaction 1).

$$H_2 \rightarrow 2H^+ + 2e^-_{C.B.} \quad (1)$$

The reaction (1) is catalyzed by the temperature and injects electrons into the TiO_2 conduction band or into the defect state of the SiO_2.

3.3.3 Conclusions

The performances of two sensitive materials, one insulating and the other one semiconducting, coupled with both L- and P-SPR, have been investigated for H_2 detection at 300 °C. Both the techniques showed good sensitivity towards hydrogen 10000 and 50000 ppm, and the mechanism involved in the sensing is linked to an electron injection which causes a blue-shift of the dips in the reflection spectra of the plasmonic crystals and of the plasmonic peak of gold NPs in the absorption spectra of the flat samples. The blue-shift measured is higher for the semiconducting sensitive layer.

References

[1] K. Lin, Y. Lu, J. Chen, R. Zheng, P. Wang, H. Ming, Surface plasmon resonance hydrogen sensor based on metallic grating with high sensitivity, Opt. express 2008, Volume 16, Issue 23, 18599-18604.

[2] M. A. Butler, Optical fiber hydrogen sensor, Appl. Phys. Lett. 1984, Volume 45, Issue 10, 1007-1009.

[3] P. Tobiska, O. Hugon, A. Trouillet, and H. Gagnaire, An integrated optic hydrogen sensor based on SPR on palladium, Sens. Act. B 2001, Volume 74, 168-172.

[4] X. Bévenot, A. Trouillet, C. Veillas, H. Gagnaire, M. Clement, Surface plasmon resonance hydrogen sensor using an optical fiber, Meas. Sci. Technol. 2002, Volume 13, Issue 1, 118–124.

[5] D. Monzón-Hernández, D. Luna-Moreno, J. Villatoro, G. Badenes, All-optical fiber hydrogen sensor based annealed Pd-Au sensing nanolayers, Proc. SPIE 6619, 66191F1-4 (2007).

[6] C. Nylander, B. Liedberg, T. Lind, Gas detection by means of surface plasmon resonance, Sens. Actuators 1982, Volume 3, 79–88.

[7] D. C. Cullen, R. G. Brown, C. R. Lowe, Detection of immuno-complex formation via surface plasmon resonance on gold-coated diffraction gratings, Biosensors 1987, Volume 3, 211–225.

[8] M. J. Jory, P. S. Vukusic, J. R. Sambles, Development of a prototype gas sensor using surface plasmon resonance on gratings, Sens. Actuators B 17, 203-209 (1994).

[9] C. R. Lawrence, N. J. Geddes, D. N. Furlong, Surface plasmon resonance studies of immunoreactions utilizing disposable diffraction gratings, Biosens. Bioelectron. 1996, Volume 11, Issue 4, 389–400.

[10] D. Zhang, P. Wang, X. Jiao, G. Yuan, J. Zhang, C. Chen, H. Ming, R. Rao, Investigation of the sensitivity of H-shaped nano-grating surface plasmon resonance biosensors using rigorous coupled wave analysis, Appl. Phys. A 2007, Volume 89, 407–411.

[11] K. H. Yoon, M. L. Shuler, S. J. Kim, Design optimization of nano-grating surface plasmon resonance sensors, Opt. Express 2006, Volume 14, Issue 11, 4842–4849.

[12] H. Giessen, P. Mai, A. Tittl, N. Liu, C. Grossmann, A. Seidel, R. Orzekowsky, T. Meyrath, IEEE Sensors 2010 Conference

[13] L. Brigo, E. Gazzola, M. Cittadini, P. Zilio, G. Zacco, F. Romanato, A. Martucci, M. Guglielmi, G. Brusatin, Short and long range surface plasmon polariton waveguides for xylene sensing, Nanotechnology 2013, Volume 24, 155502 (10pp).

[14] http://www.fisicamente.net/DIDATTICA/index-126.htm

[15] Andrei Kolmakov, Martin Moskovits, Chemical sensing and catalysis by one-dimensional metal-oxide nanostructures, Annu. Rev. Mater. Research, Volume 34, 151-180.

[16] P. Feng, Q. Wan, T. H. Wang, Contact-controlled sensing properties of flowerlike ZnO nanostructures, Appl. Phys. Lett. 2005, Volume 87, 213111.

Chapter 4

Conclusions

The present work of thesis has been realized in the framework of the PLATFORMS project and deals with Optical Plasmonic Gas Sensors.

The tested gases are of two types: reducing gases like hydrogen, carbon monoxide, VOC and A-VOC and oxidizing gases like nitrogen oxide. The reducing gases inject electrons into the gold NPs causing a blue shift of the SPR peak, while the oxidizing gases subtract electrons from the gold NPs causing a red shift of the SPR peak.

This work is divided in two main chapters. In the first part LSPR are treated, gold NPs of different shapes (rods, dumbbells and stars) are embedded in semiconducting matrices (like TiO_2 and ZnO) and coupled with Pt NPs to catalyze the reaction between the target gases and the oxide matrix (Chapter 2.1 and 2.2). The use of Pt NPs is important in the case of NPs with shapes other than spherical because they tend to spheroidize at high temperature. This forced the gas sensing test to be performed at RT, without the high temperature to catalyze the red-ox reactions with the gases, and therefore implies the need for Pt catalysis. The results obtained were very good as the performances were improved by the local field enhancement effect due to the use of this shape of NPs, as expected.

The synthesis of NRs, NDs and NSs adopted for the tests come from a visit to Colloid Chemistry Group, at University of Vigo, Spain, within a collaboration with Prof. Luis M. Liz-Marzan and Prof. Jorge Pérez-Juste.

Gold NRs were also used in single particle gas sensing measurement with DFM technique (Chapter 2.3) at Bio21 Institute of the University of Melbourne, Melbourne (VIC) Australia thanks to a fruitful collaboration with Prof. Paul Mulvaney. The innovation introduced is the use of a low scattering semiconducting matrix deposited on the gold NRs with really good results, in fact the shift of the SPR is enhanced by the presence of both the semiconducting oxide matrix, the catalytic Pt nanoparticles and the presence of oxygen ions adsorbed on the surface of the matrix.

ZnO has been used also as plasmonic material itself in Chapter 2.4, through the doping with trivalent cations like Al^{3+} or Ga^{3+} which trigger a SPR in the NIR region. This plasmon showed a good sensitivity, in particular if coupled with catalytic NPs, like Pt, this because the sensing at high temperature is not allowed. In fact the heat treatment in reducing atmosphere, done to enhance the

SPR, would be annealed by the high temperature of the sensing test, and would make the SPR disappear. Moreover, the best result is obtained combining GZO with Pt NPs, because of both: the catalytic behavior of Pt and the higher number of oxygen vacancies and consequently higher number of free charges og GZO respect to AZO.

In Chapter 2.5 the gold NPs were also used coupled with partially oxidized graphene, in collaborations with Prof. Luca Ottaviano and Dr. Francesco Perozzi (University of L'Aquila).

R-GO for its semiconducting properties enables the electrons injection/subtraction from the gold NPs through the reaction with the target gases. The presence of graphene coupled with the gold NPs improves the performances at 80°C of a simple monolayer of gold NPs, showing a good efficiency in the electron hopping from the graphene sp^2 domain into the gold NPs.

In the end, in Chapter 2.6 another sensing mechanism was used to monitor the presence of A-VOC, the π-π stacking with a phenyl group of a SiO_2 matrix with very impressive results at RT, with high variation in absorbance and very fast kinetics, in the order of few seconds.

Chapter 3, treats PSPR using as sensing devices plasmonic crystal fabricated and simulated in collaboration with Dr. Laura Brigo, Prof. Giovanna Brusatin, Mr. Enrico Gazzola, Prof. Filippo Romanato. In Chapter 3.1 this plasmonic structures were used to detect A-VOC comparing the performances of the sensitive material used in chapter 2.6 with the one of a semiconducting material without phenyl groups, like TiO_2. These structures has also been used to make a comparison between the two mechanism involved in the detection process, π-π stacking and Ti^{4+}•••π-electrons. Moreover, the same plasmonic crystals were tested towards VOC (Chapter 3.2), with a results that show a combination between the blue shift due to the electrons injection from the VOC towards the plasmonic structure, as confirmed by the XPS performed by the Surface Science Group, in particular Dr. Stefano Agnoli and Prof. Gaetano Granozzi, and the red shift due to the increase of refractive index of the ensemble film due to the substitution of the air inside the pores with VOC vapors, which have a higher refractive index (n_{air}=1, n_{MetOH}=1,33, n_{EtOH}=1.36, n_{IPA}=1.37).

In the end Chaper 3.3presents the tests of the the plasmonic crystals towards H_2. No results were notice in the RT procedure, not even with the Pt catalysis, while with the 300 °C procedure is visible a clear blue shift of the plasmonic dip for both the sensitive materials SiO_2 and TiO_2.This happens because the reaction of the kinetics of H_2 reaction with SiO_2 and TiO_2 is thermal activated as explained in the Chapter.

This thesis represents only a small step in the big field of gas sensors, of course a lot has still to be done, but the work presented here can be a valuable starting point for the implementation of the described nanocomposites inside actual devices, like SPR-based sensors with a relatively simple

and cheap experimental procedure, nonetheless providing high quality and high performances materials.

A Appendix: Materials and Methods

A.1 Instrumentation

A.1.1 X-Ray diffraction

The crystalline phases of the thin films were characterized by X-Ray diffraction (XRD) by using a Philips PW1710 diffractometer equipped with grazing incidence X-Ray optics.

The analyses were performed at 0.5° incidence, using CuKα Ni filtered radiation at 30 kV and 40 mA. Due to limited amount of produced materials, also powder samples were most often analyzed with the grazing angle optics. This was performed by depositing on a glass substrate a thick layer of powder. The X-Ray incident angle was set equal to 3°. In both cases, the average crystallite size *D* was calculated from the Scherrer equation:

$$D = k\frac{\lambda}{cos\theta\ \Delta w}$$

after fitting the experimental profiles with Lorentzian functions: in this relationship, λ=1.54 Å is the Cu k_α wavelength, θ the diffraction angle, Δ*w* the full width at half maximum (FWHM) of the diffraction peak, and *K*=1 is the shape factor.

A.1.2 Electron Microscopy

Scanning Electron Microscope (SEM) was used to evaluate the surface morphology of the nanocomposites using different microscopes: low resolution images were taken on a Philips SEM equipped with Energy Dispersive X-ray (EDX) spectroscopy for elemental analysis. High resolution images were taken on a xT Nova NanoLab SEM operating at 5kV and 0.4nA.

Transmission Electron Microscopy (TEM) analysis on scratched fragments of the film and of nanoparticles deposited from colloidal solutions both deposited on carbon-coated copper grids were performed with a Philips CM20 STEM system operating at 200 kV.

A.1.3 Optical Spectroscopy

UV-Vis-NIR absorption spectra were taken using a JASCO V-570 spectrometer. Absorption measurements of liquid samples was performed with quartz or polycarbonate cuvettes (1 cm optical path), while thin films on quartz substrates were analyzed placing the substrate perpendicularly to the light beam.

A.1.4 Spectroscopic Ellipsometry

Transmittance at normal incidence and ellipsometry quantities Ψ and Δ have been measured using a J.A. Woollam V-VASE Spectroscopic Ellipsometer in vertical configuration, at various angles of incidence (usually three angles, 65°, 70°, 75°) in the wavelength range 300-1700 nm. Refractive index *n*, absorption coefficient *k*, and film thickness have been evaluated from Ψ, Δ and transmittance data using the WVASE32 ellipsometry data analysis software, fitting the experimental data with the 3-parameter Cauchy dispersion, Gaussian and Tauc-Lorentz oscillators for the non absorbing region, Au SPR peak and oxides UV absorption edge, respectively.

A.1.5 X-ray photoelectron spectroscopy

X-ray photoemission spectroscopy (XPS) spectra have been acquired with a PHI 1257 spectrometer equipped with a monochromatic Al Kα source (hν =1486.6 eV) with a pass energy of 11.75 eV, corresponding to an overall experimental resolution of 0.25 eV. The acquired XPS spectra have been fitted with Voigt line shapes and Shirley backgrounds.

A.1.6 Atomic Force Microscopy

Atomic Force Microscopy (AFM) images have been acquired in air using a Veeco Digital D5000 system equipped with silicon tip.

A.1.6 Ultra-high-vacuum temperature programmed desorption measurement

In order to perform UHV TPD experiments, a porous silica matrix functionalized with phenyl groups was deposited on a stainless steel support by spin coating. This deposition technique furnished a fully-covered thermal and electrical conducting support (no stainless steel related X-ray photoelectron spectroscopy peaks were observed), obtaining homogeneous deposits. The sample was then spot-welded to two 0.25 mm diameter Ta wires and connected to a 4 degrees of freedom manipulator. A type K thermocouple was spot-welded to the sample rear before the manipulator was mounted in the UHV chamber. The UHV chamber, equipped with a HIDEN HAL 301 PIC quadrupole mass spectrometer with electron multiplier detector, was then pumped and baked for 12 h at 100 °C, until a base pressure of $3.0 \cdot 10^{-10}$ mbar was achieved. Before starting the experiments, a sample degas was performed by heating at 573 K for 10 min. TPD experiments were collected thermalizing the sample at 258 K, exposing it to 20 L of xylene gas (1.0 L corresponds to a 1 s dosing time at a pressure of $1.0 \cdot 10^{-6}$ Torr) and heating at different rates, from 60 to 120 K/min. By following this experimental procedure it was possible to obtain the heat of desorption (ΔE_d) by the use of the Polanyi-Wigner equation:

$$r_d = \nu_n \exp\left(-\frac{\Delta E_d}{RT}\right)\Theta^n$$

where $r_d = -\frac{d\Theta}{dt} = k_n\Theta^n$ is the desorption rate of k desorption rate constant, Θ is the surface coverage and n the desorption reaction order. The desorption rate constant k is connected to the desorption energy in the Arrhenius equation:

$$k_n = \nu_n \, exp\left(-\frac{\Delta E_d}{RT}\right)$$

where ΔE_d is the activation energy for desorption at temperature T, R is the gas constant and ν_n is the frequency factor.

If, as in our case, a series of desorption curves referring to the same probe molecule coverage are collected for different linear heating rates ($\beta = dT/dt$), the *Polanyi-Wigner* equation for a first order desorption process (n=1) can be re-written as:

$$\frac{d\Theta}{dT} = -\frac{1}{\beta}\cdot\nu_n\cdot\exp\left(-\frac{\Delta E_d}{RT}\right)\cdot\Theta^n$$

and solved for $\Delta E_d/RT_m^2$ to give:

$$\ln\frac{T_m^2}{\beta} = \ln\frac{\Delta E_d}{\nu_1 R} + \frac{\Delta E_d}{R}\cdot\frac{1}{T_m}$$

where T_m is the temperature corresponding to the desorption curve maximum. Therefore, by plotting $\ln(\frac{T_m^2}{\beta})$ as a function of the reciprocal of T_m, an estimate of ΔE_d can be obtained from the slope of a straight line interpolating experimental data.

A.2 Materials Recipes

A.2.1 Recipe for the synthesis of 15 nm Au nanoparticles

280 mg trisodium citrate in 24 ml Milli-Q water preheated at 70 °C was quickly added to a 400 mL boiling aqueous solution containing 80 mg $HAuCl_4$. After the solution turned red-wine colored, it was stirred at boiling point for an additional 15 minutes and then was cooled down to room temperature.

If the particles were to be redispersed in ethanol, PVP-10K was dissolved in water (200 mg in 4 mL) and this solution was mixed with aqueous gold colloids under constant stirring. After 2 hours the solution was concentrated in a rotary evaporator to about 100- 150 mL and Au NPs were precipitated with excess acetone, centrifuged at 4000 rpm for 5 minutes and re-dispersed in ethanol leading to a 30 mM concentrated sol.

A.2.2 Recipe for the synthesis of 3 a.r. Au nanorods

Gold NRs, with 20nm of diameter and 60nm of length, so an aspect ratio 3, were prepared according to the seed-mediated method proposed by El-Sayed [1].

The seed solution was prepared at 50 °C by mixing 4.7 mL of a 0.1 M solution of Hexadecyltrimethylammonium bromide (CTAB) with 25 μL of an aqueous solution of gold salt $HAuCl_4$, 0,05M. After complete mixing, 300 μL of a solution 0,01M of Sodium borohydride ($NaBH_4$) is added and the seed solution colour turns into light brown.

After 1 hour, the growth solution is prepared by mixing 10 mL of a 0.1 M solution of Hexadecyltrimethylammonium bromide (CTAB) with 100 μL of an aqueous solution of gold salt $HAuCl_4$, 0,05M. After 2 minutes of mixing on an hot plate at 50 °C, 75 μL of an Ascorbic acid (AA) solution 0.1M were added and the solution turns into colorless. Then 80 μL of a Silver Nitrate solution 0.005M were added and finally 60 μL of the seed solution. The solution is left at 50 °C without stirring for 30 minutes.

If the rods have to be redispersed in ethanol, PVP-10K was dissolved in water (200 mg in 4 mL) and this solution was mixed with aqueous gold colloids under constant stirring. After 2 hours the solution was concentrated in a rotary evaporator to about 100- 150 mL and Au NRs were precipitated, centrifuged at 10000 rpm for 5 minutes and re-dispersed in ethanol leading to a 30 mM concentrated sol.

A.2.3 Recipe for the synthesis of 6 a.r. Au nanorods

A seed solution was prepared at 50 °C by mixing 4.7 mL of a 0.1 M solution of Hexadecyltrimethylammonium bromide (CTAB) with 25 μL of an aqueous solution of gold salt $HAuCl_4$, 0,05M. After complete mixing, 300 μL of a solution 0,01M of Sodium borohydride ($NaBH_4$) is added and the seed solution colour turns into light brown.

After 1 hour, the growth solution is prepared by mixing 10 mL of a 0.1 M solution of Hexadecyltrimethylammonium bromide (CTAB) with 100 μL of an aqueous solution of gold salt $HAuCl_4$, 0,05M. After 2 minutes of mixing on an hot plate at 50 °C, 75 μL of an Ascorbic acid (AA) solution 0.0993M were added and the solution turns into colorless. Then 80 μL of a Silver Nitrate solution 0.005M were added and finally 60 μL of the seed solution. The solution is left at 50 °C without stirring for 30 minutes. The day after are added 5 μL of the ascorbic acid solution 0.0933M.

If the rods have to be redispersed in ethanol, PVP-10K was dissolved in water (200 mg in 4 mL) and this solution was mixed with aqueous gold colloids under constant stirring. After 2 hours the solution was concentrated in a rotary evaporator to about 100- 150 mL and Au NRs were

precipitated, centrifuged at 10000 rpm for 5 minutes and re-dispersed in ethanol leading to a 30 mM concentrated sol.

A.2.4 Recipe for the synthesis of Au nanodumbbells

Gold NDs have been also synthesized following the recipe proposed by *M. Grzelczak et al.* [2]. As seed has been used 10mL of the NRs synthetized in appendix 2.3.

The gold NDs were prepared by mixing 10 mL of a 0.1 M solution of Hexadecyltrimethylammonium bromide (CTAB) with 50 μL of an aqueous solution of gold salt $HAuCl_4$, 0,05M. After 2 minutes of mixing on an hot plate at 50 °C, 6 μL of an Potassium Iodide (KI) 0.01M were added and finally 40 μL of an Ascorbic acid (AA) solution 0.1M.

In the end 600 μL of the NRs solution were used as seed. The solution was left at 50 °C without stirring for 30 minutes.

If the dumbbells have to be redispersed in ethanol, PVP-10K was dissolved in water (200 mg in 4 mL) and this solution was mixed with aqueous gold colloids under constant stirring. After 2 hours the solution was concentrated in a rotary evaporator to about 100- 150 mL and Au NRs were precipitated, centrifuged at 10000 rpm for 5 minutes and re-dispersed in ethanol leading to a 30 mM concentrated sol.

A.2.5 Recipe for the synthesis of 50 nm Au nanostars

Finally gold NSs PVP capped have been prepared, following the recipe proposed by *Kumar et al.* [3]. The synthesis is divided in two steps, the first one is already reported in appendix 2.1. The PVP capped Au NPs in water are used as seed. The second step is to prepare a solution with 10mL of DMF (Dimethylformamide) and 1g of PVP 10.000 g/mol. Then 10 mL of a 0.0005M gold salt solution is added. When the gold salt is completely reduced 235μL of seed are added. After 30 min of stirring the NSs are formed, centrifuged and redispersed in ethanol to reach a concentration 50 mM.

A.2.6 Recipe for the synthesis of 10 nm Pt nanoparticles

In a typical synthesis, 67 mg of H_2PtCl_6 and 18.7 mg of NaCl were dissolved in 3 mL ethylene glycol, degassed and kept under intert atmosphere (nitrogen). Separately, 150 mg NaNO3 and 55 mg PVP were dissolved into 13 mL ethylene glycol, degassed, and brought at 160 °C under intert atmosphere. After 20 minutes, the former solution was quickly injected into the latter: a change in color from pale orange to black was observed within few minutes. The Pt colloidal solution was kept at 160 °C under nitrogen for 30 minutes, then cooled down to room temperature, precipitated

with excess acetone, centrifuged at 4000 rpm for 5 minutes and redispersed in ethanol leading to a 30 mM nominal concentration.

A.2.7 Recipe for the synthesis of 4 nm TiO_2 nanoparticles

In a typical synthesis, 3 g of titanium isopropoxide was added drop wise to a previously prepared solution consisting in 1.78 g of hydrochloric acid, 7.18 mL of methanol and 1.24 g of water. The solution was stirred at ambient temperature for one hour and subsequently heated to 70 °C for four hours. Particles were then precipitated with excess acetone and centrifuged at 4000 rpm for two minutes. The obtained precipitate was dispersed in minimum amount of methanol obtaining a clear colloidal sol of anatase TiO_2 NPs. The concentrated solution is stable for few days. The best is to use the solution for films deposition within the following day.

A.2.8 Recipe for the synthesis of ZnO sol-gel solution

To deposit a ZnO layer, 200 mg of Zinc acetate dihydrate (ZnAc) was dissolved in 0.9 cc ethanol, and subsequently 0.066 mL monoethanolamine (MEA) were added under stirring. After 30 minutes, 0.35 mL ethanol (or ethanolic suspension of metal NPs) were added and the solution was used for film depositions after 5 more minutes of stirring. Again, the spinning procedure is performed under nitrogen atmosphere.

A.2.9 Recipe for the synthesis of ZnO nanoparticles

500 mg of Zinc acetate dihydrate (ZnAc) are dissolved in 22.5 mL dimethyl sulfoxide (DMSO); separately, 750 mg tetramethylammonium hydroxide (TMAH) are dissolved in 7.5 mL ethanol (EtOH). The TMAH solution is added dropwise (about 2 mL/min) to the Zinc solution under vigorous stirring at room temperature; after 10 minutes the solution is heated at 40 °C for 1 hour to promote Ostwald ripening of the particles, obtaining 6-7 nm NPs. To obtain 8 nm the solution has to be heated at 50 °C. After the solution has been heated for 1 hour, it was let cool down to room temperature, precipitated with the minimum amount (about 3:1 in volume) of methyl ethyl ketone (MEK), centrifuged at 1500 rpm for 5 minutes and redispersed in ethanol to a final nominal concentration of 0.8 M in molar zinc. The concentrated solutions are stable only for few hours, so they have to be used immediately for films deposition.

A.2.10 Recipe for the synthesis of Ga^{3+} and Al^{3+} doped ZnO nanoparticles

Nanocrystal Synthesis: The synthesis is performed with standard Schlenk line techniques. $ZnSt_2$ and

$Ga(NO_3)_3$ or alluminium nitrate, $Al(NO_3)_3$ are dissolved in 7.5 mL of OA at 80 °C (solution 1) under a nitrogen stream, keeping the atomic concentration (Zn + dopant) equal to 0.4 M and the Dopant/Zn molar ratio between 0% and 5%.

Separately, 22.5 mL of TOA is heated under nitrogen at 100 °C (solution 2), degassed under vacuum for 2 min, and then, heated under nitrogen at 310 °C.

Solution 1 is then degassed for 5 min and quickly injected into solution 2 at 310 °C. The temperature drop is less than 40 °C. The total solution is let stir at 280 °C for 25 min and then cooled down to room temperature. The doped ZnO NCs are precipitated with ethanol or acetone, centrifuged at 4000 rpm for 5 min, and redispersed in hexanes. The reaction yield was found to be between 85% and 90%.

A subsequent treatment is performed in order to increase the free charge density: the NCs are dispersed in a mixture of 1-octadecene (ODE, 15 mL), TOA (0.5 mL), and OA (0.5 mL) with a nominal concentration of 0.1 M, degassed at 90 °C, and heated up to 150 °C under a nitrogen stream. Then a 5% hydrogen/95% argon mixture stream is bubbled inside the solution through a stainless steel needle for 25 min with a flow rate of approximately 0.1 L/min, and the solution is subsequently cooled down to room temperature under the reducing atmosphere. In the manuscript, we refer to this procedure as "hydrogen bubbling treatment". The NCs are then washed with acetone and redispersed again in nonpolar solvents.

If needed, GZO or AZO NCs were transferred to ethanol by exchanging the surface ligands (organic amines) with APOH: the procedure is performed by adding 5 mL of a 10 g/L APOH solution in chloroform to 7.5 mL of a 0.1 M GZO or AZO colloidal solution in tetrachloroethylene (C_2Cl_4) under stirring.

Immediately upon addition of the APOH solution, aggregates appear, suggesting partial ligand exchange. After 30 min, the aggregates are collected by centrifugation (1000 rpm, 4 min), resuspended in 5 mL of a 0.5 g/L APOH solution in chloroform to induce further ligand exchange, stirred for an additional 15 min, centrifuged (1000 rpm, 4 min), and eventually, resuspended in ethanol to a 40 mg/mL stock solution.

Thin Film Synthesis. GZO or AZO thin films are deposited from concentrated NC solutions in toluene (between 40 and 80 mg/mL) by spin coating on either SiO2 (HSQ300, Heraeus) or Si (⟨100⟩ oriented, p-type boron-doped, Silicon Materials) substrates at 1500 rpm for 40 s.

After deposition, the samples are placed on a hot plate at 60 °C for 10 min. If needed, this procedure has been repeated to increase the sample thickness. The thickness of the samples used for optical and electrical characterization is about 500 nm, but thicker samples (up to 1 μm) are easily obtained with further spin-coating depositions or by drop casting the NC solution.

Some samples have been annealed in air between 100 and 800 °C for 1 h in a muffle furnace or in a 5% H2/95% Ar mixture at 450 °C for 2 h in a tube furnace, in order to analyze the effect of temperature and annealing atmosphere on the electrical and optical properties.

A.2.11 Recipe for the synthesis of SiO_2 (PTMS or dPDMS) sol-gel solution

To deposit an SiO_2 layer, 2 mL of tetraetossisilano (TEOS) were mixed in 2.606 mL of ethanol, and subsequently 1.672 mL of Trimethoxyphenylsilane (PTMS) or 2.0266 mL of Dimethoxydiphenylsilane (dPDMS), 0.555 mL of water and 0,896 mL of Cloridric Acid 1N were added under stirring. After 3 hours, 12.13 mL ethanol were added and the solution was used for film depositions after 5 more minutes of stirring.

A.2.12 Recipe for the preparation of SiO_2 (PTMS or dPDMS) with embedded Au nanoparticles grown in situ

To deposit an SiO_2 layer, 0.865 mL of tetraetossisilano (TEOS) were mixed in 0.563 mL of ethanol, and subsequently 0.723 mL of Trimethoxyphenylsilane (PTMS) or 0.8774 mL of Dimethoxydiphenylsilane (dPDMS), 0.2014 mL of water and 0,077 mL of Cloridric Acid 1N were added under stirring.

After 2 hours of reaction, a solution with 0,230 g of Gold(III) chloride hydrate ($HAuCl_4$) in 6.7 mL of ethanol was added, then the sols were further stirred for 1 hour.

The progressive thermal reduction of gold develops with a progressively reduction from Au^{3+} to Au^0 [4], according to:

$$HAuCl_4 \cdot xH_2O \xrightarrow{100°C} AuCl_3 \xrightarrow{160°C} AuCl \xrightarrow{200°C} Au \qquad (1)$$

A.2.12 Recipe for the synthesis of Au NPs sub-monolayers

Au monolayers have been prepared on fused silica slides or silicon. The substrate was first functionalized with (3-aminopropyl) trimethoxysilane (APTMS) via immersion into a solution composed of 0.3 mL APTMS in 30 mL toluene at 60 °C for 5 minutes in a controlled environment (R.H. < 20 %). Substrates were then extracted and immediately washed thoroughly with fresh toluene, dried in a nitrogen stream and then placed on a hot plate at 70 °C for 5 minutes to remove adsorbed toluene molecules. These substrates were used within the day, in order to prevent amines oxidation.

To deposit the monolayer, we used Au NPs PVP capped whose synthesis is already reported in Appendix A.2.1. The monolayers were formed by spin-coating at 3000 rpm for 30 sec the liquid suspensions of gold NPs directly onto the APTMS. The samples were then stabilized on a hot plate at 100 °C for 15 minutes, and subsequently used as substrates themselves.

A.3 Gas sensing set up

A.3.1 Apparatus for gas sensing in transmission

Optical gas sensing tests were performed by conducting optical absorption measurements in the 200-900 nm wavelength range on films deposited on SiO_2 substrates using a Harrick gas flow cell (with 5.5 cm path length) coupled with a Jasco V-650 spectrophotometer. The operating temperature (OT) was set at room temperature, 80 °C or 300 °C, with a flow rate of 0.4 L/min. The substrate size was approximately 1 × 2 cm and the incident spectrophotometer beam was normal to the film surface and covered a 9 × 1.5 mm area of the film.

The time spent by the sensor on achieving 90% of the total absorbance change is defined as the response time in the case of gas adsorption or as the recovery time in the case of gas desorption. To better visualize the gas effect, the Optical Absorbance Change (OAC) parameter, defined as the difference between absorbance during gas exposure and absorbance in air ($OAC=Abs_{Gas}-Abs_{Air}$) is used.

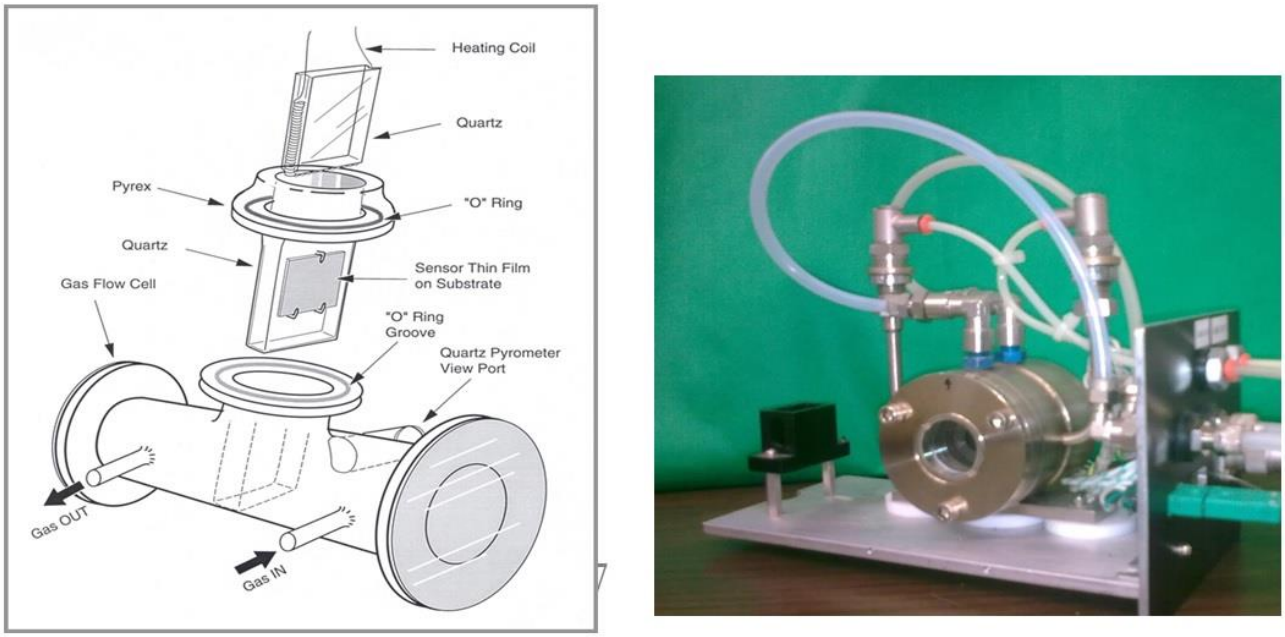

Fig. A.3.1.1 – Experimental set-up for the gas sensing tests in transmission.

A.3.2 Apparatus for gas sensing on single particles

The single-particle time-resolved gas sensing tests were performed using a Nikon TE2000-S Eclipse Inverted Microscope equipped with a Nikon dry dark-field condenser and a 40X/0.6 NA ELWD dry objective lens in transmission configuration (Fig. 1). A 100W halogen lamp was used to illuminate the sample. A Princeton Instruments IsoPlane SCT 320 imaging spectrograph with a PIXIS 1024F CCD detector was coupled to the output of the microscope. The acquisition time of all exposures was 60 seconds which was continuously repeated throughout the entire measurement. Time-

correlated longitudinal peak positions were extracted from the images by using automatic cross section line profiling and Lorentzian fitting procedures. To control the atmosphere and gas flow over the samples a continuous flow cell was developed specifically to meet the working distance restrictions of transmission dark-field microscopy. The cell (Fig. A.3.2.1) consists of two outer stainless steel mounting discs, a Teflon spacer ring with input out output flow channels, and tightening screws. The sample is mounted upside down in the top disc and a clean microscope slide of the same dimensions is mounted in the bottom disc to function as a transparent window for the cell. A needle of 0.8 mm outer diameter was connected to the gas supply and fitted into the input channel of the cell. The volume of the chamber is 800 mm^3.

The operating temperature (OT) was set at RT, with a flow rate of 0.07 L/min.

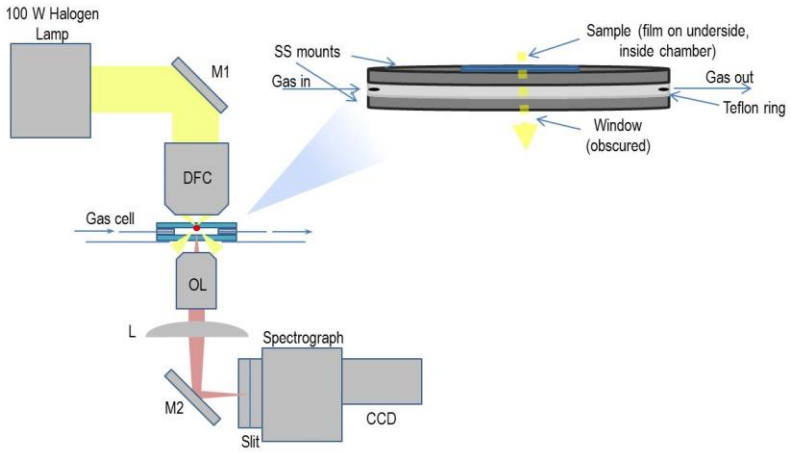

Fig. A.3.2.1 – Experimental set-up for the single-particle time-resolved gas sensing tests, including a Dark Field Microscope coupled with a spectrograph and an home-made gas sensing chamber.

A.3.3 Apparatus for gas sensing in reflection

Gas sensing test were performed by conducting reflection measurements in the 300-1500 nm wavelength range on films deposited on a plsmonic grating (described in chapter 3.1) using a J. A. Woollam Co. Heat Cell coupled with a J.A. Woolam Co. Variable Angle Spectroscopic Ellipsometer (VASE) (Fujiwara H., Spectroscopic Ellipsometry Wiley 2007) in θ/2θ configuration. The measurements have been performed with direct illumination of the sample with p-polarized light and at a fixed angle of 70° scanning the wavelength. The apparatus is reported in figure A.3.3.1. The tests have been performed at RT or 300 °C with a flow rate of 0.4 L/min.

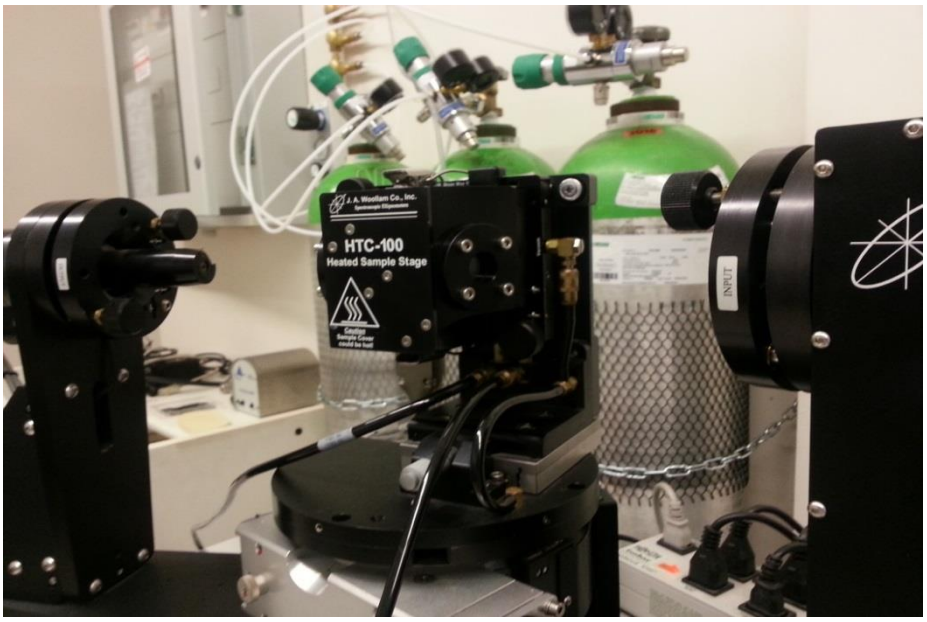

Fig. A.3.3.1 – Experimental set-up for the gas sensing tests in reflection.

A.4 LSPR simulations

Pecharromán performed for us the following simulations in order to determine the optical absoption of the SPR corresponding to spherical nanoparticles.

To do that it is necessary to estimate the effective dielectric constant of the whole system (matrix+metallic nanoparticles). In case of high dilution, the effective dielectric constant can be simplified as:

$$\langle \varepsilon \rangle = (1-f)\varepsilon_m + 3f\frac{(\varepsilon_p - \varepsilon_m)}{(1-L)\varepsilon_m + L\varepsilon_p} \qquad (0.1)$$

Where ε_p and ε_m are the dielectric constant of the nanoparticles and matrix, L the depolarization factor (L =1/3 for spheres) and f is the volume concentration of nanoparticles.

According to the Drude Model, ε_p is given by:

$$\varepsilon_p = \varepsilon_\infty - \frac{\omega_P^2}{\omega(\omega + i\gamma)} \cong \varepsilon_\infty - \frac{\omega_P^2}{\omega}\frac{\omega - i\gamma}{\omega^2} = \varepsilon_\infty - \frac{\omega_P^2}{\omega^2} + i\frac{\omega_P^2\gamma}{\omega^3} \qquad (0.2)$$

Where the plasma frequency is defined as:

$$\omega_P^2 = \frac{N_e e^2}{m_e \in_0} \qquad (0.3)$$

Then combining (0.1) and (0.2) it results:

$$\langle\varepsilon\rangle = (1-f)\varepsilon_m + 3f\,\frac{\varepsilon_\infty - \frac{\omega_P^2}{\omega^2} - \varepsilon_m + i\frac{\omega_P^2\gamma}{\omega^3}}{L\varepsilon_\infty - L\frac{\omega_P^2}{\omega^2} + (1-L)\varepsilon_m + iL\frac{\omega_P^2\gamma}{\omega^3}} \tag{0.4}$$

$$\langle\varepsilon\rangle = (1-f)\varepsilon_m + 3f\,\frac{\left(\varepsilon_\infty - \frac{\omega_P^2}{\omega^2} - \varepsilon_m + i\frac{\omega_P^2\gamma}{\omega^3}\right)\left(L\varepsilon_\infty - L\frac{\omega_P^2}{\omega^2} + (1-L)\varepsilon_m - iL\frac{\omega_P^2\gamma}{\omega^3}\right)}{\left(L\varepsilon_\infty - L\frac{\omega_P^2}{\omega^2} + (1-L)\varepsilon_m\right)^2 + \left(L\frac{\omega_P^2\gamma}{\omega^3}\right)^2} \tag{0.5}$$

The absorption, in case of high dilution medium, is nearly proportional to the imaginary part of the dielectric constant. So we have:

$$\mathrm{Im}\langle\varepsilon\rangle = 3f\,\frac{\omega_P^2\gamma}{\omega^3}\,\frac{\left(L\varepsilon_\infty - L\frac{\omega_P^2}{\omega^2} + (1-L)\varepsilon_m\right) - \left(L\varepsilon_\infty - L\frac{\omega_P^2}{\omega^2} - L\varepsilon_m\right)}{\left(L\varepsilon_\infty - L\frac{\omega_P^2}{\omega^2} + (1-L)\varepsilon_m\right)^2 + \left(L\frac{\omega_P^2\gamma}{\omega^3}\right)^2} \tag{0.6}$$

$$\mathrm{Im}\langle\varepsilon\rangle = 3f\,\frac{\omega_P^2\gamma}{\omega^3}\,\frac{\varepsilon_m}{\left(L\varepsilon_\infty - L\frac{\omega_P^2}{\omega^2} + (1-L)\varepsilon_m\right)^2 + \left(L\frac{\omega_P^2\gamma}{\omega^3}\right)^2} \tag{0.7}$$

In the case of the SPR condition, we get

$$L\varepsilon_\infty - L\frac{\omega_P^2}{\omega_{SPR}^2} + (1-L)\varepsilon_m = 0 \tag{0.8}$$

$$\omega_{SPR}^2 = \frac{\omega_P^2}{\varepsilon_\infty + (1/L - 1)\varepsilon_m} \tag{0.9}$$

$$\omega_{SPR} = \omega_P\,\frac{1}{\sqrt{\varepsilon_\infty + (1/L-1)\varepsilon_m}} = e\sqrt{\frac{N_e}{m_e \in_0 \left[\varepsilon_\infty + (1/L-1)\varepsilon_m\right]}} \tag{0.10}$$

So that, the imaginary part of the dielectric constant of medium at the SPR is given by:

$$\mathrm{Im}\langle\varepsilon\rangle = \frac{3f\varepsilon_m\omega_{SPR}^3}{L\omega_P^2\gamma} \tag{0.11}$$

The optic observable is the absorbance defined as:

$$A(\omega_{SPR}) = \frac{\omega_{SPR}}{c} z \,\mathrm{Im}\left(\sqrt{\langle\varepsilon\rangle_{SPR}}\right) \cong \frac{\omega_{SPR}}{2c} z \,\mathrm{Im}\left(\langle\varepsilon\rangle_{SPR}\right) \tag{0.12}$$

Thus, by combining (0.11) and (0.12) it results

$$\mathrm{Im}\langle\varepsilon\rangle = \frac{3zf\,\varepsilon_m \omega_{SPR}^4}{2cL\omega_P^2\gamma} \tag{0.13}$$

Therefore, by introducing equation (0.3) into (0.13) it results

$$\begin{aligned} A(\omega_{SPR}) &= \frac{3zf\,\varepsilon_m}{2cL\gamma} \frac{\omega_P^2}{\left[\varepsilon_\infty + (1/L - 1)\varepsilon_m\right]^2} \\ A(\omega_{SPR}) &= \frac{3zf\,\varepsilon_m}{2cL\gamma m_e \in_0} \frac{e^2 N_e}{\left[\varepsilon_\infty + (1/L - 1)\varepsilon_m\right]^2} \end{aligned} \tag{0.14}$$

The absorbance at the SPR position is proportional to the electron density.

Other simulations are going to be performed to understand the behavior of the single gold NR not covered or embedded into an oxide matrix.

Reference

[1] Babak Nikoobakht, Mostafa A. El-Sayed, Preparation and Growth Mechanism of Gold Nanorods (NRs) Using Seed-Mediated Growth Method, Chem. Mater. 2003, Volume 15, Issue 10, 1957-1962.

[2] M. Grzelczak, A. Sánchez-Iglesias, B. Rodríguez-González, R. Alvarez-Puebla, J. Pérez-Juste, L.M. Liz-Marzán, Influence of Iodide Ions on the Growth of Gold Nanorods: Tuning Tip Curvature and Surface Plasmon Resonance, *Adv. Funct. Mater.* 2008, Volume *18*, 3870-3876.

[3] P.S. Kumar, I. Pastoriza-Santos, B. Rodríguez-González, F.J. García de Abajo, L.M. Liz-Marzán, High-Yield Synthesis and Optical Response of Gold Nanostars, *Nanotechnology* 2008, Volume 19, 015606(1-5).

[4] J. Matsuoka, H. Yoshida, H. Nasu, K. Kamiya, Preparation of gold microcrystal-doped TiO_2, ZrO_2 and Al_2O_3 films through sol–gel process, J. Sol–Gel Sci. Technol. 1997, Volume 9, 145–155.